

**CONSTITUTIVE AND NUMERICAL MODELING OF SOIL
AND SOIL-PILE INTERACTION FOR 3D APPLICATIONS
AND
KEALAKAHA STREAM BRIDGE CASE STUDY**



**FINAL PROJECT REPORT
by**

**Shentang Wang
Horst G. Brandes, Professor
and
Ian N. Robertson, Professor
University of Hawaii at Manoa**

Prepared in cooperation with the:

**State of Hawaii
Department of Transportation
Harbors Division
and
U.S. Department of Transportation
Federal Highway Administration**



**UNIVERSITY OF HAWAII
COLLEGE OF ENGINEERING**

DEPARTMENT OF CIVIL AND ENVIRONMENTAL ENGINEERING

Research Report UHM/CEE/11-07

December 2011

Technical Report Documentation Page

1. Report No. FHWA/HI-15-48054	2. Government Accession No.	3. Recipient's Catalog No.	
4. Title and Subtitle <i>Constitutive and Numerical Modeling of Soil and Soil-Pile Interaction for 3D Applications and Kealakaha Stream Bridge Case Study</i>		5. Report Date December 2011	
		6. Performing Organization Code	
7. Author(s) Shentang Wang, Horst G. Brandes and Ian N. Robertson		8. Performing Organization Report No. 48054	
9. Performing Organization Name and Address Department of Civil and Environmental Engineering University of Hawaii at Manoa 2540 Dole Street, Holmes Hall 383 Honolulu, HI 96822		10. Work Unit No. (TRAIS)	
		11. Contract or Grant No. 48054	
12. Sponsoring Agency Name and Address Hawaii Department of Transportation Highways Division 869 Punchbowl Street Honolulu, HI 96813		13. Type of Report and Period Covered Final Report, 2008-2011	
		14. Sponsoring Agency Code	
15. Supplementary Notes Project performed in cooperation with the Hawaii Department of Transportation and the Federal Highways Administration.			
16. Abstract This study is concerned with developing new modeling tools for predicting the response of the new Kealakaha Stream Bridge to static and dynamic loads, including seismic shaking. The bridge will span 220 meters, with the deck structure being curved and sloped. In addition, the piers will be resting on opposite sides of a very deep gulch. As a result, conventional two-dimensional modeling is considered inadequate and a full three-dimensional approach to address the soil-structure interaction problem becomes necessary. The difficulty with carrying out such a comprehensive modeling effort lies, in part, on the enormous computational resources that are necessary to achieve even a moderate degree of prediction detail. Thus a computationally efficient numerical technique becomes essential. This study focuses on developing specific formulation improvements that should provide substantial computational savings and improved predictions for general finite and infinite element numerical codes. The platform that is embraced in this study is the open source code OpenSees, which is rapidly becoming the framework of choice in the earthquake engineering community for complex soil-structure interaction problems. A number of advanced constitutive soil models and miscellaneous coding improvements have been incorporated into OpenSees. It is expected that the findings of this study should lead to a computational resource that will be able to provide useful predictions for the new Kealakaha bridge and other similar bridge structures. As part of this study, a generalized integration formulation is presented in tensorial form for 3D elastoplastic problems. Two special cases of this generalized formulation, the well known implicit and explicit integration schemes, are compared for four specific soil models with regard to accuracy and efficiency. A 20-node reduced-integration brick element is implemented for this purpose. The findings provide useful guidelines for selection of particular integration schemes for nonlinear 3D problems.			
17. Key Words SOIL-STRUCTURE INTERACTION, BRIDGES, OPENSEES, FOUNDATION ANALYSIS		18. Distribution Statement No restriction. This document is available to the public from the sponsoring agency at the website http://hidot.hawaii.gov .	
19. Security Classif. (of this report) Unclassified	20. Security Classif. (of this page) Unclassified	21. No. of Pages 211	22. Price

EXECUTIVE SUMMARY

This report provides an overview of the soils and geophysical investigation performed to characterize the foundation conditions for the Kealakaha Stream Bridge Replacement project. The enhanced understanding of soil parameters will allow for incorporation of soil-structure interaction in modeling of the bridge structure after future seismic events.

This report is based on a doctoral dissertation prepared by Shentang Wang in August 2006 under the direction of Professor Brandes. The dissertation research was performed prior to construction of the Kealakaha Stream Bridge. At that time the bridge design consisted of a single cell box-girder supported on two abutments and two piers, each with sixteen drilled shafts as foundation. Subsequent to this research, value engineering by the contractor changed the structural system to a multi-box girder over the piers and drop-in I-girders in each of the three spans. Friction pendulum base isolation was used to separate the superstructure from the substructure, resulting in a reduction of the number of drilled shafts below each pier foundation to nine in place of sixteen. Even though these changes to the structural system are significant, the results presented in this report can still be used to model the response of this bridge structure during future earthquake ground shaking.

This report also includes results of a geophysical investigation performed at the Kealakaha Stream Bridge site in 2007 under the direction of Professors Brandes and Robertson (Appendix F). The geophysical investigation was performed during the early phases of work on the Kealakaha Stream Bridge.

Finally, Appendix G includes two publications stemming from this work. The first appeared in the Summer 2006 edition of Hawaiian Connections, while the second is a paper printed in the June 2011 edition of the ASCE Journal of Geotechnical and Geoenvironmental Engineering.

ACKNOWLEDGEMENTS

The authors wish to acknowledge the assistance provided by Professors Phillip S.K. Ooi, Si-Hwan Park, and Ronald H. Knapp for their review of this report and serving on Dr. Wang's Dissertation Committee. This study was funded by a grant from the Hawaii Department of Transportation and the Federal Highway Administration. This support is gratefully acknowledged.

The contents of this report reflect the views of the authors, who are responsible for the facts and accuracy of the data presented herein. The contents do not necessarily reflect the official views or policies of the State of Hawaii, Department of Transportation or the Federal Highway Administration. This report does not constitute a standard, specification or regulation.

ABSTRACT

A new bridge has been proposed to replace the existing Kealakaha bridge on Route 19 on the Island of Hawaii. This study is concerned with developing new modeling tools for predicting the response of the new bridge to static and dynamic loads, including seismic shaking. The bridge will span 220 meters, with the deck structure being curved and sloped. In addition, the piers will be resting on opposite sides of a very deep gulch. As a result, conventional two-dimensional modeling is considered inadequate and a full three-dimensional approach to address the soil-structure interaction problem becomes necessary. The difficulty with carrying out such a comprehensive modeling effort lies, in part, on the enormous computational resources that are necessary to achieve even a moderate degree of prediction detail. Thus a computationally efficient numerical technique becomes essential. This study focuses on developing specific formulation improvements that should provide substantial computational savings and improved predictions for general finite and infinite element numerical codes. The platform that is embraced in this study is the open source code OpenSees, which is rapidly becoming the framework of choice in the earthquake engineering community for complex soil-structure interaction problems. A number of advanced constitutive soil models and miscellaneous coding improvements have been incorporated into OpenSees. It is expected that the findings of this study should lead to a computational resource that will be able to provide

useful predictions for the new Kealakaha bridge and other similar bridge structures.

As part of this study, a generalized integration formulation is presented in tensorial form for 3D elastoplastic problems. Two special cases of this generalized formulation, the well known implicit and explicit integration schemes, are compared for four specific soil models with regard to accuracy and efficiency. A 20-node reduced-integration brick element is implemented for this purpose. The findings provide useful guidelines for selection of particular integration schemes for nonlinear 3D problems.

The problem of soil-pile interaction, which is of integral importance to the Kealakaha Bridge project, is addressed with respect to the parameters that affect the response under lateral loading in cohesionless soil. To model the soil-pile interaction effect, a thin layer of interface elements, which have the same material properties as the surrounding soils, except for friction angle, were adopted. In addition, to improve the accuracy of the computations, a new method has been developed to generate the soil reaction forces along the pile. It was found that the coefficient of lateral earth pressure at rest, the unit weight, and the friction angle of the soil have only a minor effect on the development of lateral resistance. On the other hand, the initial Young's modulus of the soil and the stiffness of the pile play critical roles in determining the response of the pile.

Another important aspect of modeling with regard to the Kealakaha Bridge is the selection of an appropriate set of boundary conditions in the far field. This plays a crucial

role for earthquake loading since such boundaries must be able to properly absorb the incoming energy of seismic waves. An innovative and very efficient 3D semi-analytical infinite element has been developed to model these far-field effects without virtually any geometric limitations. The most important feature of the new infinite element is that it includes an analytical solution in the infinite direction for wave problems. This provides enormous savings in computation costs compared to conventional Gauss-Laguerre quadrature integration. Another important feature of this infinite element is that it is able to deal with body, shear and Rayleigh waves. Also, the need for large numbers of degrees of freedom, which would otherwise be required for a fine mesh in the far-field, can be reduced dramatically. By coupling of the far field with conventional 3D finite element discretisation of the near-field, which would include pile, pile cap, the nearby soil, and the bridge deck structure, it may now be feasible to model the whole of the Kealakahua bridge using 3D analysis. Although all the relevant equations for the new infinite element method are presented in this study, its implementation into OpenSees is left for a future study.

Chapter 1 provides an overview of the study and Chapters 2 through 4 present the detailed findings in manuscript form. Overall conclusions are presented in Chapter 5. The Appendix includes miscellaneous formulation details and four related publications that were prepared and published as part of this Dissertation.

Table of Contents

EXECUTIVE SUMMARY	iii
ACKNOWLEDGEMENTS	iii
ABSTRACT	v
1. INTRODUCTION	1
1.1 Background.....	1
1.2 OpenSees Structure.....	3
1.3 Contributions to OpenSees Code Development	3
1.4 Implementation of a Nonlinear Cyclic Soil Model.....	5
1.5 Implementation of a Generalized Integration Scheme.....	5
1.6 The Role of Soil Nonlinearity in the Response of Piles Subjected to Lateral Loading.....	7
1.7 Improved Far-Field Boundary Simulation for Soil-Structure Interaction Problems	8
1.8 Validation of Implemented Formulations	10
1.9 Recommendations for Further Work.....	10
2. GENERALIZED INTEGRATION FORMULATION AND ITS PERFORMANCE FOR THREE-INVARIANT ELASTO-PLASTIC GEOMATERIALS	12
2.1 Introduction.....	12
2.2 Elastic Prediction	14
2.3 Plastic Corrections	16
2.4 Implementation of Formulation into OpenSees.....	27
2.5 Performance of Implicit and Explicit Integration	29
2.6 Conclusions.....	34

2.7	References:.....	35
3.	PRESSURE-DEPENDENT NONLINEAR LATERAL RESISTANCE OF SINGLE PILE IN COHESIONLESS SOIL.....	37
3.1	Introduction.....	37
3.2	Soil and Pile Constitutive Models.....	39
3.3	Finite Element Modeling	41
3.4	Methods to Determine Soil Resistance P and Pile Moment M	42
3.5	Coefficient of Lateral Earth Pressure at Rest.....	43
3.6	Unit Weight of Soil	46
3.7	Mean Soil Pressure	48
3.8	Initial Young's Modulus E_o	49
3.9	Pile Diameter	51
3.10	Pile Young's Modulus E_p	53
3.11	Soil Friction Angle.....	55
3.12	Conclusions.....	57
3.13	References.....	57
4.	FORMULATION OF TIME-DOMAIN SEISMIC SOIL-STRUCTURE INTERACTION USING A COUPLED FINITE AND INFINITE ELEMENT APPROACH.....	60
4.1	Introduction.....	60
4.2	Spatial Discretization of Kealakaha Modeling Domain	65
4.3	The Mapping and Shape Functions of the Semi-Infinite Element.....	66
4.4	Dynamic Stiffness of the Semi-Infinite Element in the Frequency Domain.....	68
4.5	Equation of Motion for Soil-Structure Systems.....	72
4.6	Equation of Motion in the Time Domain.....	74
4.7	Recursive Procedure for Solution of the Equation of Motion in the	

Time Domain	75
4.8 Conclusions.....	77
4.9 References.....	77
5. CONCLUSIONS	80
APPENDIX A CONSTITUTIVE MODEL DERIVATIVES	82
APPENDIX B THE ROLE OF THE INTERMEDIATE STRESS IN OFFSHORE SLOPE SEDIMENT MODELING	88
APPENDIX C OPENSEES MODELING OF THE 3D PLASTIC BEHAVIOR OF UNDERWATER SLOPES: ACHIEVEMENTS AND LIMITATIONS.....	106
APPENDIX D CYCLIC SIMPLE SHEAR TESTING AND MODELING OF AN OFFSHORE FINE SAND.....	121
APPENDIX E FAILURE AND POST-FAILURE MECHANICS OF SUBMARINE LANDSLIDES.....	136
APPENDIX F SEISMIC REFRACTION AND MASW SURVEYS FOR INVESTIGATION OF SUBSURFACE CONDITIONS AT KEALAKAHA STREAM REPLACEMENT BRIDGE	154
APPENDIX G PUBLICATIONS IN HAWAIIAN CONNECTIONS AND JOURNAL OF GEOTECHNICAL AND GEOENVIRONMENTAL ENGINEERING	171
REFERENCES.....	188

List of Tables

<u>Table</u>	<u>Page</u>
2-1 Plastic correction procedure.....	22
2-2 Root finding procedure.	23
2-3 Modified Pegasus unload-reload procedure.....	26
2-4 General characteristics of selected elastoplastic models.	27
2-5 Material properties and initial conditions for simulation runs.....	29
C-1 Soil properties	111
D-1 Testing program	124
E-1 Underwater landslide causes and triggers.....	139
E-2 Material constants for cyclic model.....	146

List of Figures

<u>Figure</u>	<u>Page</u>
1.1 Geometry of the Kealakaha Bridge (m).....	1
1.2 Pile behavior predicted by PLAXIS and OpenSees.....	10
2.1 Elastic prediction and plastic correction paths.....	15
2.2 Predicted unloading-reloading stress path.	25
2.3 Yield surfaces for selected constitutive models.	28
2.4 Stress paths in the deviatoric plane.....	29
2.5 Stress-strain prediction for DP and EMC models.....	31
2.6 The relative errors and time consuming of explicit and implicit integrations in DP and EMC models for LP-2 ($\theta = 300$) loading path.....	31
2.7 Stress-strain prediction for MCC and GCC models.	33
2.8 The relative errors and time consuming of explicit and implicit integrations in MCC and GCC models for LP-2 ($\theta = 300$) loading path.	34
3.1 Finite mesh used in the computation of moments.	39
3.2 Schematic for calculation of pile elements.....	43
3.3 Range of coefficient of lateral earth pressure at rest K_0 prior to lateral loading.	44
3.4 Initial stress conditions investigated.....	45
3.5 Effect of K_0 (Final lateral load $P = 671$ kN).....	46
3.6 Effect of γ (Final lateral load $P = 671$ kN).....	48
3.7 Effect of initial mean soil pressure p (Final lateral load $P = 671$ kN)	49
3.8 Effect of E_0 (Final lateral load $P = 671$ kN).....	50
3.9 Effect of D	52

3.10	Effect of E_p (Final lateral load $P = 671$ kN).....	54
3.11	Effect of E_0 and E_p (Final lateral load $P = 671$ kN).....	55
3.12	Effect of friction angle ϕ (Final lateral load $P = 671$ kN).....	56
4.1	Schematic representation of analysis model using FE and IE.....	61
4.2	Configurations and local coordinates of infinite element (IE).....	65
B.1	3D slope geometry.	90
B.2	Failure pattern for DP model.	93
B.3	Yield locations in yz-plane (DP soil model).	94
B.4	Stress paths for point D.....	95
B.5	Stress paths for point E.	96
B.6	Stress paths for point F.....	97
B.7	Deformed mesh - DP model (exaggerated by a factor of 15).....	98
B.8	Deformed mesh viewed from yz boundary (DP model).....	98
B.9	Deformed mesh viewed from xz boundary (DP model).....	99
B.10	Displacements at points D, E and F (Model DP).....	100
B.11	Displacements in x, y and z directions (Model DP).	101
B.12	Deformed mesh viewed from yz boundary (EMC model).....	102
B.13	Model comparisons for displacements at point E.....	103
C.1	Extended Drucker Prager model (EDP-I).....	108
C.2	Modified Drucker Prager model (MDP-C).....	110
C.3	2D slope geometry before and after self-weight consolidation.....	111
C.4	3D slope geometry before and after self-weight consolidation.....	113
C.5	2D slope with surface surcharge.....	113

C.6	Yield points for EDP-I model	114
C.7	Yield points for MDP-C model.....	115
C.8	Selected stress paths for model EDP-I (2D)	115
C.9	Selected stress paths for model MDP-C (2D).....	116
C.10	Volumetric strains for model MDP-C (2D)	117
C.11	Downslope displacement profiles	118
C.12	Cross section of deformed 2D mesh.....	118
D.1	Microphotograph of test sand (oversized shell fragments were removed prior to specimen preparation).....	122
D.2	Grain size distribution of sand tested.....	123
D.3	Low-density test results, LD-3.....	125
D.4	Shear stress-strain results, LD-3.....	126
D.5	High-density test results, HD-3.....	127
D.6	Shear stress-strain results, HD-3.....	128
D.7	CSR versus number of cycles to failure (NL).....	129
D.8	Shear modulus degradation for high and low density tests.....	130
D.9	Model parameters illustrated in conjunction with experimental data for cycle N=8, test LD-3.....	131
D.10	(a) Test results, LD-3; (b) predictions for test LD-3	132
D.11	Pore pressure ratio data and prediction, test LD-3.....	133
D.12	Pore pressure data and prediction, test HD-3.....	133
E.1	Limited distortion of continental slope sediments.....	138
E.2	Conceptual soil behavior up to steady-state.....	140
E.3	Undrained cyclic behavior of quartz sand, $D_r=50\%$, $CSR=0.22$, no initial driving stress (Seed et al., 2001).....	142

E.4	Undrained cyclic behavior of quartz sand, $D_r=50\%$, $CSR=0.22$, no initial driving stress (Seed et al., 2001).....	143
E.5	Model predictions for case of no bias in cyclic shear stress.....	146
E.6	Model predictions for case of cyclic loading with initial conditions.....	147
E.7	Bulk energy considerations during landsliding.....	149

Chapter 1

Introduction

1.1 Background

The impetus for this study came from the need to provide state of the art static and seismic soil-structure interaction modeling capabilities for the design and monitoring of the planned Kealakaha bridge replacement. This bridge will be located on Highway 19, in the Hamakua District of the Island of Hawaii. Modeling this structure (Figure 1.1) is a

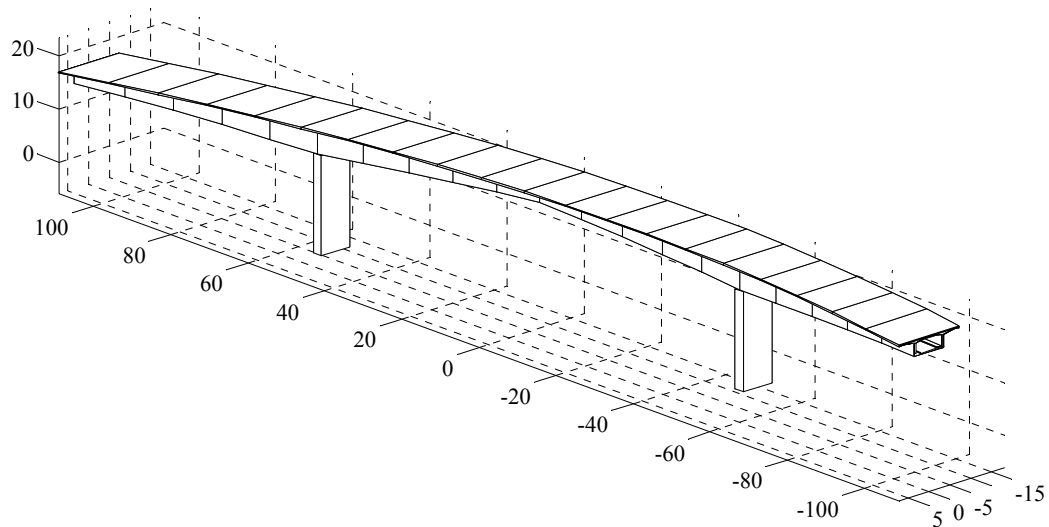


Figure 1.1 Geometry of the Kealakaha Bridge (m)

challenging proposition if any reasonable amount of geometric and material detail is desired. The bridge is curved, sloped and crosses a deep gulch with steep slopes on either side. General soil conditions vary from basaltic residual soils near the surface, including varying amounts of potentially high plasticity ash soils, to basaltic rock that decreases in

weathering with depth. The replacement structure will consist of a combination of box and pre-tensioned girders resting on two piers and two abutments, which in turn will be supported on piles. The bridge will span approximately 220 meters from one end to the other. The site is subject to periodic earthquake shaking that can be quite intense. The USGS estimates horizontal ground accelerations on the order of 0.6g with a 2% probability of exceedance in 50 years.

These complexities rule out a conventional two-dimensional modeling approach and instead require a full three-dimensional geometry. Furthermore, a relatively fine mesh is necessary near the pier foundations to properly account for interaction between the structural components and the surrounding soil. Taken together, these requirements place a tremendous burden on computations. In fact, the level of modeling detail sought for this particular bridge has not been reported for any comparable dynamic problem that encompasses all structural and soil components, i.e. bridge deck, abutments, piers, piles and non-homogeneous foundation soils. Comprehensive numerical predictions of this type are still out of reach for most computational platforms. However, significant progress is under way. On the forefront of computational earthquake engineering is the development of the open source framework OpenSees (2004) for finite element analysis. This code was initiated at the Pacific Earthquake Engineering Research Center with the express purpose of providing a quantum leap in the ability to model complex problems such as the one posed by the new Kealakaha bridge. However, much of the work has centered on providing a core computational engine and specific provisions for structural problems, with a few notable exceptions. This study makes substantial contributions to the OpenSees code with regard to the implementation of advanced soil constitutive models, evaluation of numerical integration strategies, investigation of simplified soil-pile interaction, and development of advanced infinite elements for a proper accounting of all seismic wave components propagating from the far field. The collective purpose of these developments is to improve prediction accuracy and numerical efficiency so that the Kealakaha replacement bridge can be analyzed in its entirety in the near future.

1.2 OpenSees Structure

OpenSees is an object-oriented numerical framework coded in C++ language for finite element analysis. Because of its open-source character, new components can be easily added without the need to change existing code. Core components, which make sure new components can be added and accommodated without difficulties, are in the form of abstract base classes in C++. Components are classified into four main types of functions, i.e. creation of finite element model, specification of analysis procedure, monitoring of analysis, and output of results. Correspondingly, four types of objects, the ModelBuilder, Domain, Analysis, and Recorder, are constructed in a typical analysis.

The ModelBuilder object is responsible for building the Node, Mass, Material, Section, Element, LoadPattern, TimeSeries, Transformation, Block, and Constraint objects and adding them to the Domain. The Domain is responsible for storing the objects created by the ModelBuilder and providing access to these objects for the Analysis and Recorder. The Analysis object can handle both static and transient nonlinear analysis and is composed of the following component objects: the ConstraintHandler, DOF_Numberer, AnalysisModel, SolutionAlgorithm, Integrator, SystemOfEqn, and Solver. The Recorder object records what the user specifies such as the displacement history at a node, stress or strain history at a Gauss point in an element, and the global coordinates of the Gauss points.

1.3 Contributions to OpenSees Code Development

In the present version of OpenSees, the available element types include the truss, corotational truss, nonlinear beam-column, quadrilateral, solid-fluid fully coupled brick, eight-node brick, and twenty-node brick elements. Among these elements, the nonlinear beam-column and brick elements can be chosen for three-dimensional analysis. However, the twenty seven-point Gauss integration scheme employed by the existing brick elements is not efficient. A more efficient reduced-integration-point integration scheme (Irons 1971) is implemented as part of this study by reducing the number of Gausspoints from 27 to 14 without losing significant precision. The number of integration points can

be further reduced to 6 with only a slight cost in the precision. Eight-node and twenty-node brick elements have been coded into OpenSees, with the number of integration points specified by the user depending on particular needs of efficiency and precision.

The corresponding three-dimensional material models in the present version include elastic-isotropic, Drucker-Prager, von-Mises, modified Cam-clay, rounded Mohr-Coulomb, Mazari-Dafalias, pressure-dependent elastic, fluid-solid-porous material, multi-yield-surface, pressure-dependent and pressure-independent multi-yield-surface models. These models have been developed by different researchers and often require their own type of brick elements. For example, the pressure-dependent and pressure-independent multi-yield-surface material models use a solid-fluid fully coupled element. In our study, the third stress-invariant is considered important. Therefore, a generalized Cam-clay model, an extended Mohr-Coulomb model, a cap model (also used in the code ABAQUS (2003)), and a modified Drucker-Prager model have been formulated and coded into OpenSees. All these models take the third stress-invariant into consideration. The formulation and derivations of Drucker-Prager, extended Mohr-Coulomb, modified Cam-clay and general Cam-clay models can be found in Appendix A. The associated or non-associated flow rule can be specified by users as input options for these models. The cap model was used to analyze the 3D plastic behavior of underwater slopes (Appendix C).

The initial stress states at integration points are critical for these constitutive models. This is discussed in Chapter 3. However, the determination of the initial stress state is problematic in the current version of OpenSees, at least for brick elements. In the current version, the initial stress state is obtained through self-weight analysis by allowing a single vertical degree of freedom for each node, except for nodes on bottom boundaries of typical 3D problems where they are fixed in all three directions. But when the fixity of nodes is changed for subsequent analysis, the restraint of the node is automatically replaced with zero nodal force. This not only causes numerical problems if complex elastoplastic constitutive models are employed, but also causes erroneous results

altogether. The code has been changed to fix this problem. The corrected version of OpenSees can replace a restraint with the corresponding nodal resistance force as necessary to maintain continued equilibrium.

In the current version of OpenSees, the material must be the same for all the loading stages. Users can not change the material properties after the initial stress state is obtained. Some elastoplastic constitutive models, for example the Cap model and the Cam-clay model, can result in large displacements in the self-weight loading stage. Such large displacements may be problematic for later stages of the analysis. For example, it may cause displacement inconsistencies. In this study, changes have been instituted to allow the user to change material properties midway through the modeling process. For example, deformations during self-weight analysis can be kept to a minimum by employing a 3D elastic constitutive model with large elastic stiffness constants. Thereafter, the constitutive model can be changed to a more complex elastoplastic one.

1.4 Implementation of a Nonlinear Cyclic Soil Model

Although advanced constitutive models are appealing for dealing with large-scale static loading problems, their performance can be less satisfactory when dealing with dynamic problems due to the typically large number of material properties that need to be considered. Computation costs are usually higher when compared with simpler cyclic constitutive soil models. The nonlinear cyclic soil model presented by Finn et al. (1977), and later modified by Liyanapathirana and Poulos (2002a; 2002b), was tested and implemented in a Matlab code. This program was employed to examine the failure and post-failure of submarine landslides and the cyclic behavior of an offshore fine sand. The findings were published in two articles (Brandes and Wang 2004; Brandes, Seidman et al. 2005). These manuscripts are included in Appendices E and Appendix D.

1.5 Implementation of a Generalized Integration Scheme

The integration of elastoplastic constitutive relations at Gauss integration points is very time consuming for complex material models when compared to simple elastic models.

In addition, the overall accuracy of the analysis is directly related to the accuracy of the numerical algorithm used to integrate the constitutive relations. Beginning in the 1950's, Drucker and Prager developed the first formal framework for modeling inelastic behavior of soils. Ever more complicated constitutive models have been proposed through the years, including the following ones: von-Mises (1913), Drucker-Prager (Drucker, Gibson et al. 1957), Lade and Duncan (Lade 1977), Mohr-Coulomb (Coulomb 1972), Lade double hardening (Lade 1977), Cam-clay (Roscoe, Schofield et al. 1963), Matsuoka and Nakai (1974), and various three-stress-invariant Cam-clay models (Alawaji, Runesson et al. 1992; Peric and Huang 2003). The more complicated the constitutive model, the more efficient the necessary integration strategy needs to be. Single-step explicit integration was used early on for relatively simple J_2 -type models, i.e. the von-Mises and Drucker-Prager models. It requires small loading steps and is only conditionally stable for highly non-linear constitutive models (Bathe and Wilson 1976; Ortiz and Simo 1986).

Since the early 1990s, the implicit integration scheme has commanded more and more attention due to its unconditional stability and its accuracy. But as the third stress invariant is incorporated into the potential function in some of the more complex constitutive models, evaluation of the corresponding numerical derivatives, which are necessary for integration, becomes very time consuming. Therefore, most implicit integration implementations are limited to simple non-associated potential functions to avoid computing such derivatives (Borja 1991; Hofstetter, Simo et al. 1993; Simo and Meschke 1993; Borst and Groen 2000; Luccioni, Pestana et al. 2000; Palazzo, Rosati et al. 2001; Rouainia and Wood 2001; Ahadi and Krenk 2003). Jeremic and Sture (1997) may have been the first to propose a general purpose, fully implicit integration formula for geomaterials. Three-invariant elastoplastic models can easily be coded into computer programs since the related derivatives are expressed in analytical form. An even more general scheme, the generalized midpoint integration scheme, which includes the explicit and implicit schemes as particular cases, has also been proposed (Simo and Taylor 1986; Fushi, Peric et al. 1992). But as is often the case with implicit integration schemes, their implementation is usually limited to particular constitutive models. In this study, midpoint integration has been formulated and incorporated into OpenSees in order to

accommodate a variety of soil models, including isotropic, anisotropic, simple kinematic and mixed hardening models. The performance of two particular schemes, the explicit and implicit integration algorithms, which are special cases of the midpoint procedure, are evaluated in relation to four particular soil models. Guidelines are also provided for choosing a particular integration scheme. A detailed discussion and example computations using this generalized integration scheme are presented in Chapter 2.

1.6 The Role of Soil Nonlinearity in the Response of Piles Subjected to Lateral Loading

The nonlinear character of soils plays an important role in lateral loading capacity, whether for static or seismic problems. This aspect of soil-structure interaction is of particular relevance to modeling of the Kealakaha Bridge. Chapter 3 evaluates the factors that influence the behavior of a single pile in cohesionless soil under static lateral loading. The three-stress-invariant extended Mohr-Coulomb model with non-associated flow rule is employed to investigate the effect of the third stress invariant. The factors considered include the coefficient of lateral earth pressure at rest, the unit weight of soil, the friction angle, the initial Young's modulus of the soil, and the diameter and stiffness of the pile. Some of these factors are ignored by the simplified methods that are typically used in engineering practice. For example, the ultimate lateral resistance formulas by Broms (1964a) and Fleming et al. (1992) do not count on the coefficient of lateral earth pressure at rest, the Young's modulus of the soil and the stiffness of the pile, at least not directly. The semi-analytical p - y analysis method (Reese, Cox et al. 1974), which is based on a beam-on-elastic foundation analysis and experimentally-derived p - y curves, can account for Young's modulus of the soil and the stiffness of piles. In reality, the mechanism of lateral pile resistance is complicated and the simplified methods make far-reaching assumptions. Lateral pile resistance not only involves three dimensional effects, but also involves nonlinear behavior of both soil and pile. The contrasting properties of the pile and soil materials make it even more difficult to obtain a realistic analytical solution. To evaluate the roles of all the factors mentioned above, the finite element method may be the best choice. Chapter 3 shows that in some cases 3D finite element computations can be at odds with predictions from the simplified methods.

1.7 Improved Far-Field Boundary Simulation for Soil-Structure Interaction Problems

Soil-structure systems under dynamic loading have been studied extensively using the FE method. Due to limitations in computational resources, most of these studies have been performed in two dimensions and the materials have been assumed to be linearly elastic or viscoelastic. In order to model structures embedded in a semi-infinite half space, the typical approach has been to define a finite (bounded) region that includes for example a pile, or piles, and the surrounding soil. This domain is analyzed using the FE method, which can account for the nonlinear behavior of the materials in the time domain. The far-field (unbounded) region is then represented by various artificial transmitting boundaries (Lysmer and Kuhlemeyer 1969; Kausel 1974; Smith 1974; Kausel, Rosset et al. 1975; White, Valliappan et al. 1977; Akiyoshi 1978), or it is modeled by the boundary element (BE) method (Zienkiewicz, Kelly et al. 1977; Banerjee 1978; Kaynia and Kausel 1982; Beer 1986).

Since dynamic problems involve wave propagation and modification, any artificial boundaries must be designed to absorb all out-going waves so that no reflection can occur back into the inner domain. However, due to the complicated nature of wave propagation and reflection, it is impossible to account properly for all the wave components generated in the domain during random earthquake shaking. The BE method is a powerful tool to model infinite three-dimensional space because it effectively reduces 3D geometries to only two. In addition, radiation conditions at the infinite boundary can be satisfied precisely by employing a fundamental solution. However, fundamental solutions are unrealistic for problems where such solutions do not exist or where they are too complicated (Wolf 2003). The need for storage of the entire global stiffness matrix, which becomes nonsymmetric, further reduces the attractiveness of the BE method for soil-pile-structure interaction problems.

Another method to model infinite boundaries is the newly-developed scaled boundary finite element (SBFE) method. It is formulated to adopt the advantages of the FE and BE

methods for analysis of semi-infinite complex boundary value problems. (Zhang, Wegner et al. 1999; Wolf and Song 2001; Doherty and Deeks 2003; Wolf 2003; Doherty and Deeks 2004). By applying a particular analytical solution in the infinite direction, it not only reduces the amount of spatial discretisation needed, but it can also satisfy boundary conditions precisely at infinite locations. In addition, it does not require a fundamental solution, which makes it much easier to implement. However, not all the integrands in the infinite direction are integratable for wave propagation problems involving seismic loading. In these cases, the numerical integration procedure, which takes much time, is still required. The other limitation is that the SBFEM uses time-consuming reverse Fourier transformation to transform the dynamic stiffness matrix from the frequency domain to the time domain for each element.

The infinite element (IE) method (Ungless 1973; Bettess 1977) deals with infinite domains using finite elements. By applying special interpolation functions in the infinite direction and traditional interpolation functions in the finite directions, the unbounded problem can be solved within the frame work of the FE method. Recently, an analytical frequency-dependent infinite element has been developed by Yun et al. (2000). This type of infinite element uses three types of special shape functions to simplify discretisation of multiple soil layers. It was later extended from the frequency domain to the time domain by Kim and Yun (2000). Application of two-dimensional multi-wave infinite elements to earthquake engineering problems in the time domain is reported by Choi et al. (2001). Park et al. (2004) present a three-dimensional analytical infinite element in the frequency domain based on the two-dimensional analytical frequency domain infinite elements developed by Yun et al. (2000). However, this type of 3D infinite element can only handle a curved interface between the bounded near-field and the unbounded far-field. This study presents a new semi-analytical three dimensional infinite element, based on the infinite elements mentioned above, for use in the time domain. This type of element can deal with multi-wave components and with seismic soil-pile-structure interaction problems in the time domain. The other advantage of this particular element is that it can model the far field, regardless of the shape of the near field domain. A detailed presentation of the corresponding element equations is presented in Chapter 4.

1.8 Validation of Implemented Formulations

The general midpoint integration formulations and the brick element with reduced integration points that have been implemented in OpenSees were validated by comparing the predictions with the theoretical solution for the MCC model under triaxial compression loading. The plastic shear stress-strain curves in Figures 2.7a and 2.7b reveal that the formulation predicts the theoretical results well.

In addition, the Extended Mohr-Coulomb model and the 8-node brick element with reduced integration implemented into OpenSees were validated by comparing the predictions against those obtained using the commercial code PLAXIS for a single pile in cohesionless soil under lateral loading. Figure 1.2 indicates that the behavior of the pile predicted by OpenSees is slightly stiffer than that obtained with PLAXIS. The main reason is that the soil material is pressure-dependent in OpenSees, but is not in PLAXIS. Nonetheless, the results are quite similar.

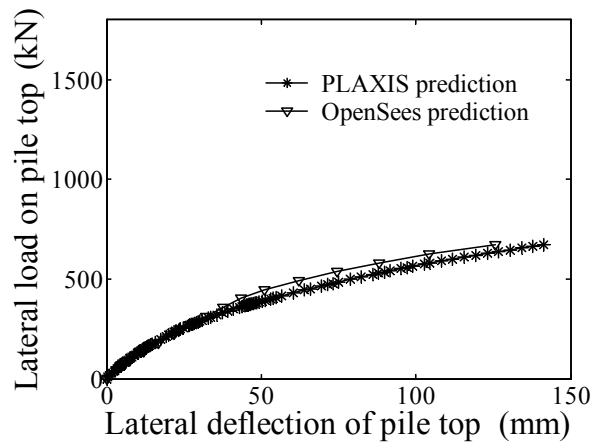


Figure 1.2 Pile behavior predicted by PLAXIS and OpenSees

1.9 Recommendations for Further Work

Reduced integration 8-node and 20-node brick elements for particular elastoplastic soil

models have been developed and coded into the OpenSees. It should now be feasible to carry out static soil-structure interaction analyses for the Kealakaha Bridge with an acceptable level of detail using readily available computational platforms. However, for even better performance of OpenSees, a more efficient interface element, as described in (Harnau, Konyukhov et al. 2005) could be implemented.

In addition, the semi-analytical infinite element described in Chapter 4 needs to be coded into OpenSees. The resulting formulation then needs to be verified, perhaps including seismic analysis of a limited portion of the Kealakaha bridge replacement. This may for example include one pier, pile cap, piles and surrounding soils.

To obtain the seismic load for 3D problems on the interface of the near-field and far-field is still a challenging proposition, even with the help of commercial computer programs such as Shake 2000. An alternative is to use the coupled FE and IE approach described in Chapter 4 to generate the boundary loading by means of a free-field analysis.

Chapter 2

Generalized Integration Formulation and Its Performance for Three-Invariant Elasto-Plastic Geomaterials

Abstract

A generalized integration algorithm for three-invariant elastoplastic soil models is described in tensorial form. This algorithm can be used in conjunction with isotropic, kinematic, and mixed hardening materials. By selecting the value of a single integration parameter, the well-known explicit and fully implicit formulations become two special cases in this general scheme. The performances of explicit and fully implicit integration are evaluated for the Drucker-Prager, extended Mohr-Coulomb, modified Cam-clay, and general Cam-clay models. It is found that the explicit and fully implicit integration provide similar levels of accuracy, but the former saves computational time. For complicated elastoplastic soil models, such as three-invariant general Cam-clay model, the advantages of explicit integration over fully implicit integration are discussed further.

Keywords: Generalized integration, explicit, fully implicit, Cam-clay

2.1 Introduction

Numerical integration of elastoplastic constitutive relationships at Gauss point level is usually accomplished by some variant of the general Newton method. A multitude of algorithms have been proposed, ranging from very simple explicit to fully implicit schemes. Fully implicit integration, which is generally regarded as unconditionally stable

(Ortiz and Popov 1985; Simo and Taylor 1986) and more accurate (Borst and Feenstra 1990; Schellekens and Borst 1990; Borst and Groen 2000) than explicit integration, is more difficult to implement for complex soil materials that require consideration of three dimensional stress space and general hardening and softening behavior. In this paper, we present a generalized integration formulation for three-invariant isotropic elastoplastic soil that includes explicit, partially implicit and fully implicit methods as special cases. The formulation is based on the generalized midpoint rule procedure of Ortiz and Popov (1985), but here we present the full set of incremental equations in tensorial form necessary for implementation in a numerical framework. The general formulation is consistent with a wide range of common soil elastoplastic constitutive relations, providing first order accuracy, convergence and numerical stability. Performance of the formulation is investigated with regard to four soil models of varying degrees of complexity. They are the Drucker-Prager (DP), Extended Mohr-Coulomb (EMC), General Cam-clay (GCC) and Modified Cam-clay (MCC) models. The corresponding derivatives for each of the models are included. The generalized formulation has been incorporated into the code OpenSees and its performance is evaluated with regard to various integration options and the four soil models. It should be noted that particular explicit and fully implicit tensorial versions of this general formulation have been presented in the past in connection with specific soil models (Jeremic and Sture 1997; Sloan, Abbo et al. 2001), but they generally do not permit a systematic comparison between explicit and implicit methods based on a common parent formulation, nor do they usually address more than one particular soil model at a time.

The performance of explicit versus implicit integration methods has been addressed in many studies, but the conclusions with regard to accuracy, stability and convergence are not always consistent. This is to be expected given the crucial role that size of increment, shape of yield surface, and general complexity of the particular soil model play. For example, Zhang (1995) reports that explicit integration runs into convergence difficulties for his adopted J_2 elastoplasticity model when the strain increment is large. Potts and Ganendra (1992) note that for the modified Cam clay model, use of the modified Newton-Rhapson method in conjunction with the explicit integration algorithm proposed

by Sloan (1987) leads to more accurate and efficient computations compared to the implicit method. Sheng and Sloan (2001) report that for critical soil models the accuracy of explicit integration is influenced by the size of the load increment, the type of flow rule, and the overconsolidation ratio. Comparative studies on the performance of the two integration strategies as applied to classical plasticity have also led to inconsistent performance trends (Gens and Potts 1988; Borst and Feenstra 1990; Yamaguchi 1993; Potts and Ganendra 1994). Borst and Feenstra (1990) found that the implicit method performs better than the explicit method when material models have a non-constant curvature in principal stress space. Gens and Potts (1988) investigated the performance of explicit, modified Euler, mid-point, and fully implicit Runge-Kutta-England 4th and 5th order algorithms with regard to the modified Cam clay model. Their findings indicate that the explicit and fully implicit methods yield the same level accuracy and that the explicit scheme may be more advantageous than higher order methods when trying to achieve moderate degrees of accuracy. Potts and Ganendra (1994) compare the implicit scheme to an explicit method with substepping for the modified Cam clay soil model. For larger strain increments, the substepping algorithm is more accurate than the implicit one.

As studies such as these indicate, it is difficult to draw broad conclusions on the merits of one method over the other. The general formulation that is described in this article allows us to revisit the performance of explicit and fully implicit schemes, in this case obtained from the same parent formulation through selection of specific values of a single algorithmic parameter. This new formulation has been compared to theoretical predictions for MCC model and it appears to make reasonable predictions.

2.2 Elastic Prediction

Given a strain increment $d\varepsilon_{kl}$ for a particular time increment Δt , the stress and hardening parameters can be determined by applying the Kuhn-Tucker loading unloading conditions of plasticity:

$$f(\sigma_{pq}, k^i, \alpha_{pq}^j) \leq 0 \quad (0.1)$$

$$d\lambda \geq 0 \quad (0.2)$$

$$f d\lambda = 0 \quad (0.3)$$

Where f is the yield function, k^i are a set of scalar hardening variables, α_{pq}^j are a set of tensor hardening variables, and λ is a plastic multiplier that is related to the magnitude of the plastic strain. If a Newton-type scheme is employed to solve the system of non-linear equations at the global level, the consistent tangent stiffness tensor E_{pqkl}^{ep} must also be known. At the beginning of a particular time increment, i.e. at time t (point A in Figure 2.1), the stresses and hardening parameters can be expressed as ${}^t\sigma_{pq}$, ${}^t k^i$, and ${}^t\alpha_{pq}^j$, respectively.

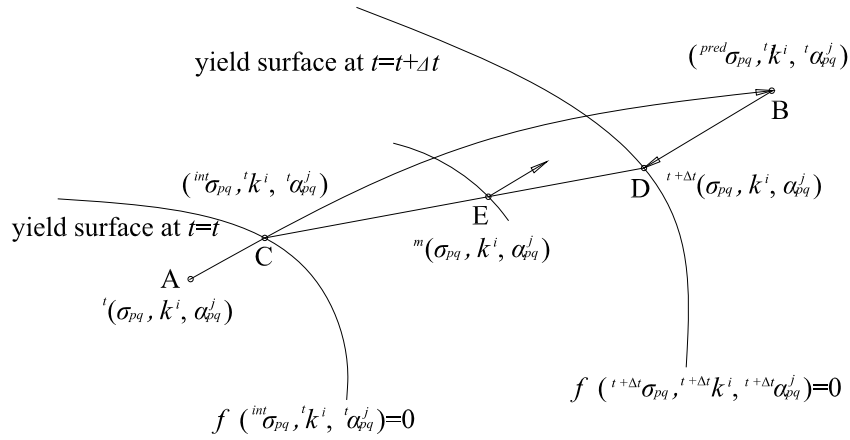


Figure 2.1 Elastic prediction and plastic correction paths.

The superscripts i and j vary between 1 and the number of hardening variables that need to be considered. At the start of the increment, the Kuhn-Tucker condition $f({}^t\sigma_{pq}, {}^t k^i, {}^t\alpha_{pq}^j) \leq F_{tol}$ is assumed to have been satisfied previously. The allowable magnitude of F_{tol} depends on the system of units and the precision of the computation platform, but is typically assumed in the range of 10^{-5} and 10^{-10} . For the time increment Δt at hand, a set of new elastic stresses can be predicted as:

$${}^{pred}\sigma_{pq} = {}^t\sigma_{pq} + E_{pqkl} d\varepsilon_{kl} \quad (0.4)$$

where E_{pqkl} is elastic stiffness tensor. If these predicted stresses satisfy the condition $f({}^{pred}\sigma_{pq}, {}^t k^i, {}^t\alpha_{pq}^j) \leq F_{tol}$, an acceptable end condition has been achieved and no plastic

correction phase is required. In this case, the updated set of variables at time $t+\Delta t$ become ${}^{t+\Delta t}\sigma_{pq} = {}^{pred}\sigma_{pq}$, ${}^{t+\Delta t}k^i = {}^tk^i$, and ${}^{t+\Delta t}\alpha^j_{pq} = {}^t\alpha^j_{pq}$.

2.3 Plastic Corrections

If the stresses predicted by Equation (0.4) are such that the Kuhn-Tucker criteria are not met, the material will have yielded and a new yield surface will have been established (Figure 2.1). A new set of stresses and hardening parameters, i.e. ${}^{t+\Delta t}(\sigma_{pq}, k^i, \alpha^j_{pq})$, need to be determined corresponding to this new condition (say point D in Figure 2.1). Thus a correction scheme needs to be used to arrive at D from the predicted state at B . A wide range of methods can be considered. If explicit integration is adopted, a corrected state can be obtained with a plastic flow direction evaluated either at the intersection point C (Sloan 1987) or at the predicted point B (Borst and Feenstra 1990). On the other hand, implicit integration uses either a plastic flow direction (and corresponding hardening parameter gradients) computed at the midpoint between states C and D (Point E), or the weighted average values at point C and point D (Ortiz and Popov 1985). Here we adopt the midpoint integration scheme.

At the end of time $t+\Delta t$, the converged stresses and hardening parameters ${}^{t+\Delta t}(\sigma_{pq}, k^i, \alpha^j_{pq})$ at point D should meet the following conditions:

$${}^{t+\Delta t}\sigma_{pq} - {}^{pred}\sigma_{pq} + \lambda E_{pqkl} {}^m B_{kl} = 0 \quad (0.5)$$

$${}^{t+\Delta t}k^i - {}^tk^i - \lambda {}^m \left(\frac{dk^i}{d\lambda} \right) = 0 \quad (0.6)$$

$${}^{t+\Delta t}\alpha^j_{pq} - {}^t\alpha^j_{pq} - \lambda {}^m \left(\frac{d\alpha^j_{pq}}{d\lambda} \right) = 0 \quad (0.7)$$

$$f({}^{t+\Delta t}\sigma_{pq}, {}^{t+\Delta t}k^i, {}^{t+\Delta t}\alpha^j_{pq}) = 0 \quad (0.8)$$

where ${}^m B_{kl} = {}^m (\partial g / \partial \sigma_{kl})$, the superscript m refers to the midpoint E and g is the plastic potential. In these equations, the primary unknowns are ${}^{t+\Delta t}\sigma_{pq}$, ${}^{t+\Delta t}k^i$, ${}^{t+\Delta t}\alpha^j_{pq}$, and λ . Note that ${}^m B_{kl}$, ${}^m (dk^i/d\lambda)$, and ${}^m (d\alpha^j_{pq}/d\lambda)$ are secondary unknowns that are functions of the primary unknowns and are evaluated at the stress state ${}^m(\sigma_{pq}, k^i, \alpha^j_{pq})$, which represents the midpoint between the intersection stress state (${}^{int}\sigma_{pq}, k^i, \alpha^j_{pq}$) and the final

stress state ${}^{t+\Delta t}(\sigma_{pq}, k^i, \alpha^j_{pq})$. The midpoint stresses and hardening parameters can be expressed as:

$${}^m\sigma_{pq} = {}^{int}\sigma_{pq}(1-\beta) + {}^{t+\Delta t}\sigma_{pq}\beta \quad (0.9)$$

$${}^m k^i = {}^t k^i(1-\beta) + {}^{t+\Delta t} k^i \beta \quad (0.10)$$

$${}^m \alpha^j_{pq} = {}^t \alpha^j_{pq}(1-\beta) + {}^{t+\Delta t} \alpha^j_{pq} \beta \quad (0.11)$$

where β is a general integration parameter ($0 \leq \beta \leq 1$), the choice of which leads to various integration schemes. ${}^{int}\sigma_{pq}$ can be obtained explicitly by a procedure described below. Although in Equations (0.5) through (0.8) the number of primary unknowns and equations are the same, these equations can not be solved explicitly for most three-invariant elastoplastic soil models. Solution requires use of the Newton-Raphson iteration method. For convenience, all superscripts relating to time will be dropped from here on. At the end of each iteration, the value of the unknowns will be denoted by σ_{pq} , k^i , α^j_{pq} , and λ . The values at the midpoint will include the superscript, i.e. ${}^m(\sigma_{pq}, k^i, \alpha^j_{pq})$. The elastic stiffness tensor E_{pqkl} is taken as constant. The residuals of Equations (0.5) through (0.8) at the end of each iteration become:

$${}^R\sigma_{pq} = \sigma_{pq} - {}^{pred}\sigma_{pq} + \lambda E_{pqkl} {}^m B_{kl} \quad (0.12)$$

$${}^R k^i = k^i - {}^t k^i - \lambda {}^m \left(\frac{dk^i}{d\lambda} \right) \quad (0.13)$$

$${}^R \alpha^j_{pq} = \alpha^j_{pq} - {}^t \alpha^j_{pq} - \lambda {}^m \left(\frac{d\alpha^j_{pq}}{d\lambda} \right) \quad (0.14)$$

$${}^R f = f(\sigma_{pq}, k^i, \alpha^j_{pq}) \quad (0.15)$$

Now differentiate Equation (0.5) with respect to λ to obtain

$$\frac{d\sigma_{pq}}{d\lambda} + E_{pqkl} {}^m B_{kl} + \lambda \beta E_{pqkl} \left(T_{pqmn} \frac{d\sigma_{mn}}{d\lambda} + \sum_i W_{kl}^i \frac{dk^i}{d\lambda} + \sum_j N_{pqmn}^j \frac{d\alpha^j_{mn}}{d\lambda} \right) = 0 \quad (0.16)$$

where:

$$T_{pqmn} = {}^m \left(\frac{\partial^2 g}{\partial \sigma_{pq} \partial \sigma_{mn}} \right) \quad (0.17)$$

$$W_{kl}^i = {}^m \left(\frac{\partial^2 g}{\partial \sigma_{kl} \partial k^i} \right) \quad (0.18)$$

$$N_{pqmn}^j = {}^m \left(\frac{\partial^2 \mathbf{g}}{\partial \sigma_{pq} \partial \alpha_{mn}^j} \right) \quad (0.19)$$

Next solve for $d\sigma_{mn}/d\lambda$ from Equation (0.16)

$$\frac{d\sigma_{mn}}{d\lambda} = -C_{pqmn} E_{pqkl} V_{kl} \quad (0.20)$$

where:

$$C_{pqmn} = \frac{1}{\delta_{pm} \delta_{qn} + \lambda \beta E_{pqkl} T_{klmn}} \quad (0.21)$$

$$V_{kl} = {}^m B_{kl} + \lambda \beta F_{kl} \quad (0.22)$$

$$F_{kl} = \sum_i W_{kl}^i \frac{dk^i}{d\lambda} + \sum_j N_{klmn}^j \frac{d\alpha_{mn}^j}{d\lambda} \quad (0.23)$$

The difference between Equation (0.8) and Equation (0.15) can be expressed as:

$$df = \frac{\partial f}{\partial \sigma_{mn}} \frac{d\sigma_{mn}}{d\lambda} d\lambda + H d\lambda = f - {}^R f = -{}^R f \quad (0.24)$$

where:

$$H = \sum_i \frac{\partial f}{\partial k^i} \frac{dk^i}{d\lambda} + \sum_j \frac{\partial f}{\partial \alpha_{pq}^j} \frac{d\alpha_{pq}^j}{d\lambda}. \quad (0.25)$$

Substituting Equation (0.20) into Equation (0.24) and solving for $d\lambda$ yields:

$$d\lambda = \frac{{}^R f}{A_{mn} M_{mnkl} V_{kl} - H} \quad (0.26)$$

where $A_{mn} = \partial f / \partial \sigma_{mn}$ and $M_{mnkl} = C_{pqmn} E_{pqkl}$

Differentiate Equations (0.12) through (0.14) for the current stress state:

$$d({}^R \sigma_{pq}) = d\sigma_{pq} + d\lambda E_{pqkl} {}^m B_{kl} + \lambda E_{pqkl} dB_{kl} \quad (0.27)$$

$$d({}^R k^i) = dk^i - d\lambda \frac{dk^i}{d\lambda} - \lambda d\left(\frac{dk^i}{d\lambda}\right) \quad (0.28)$$

$$d({}^R \alpha_{pq}^j) = d\alpha_{pq}^j - d\lambda \frac{d\alpha_{pq}^j}{d\lambda} - \lambda d\left(\frac{d\alpha_{pq}^j}{d\lambda}\right) \quad (0.29)$$

In Equation (0.28):

$$d\left(\frac{dk^i}{d\lambda}\right) = {}^m n_{rs}^i dB_{rs} \quad (0.30)$$

For Cam-clay type hardening rules:

$${}^m n_{rs}^i = \frac{{}^m \left(\frac{dk^i}{d\lambda} \right)}{{}^m B_{mm}} \delta_{rs} \quad (0.31)$$

whereas for isotropic hardening with a hardening rule given by $dk^i = a_i (d\varepsilon_{rs}^p d\varepsilon_{rs}^p)^{1/2}$, we can write:

$${}^m n_{rs}^i = {}^m \left(\frac{dk^i}{B_{mn} B_{mn}} B_{rs} \right) \quad (0.32)$$

In the above, a_i are a series of hardening constants that depend on the particular soil model (Chen 1982) and $d\varepsilon_{rs}^p$ is the plastic strain increment tensor.

In Equation (0.29):

$$d \left(\frac{d\alpha_{pq}^j}{d\lambda} \right) = \frac{\partial \alpha_{ab}^j}{\partial \varepsilon_{ab}^p} dB_{pq} \quad (0.33)$$

$$dB_{pq} = \beta \left(T_{pqmn} d\sigma_{mn} + \sum_i W_{pq}^i dk^i + \sum_j N_{pqmn}^j d\alpha_{mn}^j \right) \quad (0.34)$$

Next, substitute Equation (0.34) into Equations (0.30) and (0.33). Also, substitute Equations (0.30), (0.33), and (0.34) into Equations (0.27), (0.28) and (0.29) and solve for $d\sigma_{mn}$, dk^i , and $d\alpha_{pq}^j$:

$$d\sigma_{mn} = C_{pqmn} \left[d({}^R \sigma_{pq}) - d\lambda E_{pqkl} {}^m B_{kl} - \lambda \beta E_{pqkl} \left(\sum_i W_{kl}^i dk^i + \sum_j N_{klmn}^j d\alpha_{mn}^j \right) \right] \quad (0.35)$$

$$dk^i = \frac{d({}^R k^i) + d\lambda {}^m \left(\frac{dk^i}{d\lambda} \right) + \lambda \beta {}^m n_{mn}^i \left(T_{mnkl} d\sigma_{kl} + \sum_{j \neq i} W_{mn}^j dk^j + \sum_j N_{mnkl}^j d\alpha_{kl}^j \right)}{1 - \lambda \beta {}^m n_{kl}^i W_{kl}^i} \quad (0.36)$$

$$d\alpha_{mn}^i = \frac{d({}^R \alpha_{ab}^i) + d\lambda {}^m \left(\frac{d\alpha_{ab}^i}{d\lambda} \right) + \lambda \beta \frac{d\alpha_{ab}^i}{d\varepsilon_{ab}^p} \left(T_{abkl} d\sigma_{kl} + \sum_j W_{ab}^j dk^j + \sum_{j \neq i} N_{abkl}^j d\alpha_{kl}^j \right)}{\delta_{am} \delta_{bn} - \lambda \beta \frac{d\alpha_{rs}^i}{d\varepsilon_{rs}^p} N_{abmn}^i} \quad (0.37)$$

Equations (0.26), (0.35), (0.36), and (0.37) are the equations to be used for Newton-Raphson iteration.

As pointed out by Ortiz and Popov (1985), when $\beta < 1/2$ the stability of this integration scheme is only conditionally stable. Luccioni et al. (2001) further point out that even when $1/2 \leq \beta \leq 1$, stability is only linear and can not be guaranteed for complex constitutive models. When the Newton-Raphson iteration procedure diverges, a normal return scheme, which has been used successfully by Nayak and Zienkiewicz (1972), Owen and Hinton (1980), Sloan and Randolph (1982), and Sloan et al. (2001), can be adopted. In this scheme β is set to zero and the hardening parameters are kept constant so that only the stresses are allowed to vary. Two Newton-Raphson iterations are performed so that stresses are forced back to the current yield surface along the normal to the yield surface from the non-converged stress point:

$$d\sigma_{pq} = -d\lambda A_{pq} \quad (0.38)$$

Applying a first order Taylor expansion to the residual of the yield function:

$$f = {}^R f + A_{pq} d\sigma_{pq} = 0 \quad (0.39)$$

and substituting Equation (0.38) into Equation (0.39), we can solve for $d\lambda$:

$$d\lambda = \frac{{}^R f}{A_{pq} A_{pq}} \quad (0.40)$$

The correction to the stresses given by Equation (0.38) then becomes:

$$d\sigma_{pq} = -\frac{{}^R f A_{pq}}{A_{rs} A_{rs}} \quad (0.41)$$

This type of normal correction makes the stress path follow the nearest path back to the yield surface. The Kuhn-Tucker constraint conditions can be satisfied after several iterations. But as indicated, this type of a normal correction does not account for the change in hardening parameters. As a result, the yield surface remains in place.

In order to obtain the consistent tangent stiffness tensor, we can differentiate the equilibrium Equation (0.5) with respect to total strain and solve for $d\sigma_{ab}/d\varepsilon_{mn}$:

$$\frac{d\sigma_{pq}}{d\varepsilon_{mn}} = E_{pqmn} - \frac{d\lambda}{d\varepsilon_{mn}} E_{pqkl} {}^m B_{kl} - \lambda \beta E_{pqkl} \left(T_{klab} \frac{d\sigma_{ab}}{d\varepsilon_{mn}} + F_{kl} \frac{d\lambda}{d\varepsilon_{mn}} \right) \quad (0.42)$$

$$\frac{d\sigma_{ab}}{d\varepsilon_{mn}} = M_{abmn} - M_{abkl} V_{kl} \frac{d\lambda}{d\varepsilon_{mn}} \quad (0.43)$$

Now differentiate the consistency condition

$$df = 0 \quad (0.44)$$

with respect to total strain to obtain:

$$A_{ab} \frac{d\sigma_{ab}}{d\varepsilon_{mn}} + H \frac{d\lambda}{d\varepsilon_{mn}} = 0 \quad (0.45)$$

Substitute Equation (0.43) into Equation (0.45) and solve for $d\lambda/d\varepsilon_{mn}$:

$$\frac{d\lambda}{d\varepsilon_{mn}} = \frac{A_{ab} M_{abmn}}{A_{ab} M_{abkl} V_{kl} - H} \quad (0.46)$$

By substituting Equation (0.46) into Equation (0.43), we can obtain the elastic-plastic consistent tangent stiffness tensor:

$$E_{abmn}^{ep} = M_{abmn} - \frac{M_{abkl} V_{kl} A_{rs} M_{rsmn}}{A_{rs} M_{rskl} V_{kl} - H} \quad (0.47)$$

It should be pointed out that the elastoplastic stiffness tensor given by Equation (0.47) is no longer symmetric for $\beta > 0.0$ regardless of whether associated or non-associated flow rule is adopted. As a result, the global stiffness matrix is also non-symmetric.

A flowchart indicating how the above equations have been implemented within a Newton-Raphson scheme for correction of plastic stresses and hardening parameters is shown in Table 2-1. However, note that the initial plastic correction is performed along the normal to the potential surface at the intersection point of the stress path and the yield surface (point *C* in Figure 2.1). A procedure is needed to find this intersection point. An efficient explicit root finding method based on the Pegasus scheme of Dowell and Jarratt (1972) can be adopted. At the end of time t , the yield function satisfies $f(\sigma_{pq}^t, k^t, \alpha_{pq}^t) \leq F_{tol}$. During the interval from t to $t+\Delta t$, the strain increment is $\Delta\varepsilon_{mn}$ and the predicted stress increment is $\Delta\sigma_{pq} = E_{pqmn}\Delta\varepsilon_{mn}$. The root finding procedure becomes necessary if:

$$f(\sigma_{pq}^t, k^t, \alpha_{pq}^t) < -F_{tol} \quad (0.48)$$

$$f(\sigma_{pq}^t + \Delta\sigma_{pq}, k^t, \alpha_{pq}^t) > F_{tol} \quad (0.49)$$

Table 2-1 Plastic correction procedure.

1. Set $\sigma_{pq} = {}^{pred}\sigma_{pq}$, $d\sigma_{pq} = 0$, $k^i = {}^t k^i$, $dk^i = 0$, $\alpha^j_{pq} = {}^t \alpha^j_{pq}$, $d\alpha^j_{pq} = 0$, $\lambda = 0$, $NumIter = 0$,
 $MaxIter = 15$, $MaxValue = 10^{45}$.
 Calculate $f_{start} = f({}^t \sigma_{pq}, {}^t k^i, {}^t \alpha^j_{pq})$ and $f_{pred} = f({}^{pred}\sigma_{pq}, k^i, \alpha^j_{pq})$.
 If $|f_{start}| \leq F_{tol}$
 calculate ${}^{int}\sigma_{pq}$ by calling root finding procedure
 else
 calculate ${}^{int}\sigma_{pq}$ by calling Pegasus unload-reload procedure.
2. Calculate ${}^m \sigma_{pq} = (1 - \beta) \times {}^{int}\sigma_{pq} + \beta \times \sigma_{pq}$, ${}^m k^i = (1 - \beta) \times {}^t k^i + \beta \times k^i$ and ${}^m \alpha^j_{pq} = (1 - \beta) \times {}^t \alpha^j_{pq} + \beta \times \alpha^j_{pq}$
 Set
 ${}^{old}\sigma_{pq} = \sigma_{pq}$, ${}^{old}k^i = k^i$, ${}^{old}\alpha^j_{pq} = \alpha^j_{pq}$, ${}^{old}\lambda = \lambda$, $NumIter = NumIter + 1$
3. Calculate ${}^R f = f(\sigma_{pq}, k^i, \alpha^j_{pq})$
 If ${}^R f \geq MaxValue$ or $NumIter > MaxIter$,
 go to step 8.
 else
 calculate $d\lambda$ using Equation (2.26).
4. Calculate ${}^R \sigma_{pq}$, ${}^R d$, and ${}^R \alpha^j_{pq}$, using Equations (2.12), (2.13), and (2.14), respectively.
5. Set $d({}^R \sigma_{pq}) = -{}^R \sigma_{pq}$, $d({}^R k^i) = -{}^R k^i$, and $d({}^R \alpha^j_{pq}) = -{}^R \alpha^j_{pq}$. Calculate the new values for
 $d\sigma_{pq}$, dk^i , and $d\alpha^j_{pq}$ using Equations (2.35), (2.36), and (2.37).
6. Update the values of the unknowns
 $\sigma_{pq} = {}^{old}\sigma_{pq} + d\sigma_{pq}$; $k^i = {}^{old}k^i + dk^i$; $\alpha^j_{pq} = {}^{old}\alpha^j_{pq} + d\alpha^j_{pq}$; $\lambda = {}^{old}\lambda + d\lambda$
7. Repeat steps 2-6 until the following criteria are satisfied. Then go to step 9.
 $\|{}^R \sigma_{pq}\| \leq TOL_1$, $\|{}^R k^i\| \leq TOL_2$, $\|{}^R \alpha^j_{pq}\| \leq TOL_3$, and $|{}^R f| \leq TOL_4$
8. Set $\beta = 0$ and perform steps 2-6 twice. Then perform the following calculations until
 $|{}^R f| \leq TOL$. Then go to step 9.
 ${}^R f = f(\sigma_{pq}, k^i, \alpha^j_{pq})$, ${}^{old}\sigma_{pq} = \sigma_{pq}$, $d\sigma_{pq} = {}^R f A_{pq} / (A_{rs} A_{rs})$, and $\sigma_{pq} = {}^{old}\sigma_{pq} + d\sigma_{pq}$
9. Calculate the elastic strain ${}^{t+\Delta t} \varepsilon^e_{ab} = {}^t \varepsilon^e_{ab} + d\varepsilon_{ab} - \lambda B_{ab}$, the plastic strain, ${}^{t+\Delta t} \varepsilon^p_{ab} =$
 ${}^t \varepsilon^p_{ab} + \lambda B_{ab}$, and the consistent stiffness tensor E^{ep}_{abmn} by means of Equation (2.47).

In that case we need to find a scalar value ω which is larger than zero and less than 1 and satisfies the function $|f(\sigma_{pq} + \omega \Delta \sigma_{pq}, k^i, \alpha^j_{pq})| \leq F_{tol}$. In other words, this entails finding the single root of a non-linear, one-variable equation within a given root domain. The initial root domain (ω_0, ω_1) is such that $\omega_0=0$ and $\omega_1=1$. A series of Pegasus iterations are carried out. If after a set maximum number of iterations the root is not found, the remaining domain is divided into N equal size subdomains. If the values of f have a different sign at the ends of a particular subdomain, the root must be within that interval. The entire procedure is repeated until (a) the root is found, (b) the difference between ω_0 and ω_1 is smaller than the precision of the computational platform, or (c) a prescribed maximum number of iterations is reached. Note that the proposed Pegasus procedure (Table 2-2) improves upon the one proposed by Sloan et al. (2001) since when f at $\omega=\omega_0$ is very small (and f at $\omega=\omega_1$ is very large), the original scheme can run into convergence problems, whereas the modified scheme in Table 2-2 does not.

Table 2-2 Root finding procedure.

<ol style="list-style-type: none"> 1. Set $\omega_0=0$ and $\omega_1=1$, calculate $f_0 = f(\sigma_{pq} + \omega_0 \Delta \sigma_{pq}, k^i, \alpha^j_{pq})$ and $f_1 = f(\sigma_{pq} + \omega_1 \Delta \sigma_{pq}, k^i, \alpha^j_{pq})$. 2. Perform steps 3-4 <i>P</i>MAX times 3. Calculate $\omega = \omega_1 - (\omega_1 - \omega_0) f_1 / (f_1 - f_0)$ and $f = f(\sigma_{pq} + \omega \Delta \sigma_{pq}, k^i, \alpha^j_{pq})$. 4. If $f \leq F_{tol}$ terminate this procedure and go to step 12 with present value of ω, otherwise if $f \times f_0 < 0$ set $f_1 = f, \omega_1 = \omega$, otherwise set $f_0 = f, \omega_0 = \omega$. 5. Set $i = 1$. 6. Set $\omega = \omega_0 + i(\omega_1 - \omega_0) / N$ and calculate $f = f(\sigma_{pq} + \omega \Delta \sigma_{pq}, k^i, \alpha^j_{pq})$. 7. If $f \leq F_{tol}$ terminate this procedure and go to step 12 with present value of ω,
--

Table 2-2 (Continued) Root finding procedure.

otherwise

if $f > F_{tol}$

set $f_1 = f$, $\omega_{max} = \omega$, $i = N+1$,

otherwise

if $f > f_0$

set $f_0 = f$, $\omega_{min} = \omega$.

8. Increase i by one; perform steps 6 and 7 until $i \leq N$.

9. Set $\omega_0 = \omega_{min}$, $\omega_1 = \omega_{max}$.

10. If $|\omega_1 - \omega_0| \leq EPS$ or the number of iterations equals to $IterMax$, set $\omega = \omega_0$ and terminate this procedure and go to step 12 with present value of ω .

11. Perform step 2-9 for $IterMax$ times.

12. ${}^{int}\sigma_{pq} = {}^t\sigma_{pq} + \omega\Delta\sigma_{pq}$.

As pointed out by Sloan et al. (2001) and others, when the stress point at time t is on the yield surface, i.e. $|f({}^t\sigma_{pq}, {}^t k^j, {}^t\alpha^j_{pq})| \leq F_{tol}$, the predicted stress path may pass through an elastic zone first with $f({}^t\sigma_{pq} + \omega\Delta\sigma_{pq}, {}^t k^j, {}^t\alpha^j_{pq}) < -F_{tol}$ and $0 < \omega < 1$, and then end outside the yield surface where $f({}^t\sigma_{pq} + \Delta\sigma_{pq}, {}^t k^j, {}^t\alpha^j_{pq}) > F_{tol}$ (Figure 2.2). This occurs when the direction of the predicted stress increment has a blunt angle γ with the normal of the yield surface, i.e.:

$$\cos \gamma = \frac{A_{rs} \Delta\sigma_{rs}}{\sqrt{A_{rs} A_{rs}} \sqrt{\Delta\sigma_{rs} \Delta\sigma_{rs}}} < -Tol \quad (0.50)$$

where Tol is a small positive tolerance. In this case, the intersection point of the predicted stress path and the yield surface should be determined before proceeding with the plastic correction phase. The specific process of finding this intersection point is different from the root finding procedure described above because a narrowed root domain, which contains the intersection point, must be determined first. Afterwards, the algorithm in Table 2-2 can be used.

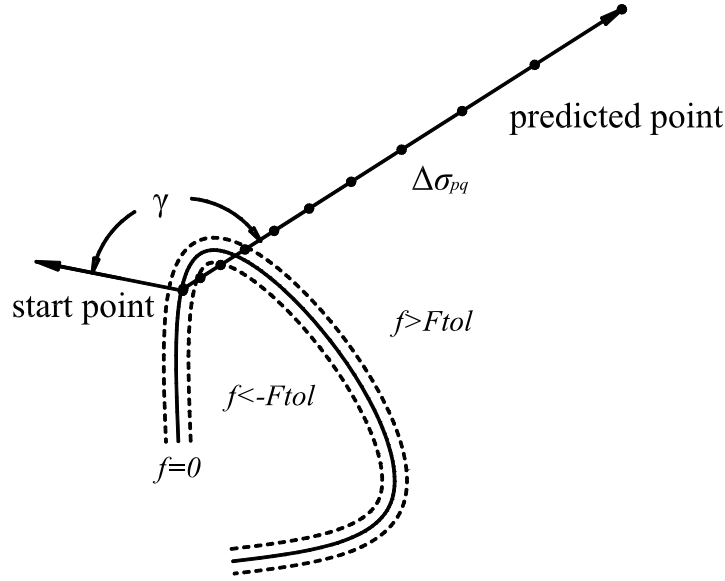


Figure 2.2 Predicted unloading-reloading stress path.

Sloan et al. (2001) describe a Pegasus unloading scheme that appears to work successfully in many cases. However, if the value of the yield function becomes very large at the predicted state, i.e. the intersection point (Point C, Figure 2.1) is very close to the starting location in relation to the predicted state, Sloan's scheme can have a difficult time finding the correct root domain. A modified Pegasus unload-reload algorithm can be described as follows. Its main purpose is to find an elastic point where the yield function has a value less than the negative tolerance, $f < -F_{tol}$. Since at the start $|f(\sigma_{pq}^t, k^i, \alpha_{pq}^j)| \leq F_{tol}$, the most likely location for the elastic point is within the immediate neighborhood of the starting point. Therefore, we divide the strain increment into a number of sub-increments, each increasing by a factor e ($e > 1.0$) from the previous one (Figure 2.2). When the value of f is very large at the predicted point, the smaller the sub-increment near the starting point, the faster the procedure to find a stress point that is located within the elastic zone. Of course, if f at the predicted point is small, and e is large, a larger number of computational steps will be necessary. Our experience suggests an optimum of 1.2 for e . The modified Pegasus unload-reload procedure is listed in Table 2-3.

Table 2-3 Modified Pegasus unload-reload procedure.

-
1. Set $\Delta\sigma_{pq} = E_{pqmn} \Delta\varepsilon_{mn}$, $\omega_0 = 0$, $\omega_{old} = 0$, $\omega_1 = 1$;
 calculate $f_0 = f(\sigma_{pq}^t + \omega_0 \Delta\sigma_{pq}, k^i, \alpha_{pq}^j)$ and $f_1 = f(\sigma_{pq}^t + \omega_1 \Delta\sigma_{pq}, k^i, \alpha_{pq}^j)$;
 set $f_{0_old} = f_0, f_{1_old} = f_1$.
 2. Set $e = 1.2$, $s_0 = (1-e)/(1 - e^{NSUB})$, $i = 1$.
 3. Set $\omega_{old} = \omega_1$, $d\omega = \omega_1 - \omega_0$, $k = 1$.
 4. Set $d\omega = d\omega_0 \times s_0 \times e^{k-1}$, $d\sigma_{pq} = \Delta\sigma_{pq} \times d\omega$, $\omega = \omega_{old} + d\omega$,
 calculate $f = f(\sigma_{pq}^t + \omega \Delta\sigma_{pq}, k^i, \alpha_{pq}^j)$
 5. If $f > F_{tol}$
 set $\omega_1 = \omega, f_{1_old} = f, k = NSUB + 1$,
 otherwise
 if $f < -F_{tol}$
 set $\omega_0 = \omega, f_{0_old} = f, k = NSUB + 1$, and $i = IterMax + 1$,
 otherwise
 set $\omega_{old} = \omega$.
 6. Set $k = k + 1$; if $k \leq NSUB$, perform steps 4 and 5 again.
 7. Set $i = i + 1$; if $i \leq IterMax$, perform steps 3 to 6 again.
 8. If $f_{0_old} < -F_{tol}$ and $f_{1_old} > F_{tol}$,
 set $d\omega = \omega_1 - \omega_0$, ${}^s\sigma_{pq} = {}^t\sigma_{pq} + \omega_0 \Delta\sigma_{pq}$, and $\Delta\sigma_{pq}^{Local} = d\omega \times \Delta\sigma_{pq}$. Take ${}^t\sigma_{pq}$ as ${}^t\sigma_{pq}$ and
 $\Delta\sigma_{pq}^{Local}$ as $\Delta\sigma_{pq}$ to perform the root finding procedure and return ω^{Local} . Calculate $\omega =$
 $\omega_0 + \omega^{Local} \times d\omega$.
 Otherwise, set $\omega = \omega_0$.
 9. ${}^{int}\sigma_{pq} = {}^t\sigma_{pq} + \omega \Delta\sigma_{pq}$.
-

2.4 Implementation of Formulation into OpenSees

The general integration scheme has been implemented into the code OpenSees (2004) along with four commonly used soil constitutive models that vary in complexity and versatility. In hierarchical order, they are the Drucker-Prager (DP), extended Mohr-Coulomb (EMC), modified Cam-clay (MCC), and general Cam-clay (GCC) models (Table 2-4). The Drucker-Prager model is the simplest one among the four and considers only two stress invariants. The EMC model is a modification of the DP model that takes into consideration the third stress invariant. As a result, the yield surface in

Table 2-4 General characteristics of selected elastoplastic models.

	Drucker-Prager	Extended Mohr-Coulomb	General Cam-clay	Modified Cam-clay
Yield and potential functions	$f = \alpha p + q - k$	$f = \alpha p + N(\theta)q - k$	$f = q^2/M(\theta)^2 + p(p-p_0)$	$f = q^2/M^2 + p(p-p_0)$
Stress invariants	p, q	p, q, θ	p, q, θ	p, q
Hardening rule	$d\alpha = Cd\varepsilon^p$	$d\alpha = Cd\varepsilon^p$	$dp_0 = v p_0 d\varepsilon_{ii}^p / (m - \kappa)$	$dp_0 = v p_0 d\varepsilon_{ii}^p / (m - \kappa)$
Parameters	For triaxial compression: $\alpha = 6\sin\phi/(3-\sin\phi)$ $k = 6c\cos\phi/(3-\sin\phi)$ For triaxial extension: $\alpha = 6\sin\phi/(3+\sin\phi)$ $k = 6c\cos\phi/(3+\sin\phi)$	$\alpha = 6\sin\phi/(3+\sin\phi)$, $k = 6c\cos\phi/(3+\sin\phi)$, $M(\theta) = \alpha/N(\theta)$, $N(\theta) = [4(1-e^2)\cos^2\theta + (2e-1)^2] / \{2(1-e^2)\cos\theta + (2e-1)[4(1-e^2)\cos^2\theta + 5e^2 - 4e]\}$, $e = (3+\sin\phi)/(3-\sin\phi)$	For triaxial compression: $M = 6\sin\phi/(3-\sin\phi)$ For triaxial extension: $M = 6\sin\phi/(3+\sin\phi)$	
Constants	ϕ - friction angle; c - cohesion; v - specific volume; m - compression index; κ - swelling index; C - hardening parameter.			

principal stress space is not circular. Of course, the two Cam-clay models have elliptical yield surfaces in the p - q plane but differ from each other in terms of the exact functional form used for the DP and EMC (Figure 2.3). The first and second order derivatives for each of these models, necessary for implementation into a numerical code, are included in tensorial form in the Appendix A.

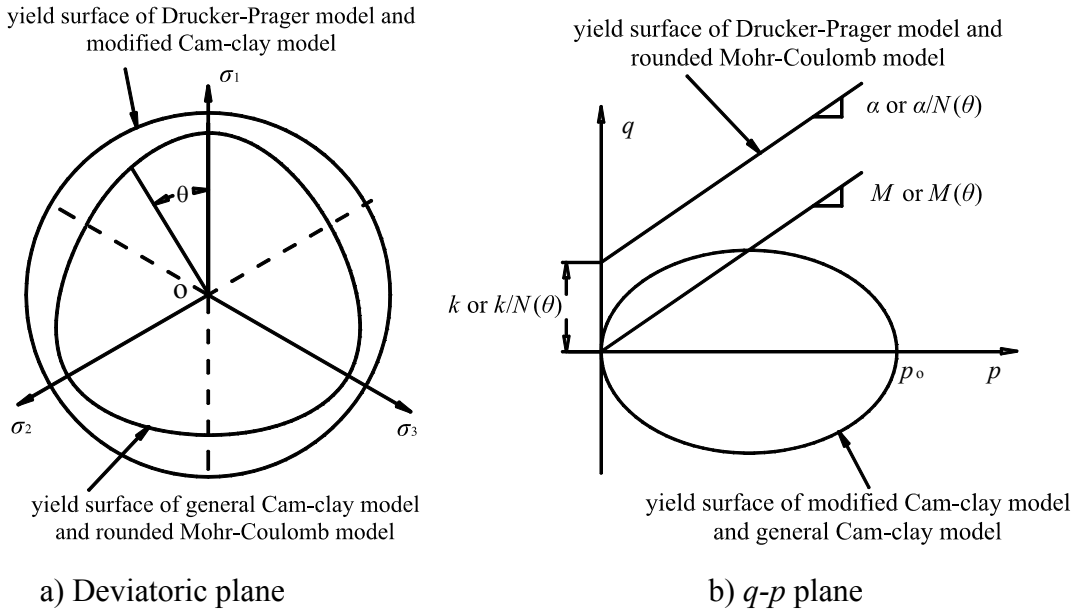


Figure 2.3 Yield surfaces for selected constitutive models.

The remainder of the article focuses on a comparison of performance among these four models for two integration options. Explicit integration is obtained by setting $\beta = 0$ and implicit integration by letting $\beta = 1$. Of particular interest is the efficiency of these two schemes with regard to the four constitutive models. For this purpose, a hypothetical cubical soil element consisting of a 20-node isoparametric brick element with 14 Irons (1971) integration points is subjected to various triaxial loadings. Typical material properties corresponding to a silty clay were assumed (Table 2-5).

Table 2-5 Material properties and initial conditions for simulation runs.

Parameter	Symbol	Value
Unit weight	γ	14.50 kN/m ³
Friction angle	ϕ	28 ⁰
Poisson's Ratio	μ	0.33
Virgin compression index	λ	0.019
Swell index	m	0.006
Pre-consolidation stress	p_0	140 kPa
Initial void ratio	e_0	0.65

2.5 Performance of Implicit and Explicit Integration

In each simulation, the soil element is first compressed isotropically to 140 kPa. Thereafter, three stress paths are investigated (Figure 2.4). Path LP-1 corresponds to deviatoric stress with $\Delta\sigma_y/\Delta\sigma_z=0$. For path LP-2, the stress ratio is kept at $\Delta\sigma_y/\Delta\sigma_z=0.5$, and for path LP-3 the stress ratio is again $\Delta\sigma_y/\Delta\sigma_z=0$ but $\Delta\sigma_z$ is negative. In each case, σ_x is kept constant at 140 kPa. The corresponding Lode angles for paths LP-1, LP-2, and LP-3 are 0⁰, 30⁰, and 60⁰, respectively (Figure 2.4). One reason that paths LP-1 and LP-3 are chosen is that analytical derivatives of the Lode angles at 0⁰ and 60⁰ are not available for the EMC and GCC models and they must instead be determined numerically. This

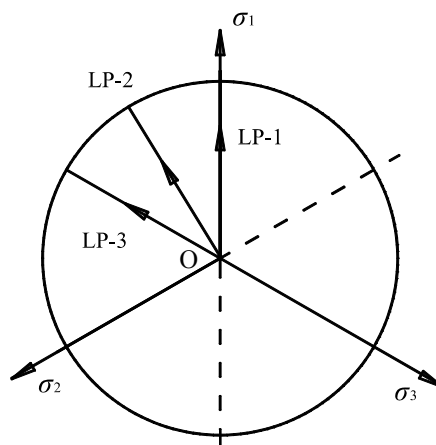


Figure 2.4 Stress paths in the deviatoric plane.

forces an evaluation of potential numerical errors. More importantly, these loading schemes, albeit somewhat simplistic and limited, span the range of possible constant stress ratio paths in the y - z plane. While plane stress loading results in three-dimensional deformations, we dispense with the complexity of considering the effects of stress changes in all directions for the time being. Use of a single element leads to equal stresses and strains at all Gauss points and therefore avoids the influence of yielding in neighboring elements that may unnecessarily cloud the resulting behavior.

The performance of explicit and implicit integration methods is discussed first with respect to the DP and EMC models, which lack an ultimate failure condition and strain hardening mechanism. Vertical loads of 460 kPa, 460 kPa, and -120 kPa are applied for the LP-1, LP-2, and LP-3 paths, respectively. The deviatoric plastic stress-strain curves are very similar for increments 15 through 1200, regardless of whether implicit or explicit integration is used (Figure 2.5). The number of increments and the type of integration method have virtually no effect on the overall predictions. The accuracy of integration can be evaluated by defining a relative error measure:

$$E_R = \frac{\sqrt{\sigma_{pq}\sigma_{pq} + \sum_i (k^i)^2 + \sum_j (\alpha_{pq}^j \alpha_{pq}^j)}}{\sqrt{{}^*\sigma_{pq} {}^*\sigma_{pq} + \sum_i ({}^*k^i)^2 + \sum_j ({}^*\alpha_{pq}^j {}^*\alpha_{pq}^j)}} \times 100 \quad (0.51)$$

where σ_{pq} , k^i , and α_{pq}^j are values at the end of a particular increment and ${}^*\sigma_{pq}$, ${}^*k^i$, and ${}^*\alpha_{pq}^j$ are the corresponding values at the end of that increment for the run with 1200 steps. A representative set of finding is shown in Figure 2.6 for the LP-2 path. The error for both explicit and implicit integration methods is very small and almost indistinguishable, as was suggested in Figure 2.5. On the other hand, there are significant savings to be had in choosing the explicit method over the implicit one for the EMC model. Of course, this is particularly true as the number of sub-increment steps increases. Computational time increases nearly linearly with number of steps. The ratio between the time used by explicit integration and that used by implicit integration in the DP model is about 1.0 while it is only about 1/3 in the EMC model. The main reason that the implicit integration procedure for the EMC model is much more time consuming is that it involves evaluating the second derivative of the third stress invariant, while the DP model does not.

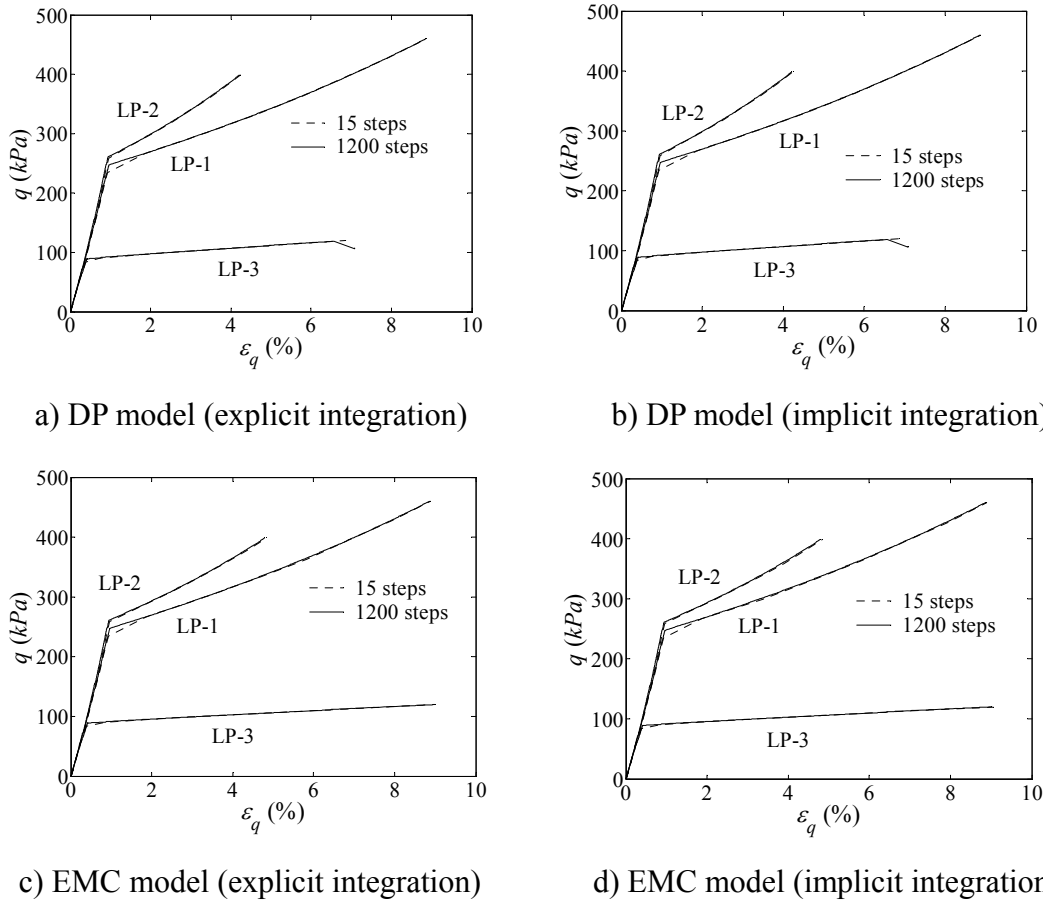


Figure 2.5 Stress-strain prediction for DP and EMC models.

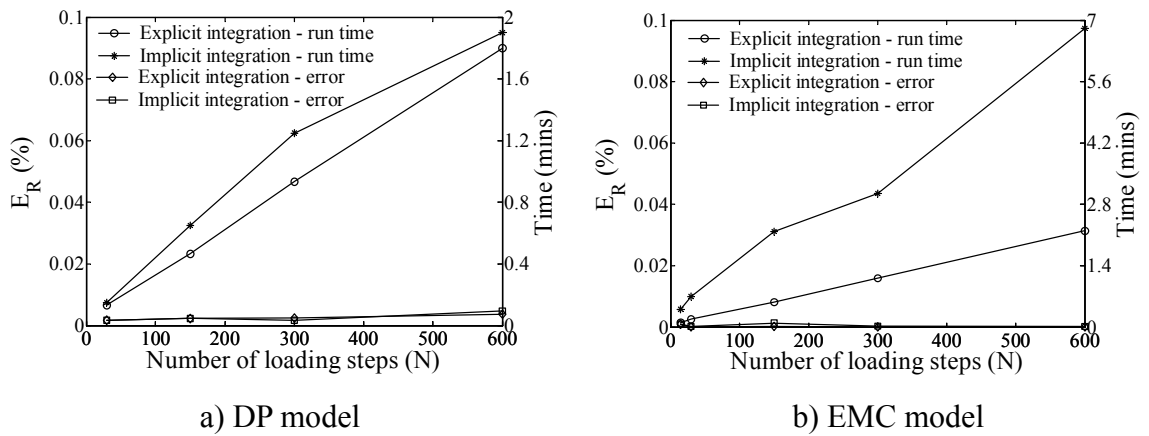
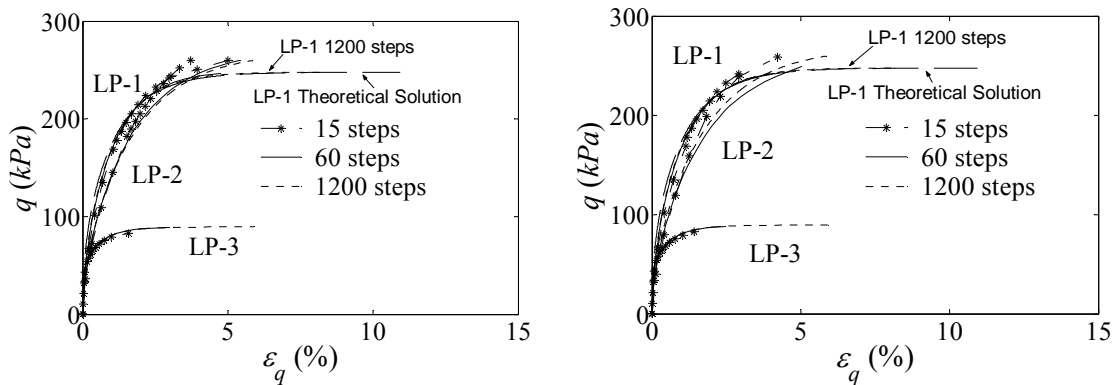


Figure 2.6 The relative errors and time consuming of explicit and implicit integrations in DP and EMC models for LP-2 ($\theta = 30^\circ$) loading path.

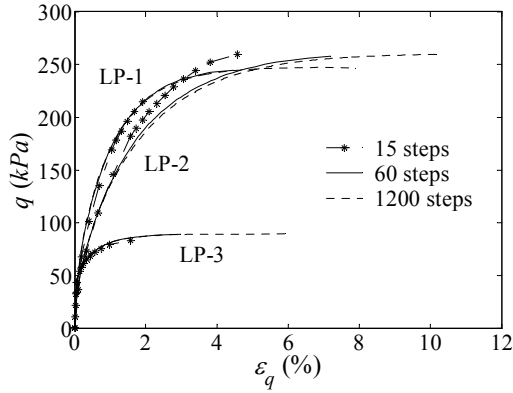
The MCC and GCC critical state models have well-defined failure and yield criteria and are clearly superior to the DP and EMC models in terms of their ability to model real soil behavior. However, as stress conditions approach failure, numerical instability may occur unless very small loading steps are chosen. For the particular problem at hand, use of 1200 steps to achieve the final load results in more accurate predictions than using only 15 or 60 steps, regardless of whether implicit or explicit integration is used (Figure 2.7). The integration formulations are also validated by comparing the finite element predictions with the theoretical predictions using the MCC model (Muir Wood 1990) under triaxial compression path LP-1 (Figures 2.7a and 2.7b).

As in DP and EMC model, Equation (0.51) is used here to calculate the relative errors. Two loads, one $\Delta\sigma_z=105$ kPa, which is smaller than the failure load and the other one $\Delta\sigma_z=150$ kPa, which is larger than failure load are chosen to test the performance of the implicit and explicit integration with the number of increments increases. Under the first load, both MCC model and GCC model do not fail but just yield (named yield loading). The second loading is called failure loading. The relative errors of implicit integration are larger than the explicit integration in most cases when the number of increments is small (Figure 2.8). In addition, both integrations show the unstable character in both models. But when the number of increments increases, the error of implicit integration decreases faster than that of the explicit integration. For the yield loading of implicit integration, 20 steps are enough to obtain relatively small errors for both MCC and GCC model. For the same level of accuracy, the explicit integration need about 50 steps. But when the time is concerned, the implicit integration uses about 2~3 times of that used by explicit

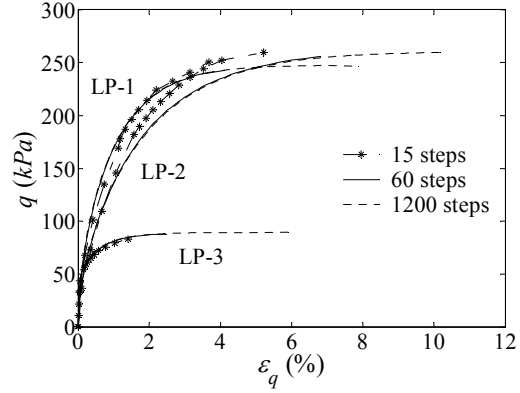


a) MCC model (explicit integration)

b) MCC model (implicit integration)



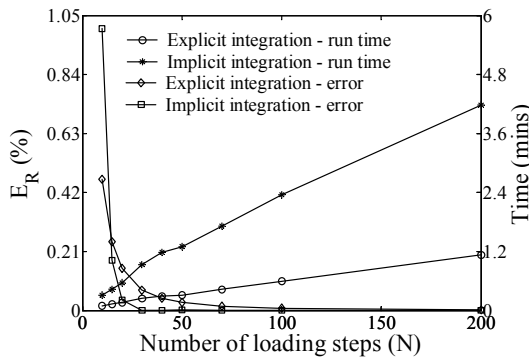
c) GCC model (explicit integration)



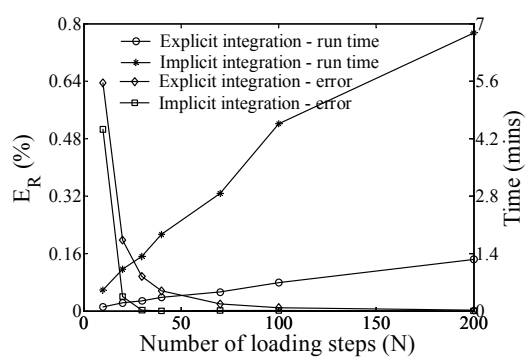
d) GCC model (implicit integration)

Figure 2.7 Stress-strain prediction for MCC and GCC models.

integration for the same level of accuracy of yield loading (Figure 2.8a and 8b). For the failure loading (Figure 2.8c and 8d) implicit integration performs better in the MCC model than in the GCC model. As the model gets more complicated, the instable character of implicit integration shows up when the number of increments is small. More loading steps are needed to arrive at a more accurate result for implicit integration for GCC model. The time used by implicit integration is about 5 times that used by explicit in GCC model for the same number of increments while this value is 4 in MCC model. This fact implies that implicit integration is less competent than explicit integration in complicated models at least for the problem investigated.



a) MCC model at yielding



b) GCC model at yielding

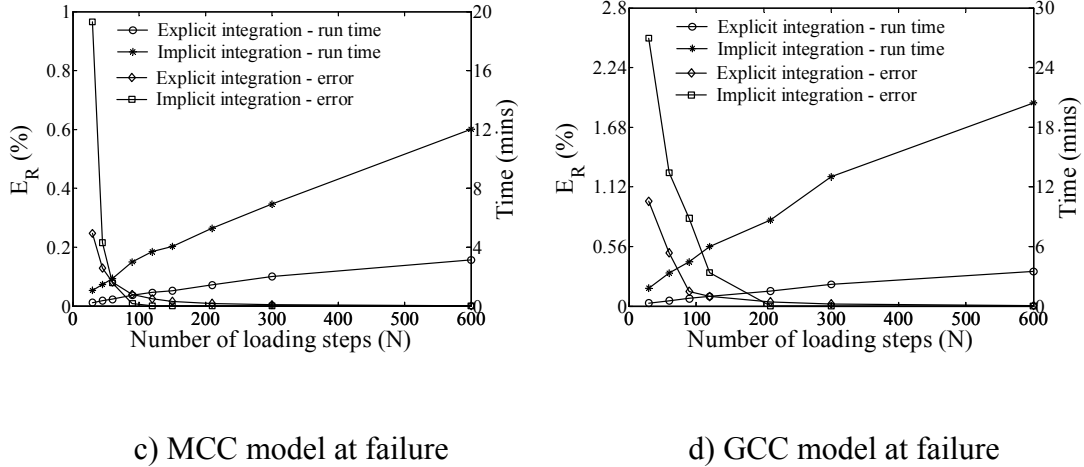


Figure 2.8 The relative errors and time consuming of explicit and implicit integrations in MCC and GCC models for LP-2 ($\theta = 30^\circ$) loading path.

2.6 Conclusions

The general form of an integration scheme was introduced and the performances of two extreme cases of this integration, which are the well-known explicit and fully implicit integration schemes, were studied. By applying to four elastoplastic soil models with different level of complexity, the performances can be summarized as follows:

- The explicit integration is much faster than the implicit integration.
- The accuracy of explicit and implicit integrations is in the same level in the DP, EMC models. The implicit integration is more accurate in MCC and GCC models in a small range of number of increments if the stress state is not approaching failure.
- The explicit integration saves more time than for models which have curved yield surfaces in both $q-p$ plane and deviatoric plane such as GCC model than other models as DP, EMC, and MCC model.
- To achieve the same level of accuracy and save more time, explicit integration is the better choice than the implicit integration in all four models.

2.7 References:

- Borst, R. D. and P. H. Feenstra (1990). "Studies in anisotropic plasticity with reference to the hill criterion." International Journal for Numerical Methods in Engineering **29**: 315-336.
- Borst, R. d. and A. E. Groen (2000). Computational strategies for standard soil plasticity models, John Wiley & Sons, Ltd.
- Chen, W. F. (1982). Plasticity in Reinforced Concrete. New York, McGrawHill.
- Dowell, M. and P. Jarratt (1972). "The Pegasus methods for computing the root of an equation." BIT **12**: 503-508.
- Gens, A. and D. M. Potts (1988). "Critical state models in computational geomechanics." Engineering Computations **5**: 178-197.
- Irons, B. M. (1971). "Quadrature rules for brick based finite elements." International Journal for Numerical Methods in Engineering **3**: 293-294
- Jeremic, B. and S. Sture (1997). "Implicit integrations in elastoplastic geotechnics." Mechanics of Cohesive-Frictional Materials **2(2)**: 165-183.
- Luccioni, L. X., J. M. Pestana, et al. (2001). "Finite element implementation of non-linear elastoplastic constitutive laws using local and global explicit algorithms with automatic error control." International Journal for Numerical Methods in Engineering **50(5)**: 1191-1212.
- Muir Wood, D. (1990). Soil behaviour and critical state soil mechanics. New York, Cambridge.
- Nayak, G. C. and A. P. Zielinski (1972). "Elasto-plastic stress analysis: a generalisation for various constitutive relations including strain softening." International Journal for Numerical Methods in Engineering **5**: 113-135.
- OpenSees (2004). Open System for Earthquake Engineering Simulation, Pacific Earthquake Engineering Research. **2005**.
- Ortiz, M. and E. P. Popov (1985). "Accuracy and Stability of Integration Algorithms for Elastoplastic Constitutive Relations." International Journal for Numerical Methods in Engineering **21(9)**: 1561-1576.
- Owen, D. R. J. and E. Hinton (1980). Finite Elements in Plasticity: Theory and Practice. Swansea, Pineridge Press.
- Potts, D. and D. Ganendra (1992). A comparison of solution strategies for non-linear finite element analysis of geotechnical problems. In proceedings of 3rd international conference on computational plasticity, Barcelona, International

Center for Numerical Methods in Engineering.

- Potts, D. M. and D. Ganendra (1994). "An Evaluation of Substepping and Implicit Stress Point Algorithms." Computer Methods in Applied Mechanics and Engineering **119**(3-4): 341-354.
- Schellekens, J. C. J. and R. d. Borst (1990). "The use of the Hoffmann yield criterion in finite element analysis of anisotropic composites." Computers & Structures **37**(6): 1087-1096.
- Sheng, D. C. and S. W. Sloan (2001). "Load stepping schemes for critical state models." International Journal for Numerical Methods in Engineering **50**(1): 67-93.
- Simo, J. C. and R. L. Taylor (1986). "A return mapping algorithm for plane stress elastoplasticity." International Journal for Numerical Methods in Engineering **22**: 649-670.
- Sloan, S. W. (1987). "Substepping schemes for numerical integration of elasto-plastic stress-strain relations." International Journal for Numerical Methods in Engineering **24**: 893-911.
- Sloan, S. W., A. J. Abbo, et al. (2001). "Refined explicit integration of elastoplastic models with automatic error control." Engineering Computations **18**(1-2): 121-154.
- Sloan, S. W. and M. F. Randolph (1982). "Numerical prediction of collapse loads using finite element methods." International Journal for Numerical and Analytical Methods in Geomechanics **6**: 47-76.
- Yamaguchi, E. (1993). A comparative study of numerical methods for computing stress increments in elastic-plastic materials. Proceedings of the Asia-Pacific Symposium on Advances in Engineering Plasticity and its Application, Hong Kong.
- Zhang, Z. L. (1995). "Explicit consistent tangent moduli with a return mapping algorithm for pressure-dependent elastoplasticity models." Computer Methods in Applied Mechanics and Engineering **121**: 29-44.

Chapter 3

Pressure-Dependent Nonlinear Lateral Resistance of Single Pile in Cohesionless Soil

Abstract

This paper presents the results of a 3D elastoplastic numerical study on the factors affecting the lateral response of single piles, including the coefficient of lateral earth pressure at rest, the unit weight of soil, friction angle, initial Young's modulus of the soil, initial confining pressure, pile diameter and stiffness. It is found that the first three parameters are of similar importance with regard to ultimate lateral resistance. They influence soil-behavior indirectly through the soil's Young's modulus. Therefore Young's modulus, which is assumed to be pressure-dependent plays a crucial role in the development of lateral resistance. The other factors are also important, although the pile's Young's modulus has no effect on the stiffness of the p - y curves.

Keywords: pile; 3D elastoplastic; soil resistance; lateral resistance.

3.1 Introduction

Lateral load transfer from pile to soil that results in any significant degree of displacement invariably leads to complex soil-structure interaction. This complexity is usually ignored in engineering practice, where the lateral resistance of piles is evaluated by simplified methods that make significant assumptions with regard to soil and pile behavior. For example, the widely-used limit state approach (Broms 1964a; 1964b) assumes perfectly plastic soil behavior, which ignores deformations prior to failure and

predicts total collapse thereafter. In the p - y method, subgrade reaction is represented by a series of discrete springs that may be linear elastic (Reese and Matlock 1956; Matlock and Reese 1960) or nonlinear (1974; M.W. and Murchison 1983). This method is unable to account for permanent deformations and usually fails to take into consideration interaction among individual springs and therefore soil continuity. Accurate p - y curves are difficult to obtain for particular pile and soil combinations without expensive field tests. The continuum method based on Mindlin's approach divides the pile into one or more one-dimensional elements and integrates the solutions for each segment along the soil-pile interface (Poulos 1971; Poulos 1971; Filho, Mendonca et al. 2005). Although this accounts for pile continuity, the pile response is assumed elastic and the soil is not modeled as a continuum.

A more rigorous approach, and the one that is used herein, discretizes the pile and the soil into three-dimensional elements within the framework of the finite element method in order to preserve soil and pile continuity (Adachi and Kimura 1994). Of course, sliding and separation along the soil-pile interface can also be considered. More importantly, the finite element is a rigorous method that combines fundamental field equations, boundary conditions and compatibility conditions with virtually any mode of soil behavior, therefore providing a means for accurate and realistic prediction of soil-pile interaction. Numerical results from finite element computations can easily be expressed in terms of p - y curves in order to model and test field behavior (Brown, Shie et al. 1989; Brown and Shie 1990a; 1990b; Brown and Shie 1991). Yang and Jeremic (2002) developed a series of p - y curves for single piles in layered clay and sand deposits employing the relatively simple von Mises and Drucker-Prager soil models. Fan and Long (2005) incorporated a more sophisticated hierarchical single-surface δ_1 -elastoplastic model and compared their computations to simplified methods of predicting ultimate soil resistance. They found that the stiffness of the pile had little influence on the p - y curves and that the ultimate soil resistance is not linearly dependent on the diameter of the pile. They also found that the coefficient of lateral earth pressure, K , contributes to the stiffness of the soil. Larger values of K result in a higher ultimate soil resistance. Nonetheless, a crucial limitation of their work is that they neglected to analyze the effects of the initial stress state, as

represented for instance by the coefficient of lateral earth pressure at rest, K_o , and the unit weight of the soil, γ . These factors play an important role in lateral pile resistance, and this is investigated in this article. The other limitation of the above FE studies is that their focus is on the p - y curves and ultimate soil resistance without truly addressing the response of the pile. In fact, there are many instances in engineering practice where the ultimate lateral loading capacity of the pile is more important than that of the soil.

The response of a pile to lateral load is a function of many factors, including the stiffness of the pile, the constitutive properties of the soil and the stress state at the start of loading. In this study, we use three-dimensional OpenSees (2004) finite element modeling to investigate the nonlinear response of a single pile in cohesionless soil, which is subjected to lateral loading. We use a pressure-dependent, elastoplastic soil model and focus on the influence of the values of K_o and E_o (initial Young's modulus), as well as the role of stiffening/softening resulting from changes in the confining soil pressure p . In addition, the influence of soil friction, pile stiffness and pile diameter are also considered.

3.2 Soil and Pile Constitutive Models

The selected problem considers a 21-meter square pile embedded in a half-space of homogenous sand (Figure 3.1). A thin layer of elements between the pile and soil are

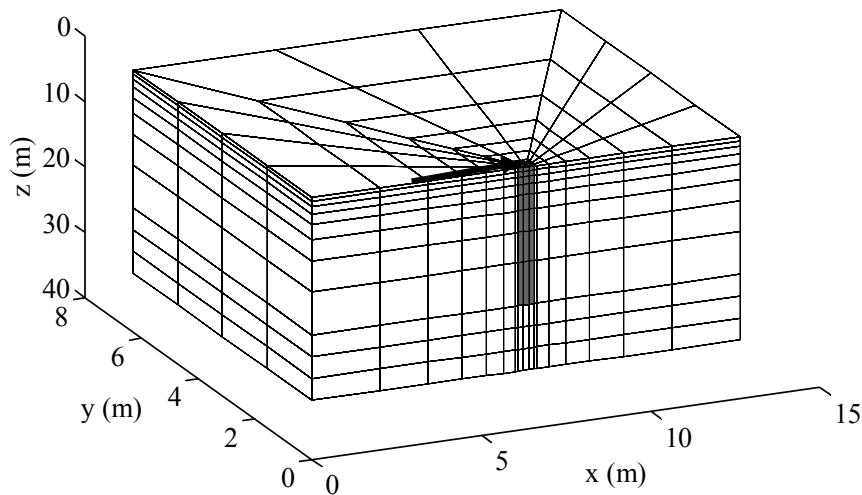


Figure 3.1 Finite mesh used in the computation of moments.

used to characterize the interface, primarily through a reduced friction angle equal to two thirds of the free-field value. The pile is modeled as an elastoplastic material that obeys the von Mises yield criterion. From here on, three types of materials are identified as ‘soil’, ‘interface’, and ‘pile’, respectively. All three are assumed to follow the non-associated von Mises flow rule, but without any plastic hardening. The von Mises potential function is given by

$$g = 3J_2 \quad (1.1)$$

where J_2 represents the second stress invariant.

The soil is a homogenous medium dense sand with a friction angle ϕ of 39° and a unit weight γ_o of 14.5 kN/m^3 . Soil nonlinearity also results from adoption of a pressure-dependent Young’s modulus E :

$$E = E_o \left(\frac{p}{p_{atm}} \right)^{0.5} \quad (1.2)$$

where E_o is the initial Young’s modulus, taken as 17.4 MPa. Also, p is the confining pressure and p_{atm} is atmospheric pressure. The soil model is based on the extended Mohr-Coulomb (EMC) elastoplastic model, which has been implemented into OpenSees as part of this study. Yielding is given by:

$$f = \alpha p + N(\theta)q - k \quad (1.3)$$

where $\alpha = 6\sin\phi/(3+\sin\phi)$, $k = 6c\cos\phi/(3+\sin\phi)$, and:

$$N(\theta) = \frac{4(1-e^2)\cos^2\theta + (2e-1)^2}{2(1-e^2)\cos\theta + (2e-1)[4(1-e^2)\cos^2\theta + 5e^2 - 4e]} \quad (1.4)$$

In Equation(1.4), $e = (3+\sin\phi)/(3-\sin\phi)$, and c is the cohesion of the soil. Deviatoric and volumetric stresses, q and p respectively, are given by:

$$q = \sqrt{\frac{3}{2}} s_{ij} s_{ij} \quad (1.5)$$

$$p = \frac{\sigma_{mm}}{3} \quad (1.6)$$

where:

$$s_{ij} = \sigma_{ij} - p\delta_{ij} \quad (1.7)$$

$$\theta = \cos^{-1}\left(\frac{\sqrt{3}}{2} \frac{s_1}{\sqrt{J_2}}\right) \quad (1.8)$$

s_1 is the first principal value of s_{ij} , and δ_{ij} is the Kronecker Delta.

The pile chosen for modeling purpose consists of a square cross-section of 400 mm by 400 mm. The Young's modulus of the pile material $E_p = 26.07$ GPa and the yield function for this material is assumed to be given by:

$$f = 3J_2 - k^2 \quad (1.9)$$

where $k = 30.3$ MPa is the yield strength of the pile material.

3.3 Finite Element Modeling

Eight-node brick elements and a reduced integration scheme with six integration points in each element were selected for the pile, interface, and soil materials. The reduced integration scheme was necessary to keep computations manageable. The six Gauss points are in the center of the six surfaces constituting the brick element. The mesh consisted of a total of 976 elements and 1248 nodes (Figure 3.1). The top 21 meters of soil and pile are divided into eight layers. Ten meters of soil were included beneath the tip of the pile to minimize boundary effects and were divided equally into three layers.

The first stage of the analysis involved self-weight loading in order to generate a static equilibrium stress state prior to lateral loading. During this phase, each node was allowed a single vertical degree of freedom, except on the bottom boundary where all degrees were fixed. After the initial stresses were set, each node was assigned three displacement degrees of freedom for the subsequent loading phase with equilibrated lateral pressures substituted for related degrees of freedom. Lateral boundaries were restrained in their respective normal directions. The bottom of the domain was restrained in all three directions. The unit weight of the pile was assumed to equal that of the soil. As already mentioned, the only difference between the interface and free field soil elements was the assumption of a reduced friction from the former (26^0).

3.4 Methods to Determine Soil Resistance P and Pile Moment M

Soil resistance p (From now on, the italic small case p denotes the soil resistance) can be obtained from the stress state at the integration points along the soil-pile boundary. The value of traction in the x -direction, which is the loading direction, is taken as:

$$T_x = \sigma_{xj} n_j \quad (j = x, y, z) \quad (1.10)$$

where $\mathbf{n} = (n_x, n_y, n_z)^T$ is the vector normal to the surface of the pile and σ_{ij} is the stress state of each integration point. Soil resistance can then be obtained as:

$$p = \int_L T_x dl \quad (1.11)$$

where L is the circumference of the pile. Unfortunately, this expression leads to different traction forces depending on whether stresses for the adjacent pile or soil elements are used. A different method involves differentiating the moment twice with respect to depth, z :

$$p(z) = \frac{\partial^2 M(z)}{\partial z^2} \quad (1.12)$$

For this purpose, the moment distribution, which is calculated from the stress state in the pile, must be expressed as a polynomial function of the vertical coordinate z (Wakai, Gose et al. 1999; Chae, Ugai et al. 2004). This is not always easy to do.

In this paper, a new method is adopted. In order to obtain the soil resistance of the i^{th} layer of soil, the i^{th} layer of pile elements are considered (Figure 3.2). The nodal forces in x direction of each pile element caused by the internal stresses are integrated from the values of all six integration points. The sum of the nodal forces in x direction, S_i , on the upper surface of the i^{th} layer of pile elements are in the same magnitude as and different sign to that on the lower surface. The distribution of the soil resistance force, $2Q_i$, along the depth of this layer is taken as constant. Therefore, it can be taken as two concentrated forces acting on the upper and lower surfaces respectively. The external shear forces on this layer caused by the upper $(i-1)^{th}$ layer and lower $(i+1)^{th}$ layer of pile elements are V_{i-1} and V_i respectively. By setting the external and internal nodal forces equal on both upper and lower surfaces, the soil resistance force, $2Q_i$, can be obtained from $V_{i-1} - Q_i = S_i$ and the shear force can be obtained from $V_i + Q_i = S_i$. For the first layer at the top of the pile,

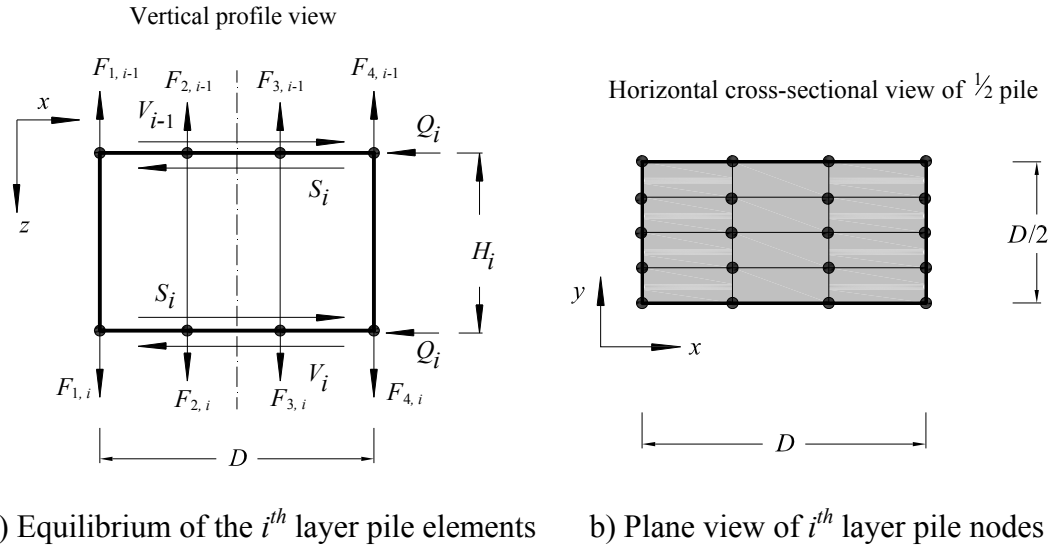


Figure 3.2 Schematic for calculation of pile elements.

V_0 is equal to the lateral load applied. The average soil resistance in the i^{th} layer, p_i , is obtained by dividing $2Q_i$ by the height H_i :

$$p_i = \frac{2Q_i}{H_i} \quad (1.13)$$

The moment in the pile can be obtained from summarizing the moment of each vertical internal nodal force to the center line of the pile cross-section (Figure 3.2):

$$M_i = \sum_{j=1}^4 F_{j,i} \left(\frac{x_1 + x_4}{2} - x_j \right) \quad (1.14)$$

where $F_{j,i}$ is the total vertical internal nodal force of the j^{th} column nodes on the i^{th} layer of pile and x_j is the x coordinate of the j^{th} column (Figure 3.2b).

3.5 Coefficient of Lateral Earth Pressure at Rest

The initial stress conditions in the soil surrounding the pile which were established by the process of self-weight consolidation can be characterized by the coefficient of lateral earth pressure at rest, K_o . Upon lateral loading, passive and active conditions develop on the leading and trailing sides of the pile, respectively. The main reason of the self-weight phase is to establish an equilibrated condition with a set of initial stresses at the Gauss

integration points. Resulting strains are of secondary importance. Therefore, during this phase, the soil and the pile are both taken as elastic materials with a very large Young's modulus and a suitable Poisson's ratio in order to avoid large initial strains. The Poisson's ratio is determined by the value of K_o as:

$$v = \frac{K_o}{1 + K_o} \quad (1.15)$$

For loose sand K_o is often approximated by Jaky's (1944) relationship, $K_o = 1 - \sin\phi$, or it may be determined from in situ tests. The soil's stress ratio:

$$\eta = \frac{3(1 - K)}{1 + 2K} \quad (1.16)$$

is a useful measure to evaluate particular stress states relative to Mohr-Coulomb limiting frictional conditions of active failure ($\eta = \eta_a$, $K = K_a$) and passive failure ($\eta = \eta_p$, $K = K_p$). If we assume that Jaky's relationship holds, then $\eta_o < \eta_a$ and $K_a < K_o < 1$. Since $\phi = 26^\circ$ for the interface ($K_a = 0.39$), the range of possible initial stresses in the deviatoric plane lies between points O and A in Figure 3.3. We can investigate the effect of initial

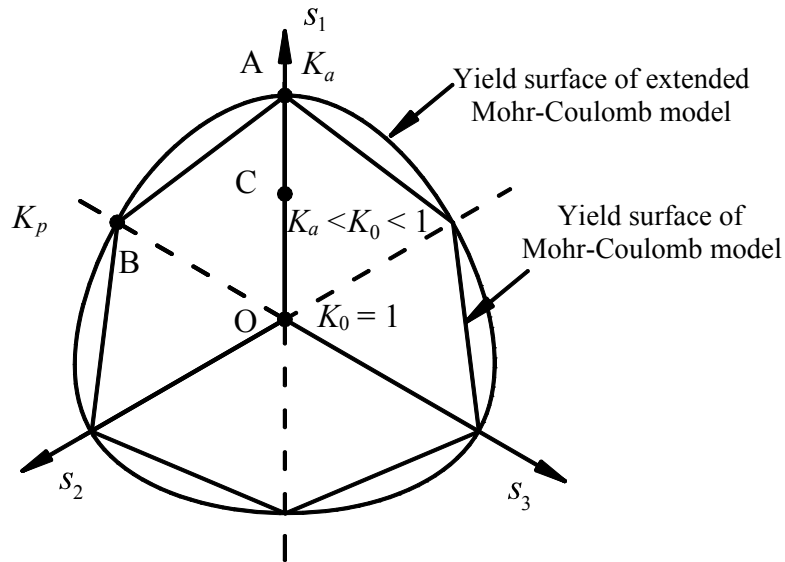


Figure 3.3 Range of coefficient of lateral earth pressure at rest K_o prior to lateral loading.

stress conditions on subsequent lateral loading by considering various values of K_o during the self-weight process. If K_o is set to 0.4, initial stresses will be quite close to active failure (for example points C_1 , C_2 or C_3 in Figure 3.4). On the other hand, if we assume that the overburden stress $\sigma_v = \gamma_0 z$ does not change, then increasing values of K_o correspond to stress conditions progressively further removed from the envelope of active failure (Figure 3.4). Therefore, increasing values of K_o corresponds with increased elastic regions and presumably to different behaviors upon lateral loading.

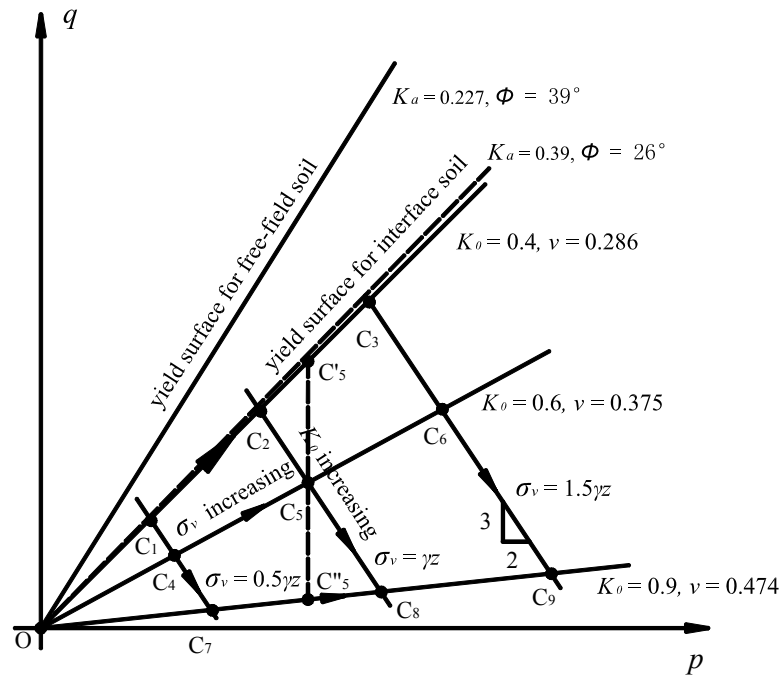


Figure 3.4 Initial stress conditions investigated.

Three simulations were carried out with $K_o = 0.4$, 0.6 , and 0.9 , respectively, with a constant $\gamma_0 = 14.5 \text{ kN/m}^3$. A lateral load of 671 kN was applied in each case. It can be seen in Figure 3.5a that a larger soil resistance develops near the upper end of the pile as the value of K_o increases, even though deflection at the pile head decreases (Figure 3.5b). Similarly, the maximum bending moment generated in the pile becomes slightly smaller (Figure 3.5c) and the stiffness of the p - y curves increases somewhat (Figure 3.5d). The combination of soil and pile characteristics are such that the pile can be considered

flexible (In this case failure is controlled by the pile properties and the maximum bending moment.) and failure is likely to occur in the pile before the soil reaches limiting conditions. Therefore, it may be argued that the lateral capacity of the pile-soil system increases with K_o . However, the effect is minimal, at least for the set of conditions investigated.

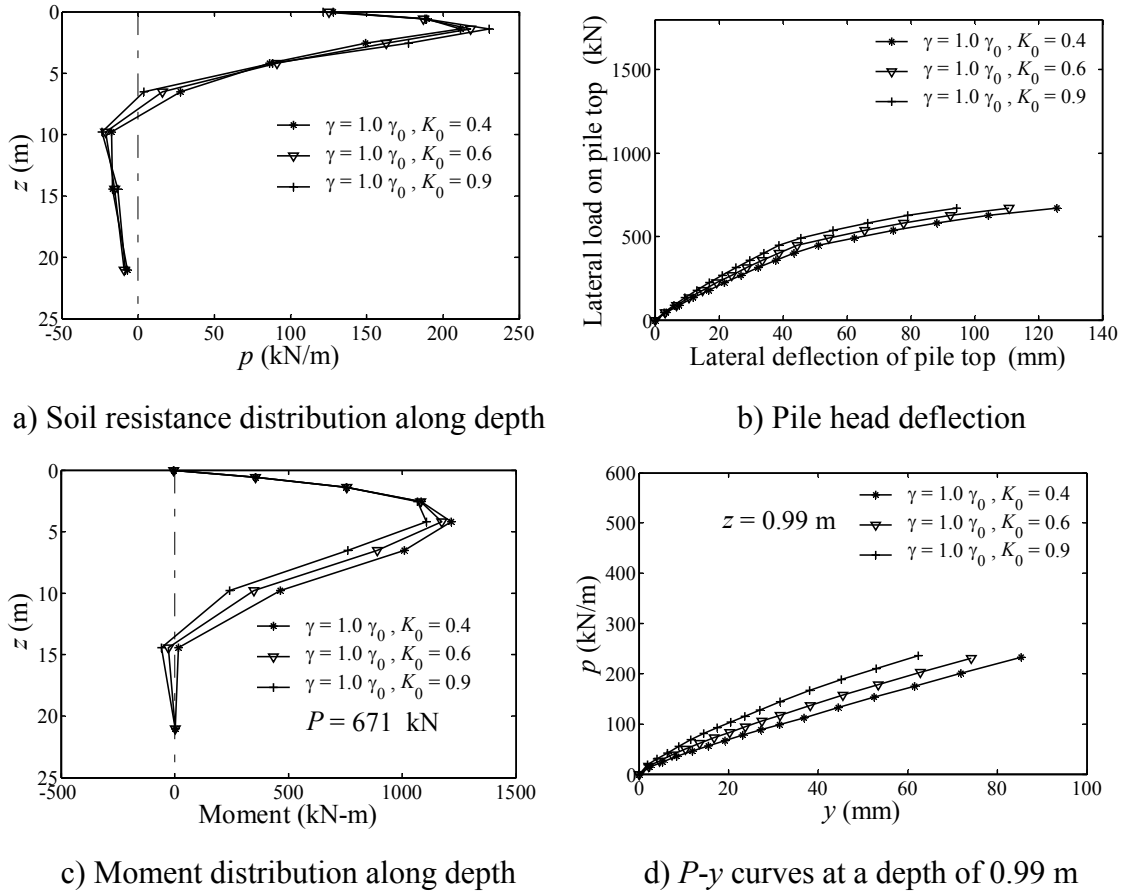


Figure 3.5 Effect of K_o (Final lateral load $P = 671$ kN)

3.6 Unit Weight of Soil

The unit weight of the soil plays an important role in the development of lateral resistance. In the Broms' (1964a) method, pile lateral resistance is as a nonlinear function of soil weight and the coefficient of passive lateral earth pressure K_p . Similarly, Reese et al. (1974), Borgard and Matlock (1980), and Meyerhof (1995) assume the ultimate lateral

resistance directly proportional to the unit weight of soil. In Meyerhof's method the ultimate lateral load is given by:

$$Q_u = 0.12\gamma DL_e^2 K_{br} \leq 0.4 p_l DL \quad (1.17)$$

where K_{br} is the resultant net soil pressure coefficient. D and L are the diameter and length of the pile, respectively. L_e stands for effective length:

$$L_e = 1.65 K_r^{0.12} L \leq L \quad (1.18)$$

where K_r is the pile's relative stiffness. Also, p_l is the limit pressure obtained from pressuremeter tests and can be given in units of kPa as:

$$p_l = 40 \tan^2 \left(45 + \frac{\phi}{2} \right) e^{\pi \tan \phi} \tan \phi \quad (1.19)$$

The pile's relative stiffness has the following form:

$$K_r = \frac{E_p I_p}{E_s L^4} \quad (1.20)$$

where E_s is the average horizontal soil modulus of elasticity. If K_r is less than 0.01 the pile is considered flexible. Figure 3.6a shows predicted soil resistance, where the unit weight of soil varies from $0.5\gamma_o$ (Point C_1 , Figure 3.4) to $1.0\gamma_o$ (Point C_2 , Figure 3.4) to $1.5\gamma_o$ (Point C_3 , Figure 3.4) while K_o remains constant. Here $\gamma_o = 14.5 \text{ kN/m}^3$. For a lateral load of 671 kN, the displacement of the pile becomes much smaller as the unit weight of the surrounding soil increases, as expected (Figure 3.6b and 3.6d). At the same time, more and more load is transferred to the upper layers, leading to smaller maximum moments and larger ultimate lateral capacities. But such an increase relationship between soil unit weight and ultimate lateral load is not linear as expected from Equation (1.17). The reason for this is redistribution of lateral soil pressures acting against the pile that occurs as the lateral load is increased. This phenomenon is not accounted for in the simplified methods. It must be stated though that the differences in predicted peak moments (Figure 3.6c) are rather small, despite the wide range of unit weights considered.

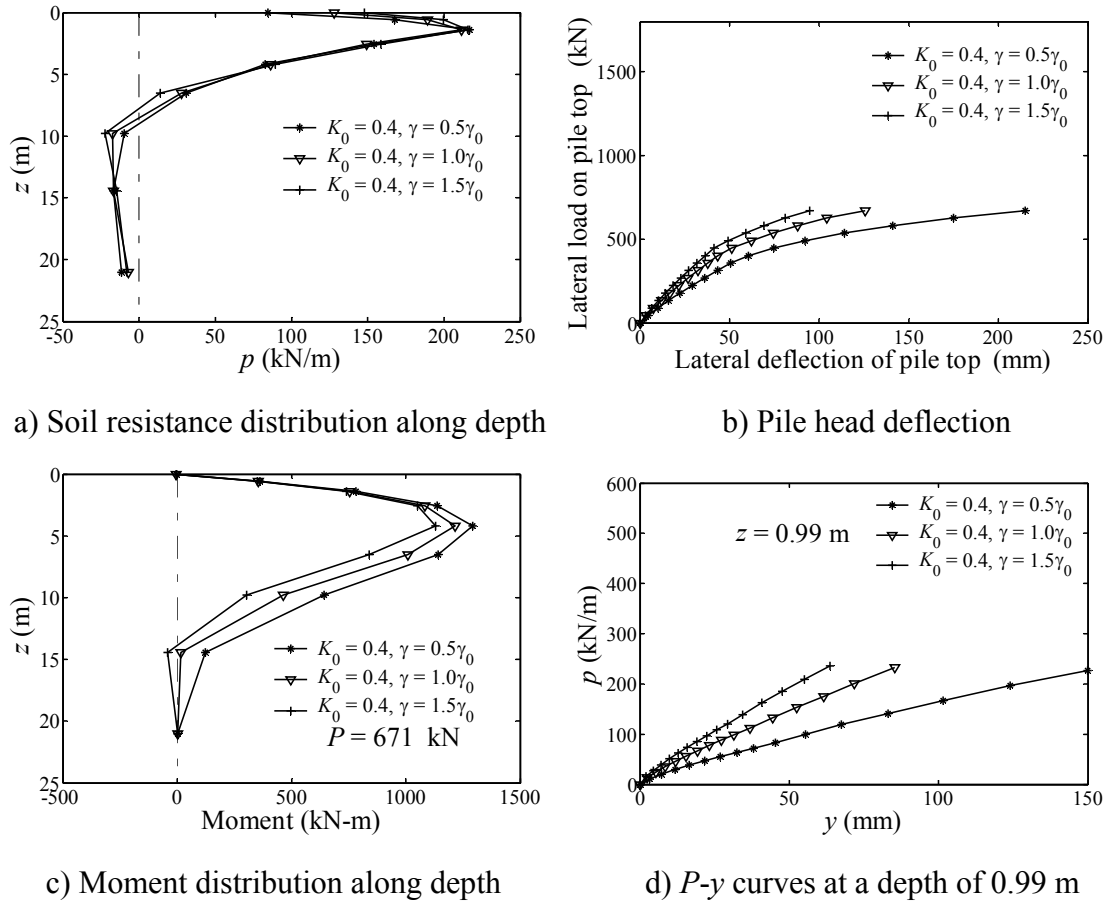


Figure 3.6 Effect of γ (Final lateral load $P = 671$ kN)

3.7 Mean Soil Pressure

Lateral resistance increases with K_o and γ_o , in part because the initial mean soil pressure, p_o , increases as well. This in turn leads to a larger soil modulus E and a stiffer ensuing behavior. In order to isolate the effect that stress distance from the active failure condition plays at constant mean pressure, three simulations are compared in Figure 3.7 corresponding to the initial states C_5' ($K_o = 0.4$, $\gamma = 11/9\gamma_o$), C_5 ($K_o = 0.6$, $\gamma = \gamma_o$), and C_5'' ($K_o = 0.9$, $\gamma = 11/14\gamma_o$) in Figure 3.4. Only small differences can be observed in p - y stiffness and pile moments. As the position of the initial stress state approaches to the hydrostatic line, beginning at C_5' and ending at C_5'' , the lateral resistance increases slightly. It therefore appears that increasing lateral resistance with K_o is due partly to an increase in developed shear resistance (as measured by the distance between the initial

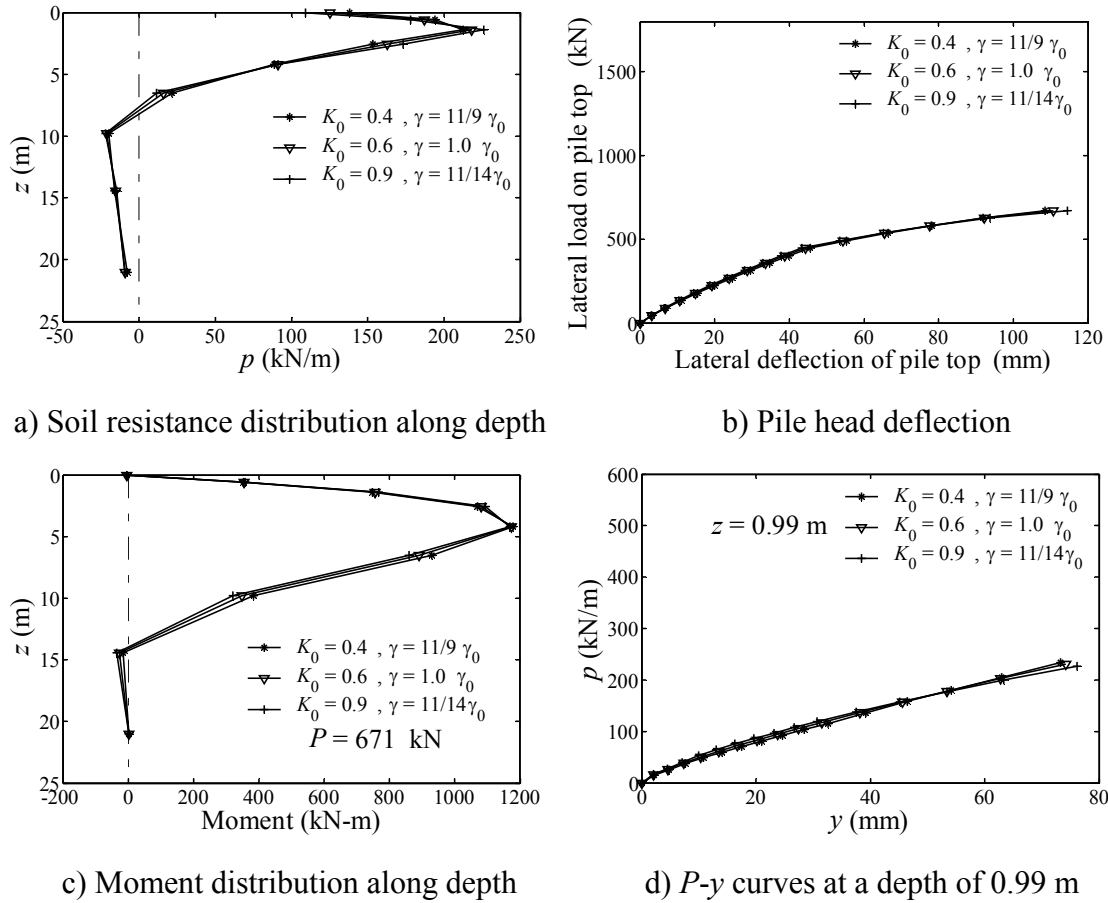


Figure 3.7 Effect of initial mean soil pressure p (Final lateral load $P = 671$ kN)

stress state and the failure surface), but more importantly due to an increase in the mean soil pressure, as noted by Fan and Long (2005). However, the lateral response of the pile is not a direct function of K_o and γ_o . These parameters play a role in establishing the initial soil stresses and thereafter lateral behavior becomes primarily a function of the nonlinear stiffness of the soil. If Young's modulus is assumed to be independent of stress state, the influence of K_o and γ_o can be neglected.

3.8 Initial Young's Modulus E_o

The initial stiffness of the soil, E_o , plays an important role in determining ultimate lateral resistance (Figure 3.8). For example, given a load of 671 kN, the deflection of the top of the pile with initial soil modulus of 1.74 MPa is about 7 times that with E_o of 17.4 MPa

and 32 times that with E_o of 174 MPa (Figure 3.8b). The modulus of subgrade reaction, which is the slope of the p - y curve, more than doubles as the value of E_o increases by a factor of ten. The effect of increasing the initial soil stiffness is to generate a higher passive soil pressure and a correspondingly lower moment near the top, whereas a lower initial stiffness leads to a more uniform lateral pressure distribution and a higher maximum moment. As mentioned before, the lateral resistance capacity of the flexible pile is controlled by failure of the pile, which occurs where the moment capacity is exceeded. Therefore, piles in soil of higher initial stiffness can be expected to have a larger capacity.

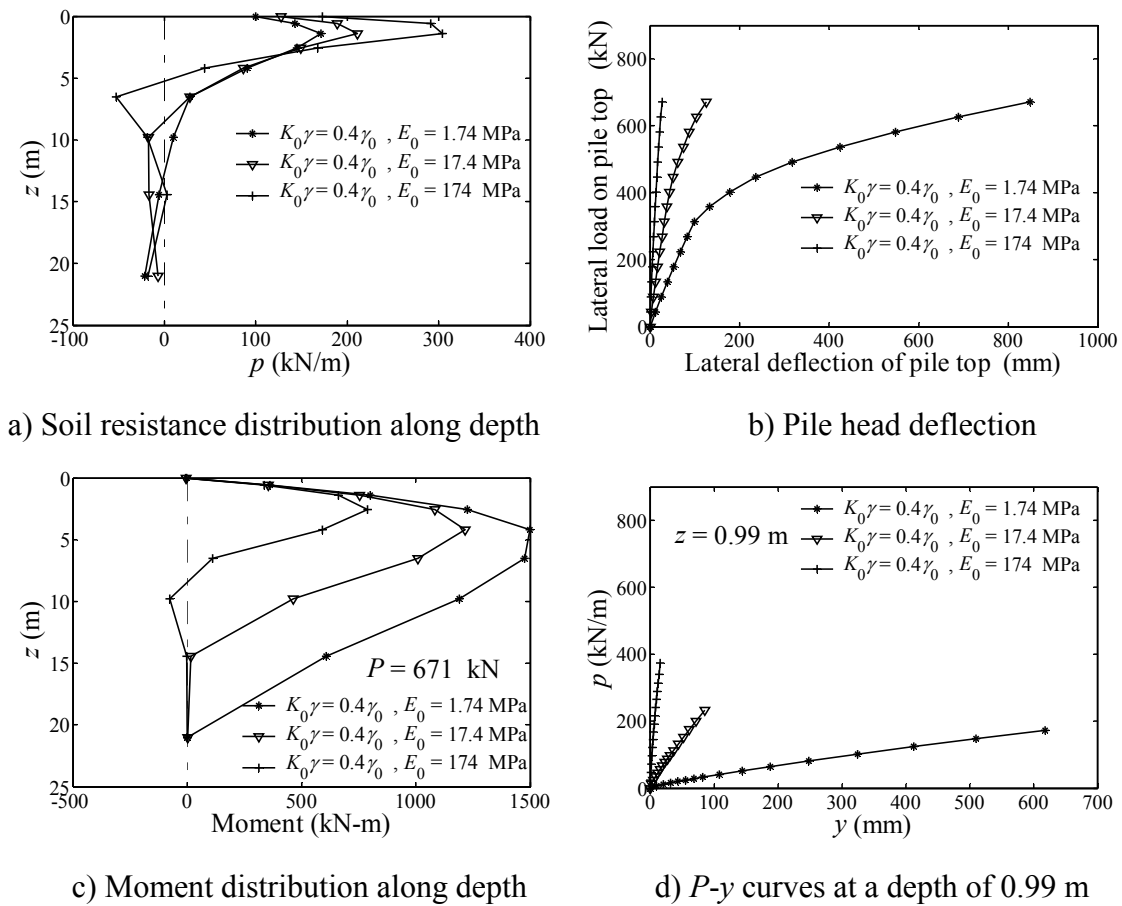


Figure 3.8 Effect of E_o (Final lateral load $P = 671$ kN)

For the pile at hand, the righthand side of Equation (1.17) is estimated to be 6090 kN for $\phi = 39^\circ$. As E_o varies from 1.74 MPa to 174 MPa, the corresponding average E value of the pile changes from 1.65 MPa to 165 MPa and the effective length L_e decreases from

12.25 m to 7.05 m (Equations (1.18) and (1.20)). As a result, the value of Q_u decreases from 2194 KN to 726.5 KN according to Equation (1.17). This trend of lower capacity with larger initial stiffness is opposite to what is suggested by the simulations in Figure 3.8. Again, the reason here is that the simplified methods do not account for stiffening of the soil that occurs on the leading edge of the pile as lateral deformation takes place. Such pressure-dependent soil stiffening has long been recognized as an important aspect of soil behavior, particularly for cases involving significant volume change, but can only be captured accurately by modeling of the type carried out in this study.

3.9 Pile Diameter

Lateral resistance in cohesionless soils along the length of the pile is usually expressed as a variant of the following equations:

$$p(z) = D\gamma zK \quad (1.21)$$

where all the terms have previously been defined. For example, in Brom's method (1964a), the ultimate resistance p_{ult} is given as:

$$p_{ult}(z) = 3D\gamma zK_p \quad (1.22)$$

where K_p is again the coefficient of passive lateral earth pressure. Brinch Hansen (1961) suggested instead that:

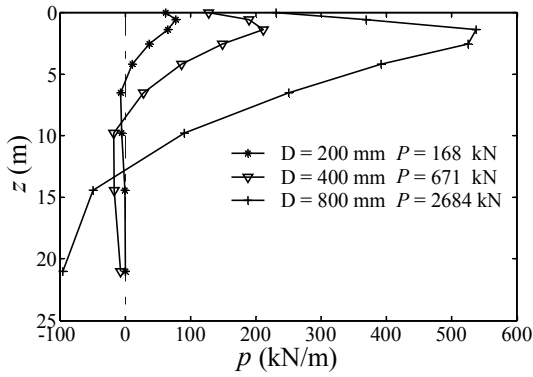
$$p_{ult}(z) = D\gamma zK_q \quad (1.23)$$

where K_q is the Hansen earth pressure coefficient, which is also a function of the friction angle ϕ . Fleming et al. (1992) used the square of K_p instead of $3K_p$ in Equation (1.22). To account for the shape of the pile, Zhang et al. (2005) proposed a function as:

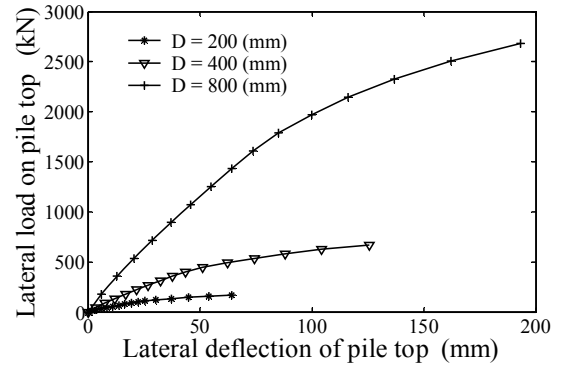
$$p_{ult}(z) = D\gamma z(\eta K_p^2 + \xi K \tan \delta) \quad (1.24)$$

where η and ξ are shape factors and δ is the interface friction angle between pile and soil.

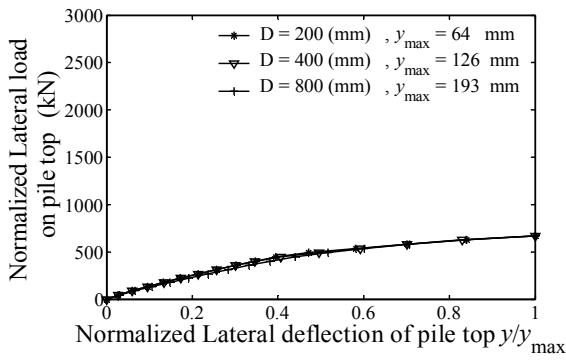
In this study, the influence of the diameter D of the pile is investigated by varying the diameter and keeping all the other parameters constant. Figure 3.9a and 3.9d reveal that the lateral load is transferred more uniformly in larger diameter piles, while the smaller



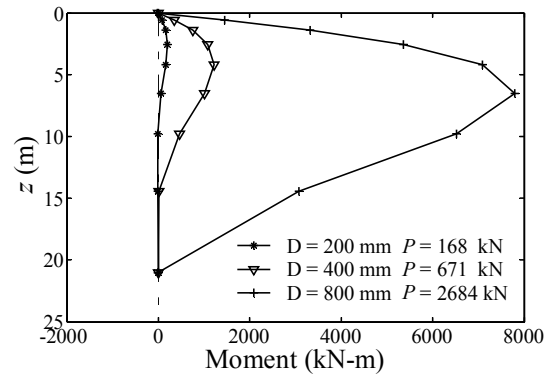
a) Soil resistance distribution along depth



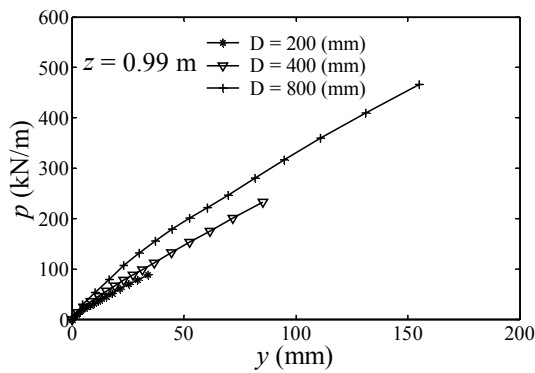
b) Pile head deflection



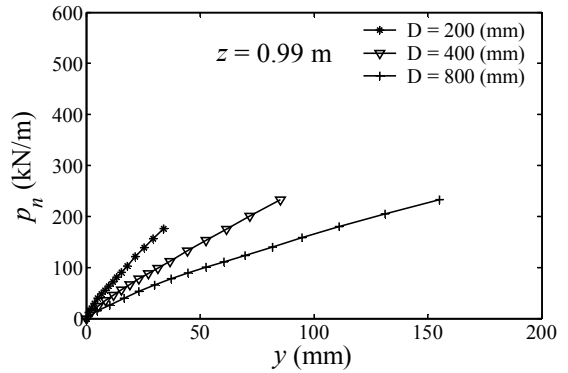
c) Normalized pile head deflection



d) Moment distribution along depth



e) P - y curves



f) P - y curves (Normalized p)

Figure 3.9 Effect of D

diameter piles transfer lateral load mainly relying on the upper portion of the pile. The results in Figure 3.9a, 9e, and 9f suggest that Equation (1.22) does a poor job as

representing the distribution of lateral resistance as a linear function of the diameter of the pile. If the relationship between the soil resistance is proportional to the diameter of the pile, then the normalized soil resistance, here defined as:

$$p_n = \frac{P}{D} \times 400 \quad (1.25)$$

with D given in mm, would be the same in all three cases in Figure 3.9f. Instead, Figure 3.9f indicates that the normalized soil resistance decreases with increasing pile diameter. This phenomenon is once more caused mainly by the nonuniform distribution of passive soil resistance along the leading edge of the pile. This was also noted by Prakash and Kumar (1996) and by Zhang et al (2005). In fact, Figure 3.9e shows a diameter-independent trend in the p - y curves in depth 0.99 m.

As expected, the calculated ultimate lateral resistance of the pile the case of D equal to 800 mm is larger than that for piles with a smaller diameter (Figure 3.9b). However, it is not proportional to D as indicated in Equation (1.17). Instead, it is proportional to D^2 as shown in Figure 3.9c. In Figure 3.9c the normalized lateral load on pile top equals to the applied lateral load multiplied by a factor of $(D/400)^2$, where D is in mm.

3.10 Pile Young's Modulus E_p

More rigid piles lead to a larger lateral load capacity (Figure 3.10). According to Equation (1.20), if for example E_p increases from 2.607 GPa to 260.7 GPa, the relative stiffness factor K_r increases 100 times. As a result, L_e increases 1.74 times to 12.25 m, which is still less than L Equation (1.18) and the ultimate lateral resistance increases by a factor of 3.02 to 2194 kN less than the maximum 6090 kN according to Equation (1.17). This increase in E_p is equivalent to decreasing E_o by a factor of 100. The results in Figure 3.10 confirm, as expected, that the implied ultimate pile resistance increases with increasing E_p . Larger pile stiffness also reduces the deflection of the pile dramatically even though the moment generated in pile with larger stiffness is also much larger Figure 3.10b and 10c. Apparently, p - y curves are independent to the pile stiffness as in Figure 3.10d, this fact can also be verified by the study on the influence of the diameter of the pile.

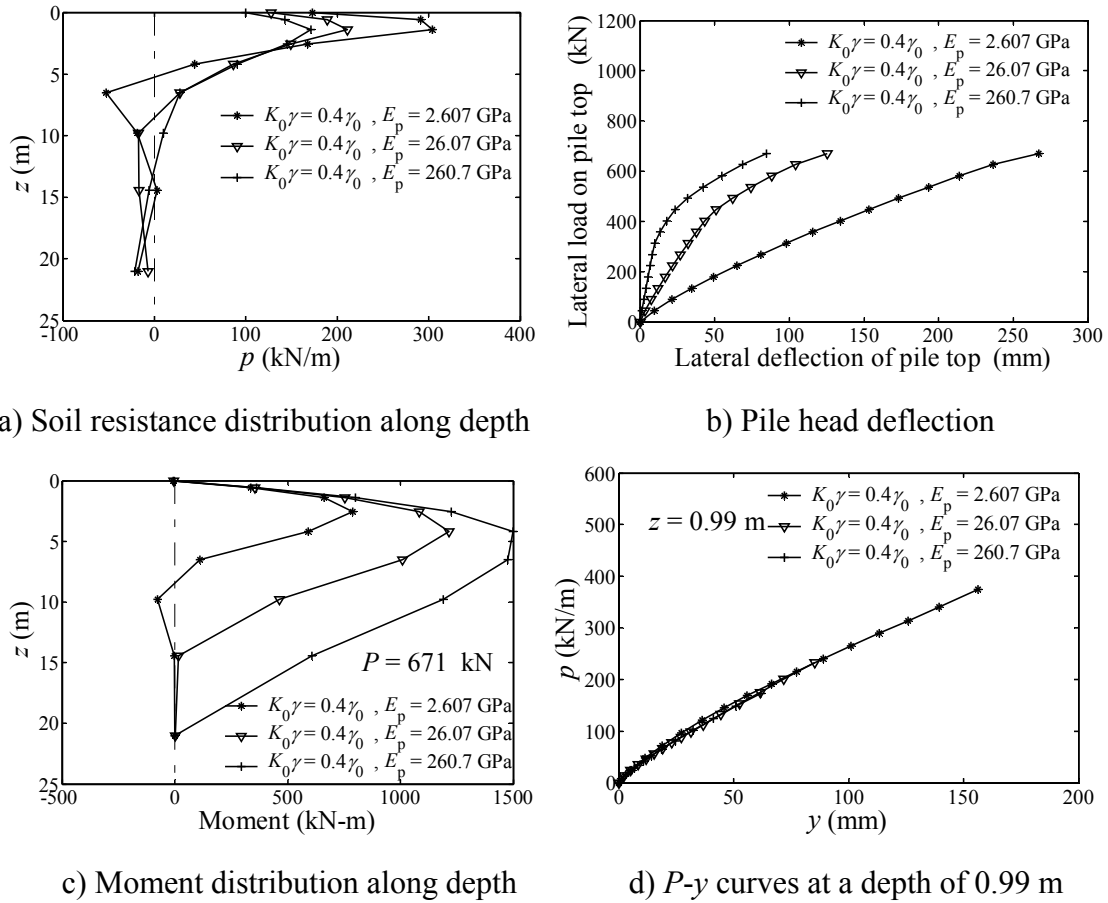


Figure 3.10 Effect of E_p (Final lateral load $P = 671$ kN)

The relative stiffness of the pile-soil system (Equation (1.20)) increases as either the pile stiffness $E_p I_p$ increases, or as the average Young's modulus of the soil decreases. As expected in Figure 3.11a and 11c the resulted soil resistance distribution (Figure 3.11a) and the moment (Figure 3.11c) generated in the pile have no difference in both cases. However, these effects lead to significant differences in terms of lateral deflections. For instance in Figure 3.11b and 11d the relatively stiffer soil-pile configurations for which the distribution of soil resistance is the same (Figure 3.11a) and so is the moment (Figure 3.11c) have a much larger deflection for soil with E_o of 1.74 Mpa than for pile with E_p of 260.7 Gpa (Figure 3.11b). As the deflection of the pile head is concerned in elastic range (Figure 3.11b), increasing the stiffness of the pile or that of the soil gives the same results. As the pile-soil system falls into the elastoplastic range under the increasing lateral load, the system appears stiffer in the case of soil stiffness increasing. It is controversial to

Equation (1.20).

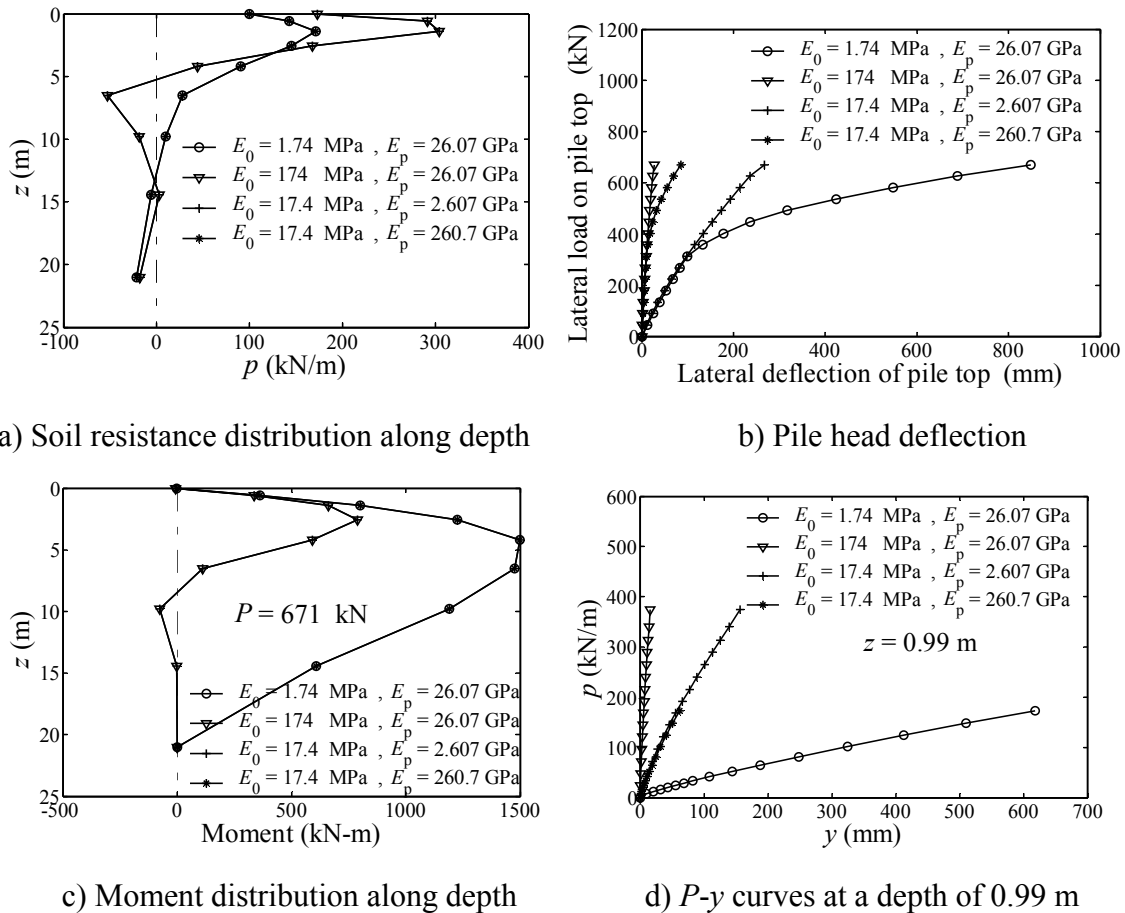


Figure 3.11 Effect of E_0 and E_p (Final lateral load $P = 671$ kN)

As pointed out previously, the p - y curves are independent of the stiffness of the pile. But they rely heavily on the stiffness of the soil. As the soil becomes weaker, the slope of the p - y curve decreases (Figure 3.11d).

3.11 Soil Friction Angle

The friction angle defines the location of the elastoplastic soil's yield surface. It is crucial in determining lateral capacity for the simplified methods (Brinch Hansen 1961; Broms 1964a; Reese, Cox et al. 1974; Fleming, Weltman et al. 1992; Meyerhof 1995; Zhang, Silva et al. 2005). Its role in the determination of the lateral resistance capacity of the pile

derives from setting the initial lateral earth pressure coefficient K_o and the limiting conditions given by K_a and K_p . In order to investigate whether ϕ plays a role in the predictions, other than through the K_o coefficient, simulations are presented in Figure 3.12 where K_o has been set to an arbitrary value of 0.4 during the self-weight loading stage, and then varying the value of during lateral load. The results indicate that the value of ϕ plays only minor role on the lateral capacity of the pile during lateral loading. It is probably caused by the small range of values of ϕ investigated. For larger values of ϕ ,

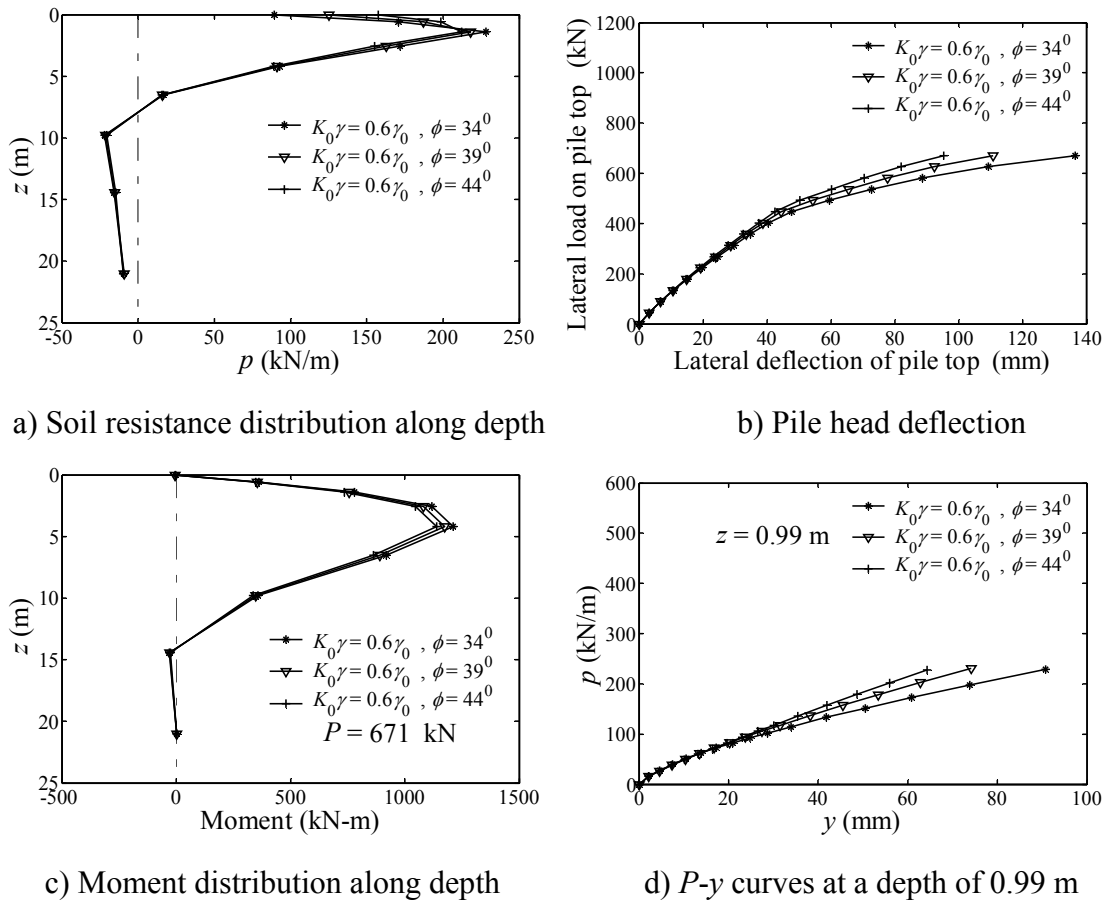


Figure 3.12 Effect of friction angle ϕ (Final lateral load $P = 671$ kN)

the soil resistance distribution appears to be slightly more uniform and the maximum bending moment slightly smaller, but this effect is very minimal. Thus, the effect of the friction angle on ultimate lateral resistance comes mainly from determining the initial value of K_o . But as for the deformation of the top of the pile, larger friction angle reduces the deflection of the pile (Figure 3.12d).

3.12 Conclusions

In this study, the influence of soil and pile constitutive parameters and pile diameter on lateral resistance are investigated for a single pile in cohesionless soil. Based on the results of several 3D elastoplastic simulations, the role of each parameter is qualified.

For a given pile, if its properties and geometry are held constant, the effects of soil unit weight, friction and initial coefficient of lateral earth pressure play a similar role in the development of lateral resistance. They act to establish the initial stress conditions in the soil surrounding the pile and influence the initial value of the soil's Young's modulus. This initial stiffness is important since the soil is assumed to become stiffer with lateral deformation as the passive region on the front of the pile increases in mean stress. Once the initial Young's modulus of the soil is set, the effect of those parameters on the lateral resistance is very limited. However, as the value of Young's modulus in the soil increases, additional larger lateral resistance develops leading to larger ultimate capacity. Of course, pressure-dependent stiffening is not accounted for in Meyerhof's (1995) method, which actually predicts a decrease in ultimate lateral capacity with an increase in soil modulus at least for the case investigated here in. On the other hand, Young's modulus of the pile has little effect on the p - y curves for the range of pile and soil parameters investigated. The role that the diameter of the pile plays on lateral resistance is also accounted for incorrectly in the methods of Meyerhof (1995) and Broms (1964a).

3.13 References

- Adachi, T. and M. Kimura (1994). Analyses of ultimate behavior of lateral loading cast-in-place concrete piles by 3-dimensional elastoplastic FEM. 8th Intl. Conf. on Computer Methods and Advances in Geomechanics, Morgantown, WV.
- Borgard, D. and H. Matlock (1980). Simplified calculation of p - y curves for laterally loaded piles in sand. Houston, Earth Technology Corporation, Inc.
- Brinch Hansen, J. (1961). The ultimate resistance of rigid piles against transversal forces. Bulletin No.12, Copenhagen, Denmark, Danish Geotechnical Institute.

- Broms, B. B. (1964a). "Lateral resistance of piles in cohesionless soils." Journal of Soil Mechanics and Foundation Division, ASCE **90**(3): 123-56.
- Broms, B. B. (1964b). "Lateral resistance of piles in cohesive Soils." ASCE Journal of the Soil Mechanics and Foundation Division Proceedings (JSMFD) **90**(SM2): 27-63.
- Brown, D. A. and C.-F. Shie (1990a). "Numerical experiments into group effects on the response of piles to lateral loading." Computers and Geotechnics **10**: 211-230.
- Brown, D. A. and C.-F. Shie (1990b). "Three dimensional finite element model of laterally loaded piles." Computers and Geotechnics **10**: 59-79.
- Brown, D. A., C.-F. Shie, et al. (1989). p-y curves for laterally loaded piles derived from three-dimensional finite element model. Proceedings of the 3rd International Symposium on Numerical Models in Geomechanics, Niagara Falls, Canada, Elsevier Applied Science.
- Brown, D. M. and C.-F. Shie (1991). "Some numerical experiments with a three dimensional finite element model of a laterally loaded pile." Computers and Geotechnics **12**: 149-162.
- Chae, K. S., K. Ugai, et al. (2004). "Lateral resistance of short single piles and pile groups located near slopes." International Journal of Geomechanics **4**(2): 93-103.
- Fan, C.-C. and J. H. Long (2005). "Assessment of existing methods for predicting soil response of laterally loaded piles in sand." Computers and Geotechnics **32**: 274-289.
- Filho, R. M., A. V. Mendonca, et al. (2005). "Static boundary element analysis of piles submitted to horizontal and vertical loads." Engineering Analysis with Boundary Elements **29**: 195-203.
- Fleming, W. G. K., A. J. Weltman, et al. (1992). Piling engineering. London, Surrey University Press.
- Jaky, J. (1944). "The coefficient of earth pressure at rest." Journal of the Society of Hungarian Architects and Engineers **7**: 355-358.
- M.W., O. N. and J. M. Murchison (1983). An evaluation of p-y relationships in sands. Research Report No. GT-DF02-83, Department of Civil Engineering, University of Houston.
- Matlock, H. and L. C. Reese (1960). "Generalized solutions for laterally loaded piles." Journal of Soil Mechanics and Foundation Division, ASCE **86**(5): 63-91.
- Meyerhof, G. G. (1995). "Behavior of pile foundations under special loading conditions: 1994 R. M. Hardy Keynote Address." Canadian Geotechnical Journal **32**(2):

204-222.

- OpenSees (2004). Open System for Earthquake Engineering Simulation, Pacific Earthquake Engineering Research. **2005**.
- Poulos, H. C. (1971a). "Behavior of laterally loaded piles: I -- single pile." Journal of Soil Mechanics and Foundation Division, ASCE **97**(SM5): 711-731.
- Poulos, H. C. (1971b). "Behavior of laterally loaded piles: II -- pile groups." Journal of Soil Mechanics and Foundation Division, ASCE **97**(SM5): 733-751.
- Prakash, S. and S. Kumar (1996). "Nonlinear lateral pile deflection prediction in sands." Journal of Geotechnical Engineering Division ASCE **122**(2): 130-138.
- Reese, L. C., W. R. Cox, et al. (1974). Analysis of laterally loaded piles in sand. Proceedings of the 6th Offshore Technology Conference, Houston, Texas.
- Reese, L. C. and H. Matlock (1956). Non-dimensional solutions for laterally loaded piles with soil modulus assumed proportional to depth. Proceedings of the 8th Texas conference on soil mechanics and foundation engineering.
- Wakai, A., S. Gose, et al. (1999). "3-D elasto-plastic finite element analyses of pile foundations subject to lateral loading." Soils and Foundations **39**(1): 97-111.
- Yang, Z. and B. Jeremic (2002). "Numerical analysis of pile behaviour under lateral loads in layered elastic-plastic soils." International Journal for Numerical and Analytical Methods in Geomechanics **26**: 1385-406.
- Zhang, L., F. Silva, et al. (2005). "Ultimate lateral resistance to piles in cohesionless soils." Journal of Geotechnical and Geoenvironmental Engineering **131**(1): 78-83.

Chapter 4

Formulation of Time-Domain Seismic Soil-Structure Interaction Using a Coupled Finite and Infinite Element Approach

Abstract

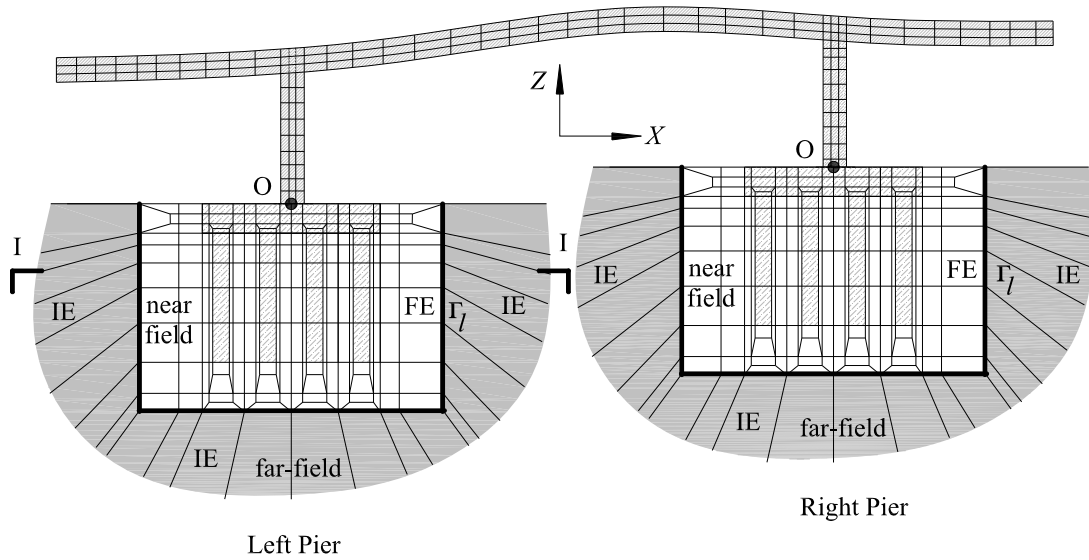
This paper presents the equations of motion for three-dimensional soil-pile-bridge interaction in the time-domain for static and seismic loading. For this purpose, a new three-dimensional semi-analytical infinite element in frequency domain is developed. This new infinite element is unique in that it can accommodate a variety of interface shapes between the near and far fields while allowing for the propagation of compressional, shear and Rayleigh waves. The equations of motion in the time domain follow in a straightforward fashion. The proposed formulation offers considerable computational efficiency compared to methodologies proposed in previous studies.

Keywords: time-domain; seismic; soil-structure; interaction; coupling; FE; IE; semi-analytical

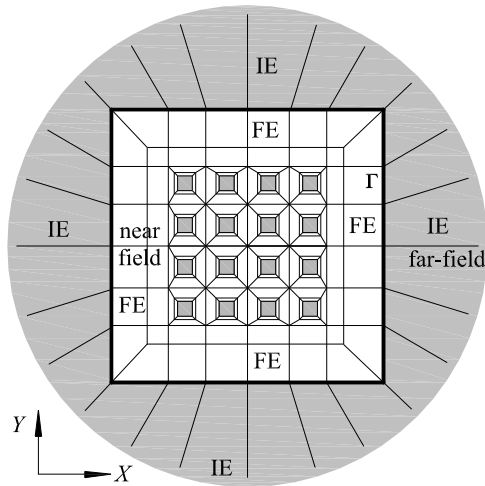
4.1 Introduction

Soil-structure interaction analysis can be a daunting task from a modeling perspective if soil nonlinearity, complex three-dimensional geometries and dynamic effects need to be included. A case in point is the planned replacement of the existing Kealakaha Bridge on the Mamalahoa Highway, north of Hilo, Hawaii. The existing bridge crosses a very deep gulch and is located in a seismically very active zone where the peak ground acceleration

with a 10% probability of exceedance in 50 years is 0.4g. The new bridge will have a curved plan view and will include two large-diameter piers, each supported by multiple piles (Figure 4.1). The two piers will be resting at different ground elevations in



a) Profiles of FE and IE mesh



b) FE and IE mesh in I-I cross-section

Figure 4.1 Schematic representation of analysis model using FE and IE

steeply sloping terrain. The overall layout is such that significant torsional effects can be expected from earthquake loading (Naeim 1989). Torsion in this case cannot be modeled

properly using a simplified two-dimensional geometry, and instead one must resort to three dimensions. In order to include seismic loading from far-field earthquakes, a substantial extent of the nearby soil also needs to be included in the problem domain with appropriate provisions for dynamic boundary conditions.

A comprehensive analysis of the new bridge's response to conceivable modes of static and dynamic loading is underway. However, accurate predictions based on conventional dynamic soil-structure interaction formulations that rely on finite element, boundary element or various coupled approaches is still largely unfeasible due to a lack of sufficient computational resources that can handle a reasonably acceptable degree of geometric and material modeling detail. Nonetheless, improvements can be sought by increasing the efficiency of existing formulations. In this article we present a semi-analytical technique for dynamic soil-structure interaction modeling in the time domain with a new infinite element, which should prove computationally efficient and effective for handling the types of complex problems such as the one described above.

Dynamic soil-structure and soil-pile-column interaction problems have been investigated extensively using the finite element method. However, not many studies have been reported using three dimensions in the time domain or that account for nonlinear near-field soil behavior. The few studies that are available (Cai, Gould et al. 2000; Maheshwari, Truman et al. 2004b; Maheshwari, Truman et al. 2004a) clearly point to the importance of soil nonlinearity, particularly with regard to dynamic interaction effects. Such nonlinearity is difficult to deal with in the frequency domain and is better handled in the time domain. Also crucial to effective three-dimensional modeling of soil-structure problems is a proper accounting of seismic wave components at the boundaries of the domain.

There are four methods available to simulate dynamic boundary conditions. In the transmitting boundary method (Lysmer and Kuhlemeyer 1969; Kausel 1974; Smith 1974; Kausel, Rosset et al. 1975; White, Valliappan et al. 1977; Akiyoshi 1978; Wolf 1985) the near field (pile cap, piles and a portion of the surrounding soil in Figure 4.1) is modeled

using conventional finite elements. The far-field soil, which is unbounded, is represented by a transmitting boundary that begins at the interface of the near-field and the far-field. However, transmitting boundaries often have at least one of the following restrictions: wave propagation through them is dependent on the incidence angle, the effects of frequency are not properly accounted for at these boundaries, and they are often unsuitable for static problems. Transmitting boundary element methods are difficult to implement in the time domain finite element formulations. In addition, in order to obtain accurate results, the bounded near field can not be too small.

Another approach is the boundary element method (Zienkiewicz, Kelly et al. 1977; Banerjee 1978; Kaynia and Kausel 1982; Beer 1986; Banerjee and Sen 1987). This constitutes a more rigorous method for unbounded three-dimensional problems since only the infinite boundaries are discretized using only two dimensions. Radiation at the infinite boundary is satisfied exactly through an analytical expression that follows from particular solutions. However, where such solutions do not exist, or they are extremely complex, the method becomes much more cumbersome or even unworkable. The boundary element method leads to a non-symmetric stiffness matrix, which further reduces its appeal for complex soil-structure interaction problems. As a result, its use has been restricted to rather simple cases such as homogeneous and isotropic foundation-soil problems with simple geometries and regular boundary shapes.

More recently, the scaled boundary method has received a lot of attention due to its suitability for both the finite element and boundary element methods. In this technique, spatial discretization is reduced by one through implementation of an analytical solution to the problem in the infinite direction. This again allows for exact compliance with the boundary conditions in that infinite direction. However, a fundamental solution is not required as is the case with the boundary element method, thus making this technique much easier to implement for a wide range of problems. However, the approach still requires Fourier transformation of the dynamic stiffness matrix from the frequency domain into the time domain at the element level, which can be quite time consuming. Most practical 3D soil-structure problems involve a large number of scaled boundary

finite elements, which is certainly the case for the Kealakaha bridge that is the impetus for this study, therefore reducing the appeal of this method.

The infinite element concept emerged in the early 1970s (Ungless 1973; Bettess 1977) and has been successfully applied to acoustic (Astley 1983; Gerdes and Demkowicz 1996; Gerdes 2000) and fluid wave propagation problems (Saini, Bettess et al. 1978). Zhang and Zhao (1987) extended the infinite element technique to soil dynamics to solve single-wave problems in connection with strip foundations. However, earthquake shaking involves the propagation of compressive, shear and Rayleigh waves, all of which need to be considered in the infinite domain. Frequency-dependent infinite elements capable of transmitting all three types of waves were developed by Medina (Medina 1980). Zhao and Valliappan (1993a) applied such a multi-wave infinite element to 3D medium. In order to account for the various wave components, an additional set of nodes for each of the three waves is necessary at the interface. An analytical frequency-dependent infinite element was developed by Yun et al. (2000). This type of element uses three kinds of geometric shapes to facilitate its use with layered soils and complex geometries. It was later extended from the frequency domain into the time domain by Kim and Yun (2000). Choi et al. (2001) applied this element to earthquake engineering problems in the time domain. Based on the two-dimensional analytical frequency domain infinite element developed by Yun et al. (2000), Park et al. (2004) presented a three-dimensional analytical infinite element in the frequency domain. However, this particular type of element can only model the interface between the near-field and the far-field using a cylindrical shape. These studies suggest that rigorous infinite element formulations have been developed that can deal with static and dynamic load propagation in both time and frequency domains. However, the most versatile of these are computationally very costly and their application to most practical problems is therefore limited. More efficient formulations are needed.

Herein we propose a new semi-analytical 3D infinite element for time domain use that is intended to provide substantial computational savings. The appealing features of this new element are: (1) it is a 3D infinite element; (2) the solution in the infinite direction is

by Wolf (2003) for his scaled boundary element method. A local coordinate axis can be established at the interface between the near and far fields, such that $\zeta = 0$ for each of the infinite elements at the interface, as shown in Figure 4.2. Use of the common center O insures that the far field is completely covered by infinite elements, yet there is no overlap between them. The lateral surfaces of the infinite element, extending outward from the interface, can have any shape at the interface with the near field. This represents a distinct improvement upon the type of elements used in previous studies, which are only able to consider a cylindrical shape at the interface.

4.3 The Mapping and Shape Functions of the Semi-Infinite Element

Mapping for the infinite element from local coordinates (ξ, η, ζ) to global coordinates (x, y, z) are given as:

$$x = (1 + \xi)\bar{x} \quad (2.1a)$$

$$y = (1 + \xi)\bar{y} \quad (4.1b)$$

$$z = (1 + \xi)\bar{z} \quad (4.1c)$$

where:

$$\bar{x} = \sum_{j=1}^N l_j(\eta, \zeta) x_j \quad (2.2a)$$

$$\bar{y} = \sum_{j=1}^N l_j(\eta, \zeta) y_j \quad (4.2b)$$

$$\bar{z} = \sum_{j=1}^N l_j(\eta, \zeta) z_j \quad (4.2c)$$

and N is the number of nodes on the interface; x_j , y_j , and z_j are global coordinates at nodes j , the $l_j(\eta, \zeta)$ is the shape function in the local η - ζ plane, which in the case of a 4-noded infinite element can be expressed as:

$$l_1(\eta, \zeta) = \frac{1}{4}(1 + \eta)(1 + \zeta) \quad (2.3a)$$

$$l_2(\eta, \zeta) = \frac{1}{4}(1 + \eta)(1 - \zeta) \quad (4.3b)$$

$$l_3(\eta, \zeta) = \frac{1}{4}(1-\eta)(1-\zeta) \quad (4.3c)$$

$$l_4(\eta, \zeta) = \frac{1}{4}(1-\eta)(1+\zeta) \quad (4.3d)$$

The range of the local coordinates are $\xi \in [0, \infty)$, $\zeta \in [-1, 1]$, and $\eta \in [-1, 1]$.

It is assumed that a total of M types of waves are to propagate through the infinite elements. They are the body wave (P -wave), the shear wave (S -wave), and several Rayleigh waves. For time domain analysis, the function space for the M wave functions can be approximated as (Kim and Yun 2000; Yun, Kim et al. 2000):

$$f_m(\xi, \eta, \zeta, \omega) = e^{-(a+i\omega)C_m r_0 \xi} \quad (m = 1, \dots, M) \quad (2.4)$$

where:

$$C_m \in \left[\frac{1}{c_p}, \frac{1}{c_s}, \frac{1}{c_{rn}} \right] \quad (n = 1, \dots, N_r) \quad (2.5)$$

and:

$$r_0(\eta, \zeta) = \sqrt{\bar{x}^2 + \bar{y}^2 + \bar{z}^2} \quad (2.6)$$

The parameter ω stands for wave frequency. The quantities c_p , c_s , and c_{rn} are velocities for the P -wave, the S -wave, and the mean of the n^{th} Rayleigh wave in the frequency range of interest. N_r is the number of the Rayleigh waves considered in the wave function space. The positive constant a takes into account the geometric attenuation of velocity and is taken as the same for all the waves. More detailed discussions on the approximation functions can be found in elsewhere (Kim and Yun 2000; Yun, Kim et al. 2000). The displacement fields for the semi-analytical infinite element can be approximated by shape functions based on the wave functions in Equation (2.4):

$$\mathbf{U}(x, y, z; \omega) = \sum_{m=1}^M \sum_{k=1}^N l_k(\eta, \zeta) f_m(\xi, \eta, \zeta; \omega) \mathbf{p}_{(m-1) \times N+k}(\omega) \quad (2.7)$$

where $\mathbf{p}_{(m-1) \times N+k}(\omega)$ is the displacement vector associated with m^{th} wave component at the k^{th} node. If the shape function is written in the form:

$$N_{(m-1) \times N+k}(\xi, \eta, \zeta; \omega) = l_k(\eta, \zeta) f_m(\xi, \eta, \zeta; \omega) \quad (2.8a)$$

or:

$$N_{(m-1) \times N+k}(\xi, \eta, \zeta; \omega) = l_k(\eta, \zeta) e^{-(a+i\omega)C_m r_0 \xi} \quad (4.8b)$$

then the displacement field can be rewritten in the expression as:

$$\mathbf{U}(x, y, z; \omega) = \sum_{j=1}^{M \times N} N_j(\xi, \eta, \zeta; \omega) \mathbf{p}_j(\omega) \quad (2.9)$$

The shape function can also be written in matrix form:

$$\mathbf{N} = [N_1 \mathbf{I}, \dots, N_N \mathbf{I} \mid N_{N+1} \mathbf{I}, \dots, N_{2 \times N} \mathbf{I} \mid \dots \mid N_{(M-1) \times N+1} \mathbf{I}, \dots, N_{M \times N} \mathbf{I}] \quad (2.10)$$

where \mathbf{I} is a 3×3 identity matrix. The corresponding displacement vector for all degrees of freedom in this infinite element can be written in the form

$$\bar{\mathbf{p}} = [\mathbf{p}_1^T, \dots, \mathbf{p}_N^T, \mathbf{p}_{N+1}^T, \dots, \mathbf{p}_{2 \times N}^T, \dots, \mathbf{p}_{(M-1) \times N+1}^T, \dots, \mathbf{p}_{M \times N}^T] \quad (2.11)$$

The first $3N$ components on the right hand side of Equation (2.11) are displacements associated with the first wave component at all the boundary nodes and can be treated as the nodal displacements associated with the interface nodes. The remaining terms are referred to as internal displacements by Park et al. (2004), whereas Yun et al (1995) classified them into bubble and side modes respectively.

4.4 Dynamic Stiffness of the Semi-Infinite Element in the Frequency Domain

At the element level, mass and stiffness matrices are associated with the j^{th} and k^{th} shape function as follows (Yun, Kim et al. 1995):

$$\mathbf{m}^{jk} = \rho \int_{-1}^1 \int_{-1}^1 \int_0^\infty \mathbf{I} N_j N_k |\mathbf{J}| d\xi d\eta d\zeta \quad (2.12a)$$

$$\mathbf{k}^{jk} = \int_{-1}^1 \int_{-1}^1 \int_0^\infty \mathbf{B}_j^T \mathbf{D} \mathbf{B}_k |\mathbf{J}| d\xi d\eta d\zeta \quad (4.12b)$$

where ρ is the mass density, and \mathbf{B}_j and \mathbf{B}_k are the strain-displacement matrices associated with the j^{th} and k^{th} shape functions N_j and N_k , respectively. N_j and N_k are given by the following expressions:

$$N_j = l_r f_s = l_r e^{-(a+i\omega)r_0 C_s \xi} \quad (2.13a)$$

$$N_k = l_a f_b = l_a e^{-(a+i\omega)r_0 C_b \xi} \quad (4.13b)$$

where:

$$j = (s-1) \times N + r \quad (s = 1, \dots, M \text{ and for each } s, r = 1, \dots, N) \quad (2.14a)$$

$$k = (b - 1) \times N + a \quad (b = 1, \dots, M \text{ and for each } b, a = 1, \dots, N) \quad (4.14b)$$

\mathbf{D} is the elastic stiffness matrix:

$$\mathbf{D} = \begin{vmatrix} D_{11} & D_{12} & D_{13} & & & \\ D_{21} & D_{22} & D_{23} & & & \\ D_{31} & D_{32} & D_{33} & & & \\ & & & D_4 & & \\ & & & & D_5 & \\ & & & & & D_6 \end{vmatrix} \quad (2.15)$$

where $D_{11} = D_{22} = D_{33} = \lambda + 2\mu$; $D_{21} = D_{12} = D_{13} = D_{23} = \lambda$; $D_4 = D_5 = D_6 = \mu$; and λ and μ are the Lamé constants. \mathbf{J} is the Jacobian matrix:

$$\mathbf{J} = \begin{bmatrix} x_{,\xi} & y_{,\xi} & z_{,\xi} \\ x_{,\eta} & y_{,\eta} & z_{,\eta} \\ x_{,\zeta} & y_{,\zeta} & z_{,\zeta} \end{bmatrix} \quad (2.16)$$

The determinant of the Jacobean matrix can be written as:

$$|\mathbf{J}| = (1 + \xi)^2 |\bar{\mathbf{J}}| \quad (2.17)$$

where the ξ -independent matrix is in the form:

$$\bar{\mathbf{J}} = \begin{bmatrix} \bar{x} & \bar{y} & \bar{z} \\ \bar{x}_{,\eta} & \bar{y}_{,\eta} & \bar{z}_{,\eta} \\ \bar{x}_{,\zeta} & \bar{y}_{,\zeta} & \bar{z}_{,\zeta} \end{bmatrix} \quad (2.18)$$

Substituting Equation (2.18) into Equation (2.17), and then substituting Equation (2.17) into Equation (4.12), results in a decoupling of the ξ terms in the integrands of Equation (4.12) from η and ζ . A semi-analytical integration scheme is employed for Equation (4.12), whereby an analytical form is used in the infinite ξ direction and Gauss-Legendre quadrature is used in the finite η and ζ directions. The analytical integration is more efficient than the Gauss-Laguerre quadrature numerical integration (Yang and Yun 1992; Yun, Kim et al. 1995; Yun, Kim et al. 2000; Park, Watanabe et al. 2004). In fact, the solution in the infinite direction is exact and therefore much more accurate than numerical Gauss-Laguerre quadrature integration. Semi-analytical integration leads to mass and stiffness matrices in which constant matrices are multiplied by frequency-dependent multipliers:

$$\mathbf{m}^{jk} = \frac{1}{a+i\omega} \mathbf{m}^{(0)} + \frac{1}{(a+i\omega)^2} \mathbf{m}^{(1)} + \frac{1}{(a+i\omega)^3} \mathbf{m}^{(2)} \quad (2.19a)$$

$$\mathbf{k}^{jk} = (a+i\omega) \mathbf{k}^{(0)} + \mathbf{k}^{(1)} + \frac{1}{(a+i\omega)} \mathbf{k}^{(2)} \quad (4.19b)$$

where:

$$\mathbf{m}^{(0)} = -\mathbf{I} \int_{-1}^1 \int_{-1}^1 |\bar{J}| \frac{1}{r_0} \frac{1}{C_b + C_s} l_a l_r d\eta d\zeta \quad (2.20a)$$

$$\mathbf{m}^{(1)} = \mathbf{I} \int_{-1}^1 \int_{-1}^1 |\bar{J}| \frac{1}{r_0^2} \frac{1}{(C_b + C_s)^2} l_a l_r d\eta d\zeta \quad (4.20b)$$

$$\mathbf{m}^{(2)} = -\mathbf{I} \int_{-1}^1 \int_{-1}^1 |\bar{J}| \frac{1}{r_0^3} \frac{1}{(C_b + C_s)^3} l_a l_r d\eta d\zeta \quad (4.20c)$$

$$\mathbf{k}^{(0)} = \int_{-1}^1 \int_{-1}^1 |\bar{J}| \begin{bmatrix} D_{11}\tilde{A}_{11} + D_4\tilde{A}_{22} + D_6\tilde{A}_{33} & D_{12}\tilde{A}_{12} + D_4\tilde{A}_{21} \\ D_{21}\tilde{A}_{21} + D_4\tilde{A}_{12} & D_4\tilde{A}_{11} + D_{22}\tilde{A}_{22} + D_5\tilde{A}_{33} \\ D_{31}\tilde{A}_{31} + D_6\tilde{A}_{13} & D_{32}\tilde{A}_{32} + D_5\tilde{A}_{23} \\ D_{13}\tilde{A}_{13} + D_6\tilde{A}_{31} \\ D_{23}\tilde{A}_{23} + D_5\tilde{A}_{32} \\ D_6\tilde{A}_{11} + D_5\tilde{A}_{22} + D_{33}\tilde{A}_{33} \end{bmatrix} d\eta d\zeta \quad (4.20d)$$

$$\mathbf{k}^{(1)} = \int_{-1}^1 \int_{-1}^1 |\bar{J}| \begin{bmatrix} D_{11}\tilde{B}_{11} + D_4\tilde{B}_{22} + D_6\tilde{B}_{33} & D_{12}\tilde{B}_{12} + D_4\tilde{B}_{21} \\ D_{21}\tilde{B}_{21} + D_4\tilde{B}_{12} & D_4\tilde{B}_{11} + D_{22}\tilde{B}_{22} + D_5\tilde{B}_{33} \\ D_{31}\tilde{B}_{31} + D_6\tilde{B}_{13} & D_{32}\tilde{B}_{32} + D_5\tilde{B}_{23} \\ D_{13}\tilde{B}_{13} + D_6\tilde{B}_{31} \\ D_{23}\tilde{B}_{23} + D_5\tilde{B}_{32} \\ D_6\tilde{B}_{11} + D_5\tilde{B}_{22} + D_{33}\tilde{B}_{33} \end{bmatrix} d\eta d\zeta \quad (4.20e)$$

$$\mathbf{k}^{(2)} = \int_{-1}^1 \int_{-1}^1 |\bar{J}| \begin{bmatrix} D_{11}\tilde{H}_{11} + D_4\tilde{H}_{22} + D_6\tilde{H}_{33} & D_{12}\tilde{H}_{12} + D_4\tilde{H}_{21} \\ D_{21}\tilde{H}_{21} + D_4\tilde{H}_{12} & D_4\tilde{H}_{11} + D_{22}\tilde{H}_{22} + D_5\tilde{H}_{33} \\ D_{31}\tilde{H}_{31} + D_6\tilde{H}_{13} & D_{32}\tilde{H}_{32} + D_5\tilde{H}_{23} \\ D_{13}\tilde{H}_{13} + D_6\tilde{H}_{31} \\ D_{23}\tilde{H}_{23} + D_5\tilde{H}_{32} \\ D_6\tilde{H}_{11} + D_5\tilde{H}_{22} + D_{33}\tilde{H}_{33} \end{bmatrix} d\eta d\zeta \quad (4.20f)$$

In Equation 4.20:

$$\tilde{A}_{mn} = E_{m1} E_{n1} A_{11} \quad (2.21a)$$

$$\tilde{B}_{mn} = (E_{m1} E_{n1} B_{11} + E_{m1} E_{n2} B_{12} + E_{m1} E_{n3} B_{13}) + (E_{m2} E_{n1} B_{21} + E_{m2} E_{n2} B_{22} + E_{m2} E_{n3} B_{23})$$

$$+(E_{m3}E_{n1}B_{31} + E_{m3}E_{n2}B_{32} + E_{m3}E_{n3}B_{33}) \quad (4.21b)$$

$$\begin{aligned} \tilde{H}_{mn} &= (E_{m1}E_{n1}H_{11} + E_{m1}E_{n2}H_{12} + E_{m1}E_{n3}H_{13}) + (E_{m2}E_{n1}H_{21} + E_{m2}E_{n2}H_{22} + E_{m2}E_{n3}H_{23}) \\ &+ (E_{m3}E_{n1}H_{31} + E_{m3}E_{n2}H_{32} + E_{m3}E_{n3}H_{33}) \end{aligned} \quad (4.21c)$$

where:

$$A_{11} = -\frac{C_s C_b}{C_s + C_b} r_0 l_r l_a \quad (4.22a)$$

$$\mathbf{B} = \begin{bmatrix} \frac{2C_s C_b}{(C_s + C_b)^2} l_r l_a & \frac{C_s}{(C_s + C_b)} l_r \left\{ \frac{\partial l_a}{\partial \eta} + \frac{C_b}{(C_s + C_b)} \frac{1}{r_0} \frac{\partial r_0}{\partial \eta} l_a \right\} & \frac{\partial l_r}{\partial \eta} \frac{\partial l_a}{\partial \eta} \\ \frac{C_b}{(C_s + C_b)} l_a \left\{ \frac{\partial l_r}{\partial \eta} + \frac{C_s}{(C_s + C_b)} \frac{1}{r_0} \frac{\partial r_0}{\partial \eta} l_r \right\} & & \frac{\partial l_r}{\partial \eta} \frac{\partial l_a}{\partial \eta} \\ \frac{C_b}{(C_s + C_b)} l_a \left\{ \frac{\partial l_r}{\partial \zeta} + \frac{C_s}{(C_s + C_b)} \frac{1}{r_0} \frac{\partial r_0}{\partial \zeta} l_r \right\} & & \frac{\partial l_a}{\partial \eta} \frac{\partial l_r}{\partial \zeta} \\ \frac{C_s}{(C_s + C_b)} l_r \left\{ \frac{\partial l_a}{\partial \zeta} + \frac{C_b}{(C_s + C_b)} \frac{1}{r_0} \frac{\partial r_0}{\partial \zeta} l_a \right\} & & \frac{\partial l_r}{\partial \zeta} \frac{\partial l_a}{\partial \zeta} \\ & & \frac{\partial l_r}{\partial \zeta} \frac{\partial l_a}{\partial \zeta} \end{bmatrix} \quad (4.22b)$$

$$\mathbf{H} = -\frac{1}{(C_s + C_b)^2} \begin{bmatrix} \frac{2C_s C_b}{(C_s + C_b)} \frac{1}{r_0} l_r l_a \\ \frac{C_b}{r_0} l_a \left\{ \frac{\partial l_r}{\partial \eta} + \frac{2C_s}{(C_s + C_b)} \frac{1}{r_0} \frac{\partial r_0}{\partial \eta} l_r \right\} \\ \frac{C_b}{r_0} l_a \left\{ \frac{\partial l_r}{\partial \zeta} + \frac{2C_s}{(C_s + C_b)} \frac{1}{r_0} \frac{\partial r_0}{\partial \zeta} l_r \right\} \\ \frac{C_s}{r_0} l_r \left\{ \frac{\partial l_a}{\partial \eta} + \frac{2C_b}{(C_s + C_b)} \frac{1}{r_0} \frac{\partial r_0}{\partial \eta} l_a \right\} \\ \frac{1}{r_0^2} \frac{\partial r_0}{\partial \eta} \left\{ l_r \frac{\partial l_a}{\partial \eta} C_s + \frac{\partial l_r}{\partial \eta} l_a C_b + \frac{C_s C_b}{(C_s + C_b)} \frac{2}{r_0} l_r l_a \frac{\partial r_0}{\partial \eta} \right\} \\ \frac{1}{r_0^2} \left\{ \frac{\partial r_0}{\partial \eta} l_a \frac{\partial l_r}{\partial \zeta} C_b + \frac{\partial r_0}{\partial \zeta} \frac{\partial l_a}{\partial \eta} l_r C_s + \frac{C_s C_b}{(C_s + C_b)} \frac{2}{r} l_r l_a \frac{\partial r_0}{\partial \eta} \frac{\partial r_0}{\partial \zeta} \right\} \end{bmatrix}$$

$$\left. \begin{aligned} & \frac{C_s}{r_0} l_r \left\{ \frac{\partial l_a}{\partial \zeta} + \frac{2C_b}{(C_s + C_b)} \frac{1}{r_0} \frac{\partial r_0}{\partial \zeta} l_a \right\} \\ & \frac{1}{r_0^2} \left\{ \frac{\partial r_0}{\partial \eta} l_r \frac{\partial l_a}{\partial \zeta} C_s + \frac{\partial r_0}{\partial \zeta} \frac{\partial l_r}{\partial \eta} l_a C_b + \frac{C_s C_b}{(C_s + C_b)} \frac{2}{r} l_r l_a \frac{\partial r_0}{\partial \eta} \frac{\partial r_0}{\partial \zeta} \right\} \\ & \frac{1}{r_0^2} \frac{\partial r_0}{\partial \zeta} \left\{ l_r \frac{\partial l_a}{\partial \zeta} C_s + \frac{\partial l_r}{\partial \zeta} l_a C_b + \frac{C_s C_b}{(C_s + C_b)} \frac{2}{r_0} l_r l_a \frac{\partial r_0}{\partial \zeta} \right\} \end{aligned} \right\} \quad (4.22c)$$

If viscous-damping is ignored, the dynamic stiffness matrix $\mathbf{S}^{(e)}(\omega)$ for the infinite element e can be obtained by assembling the static stiffness matrix $\mathbf{K}^{(e)}(\omega)$ and the mass matrix $\mathbf{M}^{(e)}(\omega)$ in the same manner as for finite elements. After some manipulation, the dynamic stiffness sub-matrix for the j^{th} and k^{th} shape functions can be expressed in the form:

$$\mathbf{S}^{jk}(\omega) = i\omega \mathbf{S}_0 + \mathbf{S}_1 + \frac{1}{a + i\omega} \mathbf{S}_2 + \frac{1}{(a + i\omega)^2} \mathbf{S}_3 + \frac{1}{(a + i\omega)^3} \mathbf{S}_4 \quad (2.23)$$

where:

$$\mathbf{S}_0 = \mathbf{k}^{(0)} + \mathbf{m}^{(0)} \quad (2.24a)$$

$$\mathbf{S}_1 = a\mathbf{k}^{(0)} + \mathbf{k}^{(1)} - a\mathbf{m}^{(0)} + \mathbf{m}^{(1)} \quad (4.24b)$$

$$\mathbf{S}_2 = \mathbf{k}^{(2)} + a^2\mathbf{m}^{(0)} - 2a\mathbf{m}^{(1)} + \mathbf{m}^{(2)} \quad (4.24c)$$

$$\mathbf{S}_3 = a^2\mathbf{m}^{(1)} - 2a\mathbf{m}^{(2)} \quad (4.24d)$$

$$\mathbf{S}_4 = a^2\mathbf{m}^{(2)} \quad (4.24e)$$

and \mathbf{S}_0 , \mathbf{S}_1 , \mathbf{S}_2 , \mathbf{S}_3 , and \mathbf{S}_4 are all constant 3×3 matrices. After assembling the dynamic stiffness for the far-field, the interface node related part can be expressed in the form:

$$\tilde{\mathbf{S}}(\omega) = i\omega \tilde{\mathbf{S}}_0 + \tilde{\mathbf{S}}_1 + \frac{1}{a + i\omega} \tilde{\mathbf{S}}_2 + \frac{1}{(a + i\omega)^2} \tilde{\mathbf{S}}_3 + \frac{1}{(a + i\omega)^3} \tilde{\mathbf{S}}_4 \quad (2.25)$$

4.5 Equation of Motion for Soil-Structure Systems

Similar to the approach proposed by Choi et al. (2001) for seismic excitation, the equation of motion for the near field in the frequency domain can be expressed as:

$$\begin{bmatrix} \mathbf{S}_{rr}(\omega) + \tilde{\mathbf{S}}_{rr}(\omega) & \mathbf{S}_{rn}(\omega) & & \\ \mathbf{S}_{nr}(\omega) & \mathbf{S}_{nn}(\omega) & \mathbf{S}_{nl}(\omega) & \\ & \mathbf{S}_{ln}(\omega) & \mathbf{S}_{ll}(\omega) + \tilde{\mathbf{S}}_{ll}(\omega) & \\ & & & \end{bmatrix} \begin{Bmatrix} \mathbf{U}_r(\omega) \\ \mathbf{U}_n(\omega) \\ \mathbf{U}_l(\omega) \end{Bmatrix} = \begin{Bmatrix} \mathbf{F}_r^f(\omega) \\ 0 \\ \mathbf{F}_l^f(\omega) \end{Bmatrix} \quad (2.26)$$

where $\mathbf{U}(\omega)$ is the vector of total displacement amplitudes in frequency domain and $\tilde{\mathbf{S}}(\omega)$ is the dynamic stiffness matrix associated with the interface nodes obtained by assembling the dynamic stiffness of infinite elements for the far-field soil region. The subscripts r and l denote the degrees of freedom on the right and left hand side of near-field boundary, respectively, and n denotes the near-field (soil, piles, and the structure of the bridge). The dynamic stiffness matrix for the bounded medium is specified as:

$$\mathbf{S}(\omega) = [\mathbf{K}](1 + 2i\zeta) + i\omega[\mathbf{C}] - \omega^2[\mathbf{M}] \quad (2.27)$$

where $[\mathbf{K}]$, $[\mathbf{C}]$, and $[\mathbf{M}]$ represent the static-stiffness matrix, the viscous-damping (radiation-damping) matrix, and the mass matrix, respectively. These are constant for a linear system. The term ζ stands for material damping (hysteretic-damping) ratio. Material damping represents frictional loss of energy, while viscous-damping represents energy loss due to the propagation. Viscous damping can be a complicated function of elastic and viscous constants. $\mathbf{F}^f(\omega)$ in Equation (2.26) is the equivalent earthquake force in frequency domain along the interface Γ between the near and far fields, which can be determined from the free-field response as (Zhao and Valliappan 1993b):

$$\mathbf{F}_r^f(\omega) = \tilde{\mathbf{S}}_{rr}(\omega)\mathbf{U}_r^f(\omega) - \mathbf{A}_r\mathbf{T}_r^f(\omega) \quad (2.28a)$$

$$\mathbf{F}_l^f(\omega) = \tilde{\mathbf{S}}_{ll}(\omega)\mathbf{U}_l^f(\omega) - \mathbf{A}_l\mathbf{T}_l^f(\omega) \quad (4.28b)$$

where $\mathbf{U}^f(\omega)$ and $\mathbf{T}^f(\omega)$ are the displacement and traction at the location of the interface obtained from a free-field analysis in the absence of the structure. \mathbf{A} is a constant transformation matrix. As suggested by Wolf (1985):

$$\mathbf{F}^f(\omega) = \tilde{\mathbf{S}}(\omega)\mathbf{U}^f(\omega) + \mathbf{S}^e(\omega)\mathbf{U}^f(\omega) \quad (2.29)$$

where $\mathbf{S}^e_{ll}(\omega)$ represents the dynamic stiffness matrix of the excluded soil that utilizes this material's properties. In addition:

$$\mathbf{T}^f(\omega) = -\mathbf{S}^e(\omega)\mathbf{U}^f(\omega) \quad (2.30)$$

where $\mathbf{T}^f(\omega)$ represents the equivalent earthquake force at the location of the interface in

the absence of the structure resulting from a given free-field motion $\mathbf{U}^f(\omega)$. Equation (2.26) can be rearranged to read:

$$\begin{bmatrix} \mathbf{S}_{rr}(\omega) & \mathbf{S}_{rn}(\omega) \\ \mathbf{S}_{nr}(\omega) & \mathbf{S}_{nn}(\omega) & \mathbf{S}_{nl}(\omega) \\ & \mathbf{S}_{ln}(\omega) & \mathbf{S}_{ll}(\omega) \end{bmatrix} \begin{Bmatrix} \mathbf{U}_r(\omega) \\ \mathbf{U}_n(\omega) \\ \mathbf{U}_l(\omega) \end{Bmatrix} = \begin{Bmatrix} \mathbf{F}_r^f(\omega) + \mathbf{F}_r^e(\omega) \\ 0 \\ \mathbf{F}_l^f(\omega) + \mathbf{F}_l^e(\omega) \end{Bmatrix} \quad (2.31)$$

where:

$$\mathbf{F}^e(\omega) = -\tilde{\mathbf{S}}(\omega)\mathbf{U}(\omega) \quad (2.32)$$

The right hand of Equation(2.31) represents the total forces acting on the bounded domain.

4.6 Equation of Motion in the Time Domain

Equation (2.31) in the frequency domain can be transformed into the time domain if damping is neglected:

$$\begin{bmatrix} \mathbf{M}_{rr} & \mathbf{M}_{rn} \\ \mathbf{M}_{nr} & \mathbf{M}_{nn} & \mathbf{M}_{nl} \\ & \mathbf{M}_{ln} & \mathbf{M}_{ll} \end{bmatrix} \begin{Bmatrix} \ddot{\mathbf{u}}_r(t) \\ \ddot{\mathbf{u}}_n(t) \\ \ddot{\mathbf{u}}_l(t) \end{Bmatrix} + \begin{bmatrix} \mathbf{K}_{rr} & \mathbf{K}_{rn} \\ \mathbf{K}_{nr} & \mathbf{K}_{nn} & \mathbf{K}_{nl} \\ & \mathbf{K}_{ln} & \mathbf{K}_{ll} \end{bmatrix} \begin{Bmatrix} \mathbf{u}_r(t) \\ \mathbf{u}_n(t) \\ \mathbf{u}_l(t) \end{Bmatrix} = \begin{Bmatrix} \mathbf{f}_r^f(t) + \mathbf{f}_r^e(t) \\ 0 \\ \mathbf{f}_l^f(t) + \mathbf{f}_l^e(t) \end{Bmatrix} \quad (2.33)$$

where $\mathbf{u}(t)$ and $\mathbf{f}(t)$ are the displacement and the force vectors in time domain; and $\mathbf{f}^e(t)$ is the equivalent earthquake input force along the interface obtained from inverse Fourier transform of $\mathbf{F}^e(\omega)$. Also:

$$\mathbf{f}^e(t) = -\int_0^t \tilde{\mathbf{S}}(t-\tau)\mathbf{u}(\tau)d\tau \quad (2.34)$$

where:

$$\tilde{\mathbf{S}}(t) = \mathcal{F}^{-1}\{\tilde{\mathbf{S}}(\omega)\} = \frac{1}{2\pi} \int_{-\infty}^{+\infty} \tilde{\mathbf{S}}(\omega)e^{i\omega t} d\omega \quad (2.35)$$

Substituting Equation (2.25) into Equation(2.35), the dynamic stiffness matrix in time domain can be obtained in analytical form as:

$$\tilde{\mathbf{S}}(t) = \tilde{\mathbf{S}}_0\delta(t) + \tilde{\mathbf{S}}_1\dot{\delta}(t) + \tilde{\mathbf{S}}_2e^{-at}H(t) + \tilde{\mathbf{S}}_3te^{-at}H(t) + 2\tilde{\mathbf{S}}_4t^2e^{-at}H(t) \quad (2.36)$$

Substituting Equation (2.36) into Equation (2.34), the analytical form of Equation (2.34) can be written as:

$$\mathbf{f}^e(t) = -\tilde{\mathbf{S}}_0 \mathbf{u}(t) - \tilde{\mathbf{S}}_1 \dot{\mathbf{u}}(t) - \int_0^t \{\tilde{\mathbf{S}}_2 + (t-\tau)\tilde{\mathbf{S}}_3 + 2(t-\tau)^2\tilde{\mathbf{S}}_4\} e^{-a(t-\tau)} \mathbf{u}(\tau) d\tau \quad (2.37)$$

The equation of motion in time domain is obtained by substituting Equation (2.37) into Equation (2.33) and rearranging:

$$\begin{aligned} & \begin{bmatrix} \mathbf{M}_{rr} & \mathbf{M}_{rn} & \\ \mathbf{M}_{nr} & \mathbf{M}_{nn} & \mathbf{M}_{nl} \\ & \mathbf{M}_{ln} & \mathbf{M}_{ll} \end{bmatrix} \begin{Bmatrix} \ddot{\mathbf{u}}_r(t) \\ \ddot{\mathbf{u}}_n(t) \\ \ddot{\mathbf{u}}_l(t) \end{Bmatrix} + \begin{bmatrix} \tilde{\mathbf{S}}_{1r} & 0 & \\ 0 & 0 & 0 \\ & 0 & \tilde{\mathbf{S}}_{1l} \end{bmatrix} \begin{Bmatrix} \dot{\mathbf{u}}_r(t) \\ \dot{\mathbf{u}}_n(t) \\ \dot{\mathbf{u}}_l(t) \end{Bmatrix} \\ & + \begin{bmatrix} \mathbf{K}_{rr} + \tilde{\mathbf{S}}_{0r} & \mathbf{K}_{rn} & \\ \mathbf{K}_{nr} & \mathbf{K}_{nn} & \mathbf{K}_{nl} \\ & \mathbf{K}_{ln} & \mathbf{K}_{ll} + \tilde{\mathbf{S}}_{0l} \end{bmatrix} \begin{Bmatrix} \mathbf{u}_r(t) \\ \mathbf{u}_n(t) \\ \mathbf{u}_l(t) \end{Bmatrix} = \begin{Bmatrix} \mathbf{f}_r^f(t) + \bar{\mathbf{f}}_r^e(t) \\ 0 \\ \mathbf{f}_l^f(t) + \bar{\mathbf{f}}_l^e(t) \end{Bmatrix} \end{aligned} \quad (2.38)$$

where:

$$\bar{\mathbf{f}}^e(t) = -\int_0^t \{\tilde{\mathbf{S}}_2 + (t-\tau)\tilde{\mathbf{S}}_3 + 2(t-\tau)^2\tilde{\mathbf{S}}_4\} e^{-a(t-\tau)} \mathbf{u}(\tau) d\tau \quad (2.39)$$

4.7 Recursive Procedure for Solution of the Equation of Motion in the Time Domain

To obtain the system response at time $t = n\Delta t$, the right hand of Equation (2.39) can be decomposed into four terms (Kim and Yun 2000):

$$\bar{\mathbf{f}}^e(t) = \bar{\mathbf{f}}_1^e(t) + \bar{\mathbf{f}}_2^e(t) + 2\bar{\mathbf{f}}_3^e(t) + \bar{\mathbf{f}}_0^e(t) \quad (2.40)$$

where:

$$\bar{\mathbf{f}}_1^e(t) = -\int_0^{t-\Delta t} \tilde{\mathbf{S}}_2 e^{-a(t-\tau)} \mathbf{u}(\tau) d\tau \quad (2.41a)$$

$$\bar{\mathbf{f}}_2^e(t) = -\int_0^{t-\Delta t} (t-\tau)\tilde{\mathbf{S}}_3 e^{-a(t-\tau)} \mathbf{u}(\tau) d\tau \quad (2.41b)$$

$$\bar{\mathbf{f}}_3^e(t) = -\int_0^{t-\Delta t} (t-\tau)^2\tilde{\mathbf{S}}_4 e^{-a(t-\tau)} \mathbf{u}(\tau) d\tau \quad (2.41c)$$

$$\bar{\mathbf{f}}_0^e(t) = -\int_{t-\Delta t}^t \{\tilde{\mathbf{S}}_2 + (t-\tau)\tilde{\mathbf{S}}_3 + 2(t-\tau)^2\tilde{\mathbf{S}}_4\} e^{-a(t-\tau)} \mathbf{u}(\tau) d\tau \quad (2.41d)$$

and:

$$\bar{\mathbf{f}}_1^e(n\Delta t) = e^{-a\Delta t} \left\{ \bar{\mathbf{f}}_1^e((n-1)\Delta t) - \tilde{\mathbf{S}}_2 \mathbf{u}((n-1)\Delta t) \Delta t \right\} \quad (2.42a)$$

$$\bar{\mathbf{f}}_2^e(n\Delta t) = e^{-a\Delta t} \left\{ 2\bar{\mathbf{f}}_2^e((n-1)\Delta t) - e^{-a\Delta t} \bar{\mathbf{f}}_2^e((n-2)\Delta t) - \tilde{\mathbf{S}}_3 \mathbf{u}((n-1)\Delta t) (\Delta t)^2 \right\} \quad (2.42b)$$

$$\begin{aligned}
\bar{\mathbf{f}}_3^e(n\Delta t) &= -\sum_{j=0}^{n-1} (n-j)^2 (\Delta t)^2 \tilde{\mathbf{S}}_4 e^{-a(n-j)\Delta t} \mathbf{u}(j\Delta t) \Delta t \\
&= -e^{-a\Delta t} \sum_{j=0}^{n-2} (n-j)^2 (\Delta t)^2 \tilde{\mathbf{S}}_4 e^{-a(n-1-j)\Delta t} \mathbf{u}(j\Delta t) \Delta t - (\Delta t)^3 e^{-a\Delta t} \tilde{\mathbf{S}}_4 \mathbf{u}((n-1)\Delta t) \\
&= e^{-a\Delta t} \left\{ -\sum_{j=0}^{n-2} 3(n-1-j)^2 (\Delta t)^2 \tilde{\mathbf{S}}_4 e^{-a(n-1-j)\Delta t} \mathbf{u}(j\Delta t) \Delta t \right\} \\
&\quad + e^{-a\Delta t} \left\{ \sum_{j=0}^{n-3} 3(n-2-j)^2 (\Delta t)^2 \tilde{\mathbf{S}}_4 e^{-a(n-1-j)\Delta t} \mathbf{u}(j\Delta t) \Delta t \right\} \\
&\quad + e^{-a\Delta t} \left\{ -\sum_{j=0}^{n-2} (n-3-j)^2 (\Delta t)^2 \tilde{\mathbf{S}}_4 e^{-a(n-1-j)\Delta t} \mathbf{u}(j\Delta t) \Delta t - (\Delta t)^3 \tilde{\mathbf{S}}_4 \mathbf{u}((n-1)\Delta t) \right\} \\
&= -3e^{-a\Delta t} \sum_{j=0}^{n-2} (n-1-j)^2 (\Delta t)^2 \tilde{\mathbf{S}}_4 e^{-a(n-1-j)\Delta t} \mathbf{u}(j\Delta t) \Delta t \\
&\quad + 3e^{-2a\Delta t} \sum_{j=0}^{n-3} (n-2-j)^2 (\Delta t)^2 \tilde{\mathbf{S}}_4 e^{-a(n-2-j)\Delta t} \mathbf{u}(j\Delta t) \Delta t \\
&\quad - e^{-3a\Delta t} \sum_{j=0}^{n-4} (n-3-j)^2 (\Delta t)^2 \tilde{\mathbf{S}}_4 e^{-a(n-3-j)\Delta t} \mathbf{u}(j\Delta t) \Delta t - e^{-2a\Delta t} (\Delta t)^3 \tilde{\mathbf{S}}_4 \mathbf{u}((n-2)\Delta t) \\
&\quad - e^{-a\Delta t} (\Delta t)^3 \tilde{\mathbf{S}}_4 \mathbf{u}((n-1)\Delta t) \\
&= -3e^{-a\Delta t} \bar{\mathbf{f}}_3^e((n-1)\Delta t) + 3e^{-2a\Delta t} \bar{\mathbf{f}}_3^e((n-2)\Delta t) - e^{-3a\Delta t} \bar{\mathbf{f}}_3^e((n-3)\Delta t) \\
&\quad - e^{-2a\Delta t} (\Delta t)^3 \tilde{\mathbf{S}}_4 \mathbf{u}((n-2)\Delta t) - e^{-a\Delta t} (\Delta t)^3 \tilde{\mathbf{S}}_4 \mathbf{u}((n-1)\Delta t) \tag{4.42c}
\end{aligned}$$

$$\bar{\mathbf{f}}_0^e(t) = -\tilde{\mathbf{S}}_2 \mathbf{u}(n\Delta t) \Delta t \tag{4.42d}$$

Finally, the equation of motion in the time domain is obtained by substituting Equation (4.42) into Equation (2.39) and then substituting Equation (2.39) into Equation (2.38):

$$\begin{aligned}
&\begin{bmatrix} \mathbf{M}_{rr} & \mathbf{M}_{rn} & \\ \mathbf{M}_{nr} & \mathbf{M}_{nn} & \mathbf{M}_{nl} \\ & \mathbf{M}_{ln} & \mathbf{M}_{ll} \end{bmatrix} \begin{Bmatrix} \ddot{\mathbf{u}}_r(t) \\ \ddot{\mathbf{u}}_n(t) \\ \ddot{\mathbf{u}}_l(t) \end{Bmatrix} + \begin{bmatrix} \tilde{\mathbf{S}}_{1r} & 0 & \\ 0 & 0 & 0 \\ & 0 & \tilde{\mathbf{S}}_{1l} \end{bmatrix} \begin{Bmatrix} \dot{\mathbf{u}}_r(t) \\ \dot{\mathbf{u}}_n(t) \\ \dot{\mathbf{u}}_l(t) \end{Bmatrix} \\
&\quad + \begin{bmatrix} \mathbf{K}_{rr} + \tilde{\mathbf{S}}_{0r} + \tilde{\mathbf{S}}_{2r}\Delta t & \mathbf{K}_{rn} & \\ & \mathbf{K}_{nn} & \mathbf{K}_{nl} \\ & \mathbf{K}_{ln} & \mathbf{K}_{ll} + \tilde{\mathbf{S}}_{0l} + \tilde{\mathbf{S}}_{2l}\Delta t \end{bmatrix} \begin{Bmatrix} \mathbf{u}_r(t) \\ \mathbf{u}_n(t) \\ \mathbf{u}_l(t) \end{Bmatrix}
\end{aligned}$$

$$= \left\{ \begin{array}{c} \mathbf{f}_r^f(t) + \bar{\mathbf{f}}_{1r}^e(t) + \bar{\mathbf{f}}_{2r}^e(t) + \bar{\mathbf{f}}_{3r}^e(t) \\ 0 \\ \mathbf{f}_l^f(t) + \bar{\mathbf{f}}_{1l}^e(t) + \bar{\mathbf{f}}_{2l}^e(t) + \bar{\mathbf{f}}_{3l}^e(t) \end{array} \right\} \quad (2.43)$$

where $t = n\Delta t$. This equation can be solved using a Newmark integration procedure. Equation (2.43) is more efficient than the methods using numerical transformation such as those based on discrete Fourier or discrete Lagrange transforms, which usually require much more intensive computational efforts.

4.8 Conclusions

Comprehensive analysis of a new bridge to be built on the Island of Hawaii requires the development of a computationally efficient numerical formulation to capture an adequate amount of detail on its 3D seismic response. For this purpose, a new three-dimensional semi-analytical infinite element is proposed. The dynamic stiffness matrix of this infinite element can be obtained using a semi-analytical method in the frequency domain and then be implemented easily in the equations of motion in the time domain. The nonlinearity of soil and structure materials, as well as seismic loading can all be considered.

4.9 References

- Akiyoshi, T. (1978). "Compatible viscous boundary for discrete models." Journal of the Engineering Mechanics Division-Asce **104**(EM5): 1253-1266.
- Astley, R. J. (1983). "Wave envelope and infinite elements for acoustical radiation." International Journal for Numerical Methods in Fluids **3**: 507-526.
- Banerjee, P. K. (1978). Analysis of axially and laterally loaded pile groups. London, Applied Science Publishers.
- Banerjee, P. K. and R. Sen (1987). Dynamic Behaviour of Axially and Laterally Loaded Piles and Pile Groups.
- Beer, G. (1986). Implementation of combined boundary element-finite element analysis with applications in geomechanics. Developments in Boundary Element Methods. P. K. Banerjee and J. O. Watson. Amsterdam, Elsevier Applied Science. **4**: 191-226.

- Bettess, P. (1977). "Infinite elements." International Journal for Numerical Methods in Engineering **11**: 53-64.
- Cai, Y. X., P. L. Gould, et al. (2000). "Nonlinear analysis of 3D seismic interaction of soil-pile-structure systems and application." Engineering Structures **22**(2): 191-199.
- Choi, J.-S., C.-B. Yun, et al. (2001). "Earthquake response analysis of the Hualien soil-structure interaction system based on updated soil properties using forced vibration test data." Earthquake Engineering & Structural Dynamics **30**(1): 1-26.
- Gerdes, K. (2000). "A review of infinite element methods for exterior Helmholtz problems." Journal of Computational Acoustics **1**: 43-62.
- Gerdes, K. and L. Demkowicz (1996). "Solution of 3D Laplace and Helmholtz equations in exterior domains using hp infinite element method." Computer Methods in Applied Mechanics and Engineering **137**: 239-273.
- Kausel, E. (1974). Forced Vibrations of Circular Foundations on Layered Media. Report R74-11, Cambridge: Massachusetts Institute of Technology.
- Kausel, E., J. M. Rosset, et al. (1975). "Dynamic Analysis of Footings on Layered Media." Journal of engineering mechanics, ASCE **101**(EM5): 697-693.
- Kaynia, A. M. and E. Kausel (1982). Dynamic behavior of pile groups. Proceedings of the 2nd International Conference on Numerical Methods in Offshore Piling. Austin, Tex., University of Texas, Austin: 509-532.
- Kim, D. and C. Yun (2000). "Time domain soil-structure interaction analysis in two dimensional medium based on analytical frequency-dependent infinite elements." International Journal for Numerical Methods in Engineering **47**: 1241-1261.
- Lysmer, J. and R. L. Kuhlemeyer (1969). "Finite Dynamic Model for Infinite Media." Journal of Engineering Mechanics Division, ASCE **95**(EM4): 859-877.
- Maheshwari, B. K., K. Z. Truman, et al. (2004a). "Three-dimensional nonlinear analysis for seismic soil-pile-structure interaction." Soil Dynamics and Earthquake Engineering **24**.
- Maheshwari, B. K., K. Z. Truman, et al. (2004b). "Three-dimensional finite element nonlinear dynamic analysis of pile groups for lateral transient and seismic excitations." Canadian Geotechnical Journal **41**: 118-133.
- Medina, F. (1980). Modeling of soil-structure interaction by finite and infinite elements. EERC/UCB-80/43, University of California, Berkeley.
- Naeim, F. (1989). The seismic design handbook. New York, NY, Van Nostrand Reinhold.

- Park, K.-I., E. Watanabe, et al. (2004). "Development Of 3d Elastodynamic Infinite Elements For Soil-Structure Interaction." International Journal of Structural Stability and Dynamics **4**(3): 423-441.
- Saini, S., P. Bettess, et al. (1978). "Coupled hydro-dynamic response of concrete gravity dams using finite and infinite elements." Earthquake Engineering & Structural Dynamics **6**: 363-374.
- Smith, W. D. (1974). "A nonreflection plane boundary for wave propagation problems." Journal of Computational Physics **15**: 492-503.
- Ungless, R. F. (1973). An infinite finite element, University of British Columbia.
- White, W., S. Valliappan, et al. (1977). "Unified boundary for finite dynamic models." Journal of the Engineering Mechanics Division-Asce **103**(EM5): 949-964.
- Wolf, J. P. (1985). Dynamic soil-structure-interaction. N.J., Prentice-Hall.
- Wolf, J. P. (2003). Scaled Boundary Finite Element Method. Chichester, UK, John Wiley & Sons Ltd.
- Yang, S.-C. and C.-B. Yun (1992). "Axisymmetric infinite elements for soil-structure interaction analysis." Engineering Structures **14**: 361-370.
- Yun, C., D. Kim, et al. (2000). "Analytical frequency-dependent infinite elements for soil-structure interaction analysis in two-dimensional medium." Engineering Structures **22**: 258-271.
- Yun, C.-B., J.-M. Kim, et al. (1995). "Axisymmetric elastodynamic infinite elements for multi-layered half-space." International Journal for Numerical Methods in Engineering **Vol.38**: 3723-3743.
- Zhang, C. and C. Zhao (1987). "Coupling method of finite and infinite elements for strip foundation wave problems." Earthquake Engineering & Structural Dynamics **15**: 839-851.
- Zhao, C. and S. Valliappan (1993a). "A dynamic infinite element for three-dimensional infinite-domain wave problems." International Journal for Numerical Methods in Engineering **36**: 2567-2580.
- Zhao, C. and S. Valliappan (1993b). "An efficient wave input procedure for infinite media." Communications in Numerical Methods in Engineering **9**: 407-415.
- Zienkiewicz, O. C., D. W. Kelly, et al. (1977). "The coupling of the finite element method and boundary solution procedures." International Journal for Numerical Methods in Engineering **11**: 355-375.

Chapter 5

Conclusions

In this study, the open source framework OpenSees is used as a research tool. High performance brick elements and integration schemes have been developed and coded to improve computational efficiency. A new approach to deal with stress and deformation consistency between loading stages has also been implemented.

A general midpoint integration algorithm at Gauss point level has been developed in tensorial form. This general integration includes fully implicit and explicit integration schemes as special cases and therefore is suitable for many J_2 and three-invariant elastoplastic soil models with isotropic, kinematic, and mixed hardening. The efficiency and precision of implicit and explicit integration schemes has been analyzed with respect to four soil models. The comparisons show that, contrary to conventional wisdom, explicit integration sometimes offers advantages over fully implicit integration for complex constitutive soil models such as the general Cam-clay model.

Lateral resistance of single piles in cohesionless soils has been investigated in detail. Findings show that the coefficient of lateral earth pressure at rest, soil unit weight, and friction angle are important in the determination of lateral pile resistance capacity, but this occurs indirectly through Poisson's ratio and the pressure-dependent Young's modulus. Soil resistance increases as the Young's modulus of the soil and the stiffness of the pile increase. The lateral resistance of the soil and the capacity of the pile are not linearly related to the diameter of the pile, as simplified methods have suggested.

Dynamic soil-pile-bridge interaction system analysis has been addressed in this study through development of a set of theoretical formulas for seismic analysis in the time domain. These relationships employ a newly developed semi-analytical infinite element for the infinite field that is computationally economical and is able to handle arbitrary problem geometries. These equations have been developed to the point where they are ready to be coded into OpenSees.

In combination, the computational improvements presented in this study should provide sufficient efficiency to begin analyzing at least sections of the replacement Kealakaha bridge, such as one pier, pile cap, piles and nearby soil.

Appendix A

Constitutive Model Derivatives

The following derivatives are necessary for implementation of the constitutive models in a numerical code such as OpenSees.

General derivatives:

$$\frac{\partial f}{\partial \sigma_{ij}} = \frac{\partial f}{\partial p} \frac{\partial p}{\partial \sigma_{ij}} + \frac{\partial f}{\partial q} \frac{\partial q}{\partial \sigma_{ij}} + \frac{\partial f}{\partial \theta} \frac{\partial \theta}{\partial \sigma_{ij}} \quad (\text{A-1})$$

$$\frac{\partial g}{\partial \sigma_{ij}} = \frac{\partial g}{\partial p} \frac{\partial p}{\partial \sigma_{ij}} + \frac{\partial g}{\partial q} \frac{\partial q}{\partial \sigma_{ij}} + \frac{\partial g}{\partial \theta} \frac{\partial \theta}{\partial \sigma_{ij}} \quad (\text{A-2})$$

$$\begin{aligned} \frac{\partial^2 g}{\partial \sigma_{ij} \partial \sigma_{kl}} &= \frac{\partial^2 g}{\partial p^2} \frac{\partial p}{\partial \sigma_{ij}} \frac{\partial p}{\partial \sigma_{kl}} + \frac{\partial^2 g}{\partial p \partial q} \frac{\partial p}{\partial \sigma_{ij}} \frac{\partial q}{\partial \sigma_{kl}} + \frac{\partial^2 g}{\partial p \partial \theta} \frac{\partial p}{\partial \sigma_{ij}} \frac{\partial \theta}{\partial \sigma_{kl}} + \frac{\partial g}{\partial p} \frac{\partial^2 p}{\partial \sigma_{ij} \partial \sigma_{kl}} \\ &+ \frac{\partial^2 g}{\partial q \partial p} \frac{\partial q}{\partial \sigma_{ij}} \frac{\partial p}{\partial \sigma_{kl}} + \frac{\partial^2 g}{\partial q^2} \frac{\partial q}{\partial \sigma_{ij}} \frac{\partial q}{\partial \sigma_{kl}} + \frac{\partial^2 g}{\partial q \partial \theta} \frac{\partial q}{\partial \sigma_{ij}} \frac{\partial \theta}{\partial \sigma_{kl}} + \frac{\partial g}{\partial q} \frac{\partial^2 q}{\partial \sigma_{ij} \partial \sigma_{kl}} \\ &+ \frac{\partial^2 g}{\partial \theta \partial p} \frac{\partial \theta}{\partial \sigma_{ij}} \frac{\partial p}{\partial \sigma_{kl}} + \frac{\partial^2 g}{\partial \theta \partial q} \frac{\partial \theta}{\partial \sigma_{ij}} \frac{\partial q}{\partial \sigma_{kl}} + \frac{\partial^2 g}{\partial \theta^2} \frac{\partial \theta}{\partial \sigma_{ij}} \frac{\partial \theta}{\partial \sigma_{kl}} + \frac{\partial g}{\partial \theta} \frac{\partial^2 \theta}{\partial \sigma_{ij} \partial \sigma_{kl}} \end{aligned} \quad (\text{A-3})$$

$$\frac{\partial p}{\partial \sigma_{ij}} = \frac{1}{3} \delta_{ij} \quad (\text{A-4})$$

$$\frac{\partial q}{\partial \sigma_{ij}} = \frac{3}{2} \frac{1}{q} s_{ij} \quad (\text{A-5})$$

$$\frac{\partial \theta}{\partial \sigma_{ij}} = \frac{3}{2} \frac{1}{q^2} \cot 3\theta s_{ij} - \frac{9}{2} \frac{1}{q^3} \frac{1}{\sin 3\theta} w_{ij} \quad (\text{A-6})$$

where:

$$w_{ij} = s_{im}s_{mj} - \frac{1}{3}s_{mn}s_{mn}\delta_{ij} \quad (\text{A-7})$$

$$\frac{\partial^2 p}{\partial \sigma_{ij} \partial \sigma_{kl}} = 0_{ijkl} \quad (\text{A-8})$$

$$\frac{\partial^2 q}{\partial \sigma_{ij} \partial \sigma_{kl}} = -\frac{9}{4} \frac{1}{q^3} s_{ij}s_{kl} + \frac{3}{2} \frac{1}{q} (\delta_{ik}\delta_{jl} - \frac{1}{3}\delta_{ij}\delta_{kl}) \quad (\text{A-9})$$

$$\begin{aligned} \frac{\partial^2 \theta}{\partial \sigma_{ij} \partial \sigma_{kl}} &= -3 \cot 3\theta \frac{\partial \theta}{\partial \sigma_{ij}} \frac{\partial \theta}{\partial \sigma_{kl}} - \frac{9}{2} \frac{1}{q^4} \cot 3\theta s_{ij}s_{kl} - \frac{9}{2} \frac{1}{q^2} s_{ij} \frac{\partial \theta}{\partial \sigma_{kl}} \\ &+ \frac{3}{2} \frac{1}{q^2} \cot 3\theta \frac{\partial s_{ij}}{\partial \sigma_{kl}} + \frac{81}{4} \frac{1}{\sin 3\theta} \frac{1}{q^5} w_{ij}s_{kl} - \frac{9}{2} \frac{1}{\sin 3\theta} \frac{1}{q^3} \frac{\partial w_{ij}}{\partial \sigma_{kl}} \end{aligned} \quad (\text{A-10})$$

where:

$$\frac{\partial s_{ij}}{\partial \sigma_{kl}} = \delta_{ik}\delta_{jl} - \frac{1}{3}\delta_{ij}\delta_{kl} \quad (\text{A-11})$$

and:

$$\frac{\partial w_{ij}}{\partial \sigma_{kl}} = \delta_{ik}s_{jl} + s_{ik}\delta_{jl} - \frac{2}{3}s_{ij}\delta_{kl} - \frac{2}{3}\delta_{ij}s_{kl} \quad (\text{A-12})$$

$$H = \sum_i \frac{\partial f}{\partial k^i} \frac{dk^i}{d\lambda} + \sum_j \frac{\partial f}{\partial \alpha_{pq}^j} \frac{d\alpha_{pq}^j}{d\lambda} \quad (\text{A-13})$$

Yield function for Drucker-Prager model:

$$f = \alpha p + q - k \quad (\text{A-14})$$

For triaxial compression:

$$\alpha = \frac{6 \sin \phi}{3 - \sin \phi} \quad (\text{A-15})$$

$$k = \frac{6c \cos \phi}{3 - \sin \phi} \quad (\text{A-16})$$

For triaxial extension:

$$\alpha = \frac{6 \sin \phi}{3 + \sin \phi} \quad (\text{A-17})$$

$$k = \frac{6c \cos \phi}{3 + \sin \phi} \quad (\text{A-18})$$

Drucker-Prager model derivatives:

$$\frac{\partial f}{\partial p} = \alpha, \quad \frac{\partial f}{\partial q} = 1, \quad \frac{\partial f}{\partial \theta} = 0 \quad (\text{A-19})$$

$$\frac{\partial^2 g}{\partial p^2} = 0, \quad \frac{\partial^2 g}{\partial p \partial q} = 0, \quad \frac{\partial^2 g}{\partial p \partial \theta} = 0 \quad (\text{A-20})$$

$$\frac{\partial^2 g}{\partial q \partial p} = 0, \quad \frac{\partial^2 g}{\partial q^2} = 0, \quad \frac{\partial^2 g}{\partial q \partial \theta} = 0 \quad (\text{A-21})$$

$$\frac{\partial^2 g}{\partial \theta \partial p} = 0, \quad \frac{\partial^2 g}{\partial \theta \partial q} = 0, \quad \frac{\partial^2 g}{\partial \theta^2} = 0 \quad (\text{A-22})$$

$$\frac{\partial f}{\partial \alpha} = p, \quad \frac{\partial \alpha}{\partial \lambda} = C \sqrt{\frac{\partial g}{\partial \sigma_{ij}} \frac{\partial g}{\partial \sigma_{ij}}}, \quad C = \frac{\alpha + 3}{\sqrt{3\alpha^2 + \frac{27}{2}}} \quad (\text{A-23})$$

$$H = \frac{\alpha + 3}{\sqrt{3\alpha^2 + \frac{27}{2}}} p \sqrt{\frac{\partial g}{\partial \sigma_{ij}} \frac{\partial g}{\partial \sigma_{ij}}} \quad (\text{A-24})$$

$$\frac{\partial^2 g}{\partial \sigma_{ij} \partial \alpha} = \frac{\partial p}{\partial \sigma_{ij}} \quad (\text{A-25})$$

Yield function for extended Mohr-Coulomb model:

$$f = \alpha p + N(\theta)q - k \quad (\text{A-26})$$

$$N(\theta) = \frac{4(1 - e^2) \cos^2 \theta + (2e - 1)^2}{2(1 - e^2) \cos \theta + (2e - 1)[4(1 - e^2) \cos^2 \theta + 5e^2 - 4e]} \quad (\text{A-27})$$

$$\alpha = \frac{6 \sin \phi}{3 + \sin \phi} \quad (\text{A-28})$$

$$k = \frac{6c \cos \phi}{3 + \sin \phi} \quad (\text{A-29})$$

$$e = \frac{3 + \sin \phi}{3 - \sin \phi} \quad (\text{A-30})$$

Extended Mohr-Coulomb model derivatives:

$$\frac{\partial f}{\partial p} = \alpha, \quad \frac{\partial f}{\partial q} = N(\theta), \quad \frac{\partial f}{\partial \theta} = q \frac{dN(\theta)}{d\theta} \quad (\text{A-31})$$

$$\frac{\partial^2 g}{\partial p^2} = 0, \quad \frac{\partial^2 g}{\partial p \partial q} = 0, \quad \frac{\partial^2 g}{\partial p \partial \theta} = 0 \quad (\text{A-32})$$

$$\frac{\partial^2 g}{\partial q \partial p} = 0, \quad \frac{\partial^2 g}{\partial q^2} = 0, \quad \frac{\partial^2 g}{\partial q \partial \theta} = \frac{dN(\theta)}{d\theta} \quad (\text{A-33})$$

$$\frac{\partial^2 g}{\partial \theta \partial p} = 0, \quad \frac{\partial^2 g}{\partial \theta \partial q} = \frac{dN(\theta)}{d\theta}, \quad \frac{\partial^2 g}{\partial \theta^2} = q \frac{d^2 N(\theta)}{d\theta^2} \quad (\text{A-34})$$

$$\frac{\partial f}{\partial \alpha} = p, \quad \frac{\partial \alpha}{\partial \lambda} = C \sqrt{\frac{\partial g}{\partial \sigma_{ij}} \frac{\partial g}{\partial \sigma_{ij}}} \quad (\text{A-35})$$

$$C = \frac{\alpha + 3}{\sqrt{3\alpha^2 + \frac{27}{2}}} \quad (\text{A-36})$$

$$H = \frac{\alpha + 3}{\sqrt{3\alpha^2 + \frac{27}{2}}} p \sqrt{\frac{\partial g}{\partial \sigma_{ij}} \frac{\partial g}{\partial \sigma_{ij}}} \quad (\text{A-37})$$

$$\frac{\partial^2 g}{\partial \sigma_{ij} \partial \alpha} = \frac{\partial p}{\partial \sigma_{ij}} \quad (\text{A-38})$$

Yield function for modified Cam-clay model:

$$f = \frac{q^2}{M^2} + \frac{p}{p - p_0} \quad (\text{A-39})$$

Modified Cam-clay model derivatives:

$$\frac{\partial f}{\partial p} = 2p - p_0, \quad \frac{\partial f}{\partial q} = \frac{2q}{M^2}, \quad \frac{\partial f}{\partial \theta} = 0 \quad (\text{A-40})$$

$$\frac{\partial^2 g}{\partial p^2} = 2, \quad \frac{\partial^2 g}{\partial p \partial q} = 0, \quad \frac{\partial^2 g}{\partial p \partial \theta} = 0 \quad (\text{A-41})$$

$$\frac{\partial^2 g}{\partial q \partial p} = 0, \quad \frac{\partial^2 g}{\partial q^2} = \frac{2}{M^2}, \quad \frac{\partial^2 g}{\partial q \partial \theta} = 0 \quad (\text{A-42})$$

$$\frac{\partial^2 g}{\partial \theta \partial p} = 0, \quad \frac{\partial^2 g}{\partial \theta \partial q} = 0, \quad \frac{\partial^2 g}{\partial \theta^2} = 0 \quad (\text{A-43})$$

$$\frac{\partial f}{\partial p_0} = -p, \quad \frac{dp_0}{d\lambda} = \frac{vp_0}{m - k} \delta_{ij} \frac{\partial g}{\partial \sigma_{ij}} \quad (\text{A-44})$$

$$H = -p \frac{vp_0}{m - k} \delta_{ij} \frac{\partial g}{\partial \sigma_{ij}} \quad (\text{A-45})$$

$$\frac{\partial^2 g}{\partial \sigma_{ij} \partial p_0} = -\frac{\partial p}{\partial \sigma_{ij}} \quad (\text{A-46})$$

Yield function for general Cam-clay model:

$$f = \frac{q^2}{M(\theta)^2} + \frac{p}{p - p_0} \quad (\text{A-47})$$

$$M(\theta) = \frac{\alpha}{N(\theta)} \quad (\text{A-48})$$

where α and $N(\theta)$ are the same as in Equations (A-28) and (A-27).

General Cam-clay model derivatives:

$$\frac{\partial f}{\partial p} = \frac{\partial g}{\partial p} = 2p - p_0; \quad \frac{\partial f}{\partial q} = \frac{\partial g}{\partial q} = \frac{2q}{\eta_p^2} N(\theta)^2, \quad \frac{\partial f}{\partial \theta} = \frac{\partial g}{\partial \theta} = \frac{2q^2}{\eta_p^2} N(\theta) \frac{dN(\theta)}{d\theta} \quad (\text{A-49})$$

$$\frac{\partial^2 g}{\partial p^2} = 2, \quad \frac{\partial^2 g}{\partial p \partial q} = 0, \quad \frac{\partial^2 g}{\partial p \partial \theta} = 0 \quad (\text{A-50})$$

$$\frac{\partial^2 g}{\partial q \partial p} = 0, \quad \frac{\partial^2 g}{\partial q^2} = \frac{2}{\eta_p^2} N(\theta)^2, \quad \frac{\partial^2 g}{\partial q \partial \theta} = \frac{4q}{\eta_p^2} N(\theta) \frac{dN(\theta)}{d\theta} \quad (\text{A-51})$$

$$\frac{\partial^2 g}{\partial \theta \partial p} = 0, \quad \frac{\partial^2 g}{\partial \theta \partial q} = \frac{4q}{\eta_p^2} N(\theta) \frac{dN(\theta)}{d\theta}, \quad \frac{\partial^2 g}{\partial \theta^2} = \frac{2q^2}{\eta_p^2} \left[N(\theta) \frac{d^2 N(\theta)}{d\theta^2} + \frac{dN(\theta)}{d\theta} \frac{dN(\theta)}{d\theta} \right] \quad (\text{A-52})$$

$$\frac{\partial f}{\partial p_0} = -p, \quad \frac{dp_0}{d\lambda} = \frac{\nu p_0}{m - k} \delta_{ij} \frac{\partial g}{\partial \sigma_{ij}} \quad (\text{A-53})$$

$$H = -p \frac{\nu p_0}{m - k} \delta_{ij} \frac{\partial g}{\partial \sigma_{ij}} \quad (\text{A-54})$$

$$\frac{\partial^2 g}{\partial \sigma_{ij} \partial p_0} = -\frac{\partial p}{\partial \sigma_{ij}} \quad (\text{A-55})$$

Set:

$$N(\theta) = \frac{K}{G + BF} \quad (\text{A-56})$$

where: $G = A \cos \theta$, $A = 2(1 - e^2)$, $B = 2e - 1$, $F = (A \cos 2\theta + D)^{1/2}$, $D = 2 - 4e + 3e^2$,

$K = A \cos 2\theta + E$, and $E = 3 - 4e + 2e^2$.

The first derivative of $N(\theta)$:

$$\frac{dN(\theta)}{d\theta} = \frac{[K'(G + BF) - K(G' + BF')]}{(G + BF)^2} \quad (\text{A-57})$$

where:

$$G' = -A \sin \theta, \quad F' = -\frac{A \sin 2\theta}{F}, \quad K' = -2A \sin 2\theta \quad (\text{A-58})$$

The second derivatives of $N(\theta)$:

$$\frac{d^2N(\theta)}{d\theta^2} = \frac{K''(G + BF) - K(BF'' + G'')}{(G + BF)^2} - 2 \frac{[K'(G + BF) - K(BF' + G')](G' + BF')}{(G + BF)^3} \quad (\text{A-59})$$

or:

$$\frac{d^2N(\theta)}{d\theta^2} = \frac{K''(G + BF) - K(BF'' + G'')}{(G + BF)^2} - 2 \frac{N'(G' + BF')}{(G + BF)} \quad (\text{A-60})$$

$$K'' = 4(E - K), \quad F'' = \frac{0.5K'' - F'^2}{F}, \quad G'' = -A \cos \theta \quad (\text{A-61})$$

Appendix B

The Role of the Intermediate Stress in Offshore Slope Sediment Modeling

Brandes, H.G. and Wang, S. (2006)

Proceedings, 16th International Offshore and Polar Engineering Conference, San Francisco, California, May 28–June 2.

Abstract

Two intersecting slopes of finite height are modeled to analyze their stress-strain behavior leading up to impending collapse. Three-dimensional brick elements and two elasto-plastic constitutive models are considered. One of these models incorporates the effect of the intermediate principal stress, and the other one does not. Results indicate moderately significant differences in stress path response and overall strains and displacements.

Keywords: Elasto-plastic, slopes, marine sediments, modeling, OpenSees, finite elements

B.1 Introduction

Submarine slopes have captured the imagination of scientists ever since the *Challenger* expedition of 1872-1876 when the first set of extensive bathymetric surveys was conducted using simple depth soundings at hundreds of locations throughout the world.

The continental slope and rise, particularly where hydrocarbons have attracted the attention of oil companies, has become the focus of intense research in recent years to characterize and quantify geohazards associated with mass wasting. Of current interest is the ability to quantify the displacement of large masses of sediments that could pose a risk to structures placed in vulnerable environments. Catastrophic failures are of obvious concern, but so are limited deformation processes that do not necessarily lead to a complete collapse. These may involve flows or slides of limited down-slope extent, which nonetheless can cause substantial damage to structures such as platform footings and anchors placed in their path.

Most of the work that has been conducted to date on slope stability has focused on two-dimensional (plane strain) cross sectional idealizations of what in reality are often highly complex three-dimensional geometries. This can result in grossly misleading findings (Duncan and Wright, 2005). The typical constitutive model that is implied in most limit equilibrium calculations consists of a simple rigid-perfectly plastic Mohr-Coulomb model, which is entirely inadequate to investigate pre-failure deformations. A more versatile and accurate approach would be one based on an elastoplastic soil model within a numerical framework that allows for three-dimensional geometries, such as the finite element method. This type of an analysis is rarely carried out for a number of reasons. Brandes and Shentang (2005) investigated pseudo three-dimensional slopes in connection with two advanced elastoplastic soil models, but only for a simple semi-infinite geometry where displacements were constrained in the down-slope and vertical directions. In this article we analyze a hypothetical configuration consisting of two intersecting slopes that are loaded through the process of self-weight consolidation. Two elasto-plastic constitutive models are considered, one of which is clearly more versatile than the other one since it takes into account the role of the intermediate principal stress.

Computations are carried out using the OpenSees code (Open System for Earthquake Engineering Simulation; Pacific Earthquake Engineering Research Center, 2004). OpenSees is an open-source software framework consisting of a set of interrelated classes,

designed as independent as possible for maximum flexibility, which control data structure, material behavior models, hierarchical element types, solution algorithms, integrators, equation solvers, databases, visualization and communication procedures. OpenSees has seen enormous growth in the last few years as developers and researchers have made use of the software's inherent flexibility to add additional capability (Elgamal et al., 2003). OpenSees has been adapted to solve a wide range of problems involving soil, soil-structure interaction, earthquake shaking, and reliability assessment (Jeremic, 2003). It has also been adopted by the Network for Earthquake Engineering Simulation as its platform for simulation and visualization.

B.2 Slope Geometry

A simple three-dimensional geometry has been chosen for all the computations (Figure B.1). It consists of two intersecting slopes, Slope I and Slope II, inclined at 35° and 20° relative to the horizontal, respectively. A number of points are shown for reference. The finite element mesh consists of 640 brick elements with 14 Gauss integration points and 20 nodes each, for a total of 3221 nodes. The bottom of the geometry is fixed and the two vertical boundaries are not allowed to move in their respective normal directions. All others surfaces are free.

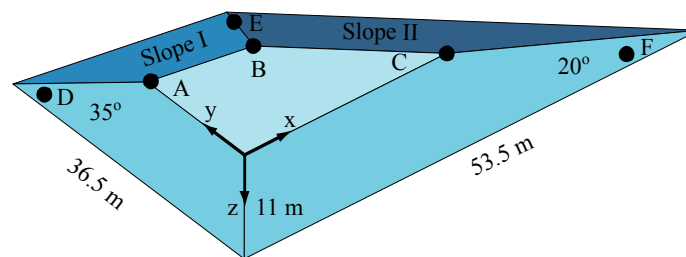


Figure B.1 3D slope geometry.

B.3 Constitutive Models

Many constitutive models have been proposed for marine sediments, ranging from simple elastic to multi-surface elasto-plastic models with complex yield and hardening laws. The

latter are often impractical since they usually require material parameters that are difficult to obtain. Here we compromise by selecting two constitutive models that embrace fundamental elasto-plastic response and frictional failure without hardening, yet are significantly different from each other in that one considers the effect of the intermediate principal stress and the other one does not.

The simpler of the two is the Drucker-Prager (DP) model (Drucker and Prager, 1952). It assumes a yield surface given by:

$$f = \alpha p + q - k \quad (\text{B-1})$$

where p is volumetric stress, q is deviatoric stress, and a and k are two materials constants. These constants are conceptually similar to the Mohr-Coulomb strength parameters f and c , and indeed are related to them:

$$\alpha = \frac{6 \sin \phi}{3 - \sin \phi} \quad (\text{B-2})$$

$$k = \frac{6c \cos \phi}{3 - \sin \phi} \quad (\text{B-3})$$

It should be noted that a and k need to be determined from triaxial compressions tests, rather than from extension or other types of strength tests, since deformation of the slope is characterized by active conditions. This model is adequate for making simple elasto-plastic predictions, although the circular nature of the failure cone does not allow for a difference between compressive and tensile yield strengths.

Consideration of the third stress invariant allows for a more versatile failure cone to overcome this shortcoming. One relatively simple model that does account for the intermediate stress is a variant of the Mohr-Coulomb model, here referred to as the Extended Mohr-Coulomb (EMC) model. Its yield surface is given by:

$$f = \alpha p + N(\theta)q - k \quad (\text{B-4})$$

where:

$$N(\theta) = \frac{4(1 - e^2) \cos^2 \theta + (2e - 1)^2}{2(1 - e^2) \cos \theta + (2e - 1)[4(1 - e^2) \cos^2 \theta + 5e^2 - 4e]} \quad (\text{B-5})$$

and:

$$\alpha = \frac{6 \sin \phi}{3 + \sin \phi}$$

$$k = \frac{6c \cos \phi}{3 + \sin \phi}$$

$$e = \frac{3 + \sin \phi}{3 - \sin \phi}$$

The angle θ is referred to as the Lode angle. Its effect is to produce a yield surface that is not in the form of a circular cone, as is the case for the DP model. Both the DP and EMC models adopt the non-associated flow rule. These models have been coded into OpenSees as part of this study.

Material parameters were selected to be representative of soft, fine-grained marine sediments. The friction angle is assumed to be 10° , the cohesion a nominal 5kPa, the initial elastic Young's modulus 10.4 MPa, and the saturated unit weight 14.5 kN/m^3 .

B.4 Loading

Herein we focus on the process of self-weight consolidation. In other words, loading is provided by the gradual imposition of gravitational stresses. This is somewhat similar to what would happen as marine sediment, which perhaps has been transported by the overlying water column, settles out of solution and begins to dewater and take on a structure of its own. Deposition of layers of sediment on the continental slope, rise and on adjacent areas of the deep ocean seafloor indeed often follows from the transport of fluidized sediment masses in the form of mudflows, turbidity currents, grain flows and various other modes of mass wasting, which eventually come to a rest as the seafloor levels out.

In the problem the final self-weight load is applied in 40 equal increments. Drained conditions are assumed, which implies that the consolidation process occurs slowly enough so that volume changes occur without the accumulation of excess pore pressures.

This may or may not be realistic, but it renders the problem much more straightforward for analysis. Emphasis can be placed on the resulting deformations without the complicating effect of time.

The problem has been set up in such a way that collapse occurs during self-weight loading. Specifically, failure conditions develop along a three-dimensional rupture surface after 70% of the full load has been applied for the DP model. Failure with the EMC model occurs after only 60% of the target load has been reached. The failure pattern is biased toward Slope I since this is the steeper of the two (Figure B.2). In fact, the three-dimensional rupture occurs virtually entirely within Slope I. The shape of the failure surface is similar for the two models.

Failure is associated with imminent collapse and results when stresses everywhere on the failure surface have reached the yield condition and the available strength has been fully mobilized along the rupture surface. At that point equilibrium is lost and numerical difficulties ensue. The location of the collapse surface can be identified by examining the distribution of Gauss points that have yielded. For example, Figure B.3 shows points in the yz -plane that have yielded for the DP model after 70% load, i.e. at the point of collapse. The shape of the failure surface approaches that of toe circle that extends almost to the rigid bottom. This is as expected for finite-height homogenous slope deposits with a shallow firm base (Terzaghi et al., 1996).

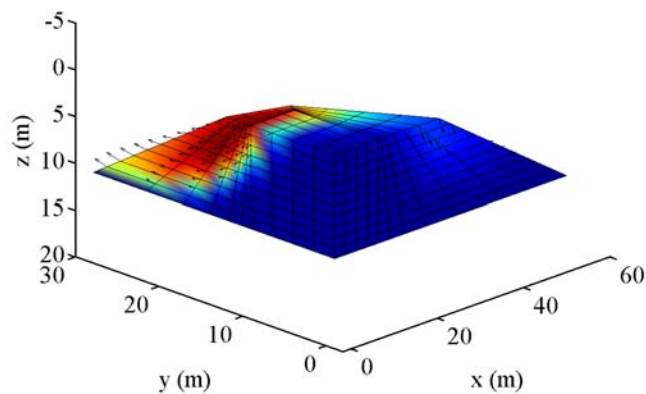


Figure B.2 Failure pattern for DP model.

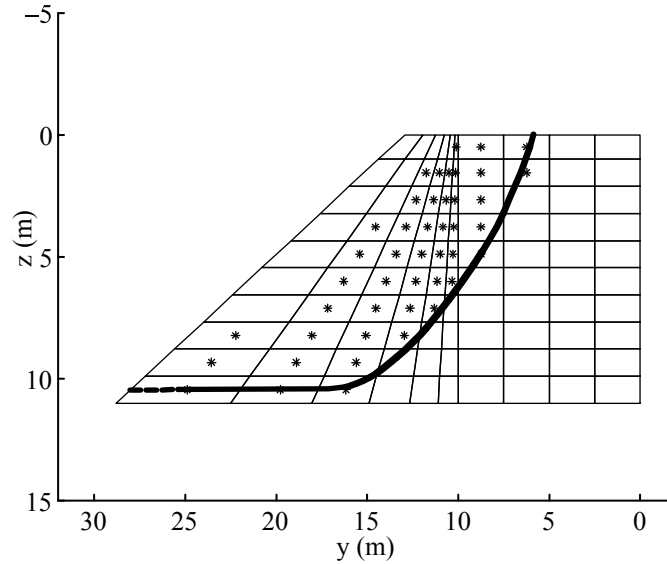


Figure B.3 Yield locations in yz -plane (DP soil model).

B.5 Stress Path Predictions

Not all stress points reach failure at the same load stage. Also, there are differences in the predicted stress paths produced by the two soil models. It is instructive to examine the stress paths followed by three Gauss points at different locations in the slope domain (points D, E and F in Figure B.1). Point D is located adjacent to the yz -plane. The stress paths followed for the two soil models at point D are shown in Figure B.4. Both soil models are set up to have the same initial yield surface and they behave similarly in the elastic range. In the case of the DP model, the stress point reaches failure and then continues along the corresponding failure surface. Collapse, which as already mentioned corresponds to the development of a kinematically viable rupture surface where all the available strength has been mobilized, does not develop until the end of the dashed stress path. As Point D continues to yield, stresses are redistributed until final collapse does occur. In the case of the EMC model, as the stress path approaches the initial yield surface, the failure surface in qp -space changes in size so that the final failure envelope is located below the initial one. This is due to the non-circular nature of the EMC model. It appears that the stress path exceeds the final failure surface for a time and then approaches it from above. To realize that the principles of plasticity are not being violated,

one must consider the stress paths and the shape of the failure envelope in three dimensions (lower part of Figure B.4). This clearly shows that the stress path does not exceed the failure surface. Nonetheless, stress redistribution after initial yielding is more effective for the DP model, which results in a higher load capacity before collapse occurs.

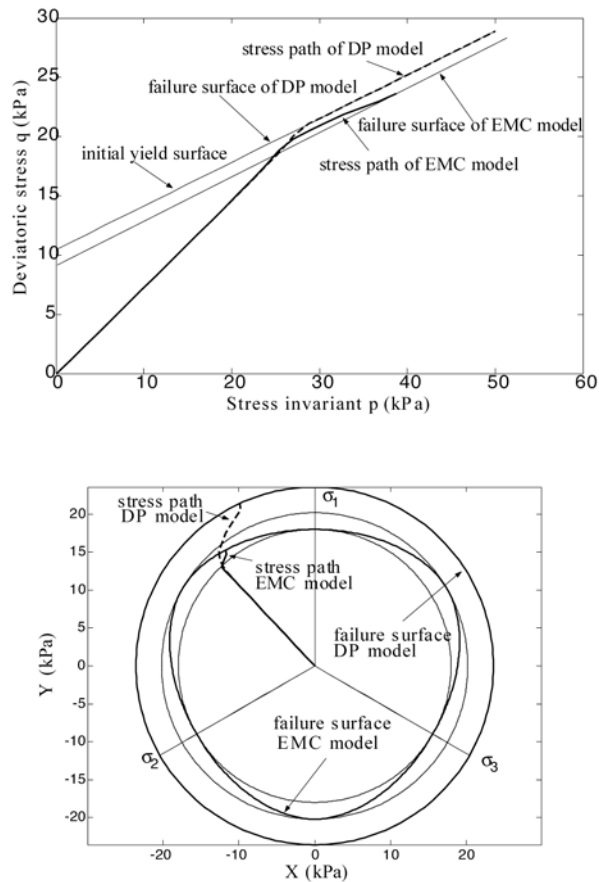


Figure B.4 Stress paths for point D.

Point E, which is located where slopes I and II intersect, reaches yield conditions with both soil models, however it does so relatively late in the loading sequence (Figure B.5). As a result, scollapse occurs soon after and little load redistribution occurs after E reaches the failure surface.

If we examine stress conditions at the far end of slope II, i.e. at point F, we find that this particular point does reach failure conditions according to the DP model, but not

according to the EMC model (Figure B.6). Even though failure stresses are achieved with the DP model virtually simultaneously with the onset of collapse, neighboring stress points have not reached stress conditions corresponding to failure and therefore the rupture plane does not extend laterally to encompass point F.

Finite element calculations are able to capture the development of the stress conditions necessary to cause collapse along a rupture surface, as well as the associated redistribution of stresses that accompanies this, which of course is not possible with simple limit equilibrium methods. In addition, the need for recursive searching for the critical failure surface, as is the case in standard limit equilibrium methods, is not necessary.

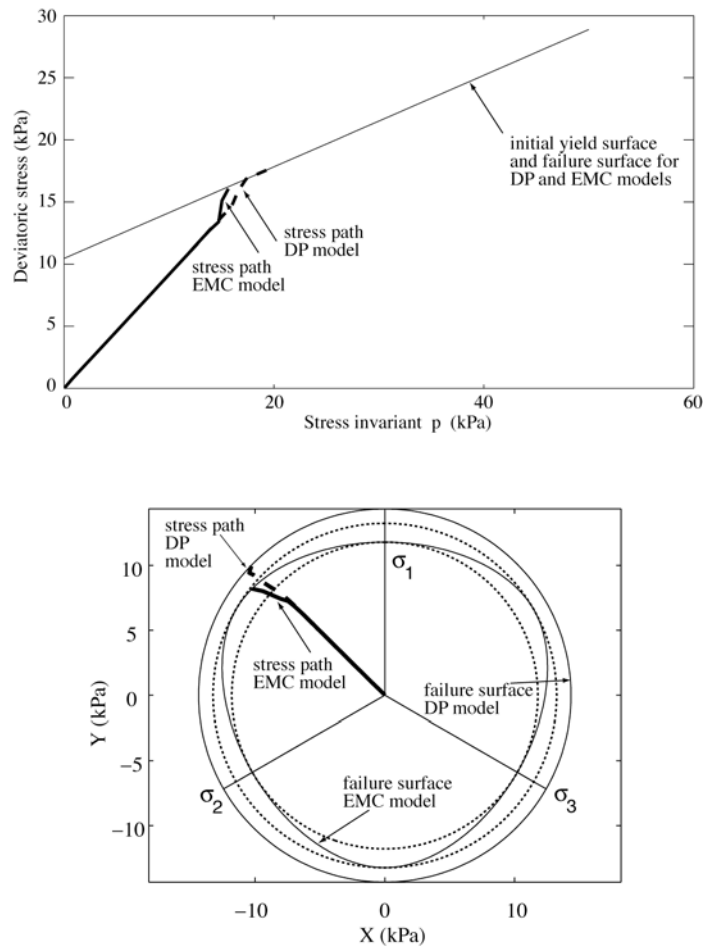


Figure B.5 Stress paths for point E.

B.6 Displacement Predictions

Another advantage of finite element calculations that use a reasonable elasto-plastic soil model is that they can provide detailed displacement predictions. These are important for estimating lateral earth pressures prior to and during collapse. In general, these pressures can be quite different from those calculated using simpler limit methods. In addition, the overall deformation pattern, particularly in three dimensions, can provide important clues on the nature of ensuing mass wasting processes. For example, it may be postulated that when significant down-slope deformation occur in the soil mass above the rupture surface, the post-failure displacement mode may tend towards that of a flow. Conversely, limited down-slope displacements in the overlaying mass may signify an impending rigid block-type of deformation pattern, at least during the initial phases of the inertial mass wasting process.

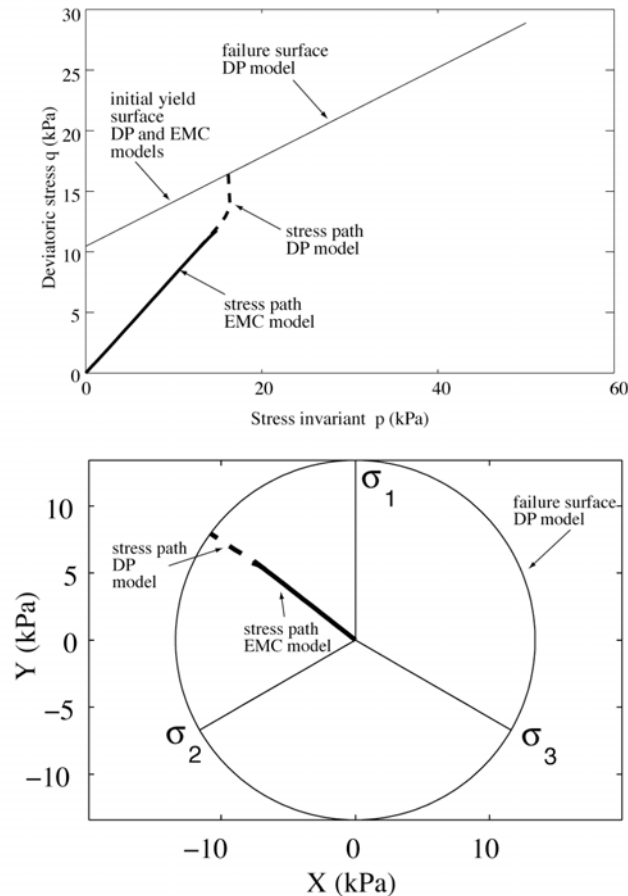


Figure B.6 Stress paths for point F.

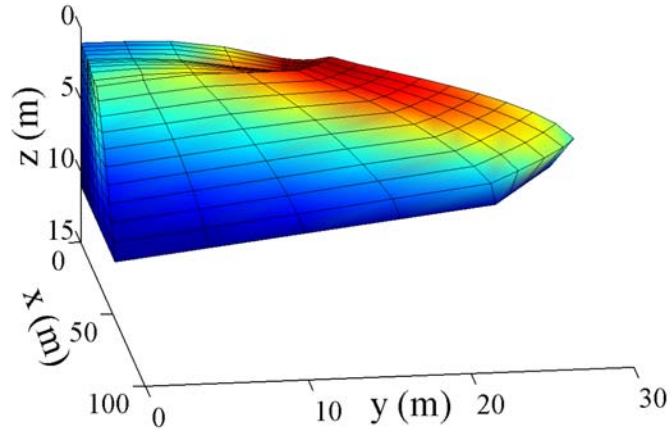


Figure B.7 Deformed mesh - DP model (exaggerated by a factor of 15)

The overall deformation pattern for the two slopes at the point of collapse is shown in Figure B.7 for the DP model. As expected, the largest amount of displacement occurs near the crest of the slope, which is free to move. Also, significantly more deformations develop in slope I as compared to slope II. This is apparent by contrasting the deformed mesh as viewed from the yz (Figure B.8) and the xz boundaries (Figure B.9). Superimposed on these views are the velocity vectors at the end of the analysis. The face of slope I has undergone significant down-slope deformation due to the widespread amount of yielding, whereas the face of slope II remains nearly unchanged since it has not yielded to any appreciable degree.

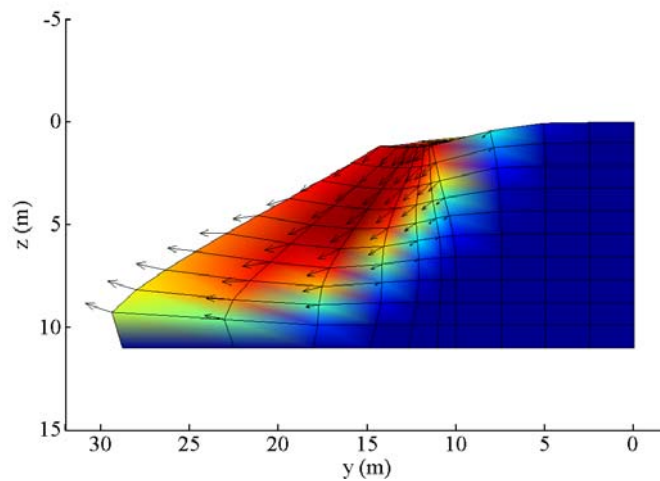


Figure B.8 Deformed mesh viewed from yz boundary (DP model)

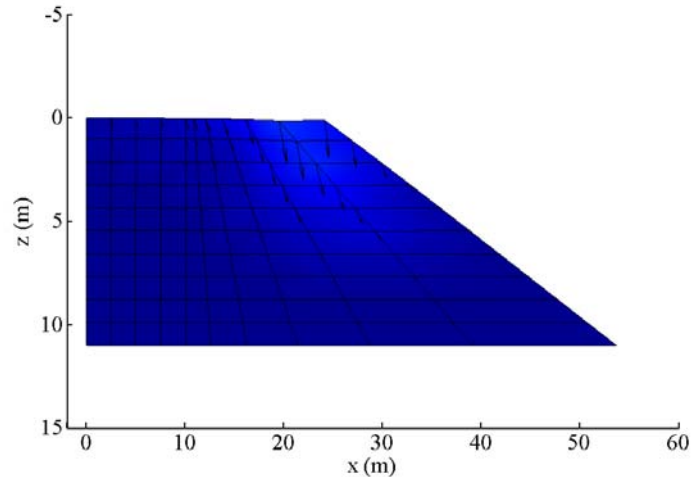


Figure B.9 Deformed mesh viewed from xz boundary (DP model)

Predictions of deformations can be examined in more detail by looking at points D, E and F. Displacements in the three directions x , y and z are shown in Figure B.10 from the start of loading. Load factor in Figure B.10 refers to the percentage of the ultimate self-weight. Points D and F are located on vertical boundaries so that D is restricted from moving in the x direction and F is similarly restricted in the y direction.

Figure B.10 suggests that the faces of slopes I and II are moving downward and outward. Point D moves further in the x direction than point E, while points D and E move about the same amount in the y direction during most of the loading. In the end though, point D does move somewhat further in the outward y direction than point E, particularly as yielding takes place. All three points undergo similar vertical deformations during elastic loading, but at the end of the analysis points E and F have settled considerably more. This can also be noted in Figure B.7.

Similar observations can be made by considering Figure B.11, which groups predictions in all three directions for each of points D, E and F. Interesting to note is the behavior of point E, located at the intersection of slopes I and II. This point displaces significantly more in the y direction than the x direction. This is to accommodate the larger outward movement of the face of slope I, which occurs predominantly in the y direction and to a

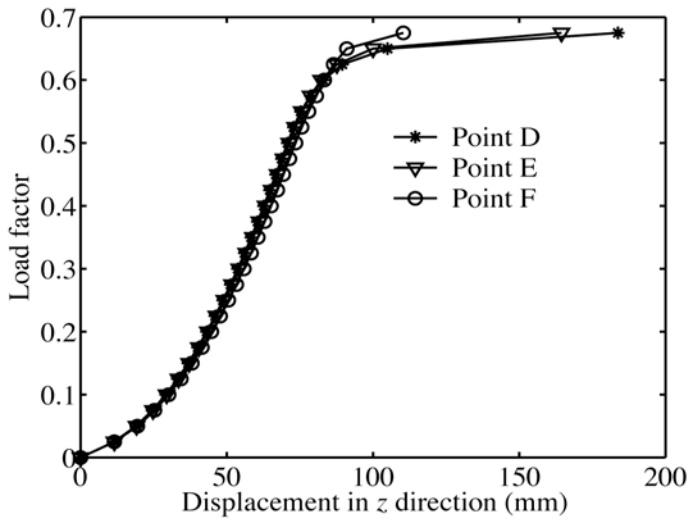
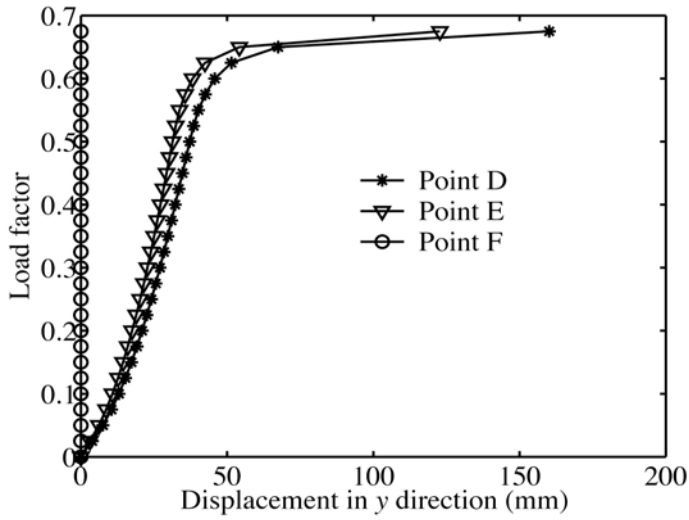
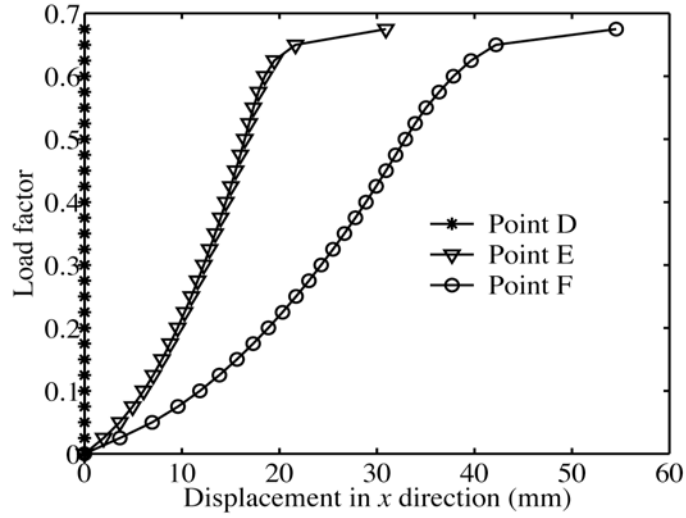


Figure B.10 Displacements at points D, E and F (Model DP).

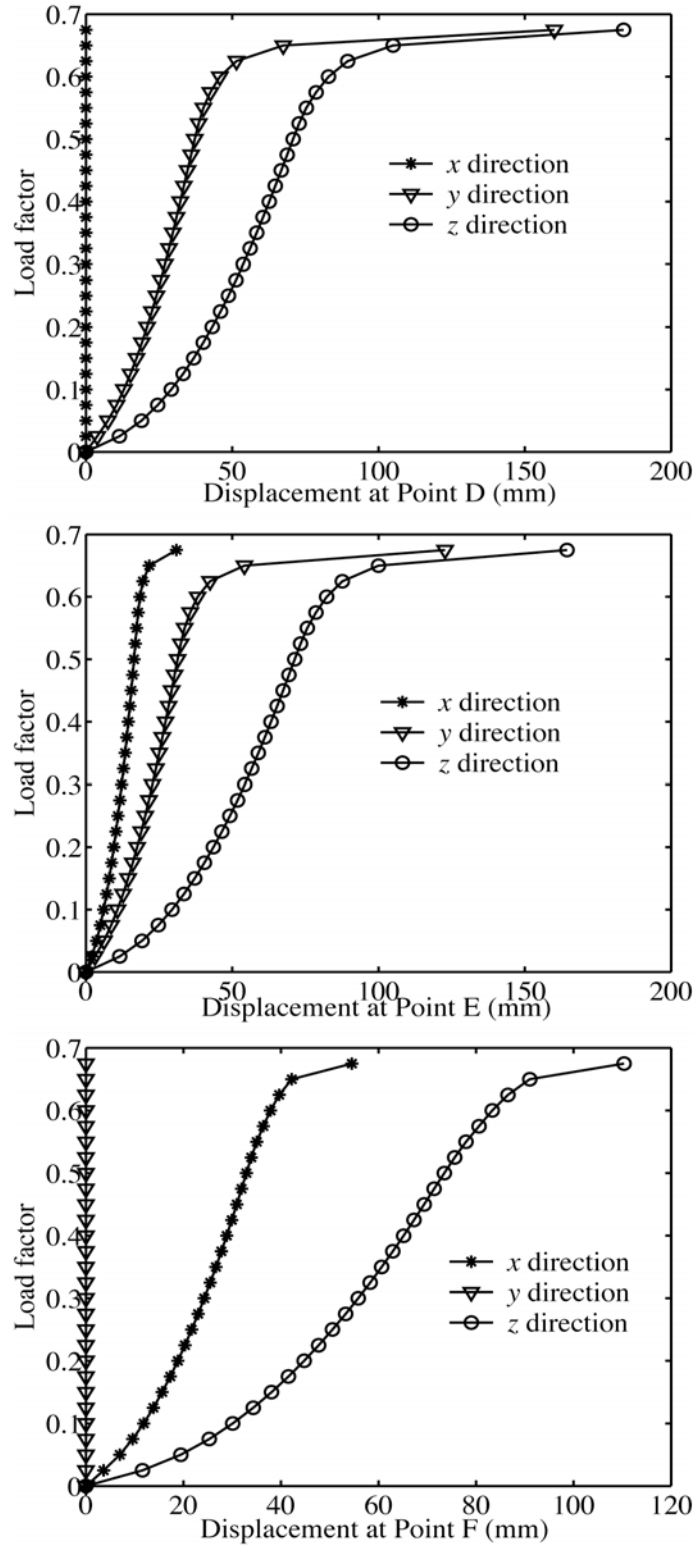


Figure B.11 Displacements in x, y and z directions (Model DP).

lesser degree in the x direction. Thus the down-slope displacement of both slopes I and II is truly three-dimensional and is a function of the relative inclination of the two intersecting slope faces.

Although somewhat different in terms of the predicted deformations at failure, the overall pattern of displacements for the EMC model is similar to that for soil model DP. For example, the deformed mesh in the yz plane for soil model DP (Figure B.8) can be contrasted to that for the EMC model in Figure B.12. In the DP model the crest of the slope is seen to settle and tilt backward to a larger extent than in the EMC model when collapse becomes imminent. Also, the bottom of the slope face protrudes out beyond the fixed bottom for the DP model, but not so for the EMC model.

To further investigate differences in predictions from the two models, we can again focus on Point E, which is removed a substantial distance from all vertical boundaries. A direct comparison between displacements using the two soil models is shown in Figure B.13. As expected, predictions prior to yielding are the same since both models assume a similar elastic response. However, upon yielding the response is significantly different. The DP model estimates larger x , y and z displacements at the point of collapse compared to the EMC model. This is partly because of a more effective re-distribution of stresses in the DP model that allows for a larger ultimate load, but also because of different stress paths followed by both models upon yielding. The latter effect is evidenced in the y and z displacement predictions in Figure B.13.

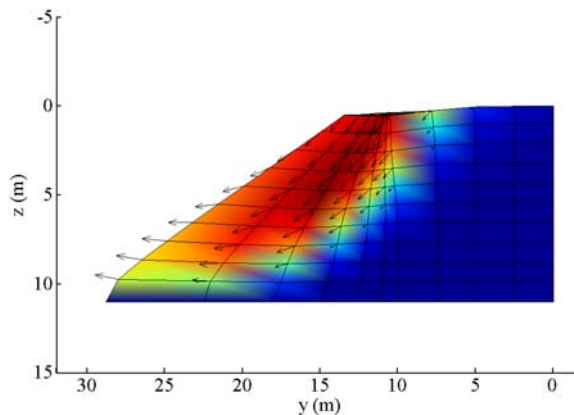


Figure B.12 Deformed mesh viewed from yz boundary (EMC model)

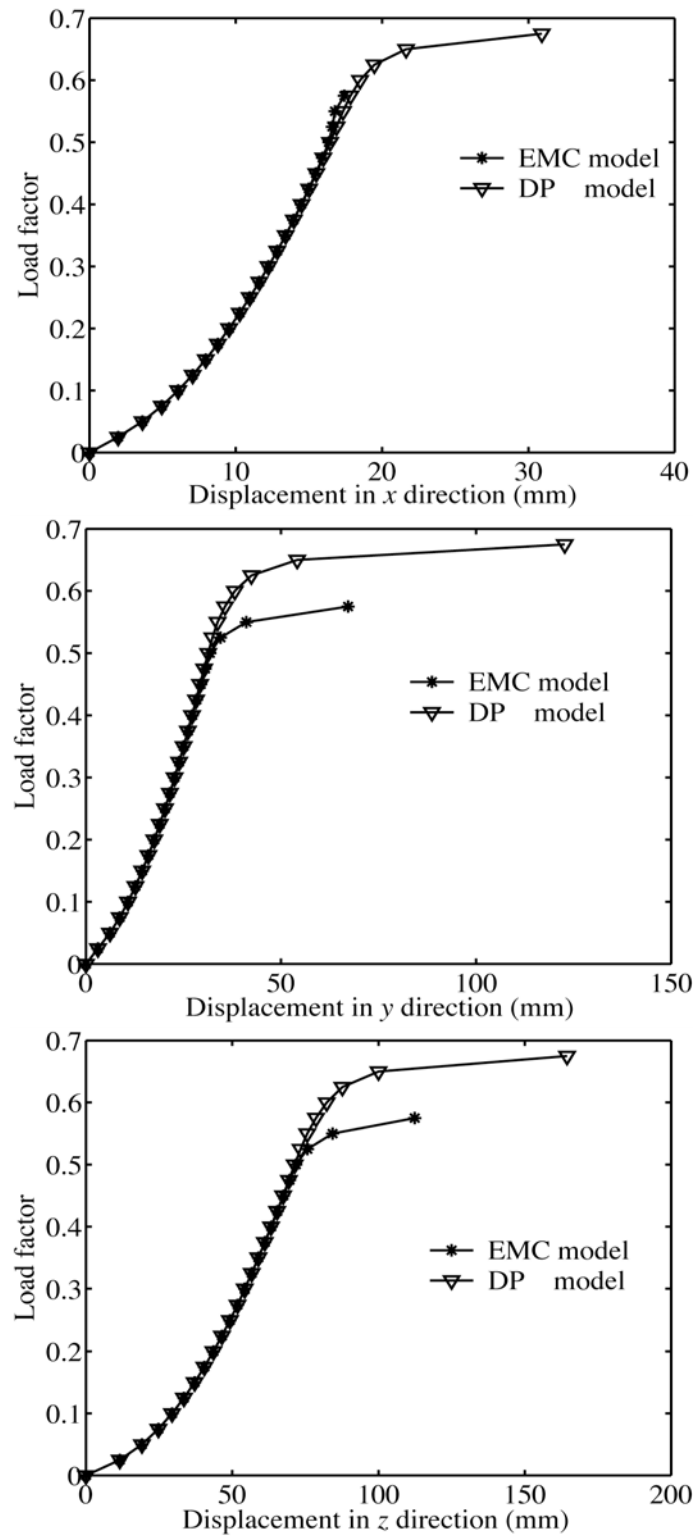


Figure B.13 Model comparisons for displacements at point E.

B.7 Conclusions

Elasto-plastic analysis of three-dimensional slopes is clearly superior to simple limit equilibrium, particularly for three-dimensional geometries. Realistic soil models embedded in a finite element framework can provide important deformation predictions and have the potential to model the progress of failure on rupture surfaces. However, as this study shows, there can be significant differences in predictions depending on the particular soil model chosen. Given the large number of such models that have been proposed, careful consideration needs to be placed on selecting an appropriate one. The choice of such a model depends on expected stress conditions and the ability to properly characterize the relevant material parameters. With regard to fine-grained marine sediments, it may often be advisable to compromise by selecting a moderately comprehensive soil model that incorporates the most important aspects of constitutive behavior yet is not so complex as to make the effort of prediction overly cumbersome.

Two particular soil models that may very well constitute such a compromise have been coded into the OpenSees code and their predictions are compared for a hypothetical embankment-type soil deposit consisting of two intersecting slopes. Although both models predict similar elastic behavior, they each lead to somewhat different stress and strain states when collapse occurs. In particular, the DP model is more effective at re-distributing stresses throughout the slope geometry than the EMC model, hence collapse occurs at a higher load intensity.

B.8 References

Brandes, H. G. and S. Wang (2005). OpenSees modeling of the 3D plastic behavior of underwater slopes: achievements and limitations. *Frontiers in Offshore Geotechnics*, ISFOG 2005, New York: Taylor & Francis.

Drucker, D. C. and W. Prager (1952). "Soil Mechanics and plastic analysis or limit design." *Quarterly of Applied Mathematics* **10**(2): 157-165.

Duncan, J. M. and S. G. Wright (2005). Soil strength and slope stability. NJ, John Wiley

and Sons.

Elgamal, A., L. Yan, et al. (2003). OpenSees modeling of bridge-foundation-foil interaction. 2003 OpenSees User Workshop, University of California at Davis.

Jeremic, B. (2003). Computational geomechanics: simulations of static and dynamic behavior of foundation system. 2003 OpenSees User Workshop, University of California at Davis.

Pacific Earthquake Engineering Research Center (2004), OpenSees web site, <http://opensees.berkeley.edu/>.

Terzaghi, K., R. B. Peck, et al. (1996). Soil mechanics in engineering practice. New York, John Wiley and Sons.

Appendix C

OpenSees Modeling of the 3D Plastic Behavior of Underwater Slopes: Achievements and Limitations

Brandes, H.G. and Wang, S. (2005)

Frontiers in Offshore Geotechnics, ISFOG 2005, Proceedings of the 1st International Symposium on Frontiers in Offshore Geotechnics, Eds: S. Gourvenec and M. Cassidy, New York: Taylor & Francis, pp. 897-902.

Abstract

The plastic response of two hypothetical slopes in response to surface loading from sediment deposition is examined with reference to two constitutive models. Predictions using a cap model are judged to be more reasonable than those from a noncap model and significant differences are noted between 2D and 3D geometries. Limitations are also discussed as far as realistic modeling of large offshore slopes is concerned.

D.1 Introduction

Modeling and simulation of complex nonlinear geotechnical problems has usually meant the use of large commercial finite element programs. Although some of these are quite powerful, the underlying codes are generally not accessible to benefit from community-wide development. Realizing that major advances in modeling and simulation were necessary in specific fields such as earthquake engineering, the National Science Foundation of the United States has supported the development of OpenSees (Open System for Earthquake Engineering Simulation; Pacific Earthquake Engineering Research

Center, 2004). OpenSees is an open-source software framework consisting of a set of interrelated classes, designed as independent as possible for maximum flexibility, which control data structure, material behavior models, hierarchical element types, solution algorithms, integrators, equation solvers, databases, visualization and communication procedures. OpenSees has seen enormous growth in the last few years as developers and researchers have made use of the software's inherent flexibility to add additional capability (Elgamal et al., 2003). OpenSees has been adapted to solve a wide range of problems involving soil, soil-structure interaction, earthquake shaking, and reliability assessment (Jeremic, 2003). It has also been adopted by the Network for Earthquake Engineering Simulation as its platform for simulation and visualization.

In this article we report on two of a series of specific soil plasticity models that we are in the process of adding to OpenSees and examine their prediction with regard to simplified two- and three-dimensional hypothetical slopes, which may be useful for understanding the behavior of slopes in the offshore environment. Of course, techniques other than the finite element method have been used extensively to analyze slopes, including limit analysis (bearing capacity, limit equilibrium) and various probabilistic approaches (Abramson, 2002; TRB, 1996). However, they do not provide the level of stress and strain detail that a numerical solution can provide and therefore generally provide less insight into the mechanics of deformation and failure of slopes.

D.2 Constitutive Models

A hierarchy of constitutive models has been proposed for frictional soil materials, ranging from the elementary Mohr-Coulomb model to sophisticated hardening plasticity models that are able to account for the most important aspects of soil behavior observed through experimentation. The perfectly-plastic Mohr-Coulomb model is adequate for simple force limit equilibrium calculations regarding slope stability, bearing capacity of footings, and active/passive pressures on retaining walls. However, generalization of the Mohr-Coulomb criteria to include the effect of all principal stresses and plastic yield deformations leads to unrealistic volume change predictions (Drucker et al., 1957) and numerical difficulties.

The latter ones arise from the discontinuity of the hexagonal yield surface in stress space along principal stress planes. Drucker and Prager (1952) proposed a generalization of the Mohr-Coulomb model that takes into account the effects of all the principal stresses and that is more amenable to numerical computation. Nonetheless, the Drucker-Prager model in its original form assumes similar behavior in compression and tension and does not correctly predict volume compression that accompanies increases in mean pressure.

An improvement upon the original model proposed by Drucker and Prager, referred to herein as the Extended Drucker Prager Model I (EDP-I), has been coded into OpenSees as part of this study. This model is conceptually similar to the one that is available in the code ABAQUS (2003). Its chief improvement upon the original Drucker-Prager model is that the resulting yield surface is non-circular, hence allowing for a compressive yield strength that is greater than the tensile yield strength. Soil is allowed to harden and/or soften isotropically. The flow rule allows simultaneous inelastic dilation and inelastic shearing (Figure C.1). A linear yield criterion is assumed:

$$f = t - p \tan \beta - d = 0 \tag{C-1}$$

where p = volumetric stress; β is the slope of the linear yield surface in the $p - t$ stress plane (i.e. friction angle); d represents the material's cohesion; and t is the deviatoric stress (ABAQUS, 2003).

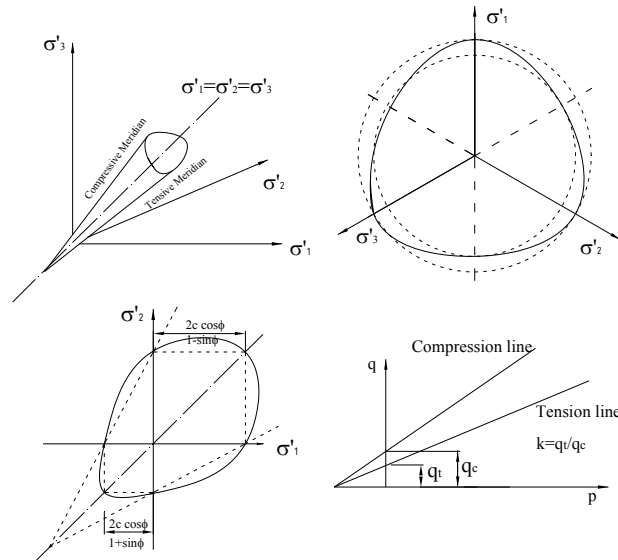


Figure C.1 Extended Drucker Prager model (EDP-I).

Frictional soil models with a single surface, such as the one just described, are unable to correctly account for volume compression upon yielding. It is well known that normally consolidated clays and loose sands exhibit a decrease in volume during shear, often almost from the beginning of loading. To correctly account for this type of behavior, a range of more versatile models have been proposed that incorporate a second yield surface, or cap, which grows or shrinks depending upon stress history. One such model, referred to herein as the Modified Drucker-Prager cap model (MDP-C), has also been coded into OpenSees (Figure C.2). Again, this model is similar to one available in ABAQUS. Frictional failure is defined as in the EDP-I model, hence Equation (C-1) applies. The elliptical cap is given by the equation:

$$f_c = \sqrt{(p - p_a)^2 + \left(\frac{Rt}{1 + \alpha - \frac{\alpha}{\cos \beta}} \right)^2} - R(d + p_a \tan \beta) = 0 \quad (C-2)$$

where R = a cap shape constant; α = a small number (typically 0.01 to 0.05); p_b = the hydrostatic compression yield stress; and p_a = an evolution parameter that is a function of plastic volumetric strain controlling the amount of hardening or softening (ABAQUS, 2003). In this equation d is the t -intercept at $p = 0$ (Figure C.2). The parameter α is used to define a transition yield surface between the one given by Equations (C-1) and (C-2). This transition yield surface has the following functional form:

$$f_t = \sqrt{[p - p_a]^2 + [t - (1 - \frac{\alpha}{\cos \beta})(d + p_a \tan \beta)]^2} - \alpha(d + p_a \tan \beta) = 0 \quad (C-3)$$

The material parameters assumed for the numerical analysis are listed in Table C-1. In addition to the EDP-I and MDP-C models, we are also in the process of adding additional constitutive models into OpenSees, such as a new and more versatile form of the modified Cam clay model.

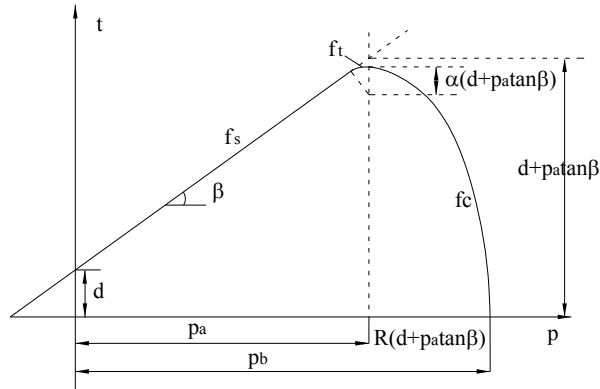


Figure C.2 Modified Drucker Prager model (MDP-C).

D.3 Slope Geometry And Modeling Approach

Computations were carried out using 20-node brick elements arranged to simulate 2D and 3D semi-infinite slopes. By 2D we mean hypothetical slopes of uniform depth and width (Figure C.3), whereas by 3D we mean equivalent slopes that also vary in depth along the cross-slope direction (Figure C.4). The intention in selecting these two geometries was to explore differences between conventional 2D modeling and potentially more realistic 3D modeling. Another aspect that is of interest is the loading of the sloping seafloor by sediment deposits (surcharge loading) that may have been transported by mass wasting or other means. This was modeled in a very simple fashion by adding sediment thickness over a portion of the 2D and 3D slopes and examining the resulting behavior (Figure C.5). The intention was to illustrate, in a very simpleminded way, the effects of placing a sediment surcharge on the seabed that is of limited extent and varies in load intensity in the down-slope direction. The slopes considered were 5m wide, 10m high and 20m long. The down-slope angle was 25° . The 3D geometry varies from the 2D one only in the sense that the bottom is slanted 40° in the cross-slope direction, as shown in Figure C.4. The slope itself was discretized using 12x6x15 elements, whereas the surcharge thickness consisted of 6x6x3 elements.

Table C-1 Soil properties

	Slope	Surcharge
c (kPa)	5	100
ϕ (Deg.)	28	37
p_d (kPa)	150	250
E (kPa)	17,400	17,400
E_0 (kPa)	17,400	17,400
ν	0.35	0.35
ρ (kg/m ³)	1,478	3,000
k	1.0	1.0
α	0.1	0.1
R	0.6	0.6
d	10.5	199.7
$\tan\beta$	1.11	1.51

The parameters listed in Table C-1 are typical for fine-grained marine sediments, with the exception of the density for the surcharge load. This density was chosen to be much higher than that of the slope sediment to focus attention on the behavior of the slope sediment and not on the surcharge material. In fact, the surcharge was assumed to have purely elastic properties.

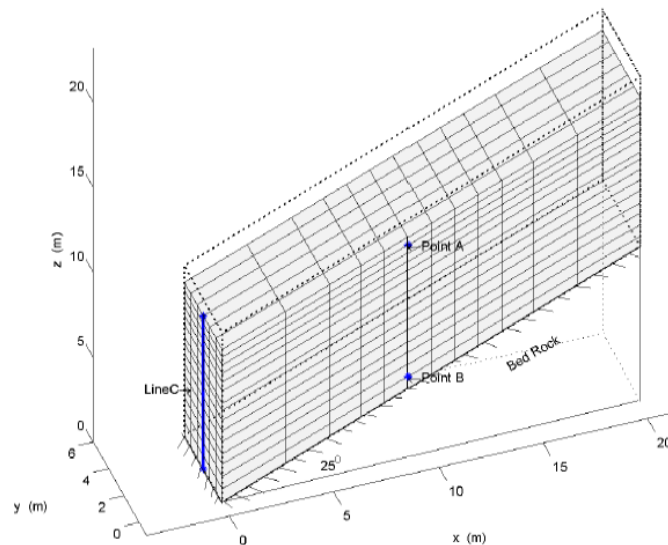


Figure C.3 2D slope geometry before and after self-weight consolidation

In all cases, time-dependency and associated primary consolidation were ignored. In other words, drained and/or long-term conditions were assumed to prevail. This may be adequate for medium and deep water slopes where sedimentation processes often occur over very long periods of time. In each case, the semi-infinite slope geometry was allowed to undergo self-weight compression first, followed by ‘excess’ loading induced by embankment-type sediment heaps as shown in Figure C.5. Self-weight compression was forced to occur in the vertical direction only by imposing roller boundary conditions on all the vertical faces and rigid conditions along the bottom. The seabed surface was allowed to deform freely. During excess loading the vertical faces on the upper and lower ends of the boxes were changed from rollers (which allowed only vertical deformations) to stress boundaries with initial lateral pressures equal to those at the end of the prior self-weight stage. Stress-strain behavior was modeled using the two constitutive models described previously. These models were implemented using a forward Euler stress incrementation technique for optimum stability.

D.4 Results

The first stage of the analysis involves modeling of the self-weight consolidation process. Roller boundary conditions on the vertical faces lead to vertical displacements (Figure C.3 and Figure C.4) and vertical stress gradients proportional to the sediment weight. Although the distribution of resulting displacements and stresses is reasonable, it can hardly be said that conventional numerical modeling of the process of self-weight consolidation is an accurate representation of what occurs in the field. After all, it is well known that complex sedimentary and post-depositional processes, which are difficult to understand and model, play an important role in subsequent slope behavior. Nonetheless, the conventional numerical approach allows the setting of initial stresses that satisfy equilibrium and boundary conditions.

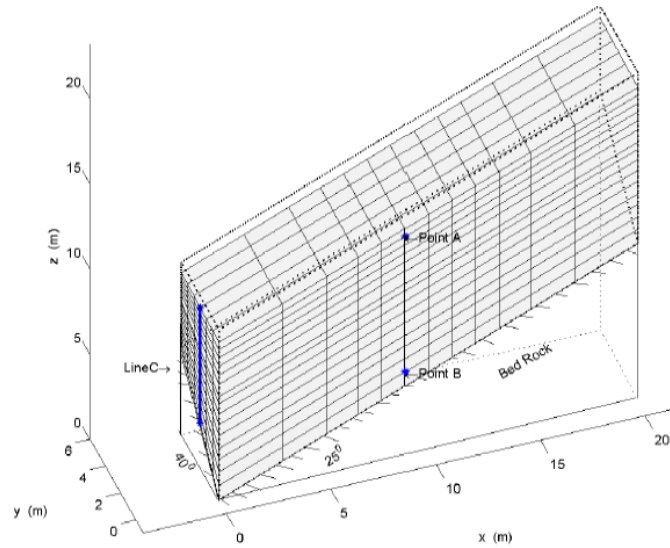


Figure C.4 3D slope geometry before and after self-weight consolidation

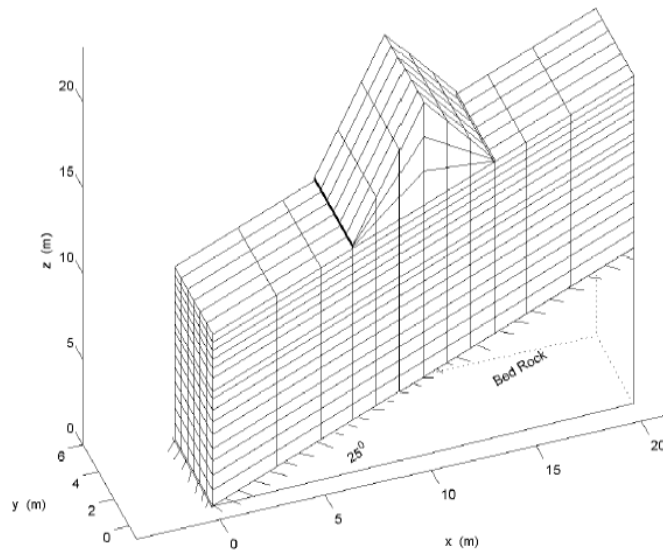


Figure C.5 2D slope with surface surcharge

Following self-weight consolidation, the surcharge load shown in Figure C.5 was added to the surface of the 2D and 3D slope geometries, and the boundary conditions along the upper and lower vertical faces were relaxed to allow for global shearing. In addition to general down-slope deformation, localized distortion in the slope region beneath the surcharge load occurs. The overall response though is very much dependent on the plastic constitutive model used. In terms of stresses, yielding is limited to the region immediately

beneath the surcharge load for the non-cap EDP-I model, whereas yielding is much more widespread (but does not occur everywhere) when the MDP-C cap model is used (Figure C.6 and Figure C.7). The reason for this of course is the presence or absence of the non-frictional yield cap. Stress points in the slope near the surcharge yield because they reach the frictional surface, i.e. Equation (C-1), regardless of which of the two models are used. On the other hand, stress points further away from the surcharge remain in an elastic state in the EDP-I model, but in many instances are seen to yield with the MDP-C model as they reach either the general cap, Equation (C-2) or the transition yield surface Equation (C-3).

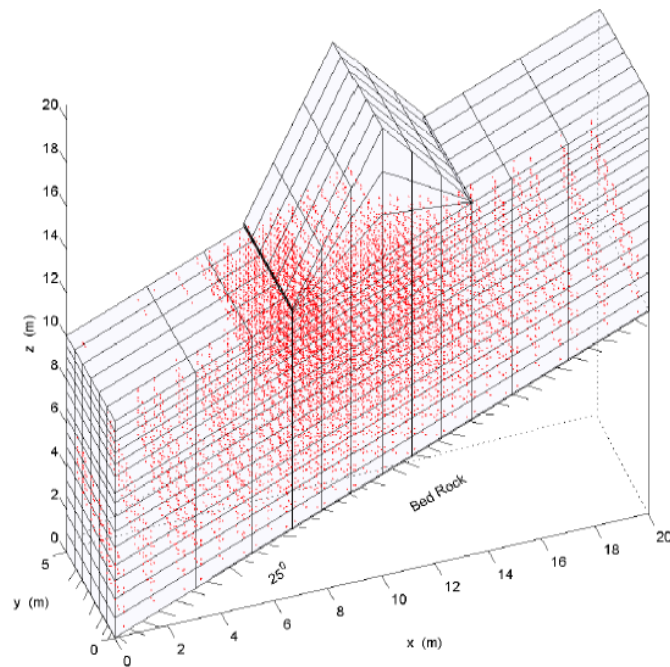


Figure C.6 Yield points for EDP-I model

This difference in behavior can be seen by following the stress path of points A and B, identified in Figure C.3. Point A, close to the surface of the slope and immediately beneath the surcharge, is seen to yield as it reaches the frictional surface, regardless of which model is used, whereas the deeper point B remains in an elastic state in the EDP-I model but yields by reaching the cap in the MDP-C model (Figure C.8 and Figure C.9). It should be noted that the surcharge itself was given material parameters such that it would not yield in order to focus on the response of the slope itself.

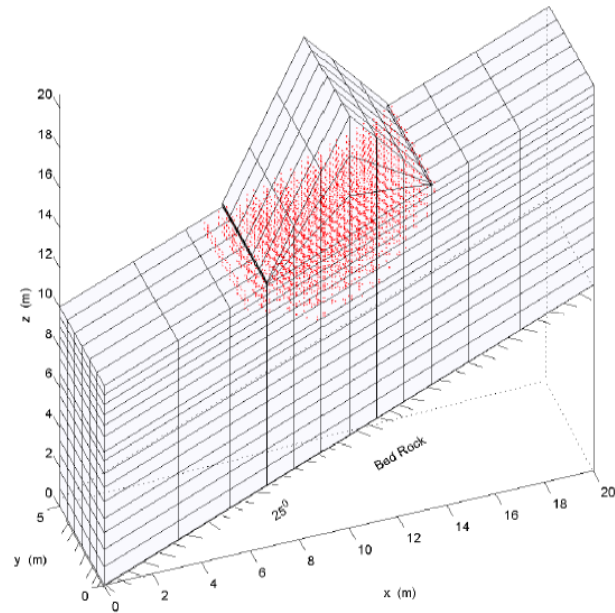


Figure C.7 Yield points for MDP-C model

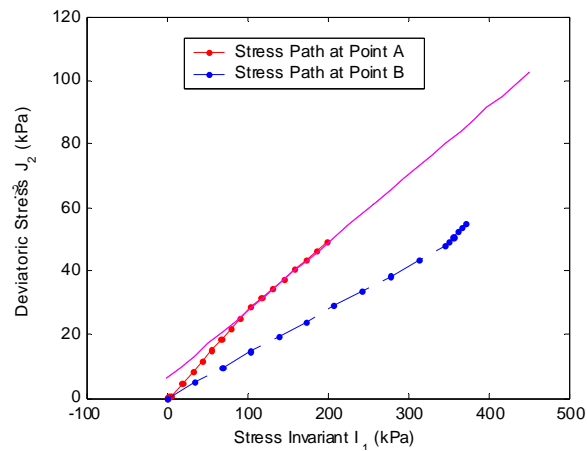


Figure C.8 Selected stress paths for model EDP-I (2D)

As already mentioned, the cap model has a distinct advantage over the non-cap model in that it is able to predict either compressive or expansive plastic volumetric strains, whereas the non-cap model is limited to the prediction of expansive inelastic strains only. For example, Figure C.10 shows plastic and total volumetric strains at points A and B for the MDP-C model. Point A reaches the frictional surface, such that the normal

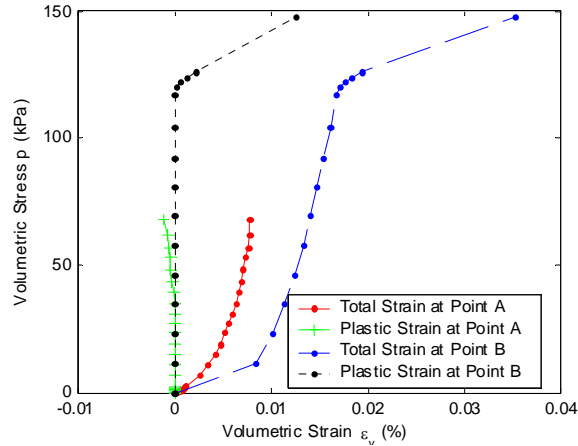


Figure C.9 Selected stress paths for model MDP-C (2D)

incremental plastic strain points upward and to the left, thus indicating plastic dilation. On the other hand, point B first reaches the cap, where the incremental plastic strain point upward and to the right. As a result, plastic volumetric strain is compressive. In other words, shallow slope sediment subjected to loading by the surcharge will tend to expand and shear under relatively low confining pressure, whereas deeper sediment will undergo less shearing and some volume compression at higher confining pressure. This makes intuitive sense and suggests that modeling of elasto-plastic behavior of slopes should always employ a cap model. Naturally, the MDP-C model chosen for this study is only one such model and many others can be considered. Among these are the widely-used modified Cam Clay model (Roscoe and Burland, 1968) and many others. One important difference between the MDP-C and the modified Can Clay model is that the former one provides a seamless transition from the cap to the frictional shear surface by means of the transition surface (Figure C.2, Equation (C-3)). While this may seem desirable since it allows for a smooth transition in terms of the direction of the incremental plastic strain at the intersection of the frictional and cap surfaces, it can lead to difficulties with certain stress integration algorithms (such as the backward Euler method) in the region of the transition yield surface when spanning the elastic-inelastic divide.

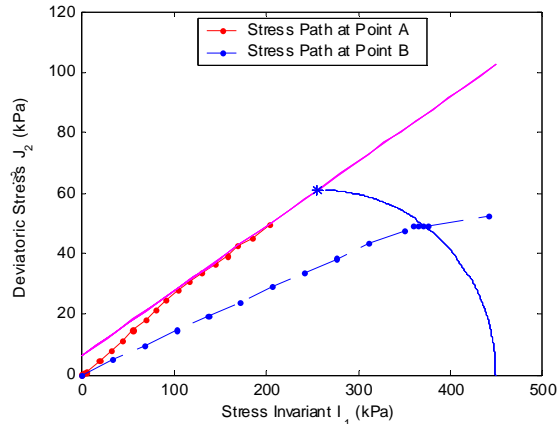


Figure C.10 Volumetric strains for model MDP-C (2D)

The contrast in predictions of global shear deformation from the two models can be considered with reference to Figure C.11. This figure shows downslope deformations along profile C, located at the lower end of the slope (Figure C.3 and Figure C.4). Interestingly, the choice of constitutive model makes little difference for the 3D slope geometry, but is very important for the 2D geometry. In the latter case, more widespread yielding leads to more significant shearing when using the MDP-C model. It is likely that if a deeper slope had been selected, the difference in predictions between the two constitutive models may have been more dramatic in the 3D case as well. The 3D configuration leads to smaller overall displacements due to a smaller volume of material that is subject to deformation. It is obvious that 2D simplification of real slopes may be inadequate to capture the true behavior of submarine slopes, particularly in cases where there are significant geometric and material variations in the cross-slope direction.

Another view of overall deformation is captured in Figure C.12, which shows displacements on a cross section of the 2D slope. As expected, the effect of the surcharge is to produce a curved indentation in the underlying slope sediment, along with a passive bulge of material in the front of the surcharge. As already noted, this occurs as stresses along the interface reach frictional yielding and significant plastic shearing.

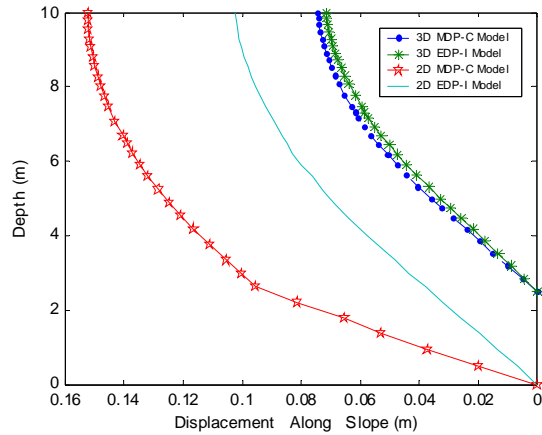


Figure C.11 Downslope displacement profiles

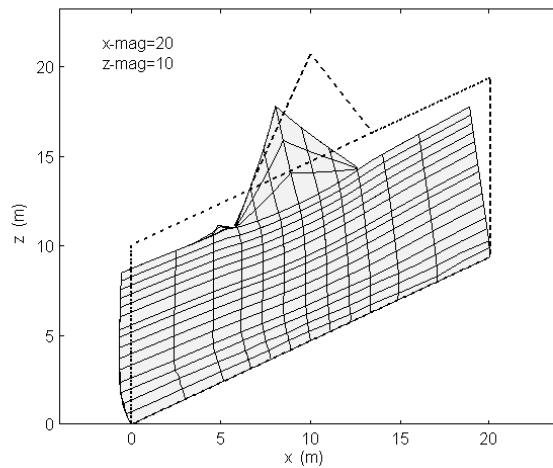


Figure C.12 Cross section of deformed 2D mesh.

D.5 Final Comments

The boundary value problem chosen for this study is not meant to be an accurate representation of any particular field slope. Instead, it was selected to investigate generic modeling issues related to constitutive soil behavior, slope geometry and surcharge loading. Monumental obstacles remain in achieving satisfactory models of offshore slopes such as may be found along the continental slope and rise. Obstacles include accurate time-history simulation of sediment transport and deposition processes, generating reasonable geometries that incorporate typical field dimensions, as well as reliable and

sufficient sediment characterization. It is not uncommon that gravity-driven slope processes involve sediment sequences that are tens or hundreds of meters deep and hundreds of meters to many kilometers in horizontal extent. This would require massive meshes and therefore enormous computational resources. For reference, the nonlinear analysis conducted for this study involved on the order of about 1,100 elements with 20 nodes each and some 40 or so load steps. Each run took about 8 hours when using the EDP-I model and about 28 hours when using the MDP-C model, all on a top of the line PC platform. Even if more optimum modeling setups can be conceived of, current computational capabilities are still unable to cope with the very large slope geometries that need to be considered to investigate the type of large scale mass wasting and sediment transport processes that are found on the continental slope and rise.

It is therefore important that quantum advances be made in computational resources and code optimization. A simple switch to supercomputer platforms is unlikely to be sufficient without a parallelization of codes. Promising in this regard is that the OpenSees program used herein is now in the process of being parallelized by its original developers. The intention is to continue our own modeling work by developing the requisite parallel constitutive models to complement these other efforts.

D.6 References

- ABAQUS (2003). ABAQUS Theory Manual Version 6.4, Hibbit, Karlsson & Sorensen, Inc.,
- Abramson, L. W., T. S. Lee, et al. (2002). Soil stability and stabilization methods. New York, John Wiley & Sons , Inc.
- Drucker, D. C., R. E. Gibson, et al. (1957). "Soil mechanics and work hardening theories of plasticity." Transactions, ASCE **122**: 1692-1653.
- Drucker, D. C. and W. Prager (1952). "Soil Mechanics and plastic analysis or limit design." Quarterly of Applied Mathematics **10**(2): 157-165.
- Elgamal, A., L. Yan, et al. (2003). OpenSees modeling of bridge-foundation-foil interaction. 2003 OpenSees User Workshop, University of California at Davis.

Jeremic, B. (2003). Computational geomechanics: simulations of static and dynamic behavior of foundation system. 2003 OpenSees User Workshop, University of California at Davis.

Muir, D. M. (1990). Soil behavior and critical state soil mechanics, Cambridge: University Press.

Pacific Earthquake Engineering Research Center (2004), OpenSees web site, <http://opensees.berkeley.edu/>.

Roscoe, K. H. and J. B. Burland (1968). "On the Generalized Stress-Strain Behavior of Wet Clay." Engineering Plasticity: 535-609.

TRB (1996). Landslides, investigation and mitigation. Special Report 247. Washington, DC, Transportation Research Board, National Research Council.

Appendix D

Cyclic Simple Shear Testing and Modeling of an Offshore Fine Sand

Brandes, H.G., Seidman, J. and Wang, S. (2005)

Proceedings, 15th International Offshore and Polar Engineering Conference, 2:679-689.

Abstract

Results from a series of cyclic simple shear tests are presented to examine the response of a shallow-water sand from the west coast of South Florida under constant volume conditions typical of earthquake or wave loading. Both low and high-density states were investigated. The strongly nonlinear response is then modeled with some success using a nonlinear cyclic model consisting of a hyperbolic stress-strain relationship and a pore pressure generation equation.

Keywords: Cyclic simple shear, cyclic soil modeling, testing, seabed sand.

D.1 Introduction

Direct simple shear (DSS) tests were conducted on a seabed sand from shallow waters off Tampa Bay, Florida, obtained as part of the U.S. Office of Naval Research's Mine Burial Prediction program. The sand was collected in bulk from the seabed by divers. It consists of 11% calcium carbonate, which is in contrast to coarser sediments only a few tens of feet away that are mixed with more abundant shell fragments and other reefoidal fragments that increase the bulk carbonate content to 65%. The non-carbonate portion of the seabed sand consists of semi-angular quartz grains in the fine sand range (Figure D.1). This quartz

fraction was transported to the Tampa Bay offshore region from the northern Gulf of Mexico by nearshore currents. The sand is well sorted and consists predominantly of grain sizes between 0.1 and 0.4 mm (Figure D.2). The bulk specific gravity is 2.74. No cementation was evident.

The purpose of this study was to gain further understanding of the cyclic behavior of seabed sands, which may be subjected to rapid time-varying loads by either shallow water waves or earthquakes.

D.2 Testing Procedures and Program

The DSS tests were performed at the University of Hawaii using the new generation DSS equipment developed by the Norwegian Geotechnical Institute. The specimen is contained in a wire-reinforced membrane that keeps the material from expanding horizontally, but allows lateral shearing with virtually no resistance. All the tests were run in an undrained mode, whereby the normal force is made to vary continuously by the vertical piston so as to keep a constant height at all times. Under such conditions of constant volume, measured changes in the vertical stress are equivalent to pore pressure (Dyvik et al., 1983).



Figure D.1 Microphotograph of test sand (oversized shell fragments were removed prior to specimen preparation).

Sample specimens were prepared by placing slightly moist sand in the reinforced wire membrane in small lifts while carefully monitoring density and final height. Once assembled into the testing device, the sand was permeated with carbon dioxide and saturated with water by inducing an upward flow through the specimen. Two series of tests were conducted, one at low density and one at high density. Loose specimens were prepared by pluviating sand from a constant height until the desired thickness was achieved (on the order of 2.5 cm). Dense specimens required hand tamping and vibration with a piston after placement of each lift. The final densities were compared to maximum and minimum values determined with a standard vibratory table and container arrangement in accordance with ASTM 4253/4254. Maximum density determined in this way was 1.83 gm/cm^3 and minimum density was 1.38 gm/cm^3 .

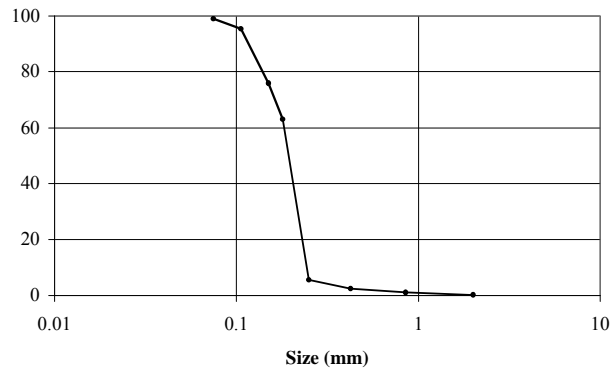


Figure D.2 Grain size distribution of sand tested.

The testing procedure involved applying a normal stress, followed by cyclic shearing at constant cyclic stress amplitude on the order of 13 kPa until liquefaction failure was observed. A frequency of 0.5 Hz was used in each case. Tests were continued until at least 15% cyclic shear strain developed. Four specimens were prepared and tested at densities as close as possible to the minimum density, and four specimens were prepared and tested near the maximum density (Table D-1). It is not expected that any of the normal loads resulted in crushing of grains.

Table D-1 Testing program

Test No.	Void ratio	Density (kN/m ³)	Relative density (%)	Normal stress (kPa)	±Shear Stress (kPa)
Low density					
LD-1	0.87	14.4	26	97	13.0
LD-2	0.88	14.3	21	162	13.0
LD-3	0.97	13.6	3	197	13.0
LD-4	0.96	13.7	4	274	13.2
High density					
HD-1	0.56	17.3	88	97	12.3
HD-2	0.53	17.6	93	143	13.5
HD-3	0.59	17.0	81	200	13.5
HD-4	0.65	16.3	69	264	13.0

D.3 Experimental Results

An example of cyclic test results for low-density test LD-3 is shown in Figure D.3. Failure is assumed to occur when shear strain first reaches 3%. Although different criteria may have been chosen, such as a certain level of strain amplitude, the corresponding onset of liquefaction would not be much different. Using the 3% criteria, failure in this test occurs after 45 cycles. At this point the pore pressure ratio has increased to 0.83. Pore pressure ratio, r_u , is herein defined as the ratio of vertical stress required to keep constant volume divided by the initial vertical stress. Shear strain accumulates rapidly after 3% strain. The test is stopped automatically when prescribed shear strain limits are exceeded. As expected, axial normal strain is virtually zero and thus constant volume conditions are effectively maintained throughout most of the test.

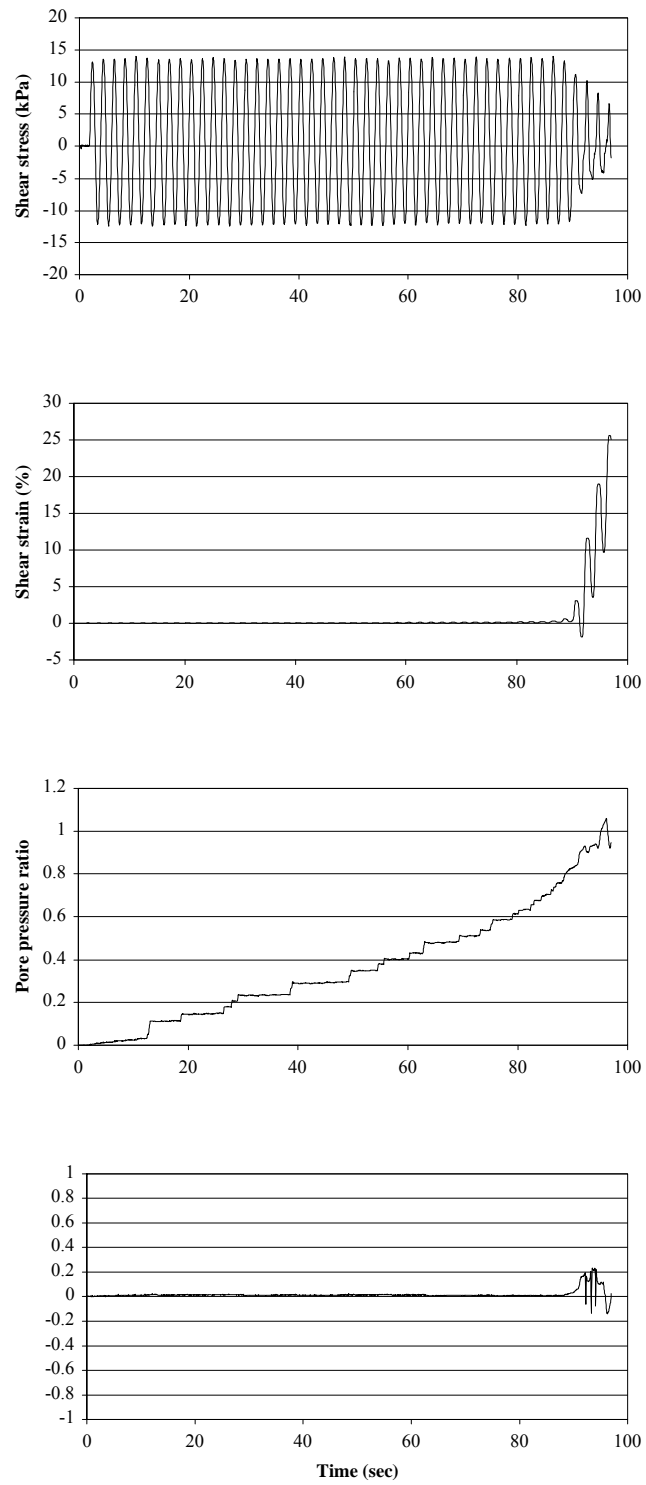


Figure D.3 Low-density test results, LD-3.

The permanent strains that are observed as liquefaction develops favor shearing in one direction over the other due to a small degree of non-symmetry in the cyclic shear stress about the zero-strain reference. Also, limited axial strain develops as liquefaction begins near the end of the test due to the equipment's difficulty in complying with large and rapid shear strain changes as the specimen loses stiffness. The loss of shear stiffness can better be appreciated in the stress-strain plot shown in Figure D.4.

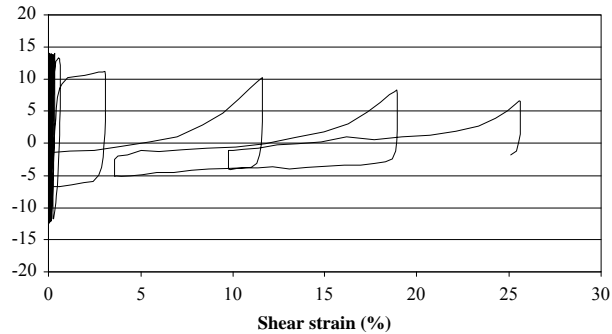


Figure D.4 Shear stress-strain results, LD-3.

Note that large changes in shear stiffness, along with the accumulation of permanent deformations, occurs rapidly after liquefaction is initiated. In contrast to the cyclic behavior at low density, Figure D.5 and Figure D.6 show the results of test HD-3 at a much higher density (Table D-1). The major difference here is that a much larger number of cycles is necessary to achieve the liquefaction criteria of 3% shear strain, namely 213 cycles.

The data from all tests is reproduced in Figure D.7 in conventional contour diagrams showing the number of load cycles necessary to cause liquefaction as a function of the cyclic stress ratio, which is defined as:

$$CSR = \frac{\tau_{cyc}}{\sigma'_{vo}} \quad (D-1)$$

where τ_{cyc} is the cyclic shear stress amplitude and σ'_{vo} is the normal stress at the start of cyclic testing (Table D-1). Again, the onset of liquefaction is assumed to occur at 3% cyclic shear strain. Two nearly linear relationships can be considered from the data, one

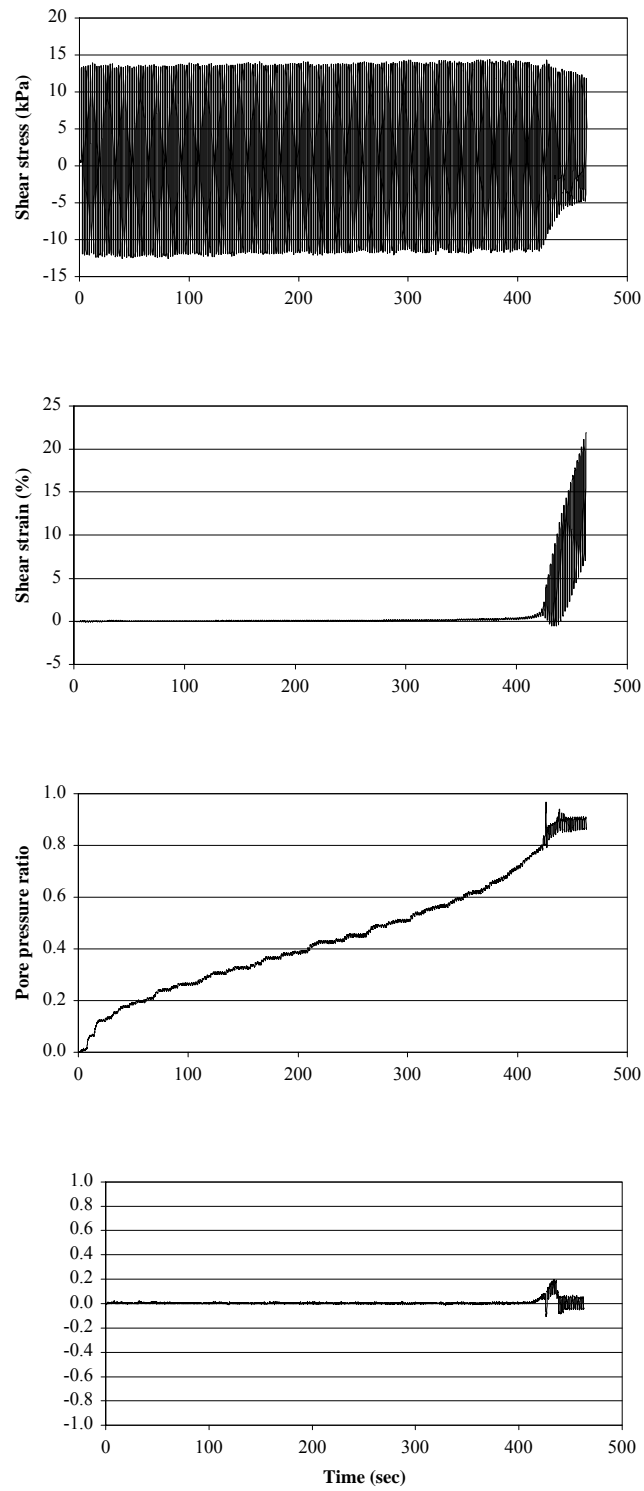


Figure D.5 High-density test results, HD-3.

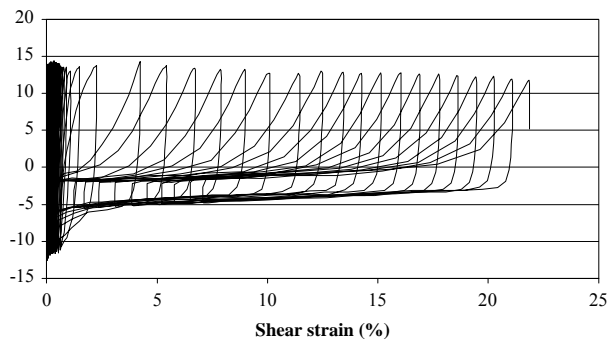


Figure D.6 Shear stress-strain results, HD-3.

for the low-density tests and one for the high-density tests. A single linear trend appears to be adequate for relative densities of 26% or less. On the other hand, the data is less conclusive for the denser specimens. A linear trend is suggested for relative densities based on the 81% and 88% tests, but clearly such a trend does not agree well with the other two tests.

Thus it would appear that the precise initial specimen density near the maximum value is much more critical in controlling the onset of liquefaction than is the initial specimen density near the minimum value. Of course, these observations are preliminary and fail to encompass a large range of CSR values. It is well known that for most sands the relationship between CSR and number of cycles to failure, at constant density, is nonlinear (see for example Kramer, 1996; Finnien et al., 1999). Nonetheless, Figure D.7 shows the same general increase in liquefaction resistance with increase in material density than the Kramer (1996) and Finnien et al. (1999) studies and countless others.

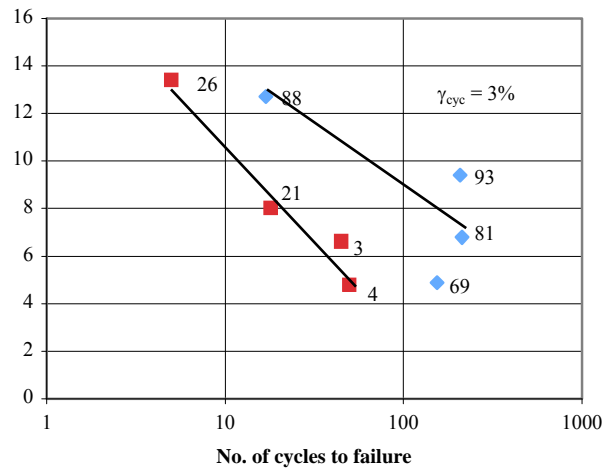


Figure D.7 CSR versus number of cycles to failure (N_L)

D.4 Shear Modulus Reduction

Of importance to the modeling of cyclic stress-strain behavior is the degradation of shear modulus that occurs as the material softens when it is subjected to repeated cycles of loading. This degradation is gradual at low shear strain amplitudes, but accelerates dramatically as liquefaction is approached (Seed and Idriss, 1970). Modulus reduction curves are typically plotted as a function of number of load cycles or shear strain. Results from the high density test HD-3 and the low density test LD-3 are combined in Figure D.8. Although both tests appear to begin with somewhat similar values of the shear modulus during the first few cycles, this may not necessarily be the case since it is difficult to determine the shear modulus accurately at low shear strains. In any case, values soon become divergent at higher strains, with the dense specimen indicating larger stiffness at equivalent number of cycles, as expected. Results from other studies have indicated an inverted ‘S’-shape correlation between shear modulus and shear strain, as opposed to the linear trend that is noted in Figure D.9. If the results were to be plotted as a function of shear strain instead of number of cycles, this would indeed be the case for our experimental data since accumulated shear strains within a single cycle increase progressively with the

number of total cycles. Nonetheless, the data in Figure D.8 indicates approximately 60 to 80% reduction in stiffness at the end of each test.

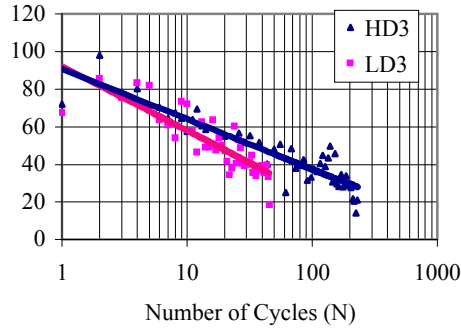


Figure D.8 Shear modulus degradation for high and low density tests

D.5 Cyclic Nonlinear Model

The hysteretic nature of soil is such that shear modulus varies not only from cycle to cycle, but also within a single loading iteration (Figure D.9). This makes development of cyclic nonlinear models particularly difficult. A variety of such models have been proposed in the literature, consisting usually of (a) a backbone curve, and (b) a series of rules governing the stress-strain behavior during both the loading and unloading phases within a full load cycle (Kramer, 1996). One of the simplest expressions that can be assumed is given by the following hyperbolic equation:

$$\frac{\tau - \tau_r}{2} = \frac{G_{mn} \left(\frac{\gamma - \gamma_r}{2} \right)}{1 + \frac{G_{mn}}{\tau_{mn}} \left(\frac{\gamma - \gamma_r}{2} \right)} \quad (\text{D-2})$$

where γ is shear strain, τ is shear stress, γ_r is the reversal shear strain at the top or bottom of the load cycle, τ_r is the reversal shear stress at the top or bottom of the load cycle, G_{mn} is the maximum (low-strain) shear modulus for cycle n at the top or bottom of the loop, and τ_{mn} is the estimated shear strength for load cycle n , obtained from extending the hyperbolic backbone curve to where it becomes horizontal (Figure D.9).

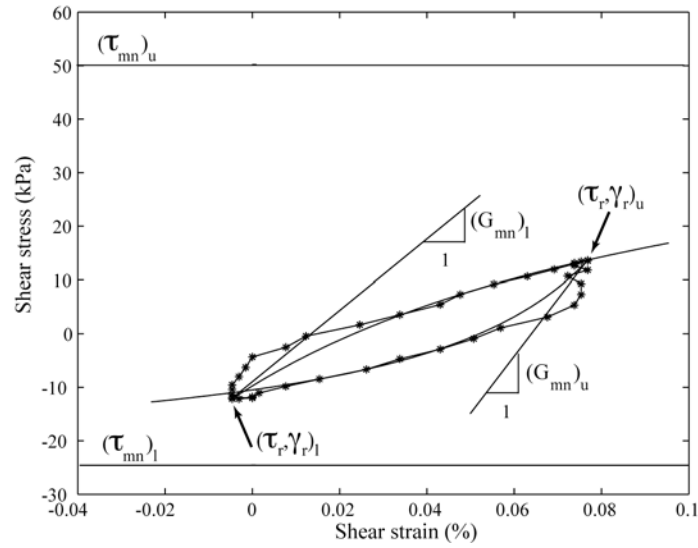


Figure D.9 Model parameters illustrated in conjunction with experimental data for cycle $N=8$, test LD-3.

This model can be used to predict the experimental results, as shown for example in Figure D.10 for test LD-3. The predictions in Figure D.10b were made by estimating both loading and unloading values of G_{mn} and τ_{mn} for each cycle using Equation (D-2). Multiple values of G_{mn} and τ_{mn} were estimated using several pairs of experimental shear strain γ and shear stress τ (Figure D.9), and the results averaged to arrive at single values of G_{mn} and τ_{mn} for each the loading and unloading phases of every cycle, respectively. Equation (D-2) was then used to predict the stress-strain behavior for the entire test, as shown in Figure D.10b.

As expected, the model is able to capture the accumulation of permanent shear strain that occurs as the test progresses. The predictions are relatively reasonable during the first 10 cycles or so, especially with regard to stiffness. However, as the test specimen approaches liquefaction, the shape of the hysteretic loops tends to grow in width, which of course is an indication that the material undergoes ever more damping. The model is not able to properly predict the stress-strain behavior at this stage. More sophisticated models and/or more careful loading and unloading paths, other than the simple *Masing*-type rules implicit in Equation (D-2), need to be worked out,

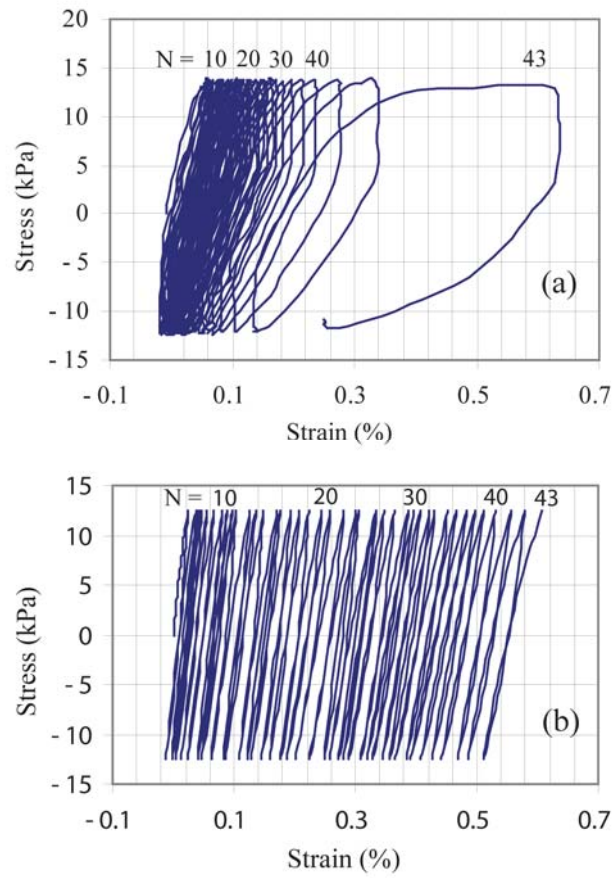


Figure D.10 (a) Test results, LD-3; (b) predictions for test LD-3

The model given by Equation (D-2) does not allow for the effects of volume change due to shearing that can lead to dilation or contraction under drained conditions, or to pore pressure changes when drainage is not allowed. In order to account for pore pressure changes that developed during the tests in this study (given the undrained test conditions that were imposed), it is necessary to resort to a separate equation. A useful relationship for pore pressure ratio r_u is the one proposed by Lee and Albaisa (1974) and DeAlba et al. (1975), which was developed specifically for stress-controlled cyclic tests:

$$r_u = \frac{1}{2} + \frac{1}{\pi} \sin^{-1} \left[2 \left(\frac{N}{N_L} \right)^{1/\alpha} - 1 \right] \quad (D-3)$$

Here N is the number of cycles, N_L is the number cycles to reach liquefaction, and α is a material constant that is a function of soil properties and test conditions.

Predictions using this equation are compared to the experimental data for tests LD-3 (Figure D.11) and HD-3 (Figure D.12). In each case an optimum value of α was sought. The correlation is quite good in both cases, which suggests that Equation (D-3) is a reasonable means of predicting pore pressure. The parameter α is obviously dependent on density. In this case it varies between 0.45 for a loose configuration and 0.75 for a dense one.

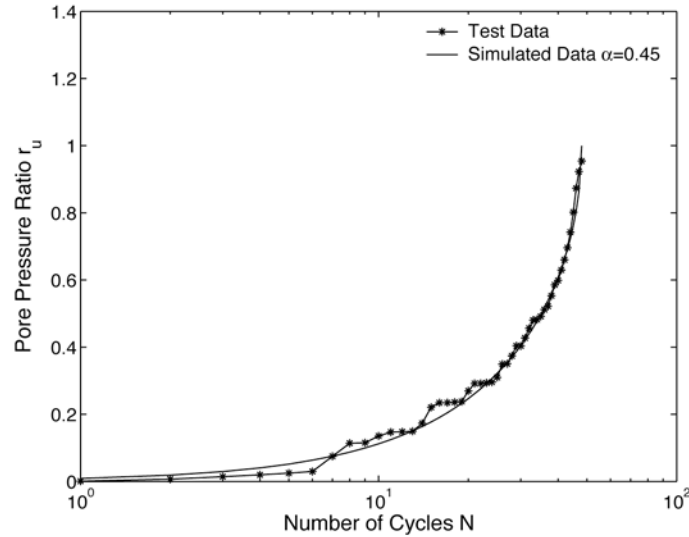


Figure D.11 Pore pressure ratio data and prediction, test LD-3

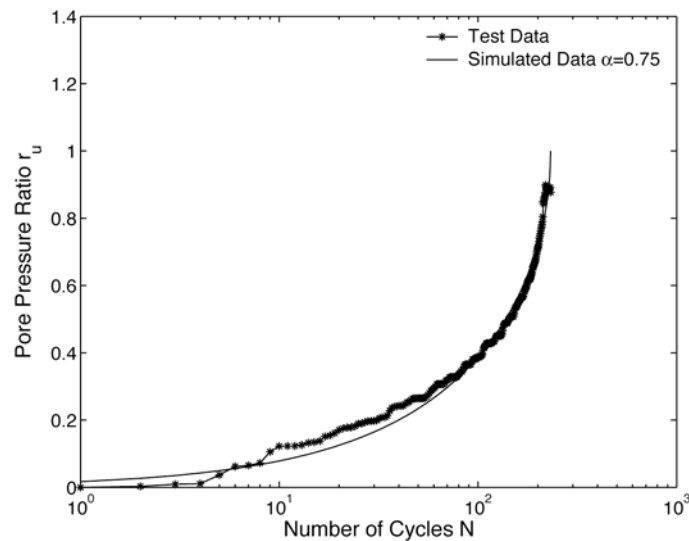


Figure D.12 Pore pressure data and prediction, test HD-3

The nonlinear model represented by Equations (D-2) and (D-3) accounts for some of the most important characteristics of granular soil response under cyclic loading. It can easily be incorporated into finite element codes for use in geotechnical engineering work. In particular, this simple model allows for the development and dissipation of pore pressures that are known to occur during and after earthquake shaking. Nonlinear phenomenological cyclic models of this type are quite useful for evaluating liquefaction hazards and they represent a marked improvement over simpler equivalent linear models. Yet they do not include the level of sophistication of more thorough elastoplastic models (which however require extensive and often difficult material characterization). Nonetheless, they represent a reasonable compromise for limited ranges of soil types and loading conditions (Brandes, 2002).

D.6 Conclusions

A series of cyclic, constant shear stress amplitude tests were conducted on an offshore sand from Florida in order to examine stress-strain behavior at constant volume. Undrained conditions are often prevalent in insitu deposits during the period of earthquake shaking. Specimens were prepared at low and high densities. As expected, the results indicate a strongly nonlinear behavior characterized by stiffness reduction and damping with accumulating shear strain. This degradation occurs faster in the low-density specimens.

A nonlinear constitutive model is examined in light of the test results, consisting of a hyperbolic stress-strain relationship and an empirical exponential-type expression for excess pore pressure. This model does a reasonable job of predicting the shear and pore pressure response for the first few cycles, but the shear strain predictions becomes less satisfactory as large numbers of load cycles accumulate and liquefaction is approached.

D.7 References

Brandes, H. G. (2002). Chapter 7: Geotechnical and Foundation Aspects. CRC

Earthquake Engineering Handbook. W.-F. Chen and C. Scawthorn: 7.1-7.61.

DeAlba, P., C. K. Chan, et al. (1975). Determination of Soil Liquefaction Characteristics by Large-Scale Laboratory Tests. Report EERC 75-14, Earthquake Engineering Research Center, University of California, Berkeley.

Dyvik, R., T. F. Zimmie, et al. (1983). Cyclic Simple Shear Behavior of Fine Grained Soils. Norwegian Geotechnical Institute Publication No.149. Oslo.

Finnie, I., B. Hoppers, et al. (1999). Cyclic Simple Shear Behavior of a Carbonate Sand. Proc. Second Int. Conf. Eng. For Calcarous Seds.

Kramer, S. (1996). Geotechnical Earthquake Engineering. Upper Saddle River, Prentice Hall.

Lee, K. L. and A. Albaisa (1974). "Earthquake Induced Settlements in Saturated Sands." Journal of the Soil Mechanics and Foundations Division, ASCE **100**(GT4).

Seed, H. B. and I. M. Idriss (1970). Soil Moduli and Damping Factors for Dynamic Response Analyses. Report EERC 70-10, Earthquake Engineering Research Center, University of California, Berkeley.

Appendix E

Failure and Post-Failure Mechanics of Submarine Landslides

Brandes, H.G. and Wang, S. (2004)

Proceedings, *23rd International Conference on Offshore Mechanics and Arctic Engineering*, OMAE 2004-51141, pp. 1-8.

Abstract

Theoretical contexts for each of the stages associated with underwater landsliding can be postulated with reasonable confidence, although specific constitutive models require additional work. Also still missing is a comprehensive numerical framework for predicting displacement fields from small pre-failure and post-depositional sediment volume changes and distortions to large-scale inertial sediment wasting.

E.1 Introduction

Mass wasting is a common occurrence in virtually every type of ocean margin environment, contributing to complex sedimentary sequences well into the deep ocean. Although new surveying technologies allow mapping of underwater slides with an unprecedented level of detail, our ability to model initiation and post-failure wasting process are not yet mature enough to make the type of reliable predictions that are required by the oil industry, the military, tsunami modelers, or those dealing with hazard assessment. In particular, much remains to be done to understand and properly model the post-failure, large-scale deformations that accompany mass wasting in the ocean.

The most dramatic form of submarine slope instability involves large-scale slumps and slides that can involve the displacement of vast amounts of sediments. Indeed, the largest slope failures on earth appear to have occurred on continental margins (Varnes 1958; 1978). For example, Heezen and Drake (1964) report on a massive slump that accompanied the 1929 Grand Banks earthquake, which resulted in multiple telephone cable breaks. The affected area spread over 27,000 km² of upper and lower continental slope. There is also evidence of an ever larger failure complex located off South Africa (Dingle 1977). Moore (1978) presents an overview of the world-wide evidence for large-scale submarine slides and slumps. He finds that the associated mass wasting constitutes a significant mechanism for the transport of sediment from the shelf to the deep ocean and is important in shaping the continental slope, especially during periods of glacially lowered sea level when the sediment load from rivers and streams is deposited near the edge of the continental slope. For example, it is estimated that the Atlantic margin adjacent to Cape Hatteras shows evidence of Pleistocene mass wasting affecting 30% to 40% of the slope and rise (Pratson and Laine 1989).

In addition to large-scale failures, there is also ample evidence of smaller sediment displacements and distortions that are sometimes almost imperceptible, i.e. barely discernible from acoustic records. These include local, minor slumps on steep, otherwise stable slopes, intermittent local slumping on gentle slopes, as well as slow, visco-plastic distortions that may be precursors of larger slides and slumps (Bjerrum 1967; Skempton 1964; Terzaghi 1957). An example is shown in Figure E.1, where it is surmised that limited deformations along a weak layer, possibly a soft clay or gassy interval, have resulted in tensile stresses in the overlying deposit, which in turn has begun to fault at the indicated location. It is conceivable that the upper unit may eventually slide with a failure plane developing in the weak layer.

Underwater landslides have a number of causes that can be of a geological, morphological, physical, or even human nature (Alexander 1992; Cruden and Varnes 1996; Locat and Lee 2002). However, only one trigger is generally associated with each landslide. A trigger is an external stimulus that results in the almost-immediate increase in

stresses or reduction in strength, leading to a rapid increase in the rate of downslope displacements (Wieczorek 1996). However, not all landslides are associated with a well-defined trigger. In some instances failure may be the result of long-term physical or chemical processes that lead to a gradual reduction in stability. Possible causes and triggers that can lead to underwater landslides are listed in Table E-1. Waves and tides only play a role in relatively shallow water. This leaves earthquakes as the only trigger mechanism in deep water where cause and effect occur in short order. Given the relatively slow pace at which most of the listed processes take place, it is of special importance to focus on the role that earthquakes play in underwater landslides, at least in seismically prone environments.

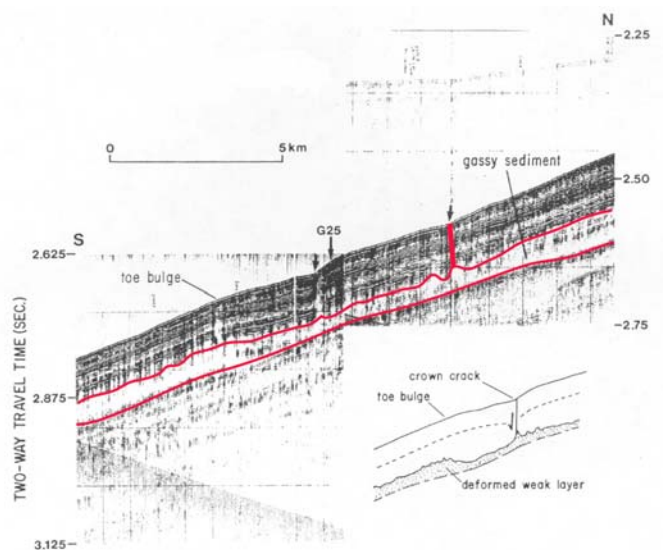


Figure E.1 Limited distortion of continental slope sediments.

Failure of slope deposits occurs when down-slope shear displacements exceed a certain threshold. This is often, but not always, accompanied by a sudden increase in the rate of movement of the displacing mass. However, there are no generally accepted criteria for the onset of failure in terms of deformation. Instead, a stress-based limit equilibrium approach is often used. Although usually satisfactory for engineering purposes, limit equilibrium methods neglect the role that deformations play and needlessly separate the issue of failure from that of pre- and post-failure deformations and displacements. In

order to model the continuum of behavior from a pre-failure state to post-failure conditions (including also the possibility of large displacements and changes in material constitution), it is necessary to consider the nonlinear mechanics of quasi-static soil, as well as the dynamic behavior of accelerated soil and mixed media. In this article we review essential aspects of soil behavior in an effort to develop an integrated model with a focus on soil deformation and seismic response.

Table E-2 Underwater landslide causes and triggers.

Causes/Processes	Triggers
Sedimentation	Earthquakes
Undercutting	Waves
Tectonic steepening	Tides
Volcanic island growth	
Salt diapirism	
Gas expansion/migration	
Glaciation	
Sediment diagenesis	
Fluid seepage	
Hydrocarbon mining	
Other human activities	

E.2 Pre-Failure Deformations

The shear and strength behavior of sediments on submarine slopes depends on the type and state of the material, as well as on its drainage and volume change characteristics. A distinction among soil types is usually made between fine-grained soils of low permeability that may also be cohesive, such as clays and some silts, and coarser-grained soils of substantially higher permeability that are purely frictional (granular) in nature, such as sands, gravels and some silts. Sediments found in the marine environment include all of these types, although they tend to decrease in size from the shoreline to the deep water (Poulos 1988).

The most important attributes of pre-failure soil deformation can be understood with reference to Figure E.2. Granular soils that exist in a loose configuration will tend to undergo volume reduction upon loading if drainage permits it, or they will develop positive pore pressures if fluid is effectively prevented from draining. On the other hand, dense granular soils will tend to dilate or develop negative excess pore pressures depending upon drainage conditions. In all cases though, experiments indicate that upon sufficient straining, soils will achieve a steady-state condition where shearing can continue virtually indefinitely under conditions of constant shear stress and constant effective confining pressure at constant volume and velocity (Casagrande 1940; Poulos 1981). At this point any vestiges of soil structure and loading/strain path have been erased and the effective confining stress becomes a function of the initial density only (though there may be some differences for extensional versus compressional modes of loading). Steady state also occurs for clays in drained shear when the ‘residual’ shear strength is reached at very large strains. It can also be reached under undrained conditions at large shear strain when the strength has dropped to its remolded value. Overconsolidated clays behave in a qualitatively similar fashion to dense sands (Figure E.2).

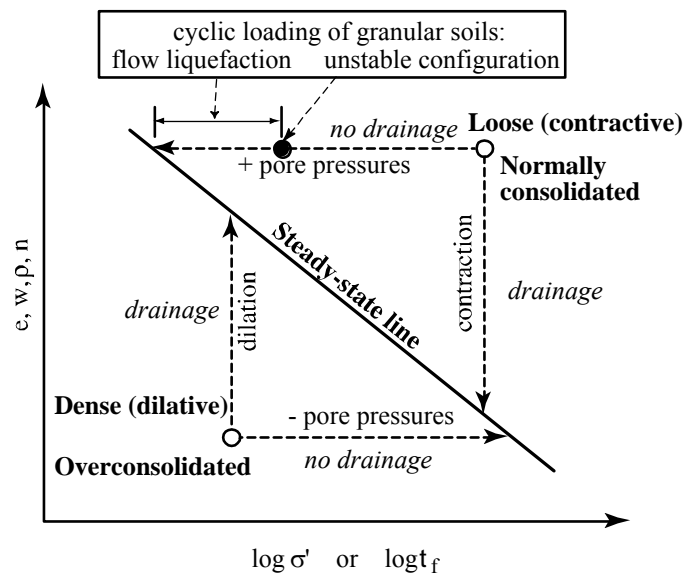


Figure E.2 Conceptual soil behavior up to steady-state.

Loading can be either monotonic or cyclic. In the case of loose granular soils, an unstable condition may be reached prior to the steady-state condition if the material is loaded

under cyclic conditions, for example due to propagating seismic shear waves resulting from an earthquake. The shaking from shear waves is usually fast enough so that undrained conditions prevail. If the soil is in a loose condition, it will attempt to densify. However, the usual short-term lack of drainage will result in a transitory build up of excess pore pressures and a reduction in effective confining stress. If the stress path reaches what is known as the flow liquefaction surface (which is represented by a single point on the undrained path illustrated in Figure E.2), pore pressure and shear strains will accelerate dramatically and strength will be reduced substantially until the steady-state conditions is reached. Again, if strength drops below the gravity-driven shear stress resulting from the overburden soil, large deformations associated with failure will follow.

Such a liquefaction condition can only be achieved if the granular soil is sufficiently loose to begin with, i.e. the soil is initially located to the right of the steady-state line. That is not to say that significant deformations cannot be obtained under conditions short of liquefaction. Cyclic mobility and ratcheting-type spreading of slope deposits in the presence of a biased gravity shear stress can be quite substantial and can cause significant damage to rigid structures such as platforms and oil pipelines, regardless of whether the soil is initially in a loose or dense state. Seismic loading of cohesive fine-grained soils can also lead to substantial pre-failure deformations and loss of strength, but not to liquefaction. These pre-failure deformations, which are for the most part irreversible, depend on the mode of loading and the character of the material. Given the important role that earthquakes are thought to play in triggering underwater landslides in seismically active regions of the world, we focus in this section on the cyclic behavior of marine sediments.

Prediction of small to moderate deformations during cyclic loading of cohesionless sediments is difficult and estimates using existing methodologies can be off by a factor of 2 or more (Seed et al. 2001). The complexity of predicting small to moderate deformations during cyclic loading can be appreciated in Figure E.3, which shows the results of undrained cyclic simple shear tests conducted on Monterey #30 sand. Within a given cycle, pore pressures are seen to fluctuate in response to repeated softening and

stiffening tendencies as shear strain varies. This type of behavior has been well documented, but remains problematic to model reliably. At higher densities, the exact onset of liquefaction is harder to discern since a relatively abrupt transition in overall behavior (as observed in Figure E.3) is usually absent. In the case of slopes, the presence of a gravity shear stress in the down-slope direction complicates the behavior even further. Figure E.4 shows the results of tests for the same sand, but in this case subjected to a preferential shear stress applied in the same direction as the cyclic loading. Not only are similar stiffening and softening tendencies observed, but in this case shear strains accumulate preferentially in the direction of load application. Slope deposits that are shaken in the cross-slope direction may respond in an even more detrimental fashion, for example by liquefying sooner when loaded at equivalent intensities and frequencies (Boulanger and Seed 1995). However, data is still relatively scarce for this mode of loading and reliable models have yet to be developed. Behavior due to multi-directional shaking represents an even greater unknown and is difficult to simulate using standard laboratory equipment. These shortcomings represent a troubling state of affairs if one considers that during an earthquake slopes are likely to be subjected to ground motions in more than just the down-slope direction.

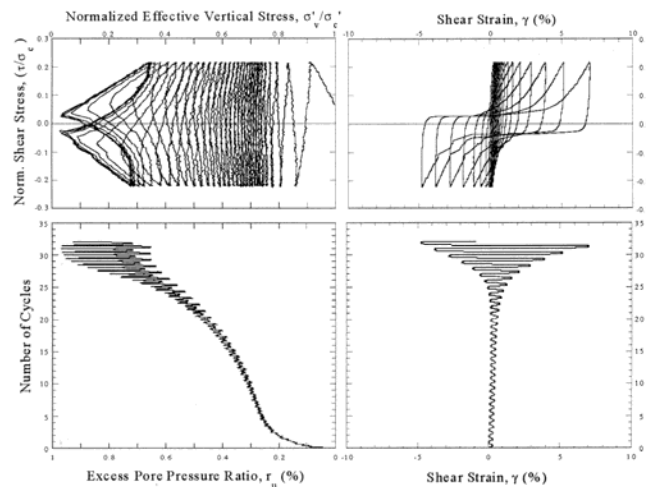


Figure E.3 Undrained cyclic behavior of quartz sand, $D_r=50\%$, $CSR=0.22$, no initial driving stress (Seed et al., 2001).

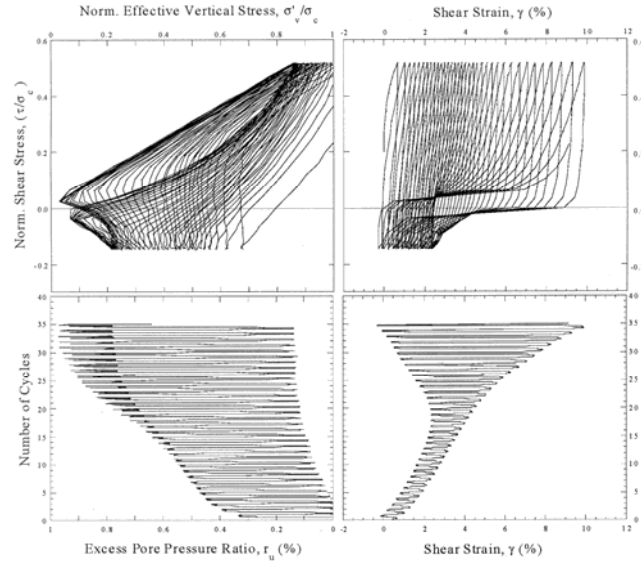


Figure E.4 Undrained cyclic behavior of quartz sand, $D_r=50\%$, $CSR=0.22$, no initial driving stress (Seed et al., 2001).

Three general approaches can be considered for modeling the pre-failure behavior of sediments: elasto-plastic coupled analysis using any of a number of constitutive models, nonlinear cyclic modeling, and simple empirical prediction. Although advanced constitutive models such as the ones described above are based on well-accepted theoretical principles and are thus appealing from a conceptual point of view, they are often impractical to implement since their description usually involves many material parameters, some of which can be difficult to obtain. Nonlinear cyclic models offer the benefit of a simpler approach that typically requires fewer material constants. The basic features of nonlinear soil behavior can still be captured as long as an effective stress approach is used that takes into account progressive degradation of stiffness and strength of soil as a result of overall pore pressure accumulation. The numerical procedure also must account for simultaneous pore pressure dissipation due to drainage. Finn et al. (1977) presented an early model along these lines that has received a fair amount of attention over the years. More recently, Liyanathirana and Poulos (2002a; 2002b) modified this model somewhat and tested it, with moderate success, for field response during the 1995 Kobe earthquake and a centrifuge test of a level sand deposit conducted by Abdoun et al. (1997).

During the initial loading phase, the stress-strain response can be described by:

$$\tau = \frac{G_{m0}\gamma}{1 + \frac{G_{m0}\gamma}{\tau_{m0}}} \quad (\text{E-1})$$

in which τ is the shear stress corresponding to a shear strain of γ , G_{m0} is the initial maximum tangent modulus, and τ_{m0} is the maximum shear stress the sand can bear without failure. As suggested by Finn et al. (1977), G_{m0} and τ_{m0} can be calculated by equations developed by Harding and Drnevich (1972). For horizontal sand layers:

$$G_{m0} = 14,760 \times \frac{(2.973 - e)^2}{1 + e} \left(\frac{1 + 2K_0}{3} \right)^{\frac{1}{2}} (\sigma_v^n)^{\frac{1}{2}} \quad (\text{E-2})$$

$$\tau_{m0} = \left[\left(\frac{1 + K_0}{2} \sin \phi^n \right)^2 - \left(\frac{1 - K_0}{2} \right)^2 \right]^{\frac{1}{2}} \sigma_v^n \quad (\text{E-3})$$

where e stands for void ratio (less than 2.0), σ_v^n for vertical effective stress, K_0 for coefficient of lateral earth pressure at rest, and ϕ^n for effective angle of friction. The equations require units of pounds and feet. Maximum shear modulus and maximum shear stress vary from cycle to cycle to allow for softening behavior. For the n^{th} cycle:

$$G_{mn} = G_{m0} \left(1 + \frac{\varepsilon_{vd}}{H_1 + H_2 \varepsilon_{vd}} \right) \left(\frac{\sigma_v^n}{\sigma_{v0}^n} \right)^{\frac{1}{2}} \quad (\text{E-4})$$

$$\tau_{mn} = \tau_{m0} \left(1 + \frac{\varepsilon_{vd}}{H_3 + H_4 \varepsilon_{vd}} \right) \frac{\sigma_v^n}{\sigma_{v0}^n} \quad (\text{E-5})$$

in which ε_{vd} is the accumulated vertical strain, σ_{v0} is the initial vertical effective stress, and H_1 through H_4 are material constants. If loading reversal occurs at (γ_r, τ_r) , subsequent loading-unloading cycles can be described by replacing τ and γ in Equation (E-1) by $(\tau - \tau_r)/2$ and $(\gamma - \gamma_r)/2$, respectively. Also, G_{m0} and τ_{m0} are replaced by their values during the n^{th} cycle, i.e. G_{mn} and τ_{mn} . Thus the stress-strain response is given by:

$$\tau - \tau_r = \frac{\gamma - \gamma_r}{\frac{1}{G_{mn}} - \frac{\gamma - \gamma_r}{2\tau_{mn}}} \quad (\text{E-6})$$

As already mentioned, undrained conditions are likely to prevail during earthquake

shaking. If the sediment has a tendency to undergo volume reduction, then excess pore pressures are generated since drainage is temporarily prevented. The increase in pore pressure, assuming an infinite bulk modulus for water, can be described according to the model of Martin and Seed (1979):

$$\Delta u = E_r \Delta \varepsilon_{vd} \quad (\text{E-7})$$

where $\Delta \varepsilon_{vd}$ is the incremental vertical strain during the n^{th} cycle. The one-dimensional rebound modulus of sand, E_r , can be estimated as follows:

$$E_r = \frac{(\sigma_v^n)^{1-m}}{mk_2} (\sigma_{v0}^n)^{n-m} \quad (\text{E-8})$$

$$\Delta \varepsilon_{vd} = C_1 (\gamma - C_2 \varepsilon_{vd}) + \frac{C_3 \varepsilon_{vd}^2}{\gamma + C_4 \varepsilon_{vd}} \quad (\text{E-9})$$

where C_1 through C_4 , k_2 , m and n are experimental constants.

Predictions using this model are shown in Figure E.5 and Figure E.6, assuming typical material values for a saturated sand (Table E-3). Figure E.5 corresponds to an initial loading from $\tau/\sigma'_{v0}=0$ to $\tau/\sigma'_{v0}=0.058$, followed by unloading and reloading between $\tau/\sigma'_{v0}=0.058$ and $\tau/\sigma'_{v0}=-0.058$. The effect of an initial shear stress is explored in Figure E.6. Here the specimen is loaded monotonically to an initial shear stress of $\tau/\sigma'_{v0}=0.029$ ($\gamma=0.01\%$), and then cycled about that shear stress with an amplitude of $\tau/\sigma'_{v0}=\pm 0.058$.

The model predicts the general hysteretic behavior of sand leading up to liquefaction ($u/\sigma'_{v0}=1.0$, Figure E.5). Stiffness reduction is associated with the continuing accumulation of pore pressure and loss of effective confining stress. As expected, large shear strains follow when liquefaction is approached. However, the model does not correctly predict the dual softening-stiffening behavior within each half-cycle that is observed at large shear strains in experimental tests such as the one in Figure E.3. This type of response is well known (Seed et al. 2001), but no reliable cyclic model is yet available to predict it.

Predictions in Figure E.6 for the case of cyclic loading about an initial shear stress

($\tau/\sigma'_{vo}=0.029$) are less satisfactory. Virtually the same stress-strain response is observed as in Figure E.5, except that individual curves are shifted upward or sideways. In other words, the model is not able to capture the dramatically different experimental response of Figure E.4, where substantial re-hardening is observed within one half of each loading cycle. Obviously, nonlinear cyclic models need further development before they can be applied to accurately predict small pre-failure strains.

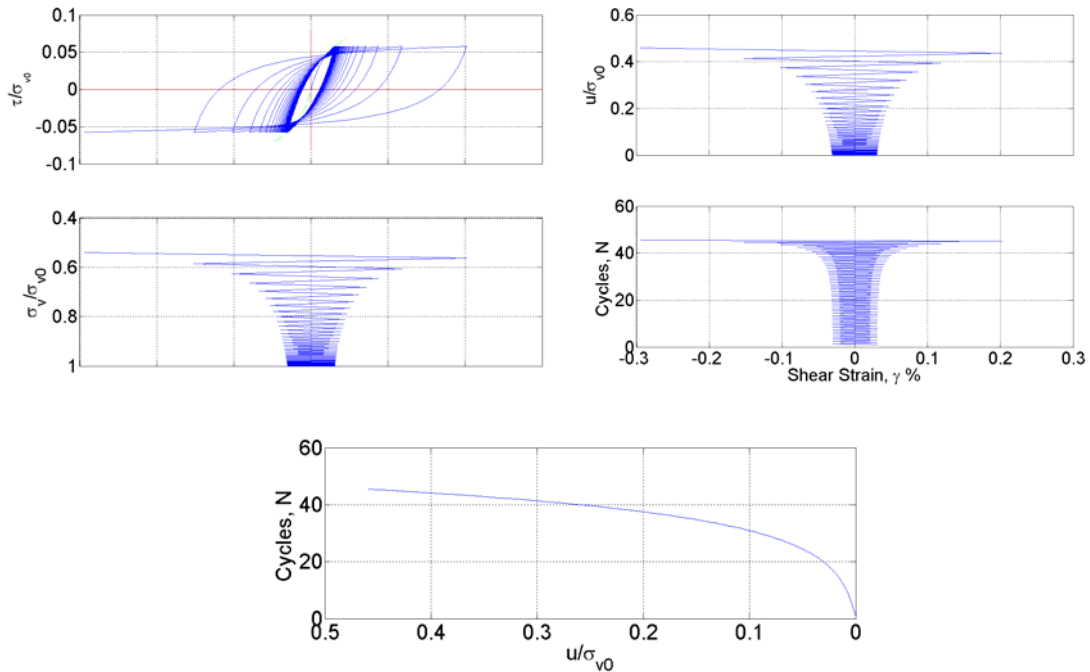


Figure E.5 Model predictions for case of no bias in cyclic shear stress.

Table E-3 Material constants for cyclic model.

Parameter	Value	Parameter	Value
H_1	10	C_1	0.8
H_2	2	C_2	0.79
H_3	5	C_3	0.5
H_4	5	C_4	0.73
k_2	0.25	m	0.23
n	0.36	e	1.0
ϕ'	25°	σ'_{vo}	4,500 psf
ϵ_{vo}	0.01%		

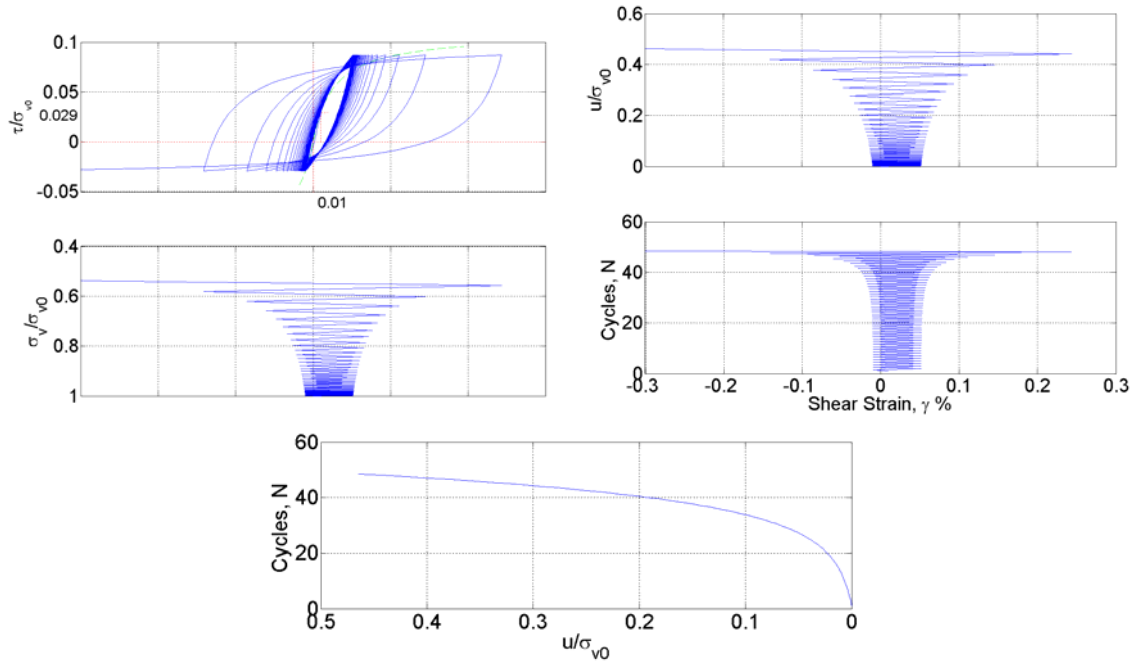


Figure E.6 Model predictions for case of cyclic loading with initial conditions

$\tau/\sigma'_{vo}=0.029$ and $\gamma=0.01\%$.

Although the above description is particularly relevant to coarse sediments with a tendency to undergo volume reduction upon cyclic loading, a similar model may also be postulated for fine-grained sediments. The major difference is that no significant pore pressure develops in these soils and softening/hardening behavior, if any, would have to be due to other mechanisms.

Regardless of the soil type, its state, or the loading mode, a critical condition will eventually be reached where shear deformations can continue unabatedly if the driving shear stress is sufficient. This is likely to correspond closely to the steady-state condition discussed earlier and represents the onset of failure. Pre-failure deformations, whether in cohesive or granular soils, can result in the significant accumulation of strains, leading to sediment displacements that may be of a scale that may be apparent in subbottom acoustic records. It is not yet clear though if these types of pre-failure soil distortions are responsible for the acoustically transparent intervals that are observed in some subbottom slope records, as for example in Figure E.1.

E.3 Failure Mechanics

Failure is usually associated with the onset of very large shear displacements that in slopes can lead to slides, slumps, and flows. Due to the difficulty in predicting pre-failure strains and establishing failure criteria based on these deformations, a much simpler approach based on stress limit equilibrium concepts is typically used instead. However, a more precise failure condition can be postulated based on soil sediment reaching the steady state condition *and* destabilizing stresses exceeding the steady-state strength. If both conditions are reached, and if at least one failure surface can be mobilized through the soil deposit, then the failed sediment mass can move along such a surface in the downslope direction until equilibrium is reestablished. Deformations prior to such a state would be modeled using conventional soil elasto-visco-plasticity, perhaps along the lines of what is discussed in the previous section. Deformations beyond failure would be modeled according to viscous and mixed fluid-grain concepts, as is outlined in the next section.

The steady-state condition could be reached by loading due to processes other than liquefaction under undrained conditions (Figure E.2). For example, sediment deposition that results in steepening of a slope would produce volume reduction due to consolidation of the sediment, but would also increase the driving stress. The general stress path for contractive sediment would be to the right and downward of the initial condition depicted in Figure E.2. Similarly, gas expansion at depth is likely to take place under undrained conditions, with a corresponding increase in excess pore water pressure and decrease in strength (i.e. it would follow an undrained path in Figure E.2). Tides over a fine-grained seabed may lock in excess pore pressures and lead to failure due to a reduction in strength along an undrained path, much the same way as the sudden drawdown of a reservoir can lead to failure of the upstream embankment if pore water is not allowed to dissipate quickly enough.

E.4 Modeling of Post-Failure Displacements

Once a steady state condition is reached and driving stresses exceed the steady state strength, soil above the mobilized failure surface begins to move downslope with inertia playing a crucial role. In addition, sediment that displaces at a substantial velocity may interact with the surrounding water and change its state by exchanging mass and momentum with the surrounding water and the seabed.

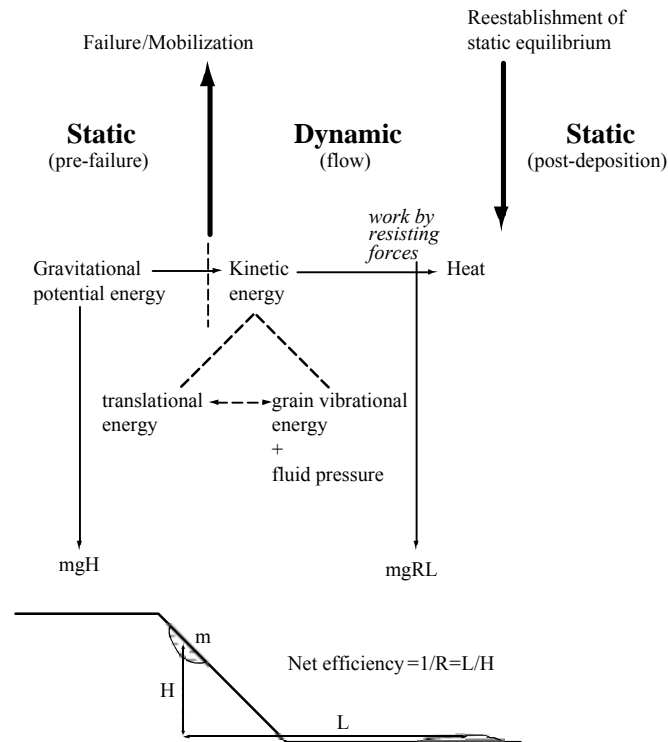


Figure E.7 Bulk energy considerations during landsliding.

The range of sliding processes from the pre-failure state to the final condition, when the wasted mass comes to a rest and reestablishes static equilibrium, is best viewed with respect to energy principles (Figure E.7). Sediment mobilization that occurs as failure is triggered involves a transformation of gravitational potential energy into kinetic energy. As sediment attains significant speed it may break up and become agitated. Thus a portion of the translational energy is converted into random internal vibration energy and fluid pressure. The rate of interchange (back and forth) can vary as the sliding proceeds.

Eventually though all energy is wasted and the sediment mass comes to a halt. A variety of approaches can be used to model the kinematics of post-failure displacements: viscoplastic modeling, grain flow theory, dimensional analysis, continuum mixture theory (steady and unsteady), and hydraulic modeling (Iverson 1997; Iverson et al. 1997). Of these, continuum mixture theory and hydraulic modeling are the most promising ones.

Momentum transport for grain-fluid mixtures involves the following important processes: inertial grain collisions, grain contact friction, viscous shear, inertial (turbulent) fluid velocity fluctuations and solid-fluid interactions. The amount of sediment disassociation that occurs as flow attains significant momentum can be characterized using the concept of granular temperature:

$$T = \langle \mathbf{v} \mathbf{n}_s^2 \rangle = \langle (\mathbf{v}_s - \bar{\mathbf{v}}_s)^2 \rangle \quad (\text{E-10})$$

This quantity arises from conversion of translational energy as grains shear along irregular surfaces. It leads to sediment dilation, dispersion, and reduced density and flow mobility. General conservation laws can be postulated for mixtures of solids and fluid fractions as follows.

Mass conservation:

$$\begin{aligned} \partial(\rho_s \nu_s) / \partial t + \nabla \cdot (\rho_s \nu_s \mathbf{v}_s) &= m_s & - \text{solids} \\ \partial(\rho_f \nu_f) / \partial t + \nabla \cdot (\rho_f \nu_f \mathbf{v}_f) &= m_f & - \text{fluid} \end{aligned} \quad (\text{E-11})$$

Momentum conservation:

$$\begin{aligned} \rho_s \nu_s [\partial \mathbf{v}_s / \partial t + \mathbf{v}_s \cdot \nabla \mathbf{v}_s] &= \\ \nabla \cdot \mathbf{T}_s + \rho_s \nu_s \mathbf{g} + \mathbf{f} - m_s \mathbf{v}_s & \quad \text{solids} \end{aligned} \quad (\text{E-12})$$

$$\begin{aligned} \rho_f \nu_f [\partial \mathbf{v}_f / \partial t + \mathbf{v}_f \cdot \nabla \mathbf{v}_f] &= \\ \nabla \cdot \mathbf{T}_f + \rho_f \nu_f \mathbf{g} + \mathbf{f} - m_f \mathbf{v}_f & \quad \text{fluid} \end{aligned}$$

where the subscripts s and f indicate solid and fluid components, ρ stands for density, ν for solid or fluid fraction, \mathbf{v} for velocity, m for mass, t for time, \mathbf{f} for interaction force and \mathbf{T} for stress.

The appeal of these equations is that they can be applied, through suitable approximations, to quasi-static motion as well (i.e. conventional soil mechanics), both prior to failure and

after final deposition. It is therefore conceivable to model the entire spectrum of landsliding from pre-failure to post-failure states with a consistent model that predicts deformations at all levels of distortion. Of course, a suitable numerical framework needs to be developed. It is likely that different numerical techniques will apply to the various kinematic regimes in Figure E.7 (for example, finite element, finite difference, boundary element, Lagrangian cell methods, etc.).

Hydraulic modeling constitutes the state-of-the-art method for modeling fast-moving sediment-fluid flows (debris flows). It uses depth-averaged equations of motion and therefore treats solid-solid and solid-fluid interactions in only a rudimentary way. However, it is able to account for experimentally observed surges (unsteady and non-uniform) with sediment concentrations that are non-homogenous.

E.5 Final Comments

It is often not sufficient to consider underwater landslide failures only from a loading/resistance point of view and thereby neglect sediment mobility altogether. There are many instances when prediction of attendant sediment deformations is essential. For example, the link between underwater landslides and potential tsunamis in current hydrodynamic codes is hampered by a lack of realistic models that describe the shape and initial mobilization of destabilized slope sections. Also, an increasing number of structures, such as oil platforms and drilling equipment, are being placed in vulnerable environments and their performance can be seriously jeopardized by even small or moderate sediment displacements.

Fortunately, a considerable amount of knowledge has been acquired with regard to the conditions necessary to cause underwater landslides and the mechanics of various mass wasting processes. Although this understanding is by no means complete, it is now possible to develop comprehensive numerical models that can provide estimates of the displacement field resulting from particular processes that affect the stability of underwater slopes.

E.6 References

- Abdoun, T., R. Dobry, et al. (1997). Centrifuge and numerical modelling of soil-pile interaction during earthquake induced soil liquefaction and lateral spreading. Geo-Logan '97. Logan, Utah: 76-90.
- Alexander, D. (1992). "On the causes of landslides: human activities, perception, and natural processes." Environmental Geology and Water Sciences **20**(3): 165-179.
- Bjerrum, L. (1967). "The third Terzaghi lecture: progressive failure in slopes of overconsolidated plastic clay and clay shales." Journal of the Soil Mechanics and Foundations Division, ASCE **93**: 1-49.
- Boulanger, R. W. and R. B. Seed (1995). "Liquefaction of sand under bidirectional monotonic and cyclic loading." Journal of Geotechnical Engineering, ASCE **121**(12): 870-878.
- Casagrande, A. (1940). "Characteristics of cohesionless soils affecting the stability of slopes and earth fills." Contributions to Soil Mechanics: 257-276.
- Cruden, D. M. and D. J. Varnes (1996). Chapter 3: landslide types and processes. Landslides: Investigation and Mitigation, Special Report 247. A. K. Turner and R. L. Schuster. Washington, DC, National Academy Press: 36-75.
- Dingle, R. V. (1977). "The anatomy of a large submarine slump on a sheared continental margin (S.E. Africa)." Journal of the Geological Society **134**: 293-310.
- Finn, W. D. L., K. W. Lee, et al. (1977). "An effective stress model for liquefaction." Journal of the Geotechnical Engineering Division, ASCE **103**(6): 517-533.
- Hardin, B. O. and V. P. Drnevich (1972). "Shear modulus and damping in soils; measurement and parameter effects." Journal of the Soil Mechanics and Foundations Division, ASCE **98**(SM6): 603-624.
- Heezen, G. R. and C. L. Drake (1964). "Grand Banks slump." American Association of Petroleum Geologists Bulletin **48**: 221-225.
- Iverson, R. M. (1997). "The physics of debris flows." Reviews of Geophysics **35**(3): 245-296.
- Iverson, R. M., M. E. Reid, et al. (1997). "Debris-flow mobilization from landslides." Annual Review of Earth and Planetary Science **25**: 85-138.
- Liyanapathirana, D. S. and H. G. Poulos (2002a). "A numerical model for dynamic soil liquefaction analysis." Soil Dynamics and Earthquake Engineering **22**: 1007-1015.

- Liyanapathirana, D. S. and H. G. Poulos (2002b). "Numerical simulation of soil liquefaction due to earthquake loading." Soil Dynamics and Earthquake Engineering **22**: 511-523.
- Locat, J. and H. J. Lee (2002). "Submarine landslides: advances and challenges." Canadian Geotechnical Journal **39**: 193-212.
- Martin, G. R. and H. B. Seed (1979). "Simplified procedure for effective stress analysis of ground response." Journal of the Geotechnical Engineering Division, ASCE **105**(GT6): 739-758.
- Moore, D. G. (1978). Submarine slides." Developments in Geotechnical Engineering. Rockslides and Avalanches, 1 Natural Phenomena. B. Voight. New York, Elsevier Scientific Publishing. **14A**: 564-604.
- Poulos, H. G. (1988). Marine Geotechnics. London, Unwin Hyman.
- Poulos, S. J. (1981). "The steady state of deformation." Journal of the Geotechnical Engineering Division, ASCE **107**(GT5): 553-562.
- Pratson, L. F. and E. P. Laine (1989). "The relative importance of gravity-induced versus current-controlled sedimentation during the Quaternary along the mid-east U.S. outer continental margin revealed by 3.5 kHz echo character." Marine Geology **89**: 87-126.
- Seed, R. B., K. O. Cetin, et al. (2001). Recent advances in soil liquefaction engineering and seismic site response evaluation. Proceedings, Fourth International Conference on Recent Advances in Geotechnical earthquake Engineering and Soil Dynamics, Rolla, University of Missouri.
- Skempton, A. W. (1964). "Long-term stability of clay slopes." Geotechnique **14**(2): 77-101.
- Terzaghi, K. T. (1957). "Varieties of submarine slope failures." **25**.
- Varnes, D. J. (1958). Landslide types and processes. Special Report 29: Landslides and Engineering Practice. E. B. Eckel. Washington, DC, HRB, National Research Council: 20-47.
- Varnes, D. J. (1978). Slope movement types and processes. Special Report 176: Landslides: Analysis and Control. R. L. Schuster and R. J. Krizek. Washington, DC, TRB, National Research Council: 11-33.
- Wieczorek, G. F. (1996). Chapter 4: landslide triggering mechanisms. Landslides: Investigation and Mitigation, Special Report 247. A. K. Turner and R. L. Schuster. Washington, DC, National Academy Press: 76-90.

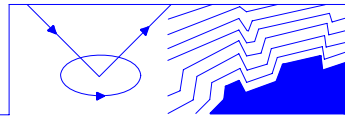
Appendix F

Seismic Refraction and MASW Surveys for Investigation of Subsurface Conditions at Kealakaha Stream Replacement Bridge

Geophysical Investigation by Advanced Geoscience, Inc.

ADVANCED GEOSCIENCE, INC.

Engineering Geology and Geophysics
Subsurface Exploration Non-Destructive Evaluation



716 Yarmouth Road, Suite 207
Palos Verdes Estates, California
90274 USA
Telephone (310) 265-8420
Fax (310) 265-8061
www.AdvancedGeoscience.com

October 30, 2007

University of Hawaii at Manoa
College of Engineering
2540 Dole Street
Holmes Hall 240
Honolulu, Hawaii 96822-2382

Attention: Dr. Horst G. Brandes
Dr. Ian Robertson

**Summary Report
Seismic Refraction and MASW Surveys
For Investigation of Subsurface Conditions
At Kealakaha Stream Replacement Bridge
Island of Hawaii, Hawaii**

INTRODUCTION

This report summarizes the results of the seismic refraction and multi-channel analysis of surface waves (MASW) surveys completed at the referenced site on June 2 and 3, 2007. These surveys were used to prepare subsurface profiles of the seismic compressional-wave and shear-wave velocity layering near the proposed bridge abutments. We understand this information will be used by the University of Hawaii to generate a seismic shear-wave velocity profile along the bridge alignment for computer modeling of earthquake vibration patterns.

The seismic refraction and MASW surveys were recorded along three survey lines, designated as Lines SL-1, SL-2, and SL-3. These survey lines were positioned at the locations shown on the site map in Figure 1. The refraction data recorded along these lines underwent computer processing using tomographic modeling to prepare two-dimensional, subsurface profiles of compressional-wave velocity variations. The MASW data were used to generate separate shear-wave velocity profiles based on modeling of the measured Rayleigh wave (ground roll) phase velocity versus frequency variations.

The site map in Figure 1 shows the starting and ending points of Lines SL-1, SL-2, and SL-3 in relation to the proposed bridge abutments. This map was prepared from the field mapping of the survey line locations provided to us by the University of Hawaii.

The following sections summarize our data collection and processing procedures. A concluding section discusses our interpretation of the seismic velocity layering shown on these profiles and our recommendations for preparing a shear-wave velocity profile along the bridge alignment.

SURVEY PROCEDURES

Data Collection

The survey lines were positioned along relatively straight-line traverses across accessible areas where the ground surface was essentially flat or evenly sloping (Figure 1). Lines SL-1 and SL-2 were positioned on two traverses setup along the highway on each side of the existing bridge. A total of 95 meters (312 feet) of geophone coverage was setup along each of these lines. Line SL-3 was positioned along a shorter, northerly traverse setup in a graded area on the west bank of the stream channel. The total geophone coverage setup along this line was 42 meters (138 feet).

The seismic data were recorded using a Seistronix 48-channel seismic acquisition system with 24-bit analog to digital resolution. This system was connected to linear arrays (or spreads) of geophones spaced 1-meter apart along each line. Lines SL-1 and SL-2 were setup with three overlapping 48-channel geophone arrays, referred to as Spreads 1, 2, and 3. Line SL-3 was setup with one 43-channel geophone array referred to as Spread 1.

The geophones setup along these spreads consisted of single 4.5-Hertz vertical geophones commonly used for refraction and MASW surveys. The geophones were planted into the ground on their attached metal spikes.

The refraction data for Lines SL-1 and SL-2 were recorded separately into Spreads 1 and 3. Seismic waves were generated at several overlapping “shot points” positioned along

each line and recorded into all 48-geophone channels. A pattern of ten shot points was recorded for Line SL-1, and fifteen shot points was recorded for Line SL-2. The first and last shot points were positioned 0.5 meters off the ends of the first and last geophone positions. The remaining shot points were positioned between the geophones at mostly 7-meter intervals.

For the shorter-length Line SL-3, the refraction data were recorded into Spread 1 with 43 geophone channels. A pattern of seven shot points was recorded for this line. These shot points were also spaced at 7-meter intervals.

A 12-pound sledge hammer was used at each shot point to generate seismic waves for both the refraction and MASW data recording. The sledge hammer was used to make multiple impacts on a metal plate placed on the ground surface. The field records from four to as many as ten impacts were summed together to increase the signal-to-noise ratio and overcome background noise vibrations.

The sledge hammer-source MASW data were recorded during a one-second time interval for Lines SL-1, SL-2, and SL-3 using an “end-on” recording configuration. The shot points were positioned off the end of an array of 24 active geophone channels moved along the line at 2-meters intervals. The constant offset from the shot point to the closest active geophone was 5 meters. The shot points started 5 meters off the first geophone position and moved down the line at 2-meter intervals. The first and last shot point positions for Lines SL-1, SL-2, and SL-3 and their corresponding first and last active geophone positions are summarized below.

Line SL-1

First shot point: -2 m
Last shot point: 68 m

Active geophone positions: 3 m to 26 m
Active geophone positions: 73 m to 96 m

Line SL-2

First shot point: -5 m
Last shot point: 65 m

Active geophone positions: 0 m to 23 m
Active geophone positions: 70 m to 93 m

Line SL-3

First shot point: -5 m	Active geophone positions: 0 m to 23 m
Last shot point: 15 m	Active geophone positions: 20 m to 43 m

Passive-source MASW data were also recorded along Lines SL-1 and SL-2 for the evaluation of deeper shear-wave velocity layering. The 48-channel geophone arrays setup along these lines were used to record ground roll vibrations during a 30-second time interval from distant vehicles heading away from one end of the line. The first and last active geophone positions used to record the passive-source MASW records are listed below.

Line SL-1

Spread 1	Active geophone positions: 3 m to 50 m
Spread 3	Active geophone positions: 51 m to 98 m

Line SL-2

Spread 1	Active geophone positions: 0 m to 47 m
Spread 2	Active geophone positions: 24 m to 71 m
Spread 3	Active geophone positions: 48 m to 95 m

Seismic Data Processing and Modeling

The 48-channel seismic refraction field records were used to pick first arrival times for seismic waves traveling through the surface layer and into deeper higher-velocity layers. These first arrival times were used to generate a series of travel time curves from each shot point along Lines SL-1, SL-2, and SL-3. Archived copies of these field records and time curves are available in our project files.

The first arrival time data were input together with geophone stationing and elevations into the computer program RAYFRACT (written by Intelligent Resources, Inc.) to generate an estimated velocity-depth model for Lines SL-1, SL-2, and SL-3. RAYFRACT used the first arrival time picks to conduct refraction tomography imaging of the seismic velocity layering. An initial velocity-depth model was first estimated

using a one-dimensional, smoothed velocity gradient averaged across the line from all the travel time curves. This initial smoothed model was then refined to produce a closer fit to the first arrival time data using the Wavepath Eikonal Traveltime (WET) tomographic inversion method with 200 iterations. This best-fit velocity-depth model was then gridded and contoured with SURFER (written by Golden Software, Inc.) to show estimated lateral and vertical variations. The resulting compressional-wave velocity profiles for Lines SL-1, SL-2, and SL-3 are shown in Figures 2, 3, and 4. For comparison each of these profiles is displayed with a 500 ft/sec contour interval and the same color velocity scale ranging from 500 to 15,000 ft/sec.

The compressional-wave velocity profile for Line 1 shows an area of “lower wave path coverage” on the first half of the line with missing deeper velocity coverage. This is the result of the limited longer-offset travel time coverage through this area caused by poor penetration of the sledge hammer’s seismic energy at certain shot points. The velocity profiles for Lines 2 and 3 do not show significant areas of limited coverage in the centers of these lines.

The MASW data were processed using the latest version of the computer program Surfseis developed by the Kansas Geological Survey. The digital SEG2 format field records from Lines SL-1, SL-2, and SL-3 were input into the program to perform a specialized sequence of processing to prepare dispersion curves showing ground roll phase velocity versus frequency.

The sledge hammer-source, MASW data were processed first. Dispersion curves were generated for each 24-channel field record. These curves were used to calculate 1-D models of shear-wave velocity layering for the center of each 24-channel geophone spread. The resulting 1-D models were generated along each line at 2-meter intervals and computer gridded and contoured to prepare several estimated shear-wave velocity profiles using different modeling parameters. These profiles were compared to the compressional-wave velocity profiles in Figures 2, 3, and 4. Based on this comparison we selected a final set of modeling parameters that generated the most consistent shear-wave velocity profiles along Lines SL-1, SL-2, and SL-3. These shear-wave velocity profiles primarily show velocity layering within 50 feet from the ground surface.

The passive-source MASW data from Lines SL-1 and SL-2 were used to extend the depth of shear-wave velocity imaging beneath these lines. The longer, 48-channel records were used to generate dispersion curves from lower-frequency, deeper penetrating ground roll. These curves were used to calculate additional 1-D models for the centers of the five 48-channel geophone spreads (Spreads 1 through 3). The resulting 1-D models were added to the 1-D models from the sledge hammer-source MASW data and computer gridded and contoured to prepare deeper shear-wave velocity profiles.

The shear-wave velocity profiles for Lines SL-1 and SL-2 from the combined sledge hammer and passive-source MASW data are shown in Figures 5 and 6. The velocity profile for Line SL-3 from the sledge hammer-source MASW data is shown in Figure 7. For comparison each of the profiles is displayed using a contour interval of 100 ft/sec and the same color velocity scale ranging from 200 to 2,500 ft/sec.

The compressional-wave and shear-wave velocity profiles for Lines SL-1, SL-2, and SL-3 (Figures 2 through 7) all show estimated velocity variations with respect to the ground surface elevations estimated from the field mapping.

More information on RAYFRACT refraction tomography and Surseis MASW modeling is available at www.rayfract.com and www.kgs.ku.edu/software/surfseis.

DISCUSSION OF RESULTS

Interpretation of Seismic Velocity Layering

The compressional-wave velocity profiles for Lines SL-1, SL-2, and SL-3 (Figures 2 through 4) all show similar patterns of velocity layering, indicating an upper, unconsolidated, soil/saprolite layer overlying a transitional, weathered basalt bedrock that quickly increases in velocity with depth. The compressional-wave velocities associated with the upper surface of the “basalt formation” are variable and appear to range mostly from 3,500 to 4,500 ft/sec. Below this 3,500 to 4,500 ft/sec layering, the velocity contours on these profiles show rapidly increasing velocity with depth, indicating increasingly harder, less weathered basalt. The 3,500 to 4,500 ft/sec velocity range and

its general elevation profile are also consistent with the logs from boreholes B-2, B-4, B-10 and B-11 which are near Lines SL-1 and SL-2. These logs describe this upper basalt formation as varying from moderately to highly weathered, fractured, vesicular, and scoriaceous, with soil inclusions. The elevations for the upper basalt formation on these logs are also somewhat consistent with the elevations of the 3,500 to 4,500 feet/sec velocity layering shown on the profiles. However, near the start of Line SL-2 the basalt surface appears to be slightly lower than the elevations it was encountered in boreholes B-10 and B-11.

Borehole B-103 was drilled on Line SL-2; however, the total depth of this boring 14.5 feet did not extend to the basalt formation. At this depth the boring encountered saprolite where the compressional-wave velocity profile for Line SL-2 shows 2,000 ft/sec.

The shear-wave velocity profiles for Lines SL-1 and SL-2 (Figures 5 and 6) show velocities that are consistent with the compressional-wave velocity profiles (Figures 2 and 3). The upper surface of the basalt formation again appears to be variable with shear-wave velocity ranging from 1,700 to 2,200 ft/sec. The shear-wave to compressional-wave velocity ratios (V_s/V_p) above and below this horizon are consistent with our expectation of these ratios for the upper unconsolidated, soil/saprolite layer and competent basalt bedrock layer. Generally, V_s/V_p ratios for soils and unconsolidated materials are near 0.4 and V_s/V_p ratios for competent rock are near 0.6 (reference: Exploration Geophysics of the Shallow Subsurface, H. R. Burger, 1992). These ratios were calculated at various points on the profiles for Lines SL-1 and SL-2 and were within the range of these values.

The deeper part of the shear-wave velocity profile for Line SL-3 (Figure 7) does not show velocities consistent with the above expectations of V_s/V_p ratios. Below elevation 820 feet, the shear-wave velocities appear to be low estimates when compared to the compressional-wave velocities in Figure 4. These lower velocities are probably caused by the MASW modeling's inability to account for a steeply-sloping basalt "half space" in this area. The topography indicates the upper surface of the basalt slopes very steeply toward the stream channel perpendicular to the orientation of Line SL-3.

Recommendations for Shear-Wave Velocity Profile

We recommend the following considerations be given for preparing an extrapolated shear-wave velocity profile along the alignment of the bridge.

1. The shear-wave velocity profiles for Lines SL-1 and SL-2 (Figures 5 and 6) provide more accurate estimates of the actual shear-wave velocity variations. Within the upper 50 feet of the ground surface these velocities are probably accurate within ± 10 percent. From 50 to 90 feet below the ground surface the velocities shown on these profiles are probably slightly less accurate. However, the profile for Line SL-3 below elevation 820 feet provides a lower estimate of these velocities. We recommend that the deeper part of this profile not be used.
2. The smaller scale shear-wave velocity variations on the profiles for Lines SL-1 and SL-2 are probably not accurately represented. We recommend that lateral velocity variations less than 40 feet in length on these profiles not be used.
3. The deeper part of the compressional-wave velocity profiles (Figures 2, 3, and 4) show higher velocities in excess of 12,000 ft/sec. Because of the positioning of these velocity layers near the bottom limit of the model these higher velocities are probably not realistic. We recommend that 12,000 ft/sec be used as the highest compressional-wave velocity layer on these profiles.
4. Shear-wave velocity estimates for the deeper, harder basalt layers shown on the compressional-wave profiles can be calculated using the V_s/V_p ratio of 0.6 for competent rock. Using this ratio, the compressional wave velocity profiles show that 7,200 ft/sec should be used as the deepest half space, shear-wave velocity layer. Beneath the center of Line SL-2 the elevation of this 7,200 ft/sec layer is about 720 feet. Beneath the southeast end of Line SL-1 the elevation of this 7,200 ft/sec layer rises to about 870 feet. These elevation variations should also be considered when preparing the deeper part of this shear-wave velocity profile.

University of Hawaii at Manoa
College of Engineering
October 30, 2007
Page 9

We hope this report provides sufficient information on the results of these surveys.
Please feel free to call us for further discussion.

We appreciate the opportunity to be of service to the University of Hawaii.

Sincerely,

Advanced Geoscience, Inc.

A handwritten signature in black ink, appearing to read "Mark G. Olson". The signature is fluid and cursive, with a large initial "M" and "O".

Mark G. Olson
Principal Geophysicist and Geologist

CA-Licensed Professional Geophysicist No. GP980
CA-Licensed Professional Geologist No. 6239

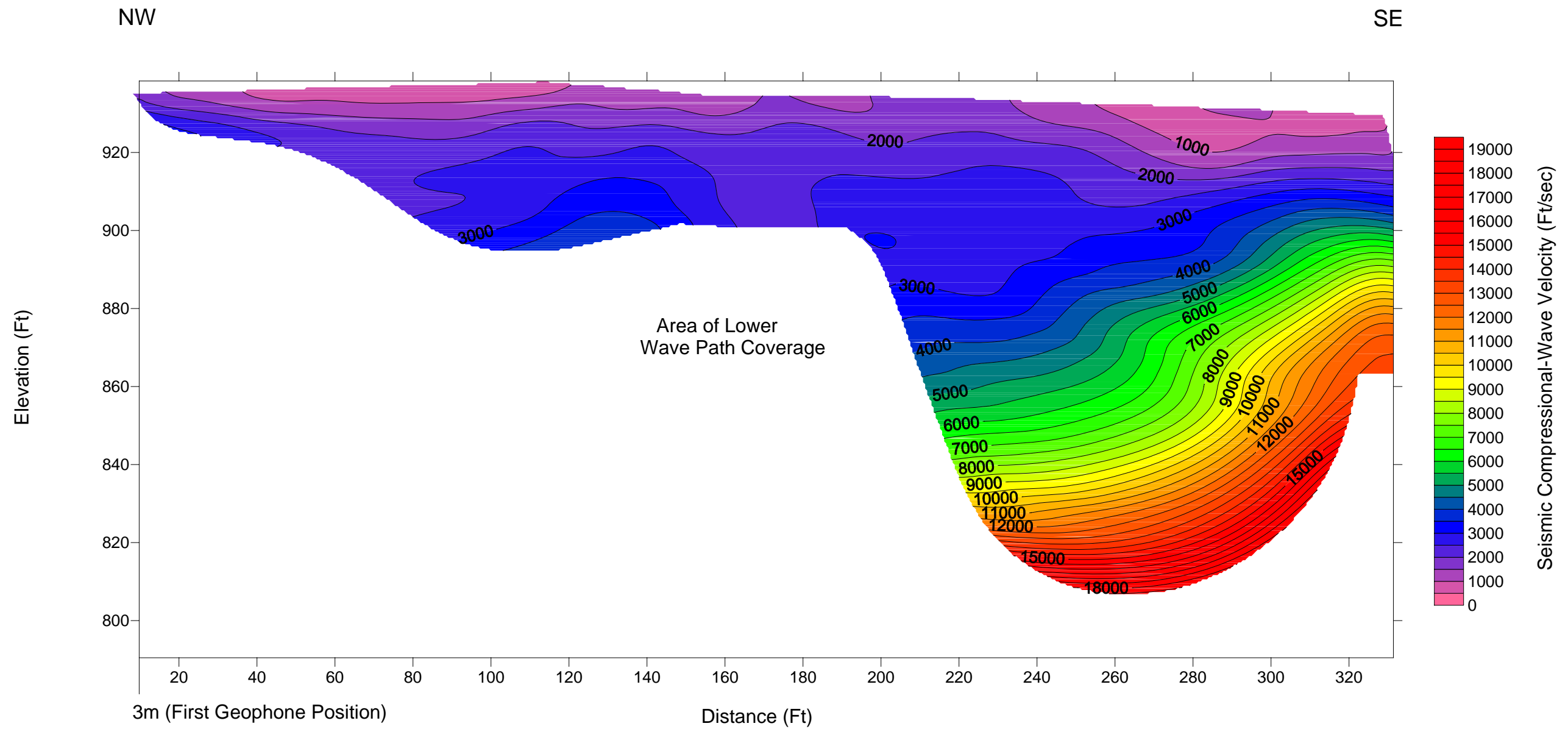
Attachments: Figures 1 through 7



Site Map Showing Locations of Survey Lines SL-1, SL-2, and SL-3 for Seismic Refraction and MASW Surveys Kealakaha Stream Replacement Bridge

Figure 1
Advanced Geoscience, Inc.

Line SL-1 Seismic Refraction Profile



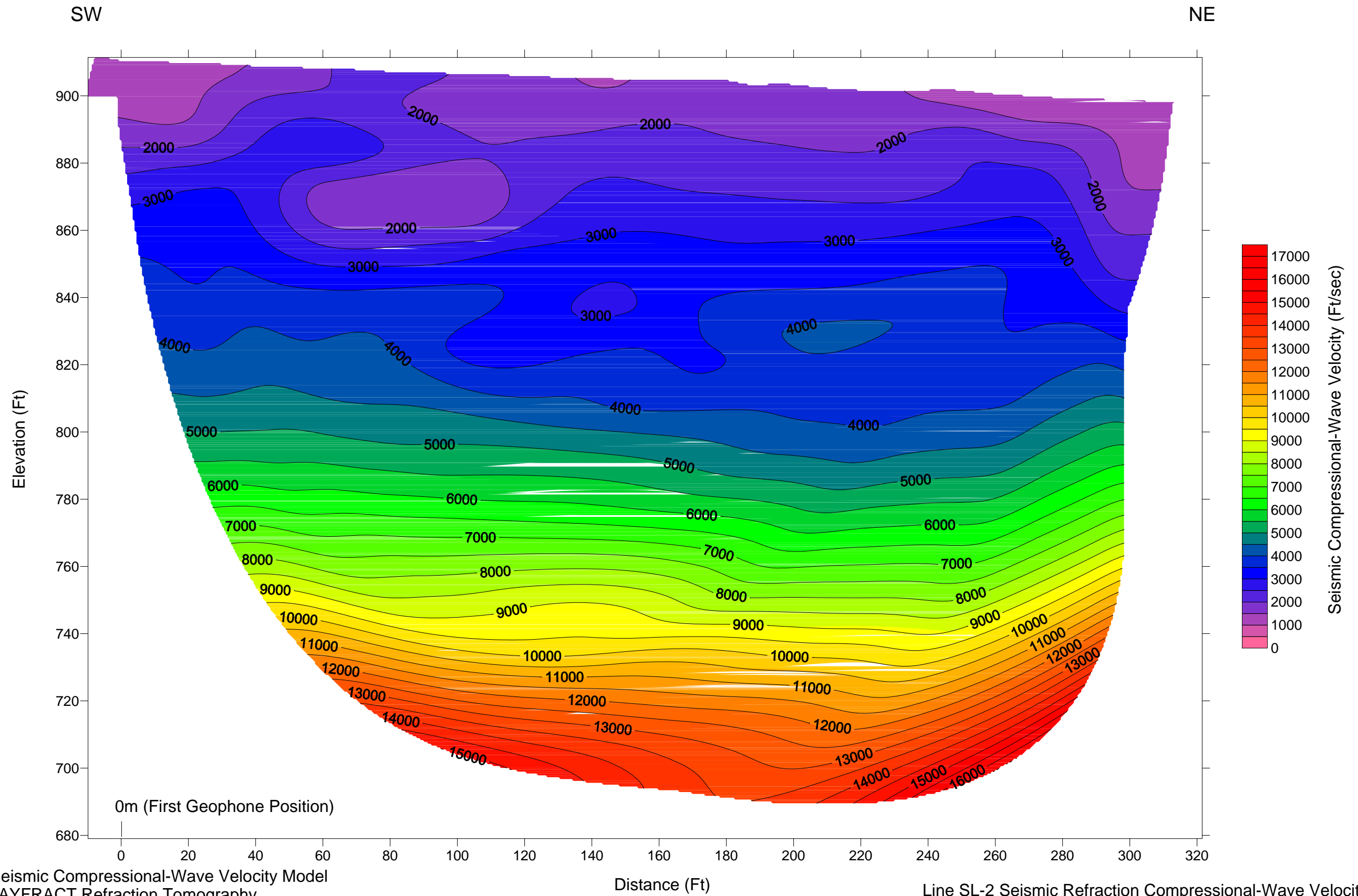
Estimated Seismic Compressional-Wave Velocity Model
Based on RAYFRACT Refraction Tomography
Using Initial 1-D Gradient Model + 200 WET Iterations

Horizontal and Vertical Scale 1 inch= 30 Ft

Line SL-1 Seismic Refraction Compressional-Wave Velocity Profile
Kealakaha Stream Replacement Bridge

Figure 2
Advanced Geoscience, Inc.

Line SL-2 Seismic Refraction Profile



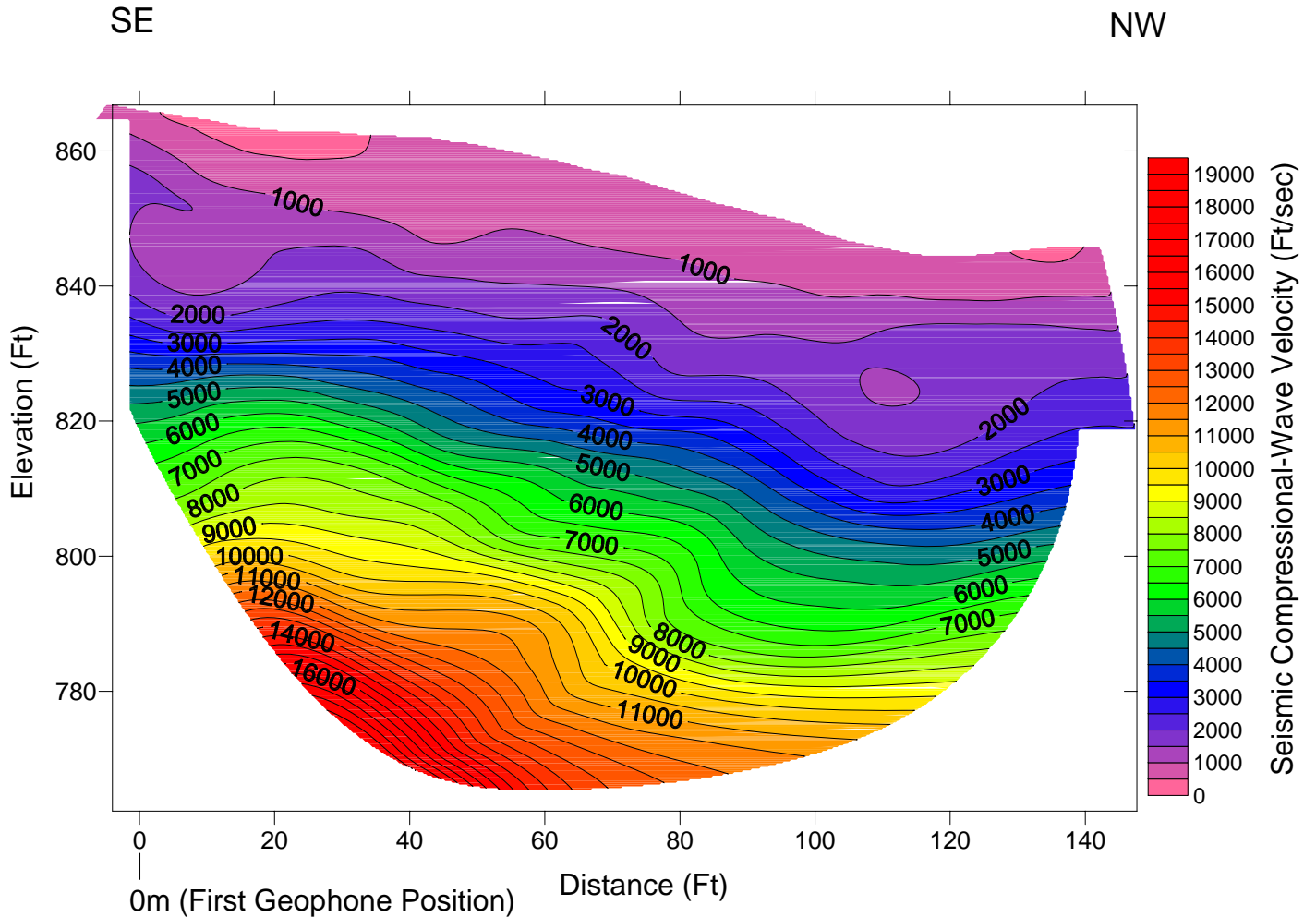
Estimated Seismic Compressional-Wave Velocity Model
Based on RAYFRAC Tomography
Using Initial 1-D Gradient Model + 200 WET Iterations

Horizontal and Vertical Scale 1 inch= 30 Ft

Line SL-2 Seismic Refraction Compressional-Wave Velocity Profile
Kealakaha Stream Replacement Bridge

Figure 3
Advanced Geoscience, Inc.

Line SL-3 Seismic Refraction Profile



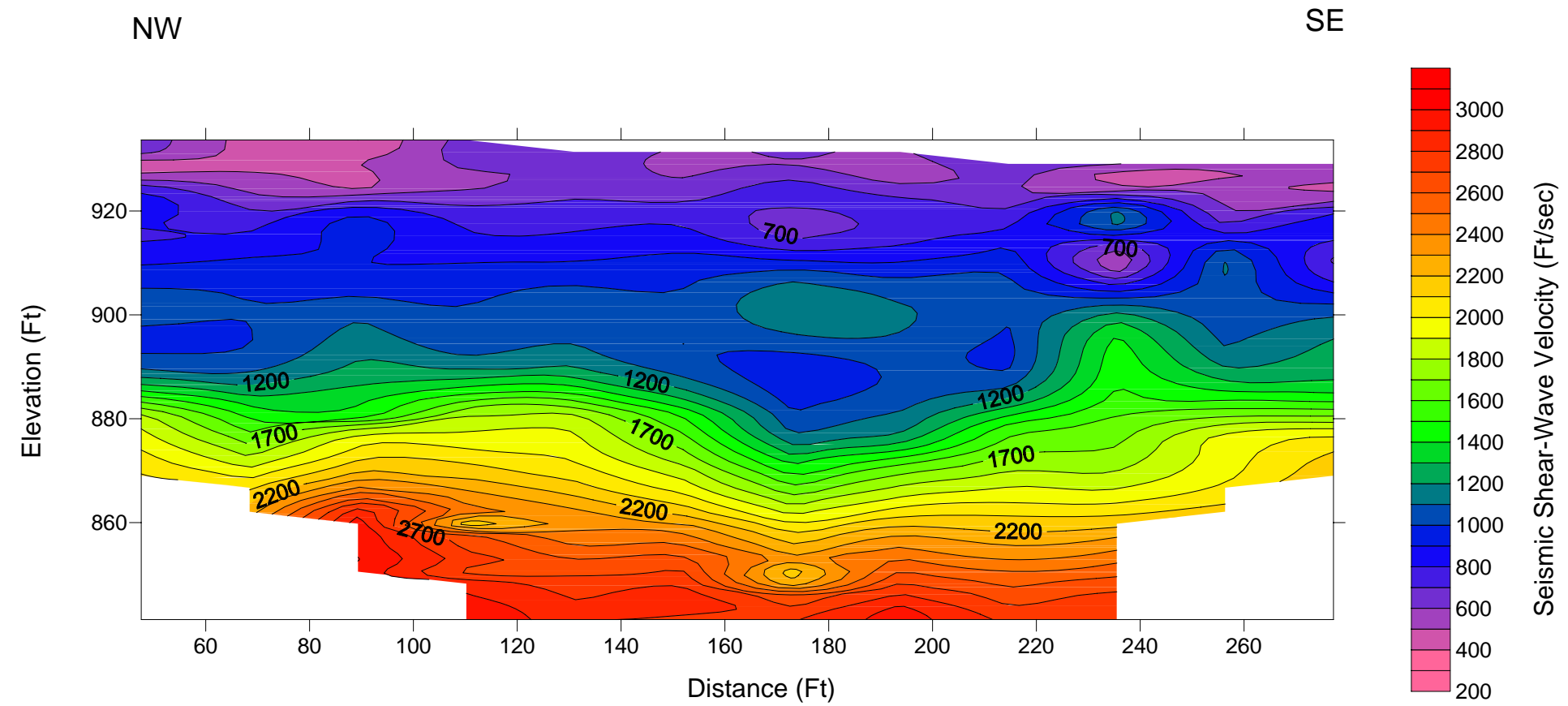
Estimated Seismic Compressional-Wave Velocity Model
Based on RAYFRAC T Refraction Tomography
Using Initial 1-D Gradient Model + 200 WET Iterations

Horizontal and Vertical Scale 1 inch= 30 Ft

Line SL-3 Seismic Refraction Compressional-Wave Velocity Profile
Kealakaha Stream Replacement Bridge

Figure 4
Advanced Geoscience, Inc.

Line SL-1 Seismic MASW Profile



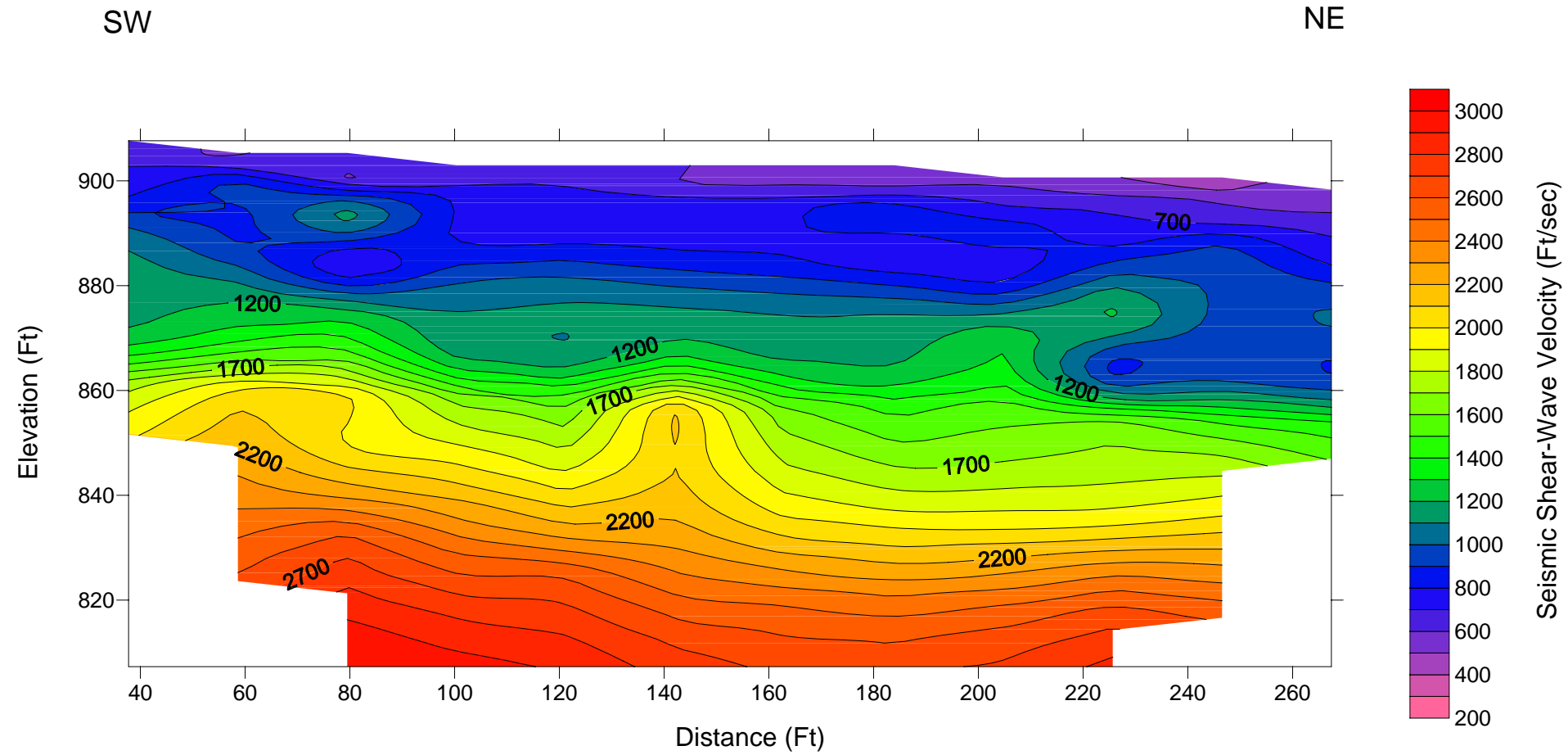
Estimated Seismic Shear-Wave Velocity Model
Based on SURFSEIS MASW Dispersion Modeling

Horizontal and Vertical Scale 1 inch= 30 Ft

Line SL-1 Seismic MASW Shear-Wave Velocity Profile
Kealakaha Stream Replacement Bridge

Figure 5
Advanced Geoscience, Inc.

Line SL-2 Seismic MASW Profile

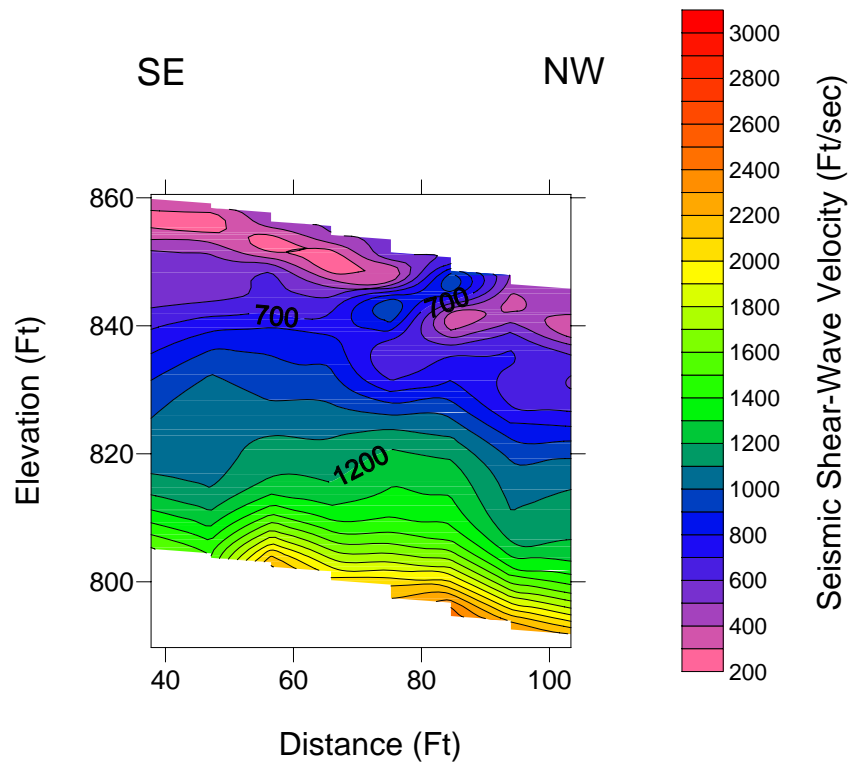


Estimated Seismic Shear-Wave Velocity Model
Based on SURFSEIS MASW Dispersion Modeling

Horizontal and Vertical Scale 1 inch= 30 Ft

Line SL-2 Seismic MASW Shear-Wave Velocity Profile
Kealakaha Stream Replacement Bridge

Line SL-3 Seismic MASW Profile*



*Note: Shear-Wave Velocity Model Below Elev. 820 Feet Appears to Represent a Low Estimate of the Actual Shear-Wave Velocity Profile in this Area.

Estimated Seismic Shear-Wave Velocity Model
Based on SURFSEIS MASW Dispersion Modeling

Horizontal and Vertical Scale 1 inch= 30 Ft

Line SL-3 Seismic MASW Shear-Wave Velocity Profile
Kealakaha Stream Replacement Bridge

Figure 7
Advanced Geoscience, Inc.

Appendix G

Publications

HAWAII DOT RESEARCH PROGRAM

Soil-Structure Interaction Modeling of the Kealakaha Bridge

By: Ian N. Robertson, Ph.D., P.E. (Principal Investigator)
 Horst Brandes, Ph.D., P.E. (Co-Principal Investigator)
 Shentang Wang, Ph.D. (Research Assistant)

Introduction

This research program involves a detailed soils investigation and soil-structure interaction modeling of the Kealakaha Stream Bridge, planned for construction on Highway 19 in the Hamakua District of the Island of Hawaii. This investigation is being performed in concert with a parallel HDOT project to install seismic instrumentation on the bridge, so as to provide more accurate modeling of the soil-foundation-structure response to future earthquake ground-shaking.

Bridge modeling

The Kealakaha bridge structure was modeled first under dynamic loading, but without its foundation or surrounding soil. Computations were carried out using the finite element method employing 3-dimensional nonlinear concrete-steel hybrid elements. This analysis was performed using OpenSees, an open source nonlinear analysis program under development by the Pacific Earthquake Engineering Research (PEER) center. This computer program allows consideration of geometric and material nonlinear effects.

As shown in Figure 1, for this structure-only model the base of the two piers are assumed to be fixed boundaries, while the ends of the girder are free to move in the longitudinal direction at the slide bearing abutment supports. The response of the bridge was investigated using input accelerations from a nearby

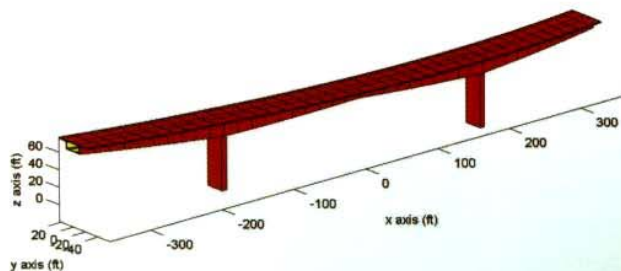


Fig. 1: Bridge discretization

accelerometer recorded during a magnitude 4.9 earthquake that took place on the Big Island on April 2, 2000. Figure 2 shows the predicted longitudinal displacements of the free ends as a function of time.

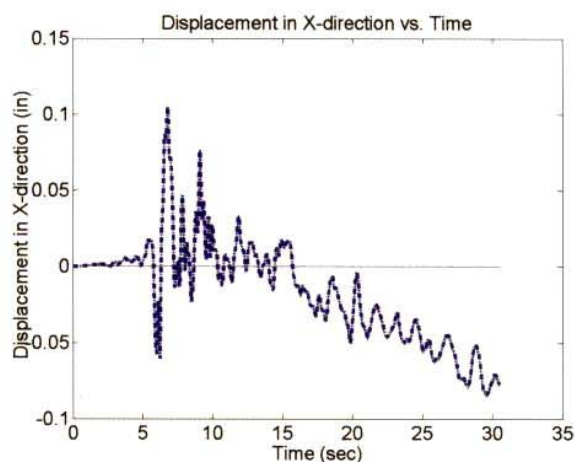


Fig. 2: Longitudinal displacement prediction

Foundation Modeling

The interaction between piles and surrounding soil has been modeled in OpenSees using more accurate soil and pile discretization and nonlinear material properties. The finite element mesh used to model the foundation and surrounding soil is shown in Figure 3. Utilizing symmetry, only half of the foundation is modeled to reduce the computational time required to analyze the model. The concrete pier, pile cap, and individual piles are modeled as elastic material with 20-node elements. The soil mass is modeled as an elasto-plastic material with 20-node elements. Assumed soil properties have been used until further soil investigations can be performed during bridge construction. The response of the model has been analyzed under static, push-over lateral loading applied at the top of the pier.

In order to model the soil more accurately, three new soil constitutive models were developed and implemented in the non-linear finite element analysis code, OpenSees. By implementing these models in the OpenSees code, they are now available for other

HAWAII DOT RESEARCH PROGRAM (Continued from Page 2)

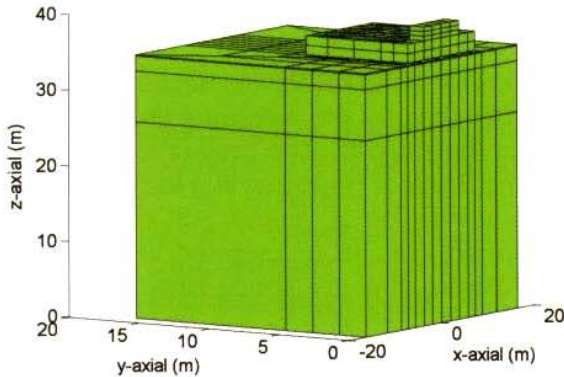


Fig. 3: Detailed pier and soil discretization researchers utilizing this open source computational tool.

Figure 4 shows a schematic of an OpenSees model under development that will incorporate both pier foundations and bridge structure, enabling non-linear analysis of the entire structure. This model, which incorporates a hybrid finite-infinite element formulation, will be available for comparison with the bridge response

during future earthquakes.

Soil Investigation

In order to improve the soil properties included in the OpenSees model, it is necessary to perform a detailed soil investigation. This investigation will involve drilling boreholes to sample the foundation materials at various depths below the surface at both pier and abutment locations. Static and dynamic testing of the sampled material will be performed in the UH Geotechnical Laboratory along with field investigations during boring to determine both linear and non-linear properties of the foundation materials. Because of delays in bridge construction, the soil investigation is yet to be performed.

Acknowledgement

Funding for this project was provided by the Research Branch of Hawaii Department of Transportation. This support is gratefully acknowledged. The opinions presented here are those of the authors and do not necessarily represent the opinions of the funding agency.

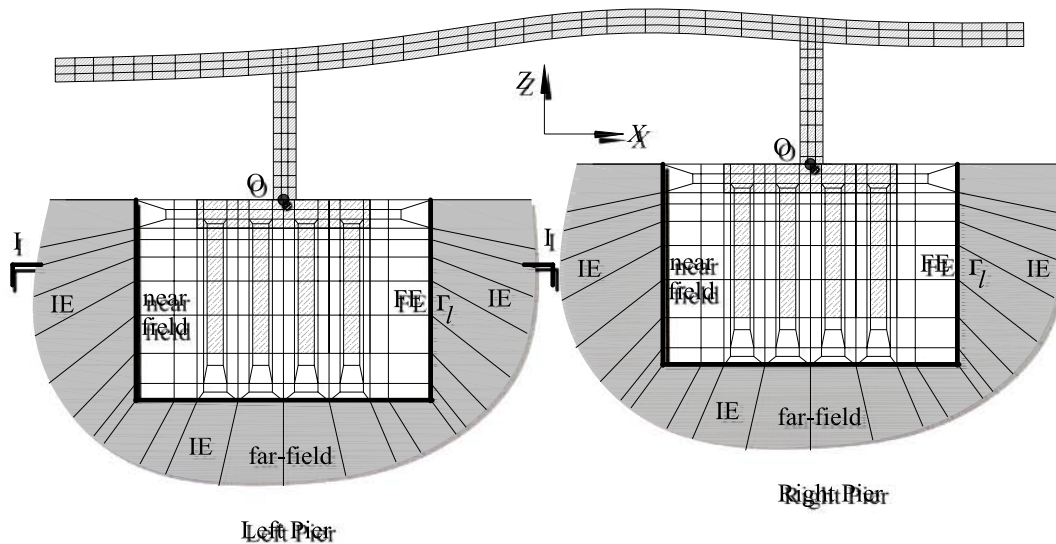


Figure 4: OpenSees computer model of soil-foundation-structure system for non-linear seismic analysis.

Soil and Rock Properties in a Young Volcanic Deposit on the Island of Hawaii

H. H. Brandes, F.ASCE¹; I. N. Robertson, M.ASCE²; and G. P. Johnson, M.ASCE³

1

Abstract: Deeply weathered lava flows of oceanic basalt reflect the mode and sequence of volcanic deposition, parent mineralogy, and postdepositional erosional and weathering processes. In turn, these are controlled by geology, geography, and climate. One particular site on the Island of Hawaii has been the focus of study to gain a better understanding of complex residual soil deposits, particularly in connection with a need to characterize seismic strong-motion propagation through decomposed surface soil and rock sequences. Materials at the site range from fully weathered volcanic soils, sometimes with unusual mineralogy and plasticity properties, to saprolite, weathered rock, vesicular basalt, and hard rock. Seismic surveys were conducted to investigate the distribution of these materials at the study site. Laboratory tests focused on saprolite and vesicular rock as two materials that are seldom reported on and that remain poorly characterized, at least with regard to conditions found in Hawaii. DOI: [10.1061/\(ASCE\)GT.1943-5606.0000453](https://doi.org/10.1061/(ASCE)GT.1943-5606.0000453). © 2011 American Society of Civil Engineers.

CE Database subject headings: Volcanic ash; Seismic effects; Soil properties; Rocks; Weathering; Hawaii.

Author keywords: Volcanic soil; Saprolite; Seismic velocity; Vesicular basalt; Rock strength; Mineralogy.

Introduction

The Island of Hawaii rises as a massive volcanic edifice from the North Pacific Ocean floor, some 3,000 km from the nearest continent. Hawaiian intraplate volcanism takes place through a thin oceanic crust made up largely of basaltic rock. In contrast, continental volcanism usually involves light granitic rock and a thicker lithosphere. The Big Island is geologically very young, with the oldest exposed rocks no more than approximately a million years old. Because of tropical conditions, volcanic lavas undergo pervasive chemical weathering upon exposure to the elements, with the rate and nature of breakdown very dependent on localized microclimate and drainage patterns. As a result, there exist a great variety of soil and rock types throughout the island, and in many respects they are different from those that exist in continental environments.

And yet Hawaiian rock and soil remain, for the most part, rather poorly characterized and understood. This represents a particularly challenging problem for earthquake engineering practice. The Island of Hawaii is seismically very active, as we were reminded by the M6.7 Kiholo Bay earthquake of 2006 (Robertson et al. 2006). Given the pace of rapid development in certain areas, there is an urgent need for a better understanding of strong-motion wave propagation through upper soil and rock layers. Very often such deposits consist of residual volcanic soil, saprolite, and weathered rock. However, it is not clear how such materials may respond to seismic shaking. For example, there is some evidence to suggest that certain surface wet-ash soil deposits may amplify seismic

waves quite a bit relative to stiffer soils and rock (Wieczorek et al. 1982). This article presents sorely lacking experimental data regarding velocity, stiffness, strength, and other properties of residual soils and basaltic rock for a deeply weathered lava-flow site on the lower slope of Mauna Kea.

The general lack of understanding regarding the seismic response of deeply weathered lava flows posed a challenge during the recent design and performance analysis of a replacement for the Kealakaha Bridge, which is located on Route 19 in the Hamakua District of Hawaii (Fig. 1). This bridge, along with several others located north of Hilo, has been targeted for replacement because it was deemed to be seismically inadequate. To develop a better understanding of seismic soil-structure interaction for tropical basaltic environments, the Hawaii Department of Transportation decided to carry out a companion study on site characterization, seismic instrumentation, and modeling in connection with replacement of the old Kealakaha Bridge.

The new Kealakaha Bridge consists of a three-span, posttensioned superstructure spanning 220 m over two abutments and two intermediate piers. The center span is 110 m long, whereas each abutment span is 55 m long. The bridge superstructure is composed of cast-in-place, multicell, tapered box-girder sections cantilevering on either side of the two intermediate piers, with drop-in precast I-girders to complete the middle span and abutment spans. Continuity posttensioning connects all drop-in girders and box-girder sections to create a continuous superstructure. To reduce the seismic demand on the bridge foundations, the contractor elected to redesign the bridge by using seismic base isolators. Two inverted-pendulum, friction-type base isolators were installed at each abutment and at the top of each pier to support the superstructure. This is the first application of base isolation in the State of Hawaii. To monitor the bridge performance during future seismic events, the Hawaii Department of Transportation has funded the installation of an extensive instrumentation system. Accelerometers will be located throughout the bridge super- and substructure, including downhole field accelerometers on either side of the stream gulch. Displacement transducers will be installed to monitor movement at the base isolators.

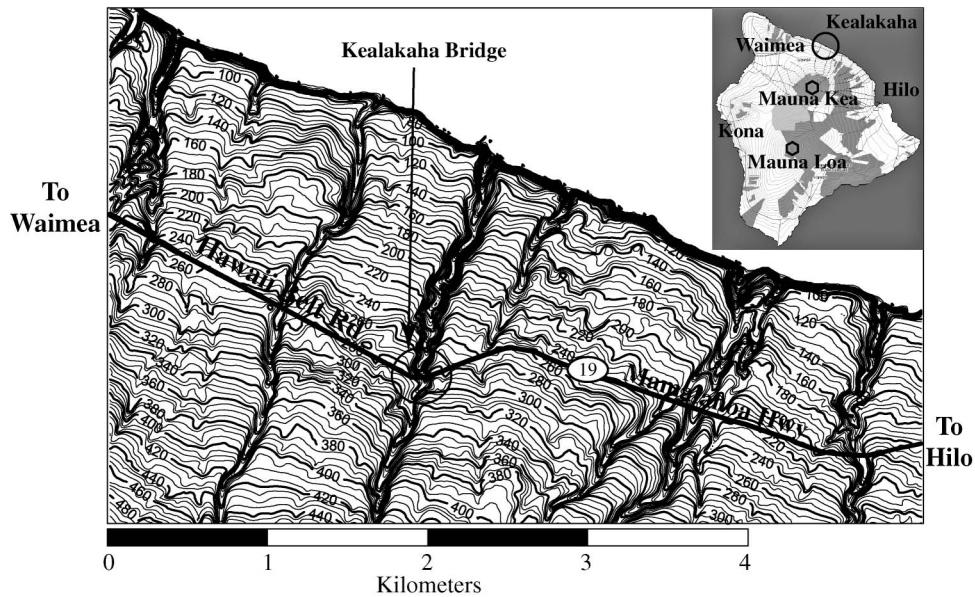
2

¹Associate Professor, Dept. of Civil & Environmental Engineering, Univ. of Hawaii, Honolulu, HI 96822

²Professor, Dept. of Civil & Environmental Engineering, Univ. of Hawaii, Honolulu, HI 96822

³Assistant Researcher, Dept. of Civil & Environmental Engineering, Univ. of Hawaii, Honolulu, HI 96822

Note. This manuscript was submitted on November 16, 2009; approved on September 24, 2010; published online on September 29, 2010. Discussion period open until November 1, 2011; separate discussions must be submitted for individual papers. This paper is part of the *Journal of Geotechnical and Geoenvironmental Engineering*, Vol. 137, No. 6, June 1, 2011. ©ASCE, ISSN 1090-0241/2011/6-0-0/\$25.00.



a. Location of Kealakaha Bridge on Hawaii Belt Road northwest of Hilo (Elevations in meters above mean sea level)



b. Old bridge crossing and construction of pier for new bridge over Kealakaha Gulch (Hilo side)

Fig. 1. Kealakaha Bridge, Island of Hawaii: (a) location of Kealakaha Bridge on Hawaii Belt Road northwest of Hilo (elevations in meters above mean sea level); (b) old bridge crossing and construction of pier for new bridge over Kealakaha Gulch (Hilo side) (image courtesy of the authors)

This paper presents results from field and laboratory testing to describe the general stratigraphy at the Kealakaha Bridge site. Wave measurements from geophysical surveys in the field and from laboratory tests provide seismic characterization of volcanic soil and weathered rock that is seldom found in the literature. In particular, a series of strength and velocity measurements on relatively unweathered vesicular basalt provide insight into the behavior of this type of material.

Geology

The base of the oceanic crust beneath Hawaii is 15 to 19 km below sea level. Magma seen erupting from active volcanoes comes from

the melting of solid rock near the outer edge of the Earth's mantle. By the time magma reaches the surface, it has been altered significantly from the parent peridotite that makes up the mantle. To be more precise, the source of magma in the upper mantle directly beneath Hawaii is a rock called *lherzolite*, a variant of the more common peridotite, both of which are rich in pyroxene and olivine. Important mineralogical changes occur as the mantle rock first melts, ascends to the surface, and then cools. By the time magma reaches the surface, it is typically richer in silicon and poorer in iron and magnesium than peridotite. Gases that enter the magma at great depths, chiefly water vapor and carbon dioxide, are released as it nears the surface, leaving behind small bubbles or cavities referred to as vesicles (Hazlett and Hyndman 1996; Macdonald et al. 1983;

Kennett 1982). These vesicles, or macropores, can have an important effect on wave propagation and mechanical properties, as our testing indicated.

As magma turns into lava upon eruption, it cools fairly quickly, leaving behind a relatively homogenous gray to black fine-grained rock commonly referred to as basalt. The matrix is composed almost entirely of calcium-rich plagioclase feldspar and pyroxene, although other minerals, such as olivine, may be present in smaller quantities. Embedded within the fine-grained matrix are sometimes larger crystals of olivine, plagioclase feldspar, or pyroxene, which are often visible with the naked eye. These crystals form in shallow magma chambers or similar formations where the ascending magma pauses for a time and the rate of cooling is reduced, allowing the formation of the larger crystals.

Two major types of basaltic rock are generally recognized in Hawaii. Tholeiitic basalt, which is relatively rich in silica and poor in sodium and potassium, and alkalic basalt, comparatively poor in silica but rich in the alkalis sodium and potassium. Other types of igneous rocks, such as trachyte and nephelinite, are occasionally encountered as well, but they are far less common. The large shield volcanoes responsible for the major growth of the islands produce theliitic basalt during most of their lives, but shift to alkalic basalt as they begin to decline. Rejuvenated volcanic activity tends to produce alkalic and other basalt types, but rarely theliitic basalt. The reason for the change from theliite to alkalic lava is not clear (Macdonald et al. 1983). In any case, there is no evidence that weathering products derived from theliitic or alkalic basalt are significantly different from one another in terms of geotechnical properties, although admittedly there have been no definitive studies on this.

Perhaps the greatest difference between Hawaiian and continental igneous rock is the absence of granite and the lack of other quartz-rich rocks in Hawaii, which are among the most common types of igneous rock found on continents. Therefore, it may be conjectured that soils formed from Hawaiian basalt may not always behave the same way as soils that derive from continental igneous rocks.

Further differences between volcanism in Hawaii and volcanism at the edge of continents, which play a role in the development of soils, have to do with the type of eruptions that are most commonly observed. During most of their active lives, Hawaiian shield volcanoes tend to erupt large quantities of very hot and fluid lavas that can travel large distances before coming to a halt. This is in contrast to more violent eruptions that take place for volcanoes at the edge of tectonic plates. Thus, rather than extensive pyroclastic deposits, the bulk of the Hawaiian islands consist of layer upon layer of lava flows, usually no more than 10 m thick, forming massive shields that slope gently from crater to ocean. One important implication here is that many deeply weathered locations do not simply consist of a conventional residual transition from soil near the surface to progressively less weathered rock at depth. Instead, it is very common to observe repeated residual sequences, suggesting that earlier flows have undergone varying amounts of weathering before being covered by new flows.

A distinction between two major types of lava flows has long been recognized. Pahoehoe lava has a billowy or ropy appearance. Fresh pahoehoe is very hot and fluid. Its relatively low viscosity allows it to flow downhill in units no more than a few meters thick. As the lava cools, a thin smooth outer skin forms first, whereas hot fluid may continue to flow underneath for some distance. In some cases, the lava may run out from under a cooled hardened surface and leave behind a cavity. These cavities, referred to as lava tubes, are found quite often in older pahoehoe flows. A single eruption can involve many such flows crisscrossing over one another.

In contrast, 'a'ā flows are more viscous and usually carry larger amounts of gas. The result is thicker units that may range from 3 to 10 m in height or more. 'A'ā flows are texturally very different from pahoehoe ones. They consist of disorganized, jagged, and spiny basalt blocks and rubble. Hawaiians use the term 'a'ā to describe the pain that is experienced when walking over such flows without adequate foot protection. An advancing 'a'ā flow usually consists of a viscous molten core flow and solid rubble material that is transported along on its top. As the lava flow advances, some of the rubble is rolled over the front and becomes trapped beneath the core. Eventually the core cools and solidifies as well. The stacking of multiple flows then leads to alternating thick units of disorganized rubble, often referred to as clinker, and thinner intervals of more homogeneous solid rock. Despite the apparent textural contrast between pahoehoe and 'a'ā lavas, there is no consistent difference in composition (Macdonald et al. 1983).

General Site Conditions and Geophysical Surveying

Five major volcanoes have at one time or another contributed to the growth of the Big Island: Mauna Kea, Kohala, Hualalai, Mauna Loa, and Kilauea. Of these, only the last three are considered either active or nominally dormant. Hualalai last erupted in 1801 and Mauna Loa in 1985. Kilauea has been erupting continuously since 1983. The Kealakaha Bridge is located on the northeastern slope of Mauna Kea's extinct shield. The rocks at the study site are part of the Hamakua formation and consist primarily of alkalic basalt, approximately 60,000 to 200,000 years old (Wolfe and Morris 1996). A thin layer of ash material, known as Pahala ash, is found in the upper few feet throughout the area.

Mauna Kea's Hamakua Coast is an excellent example of the effect of microclimate on erosion. Abundant trade wind rains and warm temperatures have resulted in extensive chemical weathering of the upper lava flows. Numerous deep and narrow erosional gulches cut into the gentle slope that descends from Mauna Kea (Fig. 1). All these changes have occurred rather rapidly, which is in marked contrast to the drier leeward side of Mauna Kea where significantly less weathering has taken place. The Kealakaha Bridge crosses a small stream of the same name. The gulch beneath is 45 m deep and 140 m wide, although it becomes much deeper further toward the ocean. Erosion has exposed layer upon layer of pahoehoe and 'a'ā flows more or less parallel to the ground surface and dipping at approximately 6° in the direction of the coastline. Weathering extends deeply into the subsurface as a result of downward infiltration of rainfall, but also because of downhill seepage flows through permeable clinker and fractured rock zones.

Chemical weathering processes, including oxidation, hydration, hydrolysis, carbonation, cation exchange, and solution, are all important in the decomposition of Hawaiian rocks. The primary agents are oxygen from the air, water from rainfall, and carbon dioxide from vegetation. Carbonic and humic acids work to break down the original minerals in the basaltic rock, chiefly plagioclase (albite and anorthite), pyroxene, and olivine. The main products of the decomposition are sodium, calcium, and magnesium carbonates, which are soluble and are readily carried away by water, and insoluble components left behind that include kaolinite, numerous ferrous oxides, various amounts of amorphous silica (SiO₂), and occasionally gibbsite. Among the residual oxides are decomposed products such as hematite, magnetite, and ilmenite (Mitchell and Soga 2005; Macdonald et al. 1983).

Of particular interest to this study were the approach flanks to the old and new bridges. To gain a better understanding of the site conditions, three seismic survey lines were laid out as shown in

6
7
Fig. 2. Seismic line 1 (SL1) and SL2 were placed along the side of the road and line SL3 was located somewhat below the top of the gulch, along the Waimea (northwest) side of the bridge and approximately parallel to the stream. Geophysical surveying consisted of seismic refraction and multichannel analysis of surface waves (MASW). The MASW method records seismic surface waves generated from a variety of sources along a string of surface receivers. Measured travel times, and hence propagation velocities, are proportional to the stiffness of the subsurface materials and can be processed to yield the variation of shear-wave velocity below the surveyed area. In the active mode, energy is generated in a deliberate manner by dropping a sledgehammer on a metal plate at ground surface, for example. Sources and receivers are usually arranged in line. In the passive mode, energy is collected from miscellaneous sources such as road or air traffic. A common passive arrangement uses a receiver string deployed along the side of a road to collect the energy produced by moving traffic. The data from both active and passive sources can then be combined to extend the effective depth of the survey. This is precisely what was done at the Kealakaha Bridge site for lines SL1 and SL2, whereas for SL3 only active data was collected. The maximum depth of investigation in active MASW surveys is typically limited to 10 to 30 m, depending on subsurface conditions and the type of source (Park et al. 1999). The combined active-passive method at the study site yielded maximum penetration of slightly over 30 m.

The string of receivers consisted of 48 low-frequency geophones spaced 1 m apart. The receivers were advanced along each survey line for a total coverage of 95 m along lines SL1 and SL2, and 42 m along line SL3. Active energy was generated with a 5.2-kg sledgehammer and passive energy was recorded from oncoming

traffic along Route 19 during 30-second time intervals. Overlapping shot points were used to provide refraction data along the length of each of the three surveys.

8
9
10
The seismic and MASW data was processed and modeled by using conventional methods. The first arrival time data for each of the geophones was input into the program RAYFRACT (Intelligent Resources, Inc.) to estimate velocity-depth models for each line. Initial models were further refined by using the Wave-path Eikonal tomographic inversion method with 200 iterations. The best-fit models were gridded and contoured. The resulting compressional wave velocity profiles for lines SL1, SL2, and SL3 are shown in Figs. 3–5, respectively. Processing of the MASW data made use of the program SurfSeis (Kansas Geological Service). This involved a series of specialized processing sequences to prepare dispersion curves yielding phase velocity versus frequency. Dispersion curves were in turn inverted for an estimate of preliminary shear-wave velocities. These profiles were compared to the compressional wave velocities in Figs. 3–5 to refine the modeling parameters and then improve the shear-wave velocities. A similar approach was used to process the passive data, although the dispersion imaging process is slightly different to account for differences in the location and nature of the traffic source. Final processing combined both active and passive MASW results to yield the shear-wave velocity profiles shown in Figs. 6–8. It is estimated that the velocities are accurate within $\pm 10\%$ in the upper 15 m, and slightly less below that depth. The deeper portions of the compressional wave profiles show velocities in excess of 3,500 m/s. Because these occur near the lower limits of the model space, they need to be viewed with caution and may not be realistic.

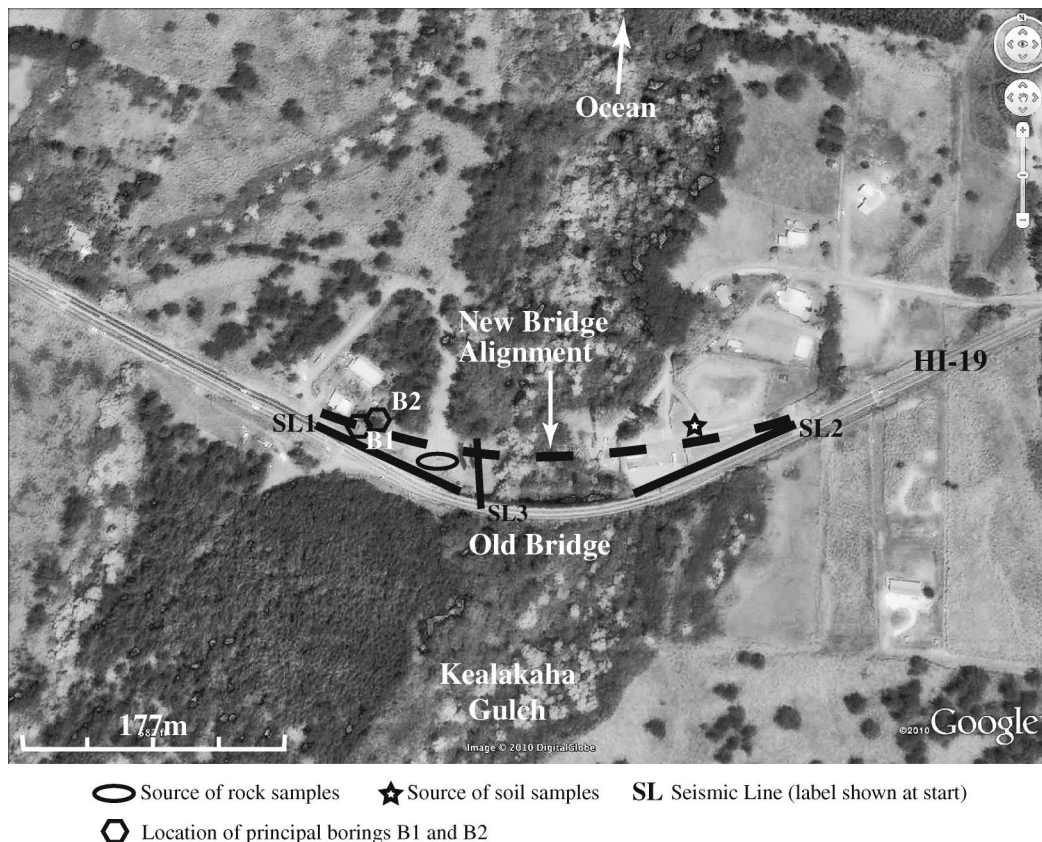


Fig. 2. Seismic lines and sampling locations relative to old Kealakaha bridge and new bridge alignment (satellite image courtesy of DigitalGlobe, ©2010 Google)

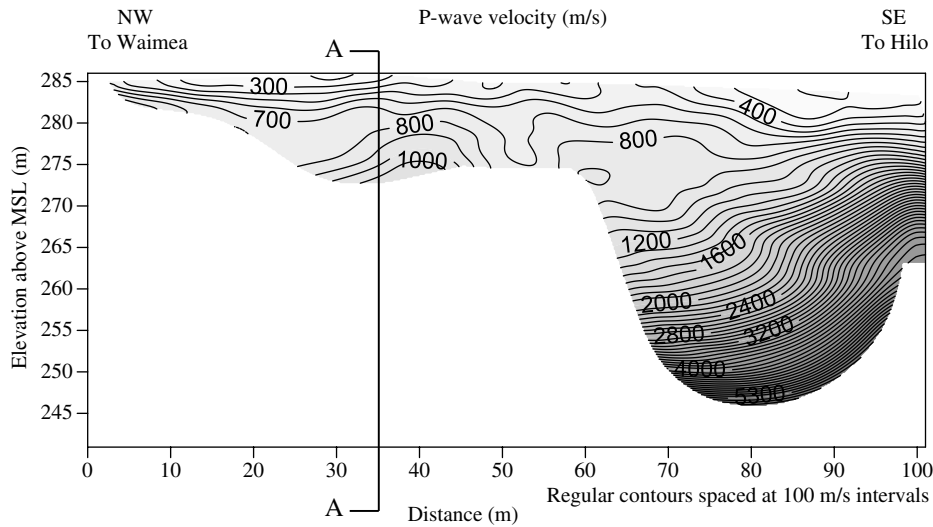


Fig. 3. Line SL1 seismic refraction profile

Stratigraphy and Geotechnical Characteristics of Soil Profile

The locations surveyed and drilled represent successive ‘a‘ā flow deposits, as indicated by the highly disorganized and inhomogeneous nature of the soil and rock materials that could be observed along the steep walls of the gulch. A number of borings were drilled near these survey lines (Geolabs, Inc. 2001) and they help to delineate the basic subsurface conditions at the site. Borings B1 and B2 were located within a few meters of line SL1, adjacent to cross section A-A in Figs. 3 and 6 (also refer to Fig. 2). Boring records and observation of exposed grading cuts were used to assess the vertical distribution of soils and rock at section A-A. The deduced

stratigraphy at this location, along with velocities determined from geophysical surveying, is summarized in Fig. 9.

Given the interest in strong-motion propagation through surface layers, it is instructive to view the subsurface materials in terms of the earthquake site-classification provisions contained in the *International Building Code* (IBC Table 1613.5.2; *International Code Council* 2009), and also in terms of the widely used Deere and Patton tropical residual soil-classification system for igneous rocks (Deere and Patton 1971). The latter has been adapted for residual profiles as they are found in the Hawaiian Islands and is shown in Fig. 10. A broad correspondence exists between IBC site classes and weathering horizons as indicated by the links 11 shown between the two systems.

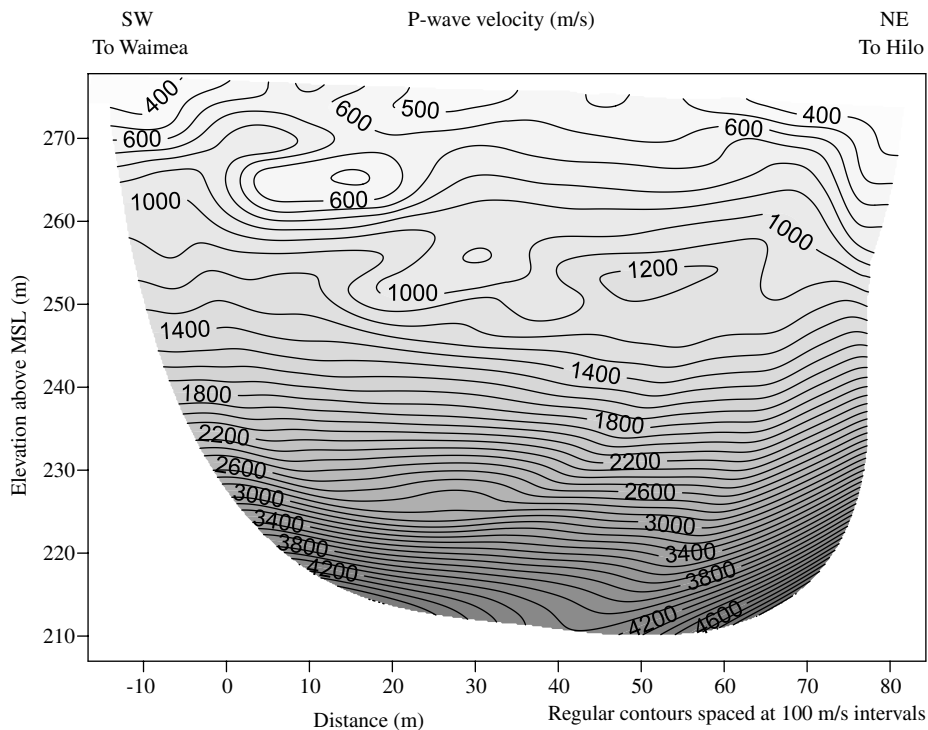


Fig. 4. Line SL2 seismic refraction profile

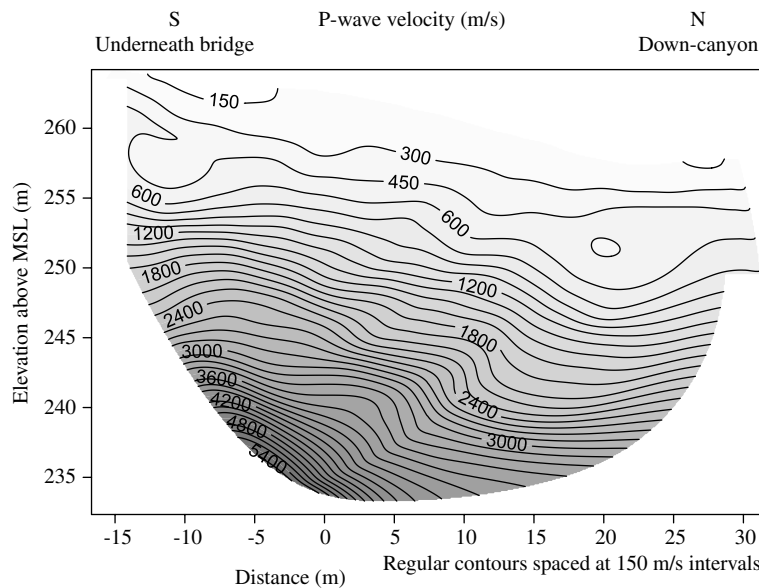


Fig. 5. Line SL3 seismic refraction profile

At location A-A, the upper 5.2 m consist of clayey silt of high plasticity (MH) with occasional larger fractions that range from sand to cobbles and boulders (Fig. 9). This represents the IA to IB horizon in the Deere and Patton (1971) system and consists of fully, or nearly fully, decomposed matrix residual soil. Where ash is mixed in, soils tend to have elevated water contents and plastic limits. Shear-wave velocities are less than 183 m/s, corresponding to IBC site class E.

The fully destructured upper soil is followed by saprolite between depths of 5.2 and 15.2 m. Saprolite represents basalt lava that has been thoroughly weathered but that retains relic rock structures. In Hawaii it is often mottled from the accumulation of oxides and various leaching products. It may also retain the vesicular appearance of the parent rock. That is indeed the case for this interval, which corresponds to Horizon IC in the Deere and Patton (1971) system. Shear-wave velocities and standard penetration numbers indicate that the saprolite is associated with IBC site class D. The material in this interval is not uniform, and there are numerous

boulders and less weathered zones throughout. Nonetheless, shear-wave velocities do not increase much throughout the saprolite zone, at least not when compared to the weathered rock layer beneath.

The extent of chemical weathering in shallow saprolite was examined by conducting quantitative X-ray diffraction analyses on two specimens at depths of 3 and 5 m. Although taken from a cut in an access road on the opposite bank of the gulch, near seismic line L2 (Fig. 2), the saprolite tested is quite similar to that found along line L1 below 5.2 m. The results are shown in Table 1 and indicate that all the plagioclase, pyroxene, and olivine of the parent basalt have been decomposed into various oxides, especially magnetite and hematite, and halloysite and a smaller amount of smectite. In other words, the saprolite reflects profound weathering despite the relatively young age of the parent lava flows. Gradation and plastic limits indicate that the saprolite breaks down to high plasticity silt (MH), with increasing sand fraction with depth (Fig. 11). The halloysite is of the nonhydrated type with crystal lattice spacings nearly the same as for kaolinite. Nonhydrated

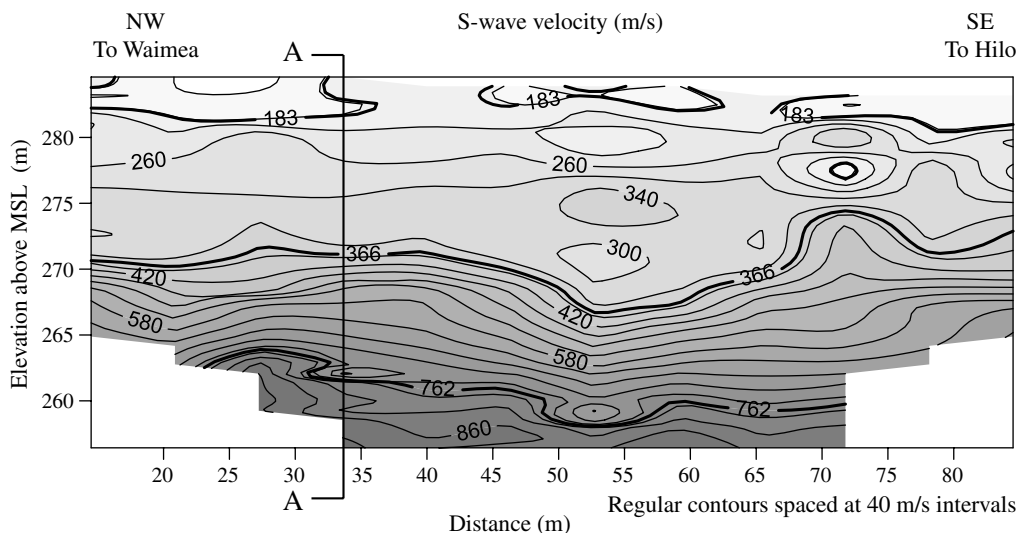


Fig. 6. Line SL1 seismic MASW profile (IBC site class boundaries indicated by thickened contours)

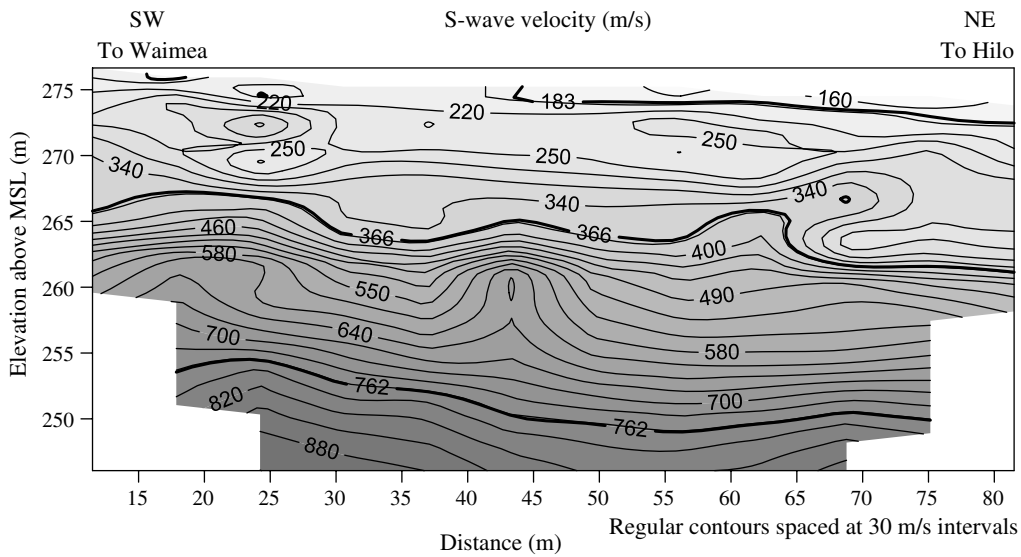


Fig. 7. Line SL2 seismic MASW profile (IBC site class boundaries indicated by thickened contours)

halloysite shares many characteristics with kaolinite in terms of moisture content and plasticity, for example. Specific gravity for the residual saprolite is larger than for common clay minerals because of the accumulation of the heavier ferrous oxides. Hydrated halloysite, which is more abundant in ash deposits closer to the town of Hilo, is usually found at very high moisture contents and exhibits very large plastic limits. Upon drying in an oven, such ash soils change irreversibly and take on the texture of sand.

18 One CU triaxial test was conducted on a sample of the saprolite from a depth of 3 m. The specimen was obtained from the same

location as the mineralogy samples and was of very good quality (further undisturbed sampling was unsuccessful). A confining stress of 70 kPa was used, which is in line with the estimated overburden stress. The results indicate a peak deviatoric stress at 8.1% axial strain, followed by mild softening. An effective peak friction angle of 33° can be estimated, assuming no cohesion intercept. Of course, a single triaxial test is insufficient to properly characterize the strength of the saprolite at the study site. On the other hand, this friction value agrees with triaxial test results conducted on similar soil some 6 km away near the town of Paauilo, which also indicate a

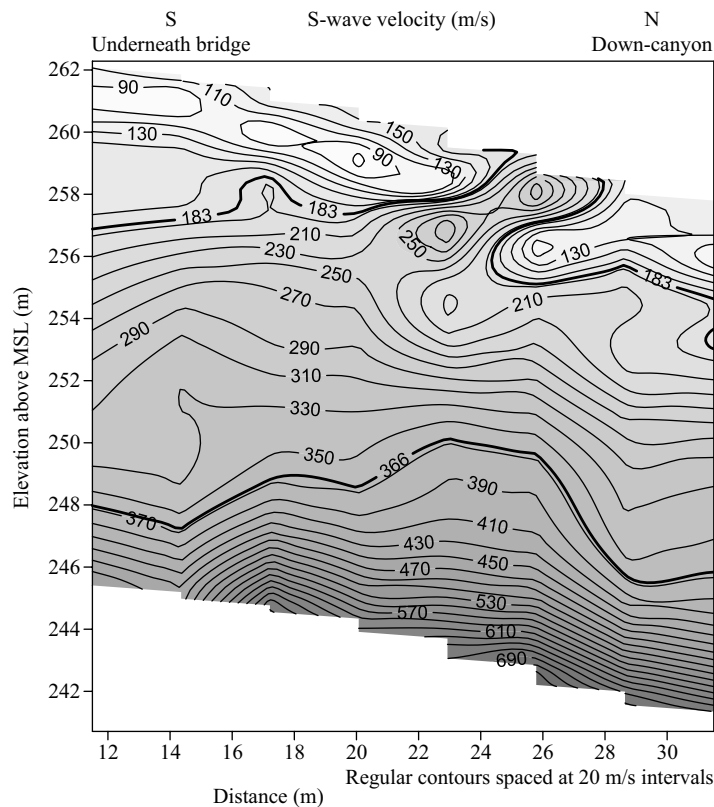


Fig. 8. Line SL3 seismic MASW profile (IBC site class boundaries indicated by thickened contours)

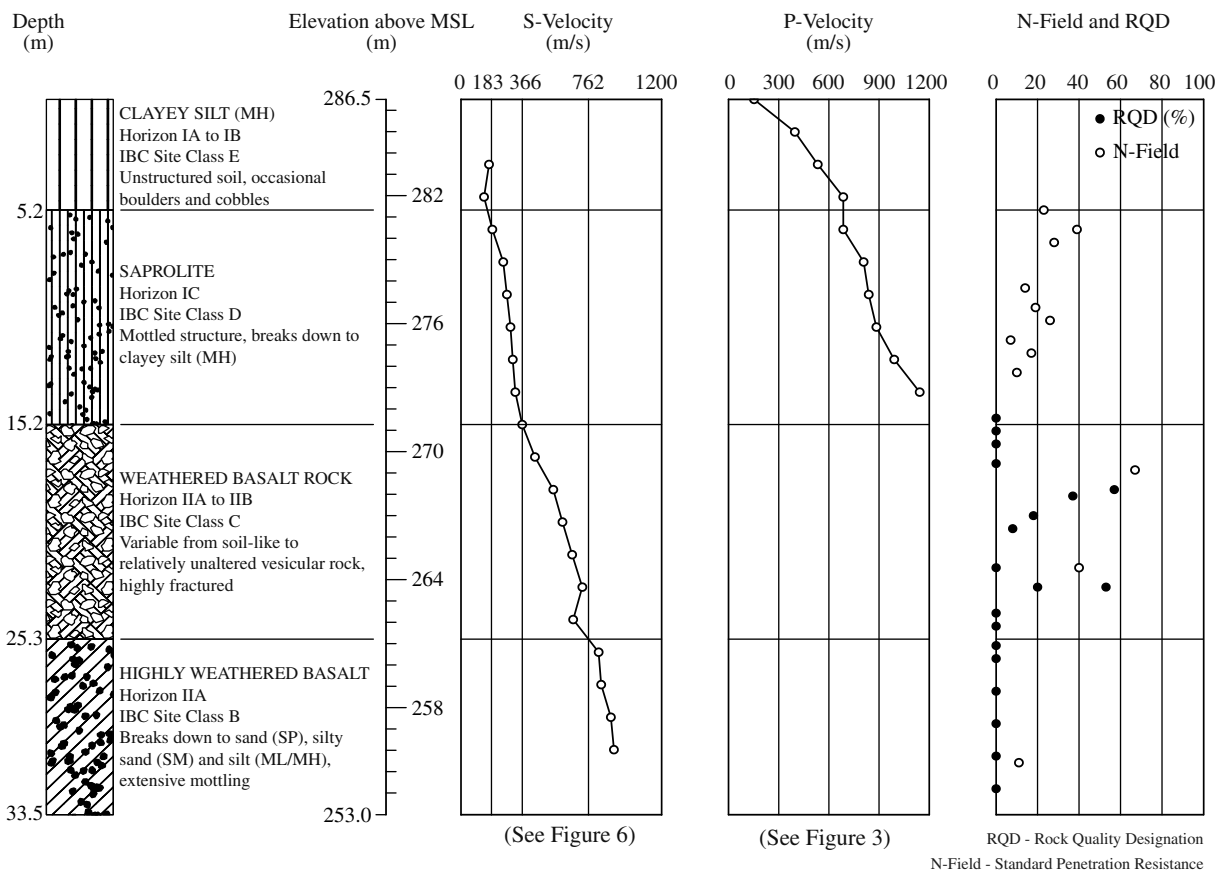


Fig. 9. Soil and rock profile at section A-A in seismic line SL-1 (refer to Fig. 10 for a description of soil horizons and IBC site classes)

friction angle of 33° (Hirata & Associates, Inc. 2001). Lumb (1975) reports a friction angle of 36° for volcanic saprolite from Hong Kong, whereas Fredlund (1987) indicates a value of 33°, also for Hong Kong saprolite. Tests conducted on B and C horizon soils from the islands of Oahu and Kauai suggest a wider range of values, from as little as 28° to upward of 44° (Tuncer and Lohnes 1977; Hirata & Associates, Inc. 2003). A wide range of friction values

(and cohesion intercepts) is not surprising given that the strength of saprolites is very dependent on weathering, cementation, moisture content, saturation, and the presence of relict joints (Mitchell and Sitar 1982), all of which can be expected to vary substantially throughout Hawaii's geology and microclimate regions. In general, our experience indicates that the strength of Hawaiian saprolites is significantly higher than of most fully weathered, normally

Weathering Profile for Hawaiian Lava Flows

Zone ¹	Description ²	RQD ³	N-Field ³
I, Residual soil			
IA, A Horizon	Topsoil, roots, organic material; zone of intense leaching	N/A	<15
IB, B Horizon	Silt- and clay-rich; accumulation of Fe, Al, and Si; may be lightly cemented; little or no soil structure	N/A	10-20
IC, C Horizon (saprolite)	Relict rock structure; breaks down easily to silt/clay/some sand; mottling, stains; some highly weathered core stones	0 or N/A	20-40
II, Weathered rock			
IIA, Transition	Highly variable, soil-like to rock-like; silty/sandy/gravelly residue; extensive staining; spheroidal and vesicular weathering of core stones	Generally 0-50	30-50
IIB, Partially weathered rock	Rock-like soft to hard rock; difficult to break down by hand; variable amounts of vesicles and fracturing; some alteration of plagioclase, pyroxene and olivine	Generally 50-75	>40 or N/A
III, Unweathered rock	No stains or weathering, although unaltered vesicles may be present; light-weight to very dense; often referred to as 'blue rock'	Generally >75	N/A

2009 International Building Code Seismic Site Classes⁴

IBC Site Class	Soil Profile Name	Shear Wave Velocity, V_s	N-Field
F	-	N/A	-
E	Soft soil	$V_s < 183$ m/s ($V_s < 600$ ft/s)	$N < 15$
D	Stiff soil	$183 \leq V_s \leq 366$ m/s ($600 \leq V_s \leq 1,200$ ft/s)	$15 \leq N \leq 50$
C	Very dense soil and soft rock	$366 \leq V_s \leq 762$ m/s ($1,200 \leq V_s \leq 2,500$ ft/s)	$N > 50$
B	Rock	$762 \leq V_s \leq 1,524$ m/s ($2,500 \leq V_s \leq 5,000$ ft/s)	N/A
A	Hard rock	$V_s > 1,524$ m/s ($V_s > 5,000$ ft/s)	N/A

⁴International Code Council (2009)

¹Deere and Patton (1971) ²Adapted to Hawaii soils from Deere and Patton (1971) and Lambe (1996)

³Approximate ranges for Hawaii soils N/A - Not Applicable

RQD - Rock Quality Designation N-Field - Standard Penetration Resistance

Fig. 10. Relationship between weathering profile for unit lava flows and IBC site classes

Table 1. Sapolite Soil Properties

	Sapolite (3 m)	Sapolite (5 m)
Mineralogy (%)		
Ilmenite		14
FeTiO ₃		
Kennedyite	10	
Fe ₂ MgTi ₃ O ₁₀		
Magnetite	5	30
alpha – Fe ₃ O ₄		
Hematite	28	
alpha – Fe ₂ O ₄		
Goethite	3	5
alpha – FeOOH		
Akaganeite	4	
beta – FeOOH		
Halloysite (nonhydrated)	48	48
Al ₂ Si ₂ O ₅ (OH) ₄		
Mixed-layered illite/smectite	2	3
K _{0.5} Al ₂ (Si, Al) ₄ O ₁₀ (OH) ₂ · 2H ₂ O		
Water content & plasticity (%)		
Water content	77	71
Liquid limit	77	71
Plastic limit	59	62
Gradation (%)		
Sand	12	25
Fines	88	75
Weight		
Specific gravity	3.15	3.07
Effective strength		
Friction angle (Degrees)	33	
Cohesion (kPa)	0	

consolidated alluvial fine-grained soils, for example, kaolinite or halloysite, which typically have friction angles on the order of 20 to 28° (Terzaghi et al. 1996; Mitchell and Soga 2005).

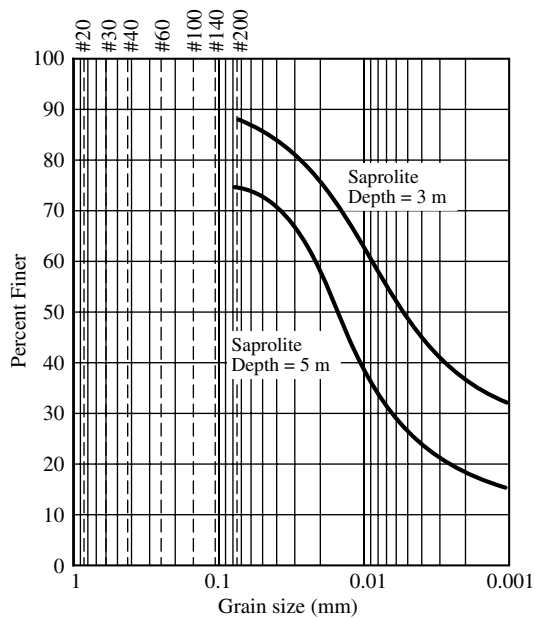


Fig. 11. Gradation of sapolite after breaking down to soil size (hydro-meter method)

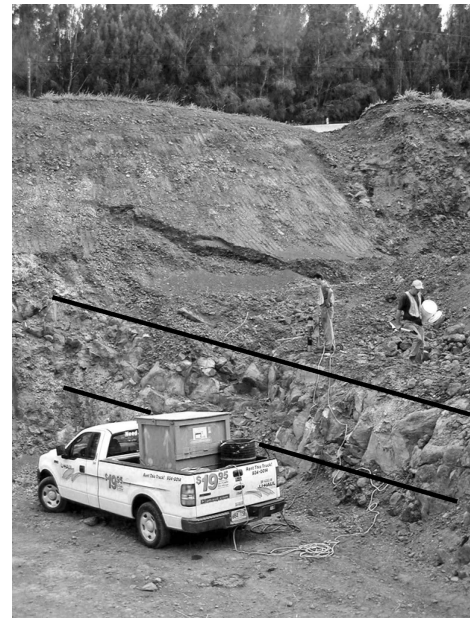


Fig. 12. Unweathered core of 'a'ā lava flow protruding from beneath abutment of old bridge (image courtesy of the authors)

Higher strength for partially weathered sapolite is attributed varyingly to remnant rock strength, the presence of coarser grains, cementation from leaching agents such as oxides and organic compounds, partial saturation, and the presence of certain structural inhomogeneities.

At 15.2 m, the sapolite gives way to weathered rock. The degree of decomposition varies widely from extensively weathered rock, similar in many respects to sapolite, to very hard and dense

Table 2. Unit Weight and Absorption Properties of Rock Samples

Sample	CoreLok unit weight (kN/m ³)	ASTM C127			Absorption (%)
		OD unit weight (kN/m ³)	SSD unit weight (kN/m ³)	Apparent unit weight (kN/m ³)	
5C-2	14.2	14.6	15.2	15.6	4.47
5C-1	14.1	14.5	15.1	15.5	4.45
5B	15.6	15.6	16.2	16.6	3.76
5A	15.7	15.6	17.0	18.2	8.81
2	15.9	15.9	16.7	17.3	4.99
4A	16.2	16.3	17.3	18.2	6.13
3A	17.0	17.2	17.9	18.4	3.70
1	17.3	17.4	18.5	19.5	6.01
4B	19.3	19.7	20.5	21.5	4.25
3B	19.7	20.1	20.9	21.8	3.72
6	21.0	21.2	22.0	23.0	3.63
KR2	24.6	25.4	26.3	28.0	3.53
7C	24.6	25.8	26.6	28.0	2.93
8D	23.9	26.4	26.8	27.6	1.64
8E	24.2	26.5	26.9	27.8	1.78
7A	25.2	26.4	26.9	27.8	1.82
7B	25.6	25.6	26.2	27.1	2.07
8C	25.4	26.0	26.6	27.6	2.13
8B	25.6	26.7	27.2	28.1	1.75
8A	25.4	26.3	26.8	27.7	1.87
7D	25.8	26.9	27.4	28.3	1.85
KR1	25.8	26.8	27.2	28.1	1.73

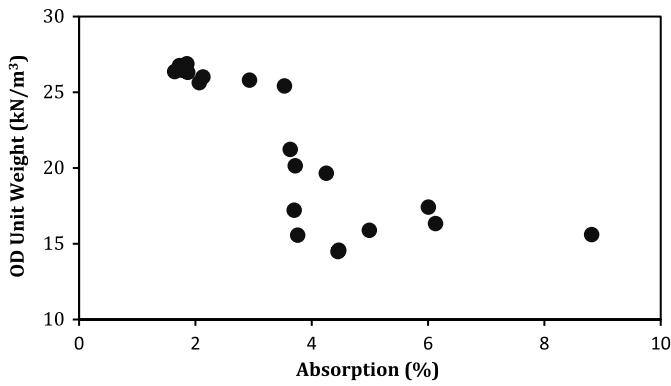


Fig. 13. OD unit weight as a function of absorption

Table 3. Correlation between Unit Weights and Absorption (linear R-coefficient)

	CoreLok unit weight	OD unit weight	SSD unit weight	Apparent unit weight
Absorption	0.80	—	0.79	0.77

19 rock requiring slow drilling [Horizons IIA and IIB in Deere and Patton's (1971) classification system]. Shear-wave velocities range from 366 to 762 m/s, corresponding to IBC seismic class C. Most rock zones are highly fractured with rock quality designation (RQD) that can be quite low. The transition from saprolite to weathered rock is gradual and usually difficult to discern from a cursory inspection of borehole samples alone. On the other hand, an examination of Fig. 6 indicates that the change to Horizon IIA and seismic site class C is accompanied by a rapid increase in the rate at which shear-wave velocity increases with depth. The contours beyond 366 m/s are spaced much closer together.

20 The layer beneath the weathered rock interval, starting at a depth of 25.3 m, is a good example of the complexity in Hawaiian residual soil profiles. Here the intensity of weathering is not simply a function of depth, but instead reflects complex and variable processes of lava-flow deposition and the abrupt truncation of weathering horizons. The nearby borings indicate a generally weaker rock in terms of penetration resistance and RQD values. The decomposed rock breaks down to sandier, less plastic soil (SP, SL, ML, some MH) than at shallower depths. It is possible that this deeper interval represents an older flow that was allowed to weather for only a limited amount of time before it was covered by a more recent flow. The fractured and generally permeable nature of the deeper 'a'ā deposit may have allowed weathering to continue to the present as a result of seepage flows. Borehole

Table 4. Summary of Velocity and Strength Measurements

Sample	ASTM C127		ASTM D2845		Young's modulus (kPa)	Poisson's ratio	ASTM D5731 Point load index (kPa)	ASTM D7012 Compressive triaxial strength (kPa)
	OD unit weight (kN/m ³)	Absorption (%)	P-wave velocity (m/s)	S-wave velocity (m/s)				
5C-1	14.5	4.45	2,101	1,184	5,251,000	0.27	1,227	20,900
5B	15.6	3.76	2,215	1,240	6,220,000	0.27	3,903	30,300
5A	15.6	8.81	1,689	958	3,686,000	0.26	807	24,300
3A	17.2	3.70	2,167	1,208	6,519,000	0.27	745	45,700
4B	19.7	4.25	1,612 ^a	1,251	—	—	3,620	19,300
KR2	25.4	3.53	2,656	1,429	13,705,000	0.30	1,255	57,000
KR1	26.8	1.73	2,898	1,495	16,107,000	0.32	3,710	92,500

^aQuestionable P-wave velocity (refer also to Table 6 and Fig. 15).

Table 5. Correlation between Index Parameters and Velocity (linear R-coefficient)

	OD unit weight	CoreLok unit weight	SSD unit weight	Apparent unit weight	Absorption	Point load index
P-wave velocity (all data)	0.73	0.71	0.70	0.67	0.73	0.16
P-wave velocity (excluding 4B) ^a	0.89	0.88	0.87	0.84	0.88	0.52
S-wave velocity	0.85	0.84	0.82	0.79	0.91	0.46

^aSample 4B yielded a questionable P-wave velocity (refer to Table 6 and Fig. 15).

samples at this depth were definitely moist. Chemical weathering at depth is presumed to occur with less organic acids produced by surface vegetation.

Shear-wave velocities in this zone continue to increase, albeit with some lower velocity zones such as the one at elevation

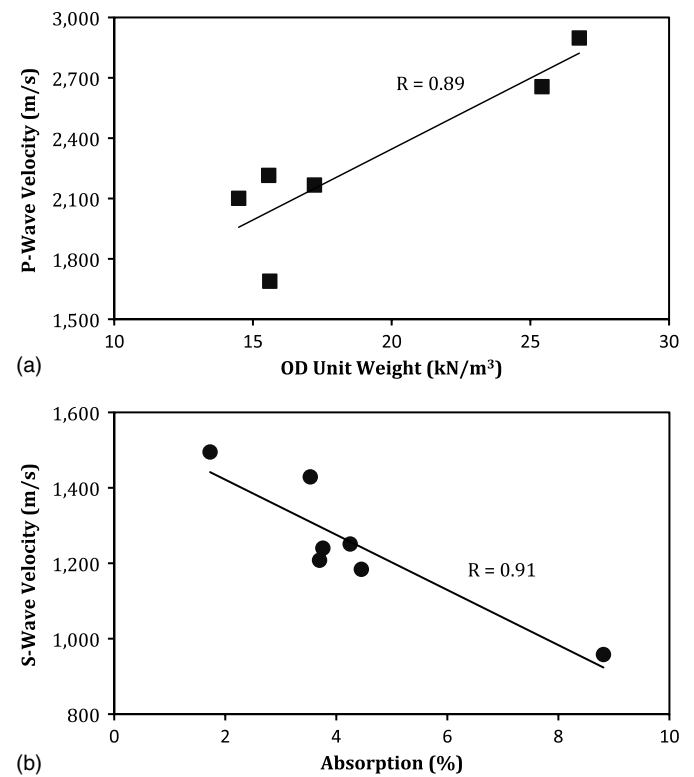


Fig. 14. Velocity as a function of index parameters: (a) P-wave velocity; (b) S-wave velocity

Table 6. Summary of Triaxial Test Results for Selected Basalt Rock Samples (confining stress = 1,500 kPa)

Sample	Stress range (kPa)	Young's modulus ^a (kPa)	Poisson's ratio	Compressive strength (kPa)	Failure axial strain (%)
5C-1	0–6,900	27,180,000	0.20	20,900	0.08
	6,900–13,800	25,056,000	0.17		
	13,800–20,700	24,925,000	0.33		
5B	6,900–13,800	33,358,000	0.21	30,300	0.10
	13,800–20,700	32,372,000	0.26		
	20,700–27,600	29,262,000	0.30		
5A	0–6,900	15,562,000	0.17	24,300	0.18
	6,900–13,800	15,100,000	0.19		
	13,800–20,700	12,252,000	0.31		
3A	0–13,800	36,440,000	0.26	45,700	0.13
	13,800–27,600	40,143,000	0.38		
	27,600–41,400	34,158,000	0.36		
4B	^b	^b	^b	19,300	0.61
KR2	6,900–20,700	29,304,000	0.11	57,000	0.29
	20,700–34,500	23,009,000	0.09		
	34,500–48,300	16,203,000	0.13		
KR1	13,800–27,600	63,275,000	0.18	92,500	0.19
	27,600–41,400	51,526,000	0.14		
	41,400–55,200	41,163,000	0.10		
	55,200–69,000	31,669,000	0.10		
	69,000–82,800	40,322,000	0.32		

^aValues are calculated by using the tangent to the line in the stress range specified.

^bYoung's modulus and Poisson's ratio could not be determined from the strain gauge data.

262 m (Figs. 6 and 9). Although the compressional wave-velocity profile at section A-A is missing at this depth (Fig. 3), results further to the southeast along line SL1 suggest that velocities increase dramatically with depth once they reach a value of 1,600 m/s. Values quickly approach those for very dense, unweathered basalt (Bonner and Shock 1981; Manghnani and Woollard 1968). Such higher velocities, well in excess of 3,000 m/s, are associated with the type of very dense, low-porosity rock that was encountered during deep drilling for construction of the new bridge foundations. In any case, the accuracy of the velocities near the bottom of the contoured plots needs to be viewed with caution because of the inherent limitations in the seismic models, as discussed previously.

Rock Testing

The downhill area adjacent to the old Kealakaha Bridge was graded on the Waimea side prior to the authors' field work in preparation for construction of one of the piers for the new bridge. The grading revealed a distinct layer of nearly unweathered but moderately frac-

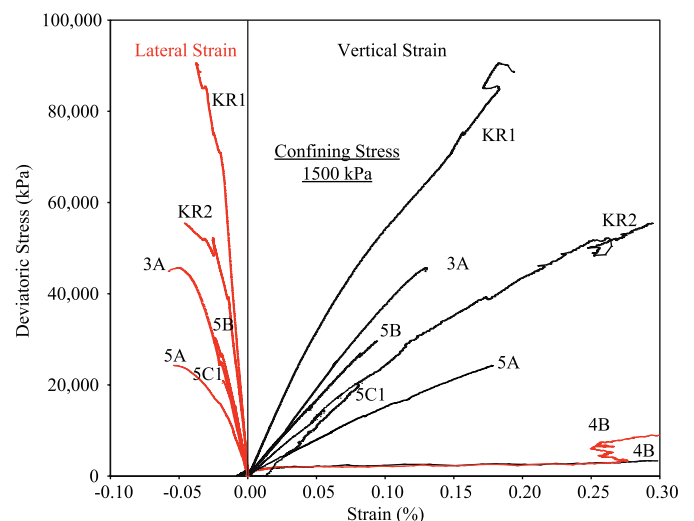


Fig. 15. Triaxial stress-strain test results for rock specimens

Table 7. Correlation between Index Parameters and Triaxial Compressive Strength (linear *R*-coefficient)

	OD Unit Weight	P-wave velocity ^a	S-wave velocity	Absorption	Point load index
Compressive strength	0.84	0.89	0.78	0.64	0.21

^aSimilar value whether sample 4B is included or not.

tured rock protruding from beneath the abutment of the old bridge. This rock interval, approximately 3 m thick, represents the core of an 'a' flow with sharply different clinker material above and below it (Figs. 2 and 12). The unweathered core also appears in the borings drilled at the site prior to grading. It occurs near the bottom of the weathered basalt unit in Fig. 9, at an elevation of approximately 262 m. This corresponds to a zone of lower shear-wave velocity intersected by cross section A-A just above the 762 m/s velocity contour in Fig. 6. The lower velocity is presumed to correspond to a noticeably looser material observed in the field immediately above

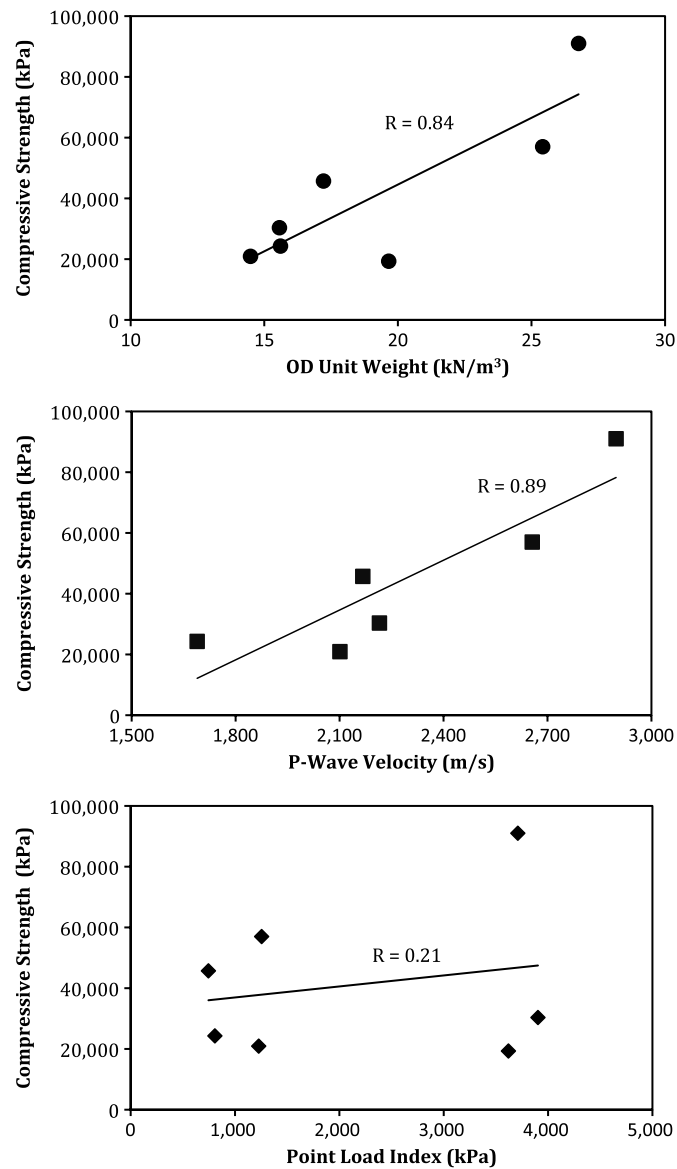


Fig. 16. Triaxial compressive strength as a function of index parameters

the rock core (Fig. 12). The authors proceeded to subsample this unit to examine the acoustic and strength properties of rock that appeared to be largely unaltered by chemical weathering. The intention was to obtain values that could be used as upper bounds for velocities and strength of residual soil and weathered rock materials. The sampling stayed clear of obvious fractures but included specimens with varying amounts of vesicles and a range of unit weights. This allowed examining the influence of these variables on wave propagation, strength, and stiffness properties.

A total of 22 samples, 4 inches in diameter, were cored from this layer. Each specimen was measured, photographed, and weighed. Oven dried (OD), saturated surface dry (SSD), and apparent unit weights, and absorption, were determined in accordance with ASTM C127. A CoreLok apparatus was also used to obtain the bulk unit weight for each specimen. This device attempts to overcome inaccuracies in sample volume measurement by sealing specimens in special bags under vacuum and allowing for the determination of accurate water displacements in a specially designed chamber. As with any porous material, there may be differences between the various unit weights, and this is expected to depend on the amount of vesicles present. Measured values for all the samples are listed in Table 2. Unit weights vary by as much as 3.7 kN/m³ for any one specimen. This suggests that when reporting values for porous rocks, the type of unit weight should be indicated, much as it is done for aggregate materials.

The amount of vesicles in basalt can be expressed in terms of porosity, but it can be measured and characterized more conveniently by the amount of water absorption upon submergence. Of course, vesicles that are effectively isolated are not accounted for in this way, and therefore the measured values underestimate the true volume of voids to a certain extent. Nonetheless, the measured absorption is deemed a useful index to the true porosity of the rock and can be used for relative comparisons. One would expect an inverse correspondence between absorption and unit weight because higher degrees of absorption point to a more porous rock structure, hence a lower unit weight. This is generally the case, as for example shown in Fig. 13, although the data is not deemed sufficient to draw any sort of correlation. The correlation factors for the various unit weights are not as high as hoped for (Table 3), but this is not surprising given that the absorption values may not reflect the true porosity. Despite this, unit weights appear to be highly dependent on absorption, or porosity, spanning a range of 12.4 kN/m³ over an absorption range of 4.5%.

A subset of seven samples was selected for further testing. This included measurement of compressional and shear-wave velocities with no confinement (ASTM D2845), point load strength determination (ASTM D5731), and testing for triaxial compressive stress-strain and strength properties at a single confining stress (ASTM D7012). Pulse velocities were measured prior to confinement and deviatoric loading. They were determined with piezoelectric transducers mounted at both ends of the cylindrical specimens and measuring the amount of time needed for transmission of a pulse from one end to the other. Careful attention was placed to aligning the transducers properly in accordance with ASTM D7012.

Shear-wave and compressional wave-velocity measurements, and derived small-strain elastic stiffnesses and Poisson's ratios, are listed in Table 4 for the subset of seven specimens. These velocities were measured prior to shearing under atmospheric pressure. The compressional wave velocity for sample 4B is considered to be rather low, although the reason for this is not clear. In any case, the velocities in Table 4 are significantly lower than values typically reported for basalt (Bonner and Schock 1981; Manghni and Woollard 1968). Most studies indicate compressional velocities

that start near 3,000 m/s and reach as high as 5,000 m/s. Similarly, typical reported shear-wave velocities range between approximately 1,500 m/s and as much as 3,700 m/s. These reported values are presumably for low-porosity rock and do not account for the presence of vesicles. Our results indicate that velocities in vesicular rock can be much lower than normally expected. Lower velocities reflect a reduced elastic stiffness at ultrasonic strain levels as a result of the porous rock matrix. From a theoretical perspective, elastic-wave velocities are also a function of density. However, past measurements on oceanic basalts indicate a poorly defined correspondence and much scatter in the data (Manghnani and Woollard 1968; Nafe and Drake 1968). In contrast, our results indicate a relatively good correspondence. As shown in Table 5 and Fig. 14, P-wave velocities correlate best with OD unit weight and absorption, whereas S-wave velocity is remarkably well correlated with absorption (but also with OD unit weight). Thus simple index parameters such as bulk density and absorption may be good indicators of velocity magnitudes in vesicular basalt.

Triaxial tests were conducted to examine the large-strain characteristics of basalt and to assess the effects of vesicles and unit weight (Table 6; Fig. 15). A consistent and relatively low confining stress of 1,500 kPa was chosen for all the tests, which represents an overburden of approximately 60 m. Ideally, a series of tests on identical specimens should be conducted at various confining stresses in order to determine Mohr-Coulomb or Hoek-Brown strength parameters, but such a suite of samples is difficult to obtain for porous rock. Instead, a comparison of results using a single confining stress can still provide insight into stress-strain and compressive strength behavior as a function of porosity. Point load index tests were also carried out on companion specimens. Compressive strengths and Young's moduli were generally low compared to reported values for generic and oceanic basalts (Gu et al., 2008; Christaras, 1995; Bauer and Handin, 1983). Only specimens KR2 and KR1, with the lowest levels of absorption, and hence vesicles, are considered of medium to high strength. The same is true for stiffness, with values that are low in comparison to published results (Bauer and Handin, 1983). Again, the reason is attributed to the vesicular nature of the rock samples. With regard to compressive strength, an acceptable correlation is found with OD unit weight, but the agreement with absorption is weaker. On the other hand, compressional wave velocity appears to be a relatively good index to compressive strength, whereas the point load index shows increasing strength with increasing index value, but a rather poor overall correlation (Table 7, Fig. 16). The poor correlation is not surprising. It has long been recognized that the point load index test is a notoriously imprecise index to more comprehensive strength parameters (Brady and Brown 2004), and this is particularly so for porous, inhomogeneous rock. However, these trends are on the basis of a set of specimens from a single location, and the exact relationships could be different depending on the geologic material.

Young's modulus values calculated from wave velocities (Table 4) are smaller than those determined from triaxial shearing (Table 6). This would appear to be contrary to normal expectations. However, the presence of vesicles that are large in comparison to the wavelength of the ultrasonic pulse leads to velocities that are smaller than for solid rock. Hence elastic parameters calculated from these velocities will also be lower. This also explains why seismic velocities observed in the field, which are based on wave lengths generally larger than field voids and cracks, are higher than the ultrasonic values. As already noted, the measured compressional and shear-wave velocities in the rock cores are significantly lower than values reported elsewhere for low-porosity basalt.

Summary

Weathering of oceanic basalt flows in humid tropical environments can extend to depths easily exceeding 30 m. This is particularly true where rapid chemical breakdown occurs in tandem with deposition of fresh flows during episodes of continuing eruption. The lower part of the Hamakua Coast, which last received new volcanic flows some 60,000 years ago, has been thoroughly weathered and supports a lush vegetation. One particular site, adjacent to the Kealahaha Gulch, was investigated in connection with a bridge replacement project. The soil and rock characteristics there were determined through field geophysical surveys, drilling and laboratory testing.

The upper few meters consist of thoroughly decomposed volcanic soils rich in halloysite-kaolinite and various ferrous oxides. The presence of decomposed ash fractions can lead to high moisture contents and plasticity. When that is the case, particularly closer to the town of Hilo, seismic strong-motion recordings indicate that ground amplification may be greater than expected. These soils usually correspond to IBC seismic class E (residual horizon IA to IB). Surface soils transition to saprolite at depth. Shallow saprolite shows signs of extensive weathering, with virtually none of the parent basalt minerals left intact. Saprolite is quite strong owing to cementation and suction stresses, and vertical cuts remain stable over long periods of time. Saprolite breaks down with relative ease to high-plasticity MH soil near the surface and to coarser sand-silt combinations at depth. Velocities and penetration values suggest that saprolite corresponds to IBC seismic class D and residual horizon IC. Residual core stones are quite common. Weathered rock beneath the saprolite is variable in texture, fracturing, and degree of weathering, partly as a result of the type of lava flow responsible for its deposition. Shear-wave velocities are typically above 366 m/s and thus weathered rock corresponds to IBC site class C. The transition from saprolite to weathered rock, and then to intact rock, is gradual. It is not uncommon to find relatively competent rock followed by more heavily weathered intervals of saprolite, rubble, and soil. Drilling for the piers during construction of the new bridge indicates that hard solid rock (IBC site class A) may begin at depths on the order of 35 m or more.

Relatively unweathered basalt, from which the above weathered materials were formed, is often vesicular in nature. S-wave velocities measured on representative samples, all less than 1,500 m/s, indicate that vesicular unweathered rock of this type is of IBC seismic class B. Presumably then hard rock of IBC class A would have to be free, or nearly free, of vesicles. The author's results indicate that elastic and inelastic properties of vesicular rock, such as unit weight, compressional and shear-wave velocities, stiffness and strength, can deviate significantly from values that are commonly assumed for IBC class A nonporous basalt. Unit weight and absorption are found to be somewhat reliable measures of these properties. Unit weight is quite sensitive to the amount of vesicles present, as measured by the degree of water absorption, although the data are not sufficient to draw any specific correlation between the variables. Ultrasonic velocities decrease with an increase in the amount of vesicles. In turn, unit weight and P-wave velocity are positively correlated with triaxial compressive strength. Point load index, on the other hand, is found to be a poor measure of vesicular rock strength.

Acknowledgments

This study was made possible by a grant from the Hawaii Department of Transportation and the Federal Highway Administration. Their support is gratefully acknowledged. We also wish to thank

Advanced Geoscience, Inc., for assistance with the geophysical surveying.

References

- 28 Bauer, S. J., and Handin, J. (1983). "Mechanical properties of basalt cores from deep sea drilling project hole 504B." *Initial reports of the deep sea drilling project*, 83, 371–375, U.S. Government Printing Office, Washington.
- 29 Bonner, B. P., and Schock, R. N. (1981). "Seismic wave velocities." *Physical properties of rocks and minerals*, Y. S. Touloukian, and C. Y. Ho, eds., II-McGraw-Hill, CINDAS data series on material properties, New York 221–256.
- 30 Brady, B. H., and Brown, E. T. (2004). *Rock mechanics for underground mining*, Kluwer Academic Publishers, Dordrecht, Netherlands.
- Christaras, B. (1995). "Data report: mechanical behavior of basalt from Costa Rica rift, hole 504B, leg 137." *1995 Proc. of the Offshore Drilling Project, Scientific Results*, , 137/140, Ocean Drilling Program, College Station, TX, 347–351.
- Deere, D. U., and Patton, F. D. (1971). "Slope stability in residual soils." *Proc. 4th Panamerican Conf. on Soil Mechanics and Foundation Engineering*, ASCE, New York 1, 87–170.
- Fredlund, D. G. (1987). "Slope stability analysis incorporating the effect of soil suction." *Slope stability: Geotechnical engineering and geomorphology*, M. G. Anderson, and K. S. Richards, eds., Wiley, New York, 113–144.
- 31 GeoLabs, Inc.. (2001). "Geotechnical engineering exploration, Kealakaha stream bridge replacement project no. BR-019-2(26), Kealakaha, Hamakua, Hawaii." *Report Prepared for Sato & Associates, Inc., and State of Hawaii Department of Transportation, Highways Division*, Braintree, MA.
- 32 Gu, D. X., Tamblyn, W., Lamb, I., and Ramsey, N. (2008). "Effect of weathering on strength and modulus of basalt and siltstone." *Proc. 42nd U.S. Rock Mechanics Symposium, Paper ARMA 08-207*, American Rock Mechanics Association, 1–10.
- Hazlett, R. W., and Hyndman, D. W. (1996). *Roadside geology of Hawaii*, Mountain Press Publishing Company, Missoula, MT.
- Hirata & Associates, Inc. (2001). "Soils stability investigation, Paauilo reservoir, Paauilo reservoir lining project." *Lower Hamakua ditch watershed project, Report for, R. M. Towill Corporation, Honolulu, Hawaii*, Aiea, HI.
- Hirata & Associates, Inc. (2003). "Soils investigation, stability study vicinity of Koloko reservoir, Kilauea, Kauai, Hawaii." *Report for Ayer Architects, Honolulu, TMK: 5-1-02:01*, Hawaii, 43.
- International Code Council. (2009). *International building code 2009*, Falls Church, Virginia, 676.
- Kennett, J. P. (1982). *Marine geology*, Prentice-Hall, Inc., Englewood Cliffs, NJ.
- Lumb, P. (1975). "Slope failures in Hong Kong." *Q. J. Eng. Geol. Hydrogeol.*, 831–65. 33
- Macdonald, G. A., Abbott, A. T., and Peterson, F. L. (1983). *Volcanoes in the sea*, University of Hawaii Press, Honolulu.
- 34 Manghnani, M. H., and Woollard, G. P. (1968). "Elastic wave velocities in Hawaiian rocks." *The crust and upper mantle of the Pacific area*, C. L. Drake, ed., American Geophysical Union, Geophysical Monograph No. 12, 501–516.
- Mitchell, J. K., and Sitar, N. (1982). "Engineering properties of tropical residual soils." *Proc., ASCE Geotechnical Engineering Special Conf., Engineering and Construction in Tropical and Residual Soils*, ASCE, New York, 30–57.
- Mitchell, J. K., and Soga, K. (2005). *Fundamentals of soil behavior*, Wiley, Hoboken, NJ.
- Nafe, J. E., and Drake, C. L. (1968). "The physical properties of rocks of basaltic composition." *The Poldervaart treatise on rock of basaltic composition*, H. Hess, and A. Poldervaart, eds., 2, Interscience Publishers, New York.
- Park, C. B., Miller, R. D., and Xia, J. (1999). "Multichannel analysis of surface waves (MASW)." *Geophysics*, 64(3), 800–808. 35
- Robertson, I. N., Nicholson, P. G., and Brandes, H. G. (2006). "Reconnaissance following the October 15th, 2006 earthquakes on the island of Hawaii." *Department of Civil & Environmental Engineering Research Report UHM/CEE/06-07.*, University of Hawaii, Honolulu, 75.
- Terzaghi, K., Peck, R. B., and Mesri, G. (1996). *Soil mechanics in engineering practice*, Wiley, New York, 549.
- Tuncer, E. R., and Lohnes, R. A. (1977). "An engineering classification for certain basalt-derived lateritic soils." *Eng. Geol.*, 11(4), 319–339. 36
- Wieczorek, G. F., Jibson, R. W., Wilson, R. C., and Buchanan-Banks, J. M. (1982). "Geotechnical properties of ash deposits near Hilo." *USGS Open-File Report 82-279*, Hawaii.
- Wolfe, E. W., and Morris, J. (2001). Geologic map of the island of Hawaii. *USGS Geologic Investigations Series Map, I-2524-A*.

References

- ABAQUS (2003). ABAQUS Theory Manual Version 6.4, Hibbit, Karlsson & Sorensen, Inc.
- Adachi, T. and M. Kimura (1994). Analyses of ultimate behavior of lateral loading cast-in-place concrete piles by 3-dimensional elastoplastic FEM. 8th Intl. Conf. on Computer Methods and Advances in Geomechanics, Morgantown, WV.
- Ahadi, A. and S. Krenk (2003). "Implicit integration of plasticity models for granular materials." Computer Methods in Applied Mechanics and Engineering **192**(31-32): 3471-3488.
- Akiyoshi, T. (1978). "Compatible viscous boundary for discrete models." Journal of the Engineering Mechanics Division-Asce **104**(EM5): 1253-1266.
- Alawaji, H., K. Runesson, et al. (1992). "Implicit integration in soil plasticity under mixed control for drained and undrained response." International Journal for Numerical and Analytical Methods in Geomechanics **16**(10): 737-756.
- Astley, R. J. (1983). "Wave envelope and infinite elements for acoustical radiation." International Journal for Numerical Methods in Fluids **3**: 507-526.
- Banerjee, P. K. (1978). Analysis of axially and laterally loaded pile groups. London, Applied Science Publishers.
- Banerjee, P. K. and R. Sen (1987). Dynamic Behaviour of Axially and Laterally Loaded Piles and Pile Groups.
- Bathe, K. J. and E. L. Wilson (1976). Numerical Methods in Finite Element Analysis. Englewood Cliffs, Prentice-Hall.
- Beer, G. (1986). Implementation of combined boundary element-finite element analysis with applications in geomechanics. Developments in Boundary Element Methods. P. K. Banerjee and J. O. Watson. Amsterdam, Elsevier Applied Science. **4**: 191-226.
- Bettess, P. (1977). "Infinite elements." International Journal for Numerical Methods in Engineering **11**: 53-64.
- Borgard, D. and H. Matlock (1980). Simplified calculation of p-y curves for laterally loaded piles in sand. Houston, Earth Technology Corporation, Inc.
- Borja, R. I. (1991). "Cam Clay Plasticity .2. Implicit Integration of Constitutive Equation

- Based on a Nonlinear Elastic Stress Predictor." Computer Methods in Applied Mechanics and Engineering **88**(2): 225-240.
- Borst, R. D. and P. H. Feenstra (1990). "Studies in anisotropic plasticity with reference to the hill criterion." International Journal for Numerical Methods in Engineering **29**: 315-336.
- Borst, R. d. and A. E. Groen (2000). Computational strategies for standard soil plasticity models, John Wiley & Sons, Ltd.
- Brandes, H. G., J. Seidman, et al. (2005). Cyclic Simple Shear Testing and Modeling of an Offshore Fine Sand. The Proceedings of the 5th International Offshore and Polar Engineering Conference, Seoul, Korea.
- Brandes, H. G. and S. Wang (2004). Failure and post-failure mechanics of submarine landslides. 23rd International Conference on Offshore Mechanics and Arctic Engineering, Vancouver, Canada.
- Brinch Hansen, J. (1961). The ultimate resistance of rigid piles against transversal forces. Bulletin No.12, Copenhagen, Denmark, Danish Geotechnical Institute.
- Broms, B. B. (1964a). "Lateral resistance of piles in cohesionless soils." Journal of Soil Mechanics and Foundation Division, ASCE **90**(3): 123-56.
- Broms, B. B. (1964b). "Lateral resistance of piles in cohesive Soils." ASCE Journal of the Soil Mechanics and Foundation Division Proceedings (JSMFD) **90**(SM2): 27-63.
- Brown, D. A. and C.-F. Shie (1990a). "Numerical experiments into group effects on the response of piles to lateral loading." Computers and Geotechnics **10**: 211-230.
- Brown, D. A. and C.-F. Shie (1990b). "Three dimensional finite element model of laterally loaded piles." Computers and Geotechnics **10**: 59-79.
- Brown, D. A., C.-F. Shie, et al. (1989). p-y curves for laterally loaded piles derived from three-dimensional finite element model. Proceedings of the 3rd International Symposium on Numerical Models in Geomechanics, Niagara Falls, Canada, Elsevier Applied Science.
- Brown, D. M. and C.-F. Shie (1991). "Some numerical experiments with a three dimensional finite element model of a laterally loaded pile." Computers and Geotechnics **12**: 149-162.
- Cai, Y. X., P. L. Gould, et al. (2000). "Nonlinear analysis of 3D seismic interaction of soil-pile-structure systems and application." Engineering Structures **22**(2): 191-199.
- Chae, K. S., K. Ugai, et al. (2004). "Lateral resistance of short single piles and pile groups located near slopes." International Journal of Geomechanics **4**(2): 93-103.

- Chen, W. F. (1982). Plasticity in Reinforced Concrete. New York, McGrawHill.
- Choi, J.-S., C.-B. Yun, et al. (2001). "Earthquake response analysis of the Hualien soil-structure interaction system based on updated soil properties using forced vibration test data." Earthquake Engineering & Structural Dynamics **30**(1): 1-26.
- Coulomb, C. A. (1972). Essai Sur Une Application des Regles de Maximis et Minimis A Quelques Problemes de Statique Relatifs A L'Architecture. Cambridge, England, Cambridge University Press.
- Doherty, J. P. and A. J. Deeks (2003). "Scaled boundary finite-element analysis of a non-homogenous axisymmetric domain subjected to general loading." International Journal for Numerical and Analytical Methods in Geomechanics **27**: 813-835.
- Doherty, J. P. and A. J. Deeks (2004). "Semi-analytical far field model for three-dimensional finite-element analysis." International Journal for Numerical and Analytical Methods in Geomechanics **28**: 1121-1140.
- Dowell, M. and P. Jarratt (1972). "The Pegasus methods for computing the root of an equation." BIT **12**: 503-508.
- Drucker, D. C., R. E. Gibson, et al. (1957). "Soil mechanics and work hardening theories of plasticity." Transactions, ASCE **122**: 1692-1653.
- Fan, C.-C. and J. H. Long (2005). "Assessment of existing methods for predicting soil response of laterally loaded piles in sand." Computers and Geotechnics **32**: 274-289.
- Filho, R. M., A. V. Mendonca, et al. (2005). "Static boundary element analysis of piles submitted to horizontal and vertical loads." Engineering Analysis with Boundary Elements **29**: 195-203.
- Finn, W. D. L., K. W. Lee, et al. (1977). "An effective stress model for liquefaction." Journal of the Geotechnical Engineering Division, ASCE **103**(6): 517-533.
- Fleming, W. G. K., A. J. Weltman, et al. (1992). Piling engineering. London, Surrey University Press.
- Fushi, P., D. Peric, et al. (1992). "Studies on generalized midpoint integration in rate-independent plasticity with reference to plane stress J_2 flow theory." Computers & Structures **43**: 1117-1133.
- Gens, A. and D. M. Potts (1988). "Critical state models in computational geomechanics." Engineering Computations **5**: 178-197.
- Gerdes, K. (2000). "A review of infinite element methods for exterior Helmholtz problems." Journal of Computational Acoustics **1**: 43-62.
- Gerdes, K. and L. Demkowicz (1996). "Solution of 3D Laplace and Helmholtz equations

- in exterior domains using hp infinite element method." Computer Methods in Applied Mechanics and Engineering **137**: 239-273.
- Harnau, M., A. Konyukhov, et al. (2005). "Algorithmic aspects in large deformation contact analysis using 'solid-shell' elements." Computers & Structures **83**: 1804-1823.
- Hofstetter, G., J. C. Simo, et al. (1993). "A modified cap model: closest point solution algorithms." Computers & Structures **482**: 203-214.
- Jaky, J. (1944). "The coefficient of earth pressure at rest." Journal of the Society of Hungarian Architects and Engineers **7**: 355-358.
- Jeremic, B. and S. Sture (1997). "Implicit integrations in elastoplastic geotechnics." Mechanics of Cohesive-Frictional Materials **2(2)**: 165-183.
- Kausel, E. (1974). Forced Vibrations of Circular Foundations on Layered Media. Report R74-11, Cambridge: Massachusetts Institute of Technology.
- Kausel, E., J. M. Rosset, et al. (1975). "Dynamic Analysis of Footings on Layered Media." Journal of engineering mechanics, ASCE **101(EM5)**: 697-693.
- Kaynia, A. M. and E. Kausel (1982). Dynamic behavior of pile groups. Proceedings of the 2nd International Conference on Numerical Methods in Offshore Piling. Austin, Tex., University of Texas, Austin: 509-532.
- Kim, D. and C. Yun (2000). "Time domain soil-structure interaction analysis in two dimensional medium based on analytical frequency-dependent infinite elements." International Journal for Numerical Methods in Engineering **47**: 1241-1261.
- Lade, P. V. (1977). "Elastoplastic stress-strain theory for cohesionless soil with curved yield surfaces." International Journal of Solids and Structures **13**: 1019-1035.
- Liyanapathirana, D. S. and H. G. Poulos (2002a). "A numerical model for dynamic soil liquefaction analysis." Soil Dynamics and Earthquake Engineering **22**: 1007-1015.
- Liyanapathirana, D. S. and H. G. Poulos (2002b). "Numerical simulation of soil liquefaction due to earthquake loading." Soil Dynamics and Earthquake Engineering **22**: 511-523.
- Luccioni, L. X., J. M. Pestana, et al. (2000a). "An implicit integration algorithm for the finite element implementation of a nonlinear anisotropic material model including hysteretic nonlinearity." Computer Methods in Applied Mechanics and Engineering **190(13-14)**: 1827-1844.
- Luccioni, L. X., J. M. Pestana, et al. (2001b). "Finite element implementation of non-linear elastoplastic constitutive laws using local and global explicit algorithms with automatic error control." International Journal for Numerical Methods in

- Engineering **50**(5): 1191-1212.
- Lysmer, J. and R. L. Kuhlemeyer (1969). "Finite Dynamic Model for Infinite Media." Journal of Engineering Mechanics Division, ASCE **95**(EM4): 859-877.
- M.W., O. N. and J. M. Murchison (1983). An evaluation of p-y relationships in sands. Research Report No. GT-DF02-83, Department of Civil Engineering, University of Houston.
- Maheshwari, B. K., K. Z. Truman, et al. (2004a). "Three-dimensional nonlinear analysis for seismic soil-pile-structure interaction." Soil Dynamics and Earthquake Engineering **24**.
- Maheshwari, B. K., K. Z. Truman, et al. (2004b). "Three-dimensional finite element nonlinear dynamic analysis of pile groups for lateral transient and seismic excitations." Canadian Geotechnical Journal **41**: 118-133.
- Matlock, H. and L. C. Reese (1960). "Generalized solutions for laterally loaded piles." Journal of Soil Mechanics and Foundation Division, ASCE **86**(5): 63-91.
- Matsuoka, H. and T. Nakai (1974). "Stress-deformation and strength characteristics of soil under three different principal stresses." Proceedings of the Japan Society of Civil Engineers **232**: 59-70.
- Medina, F. (1980). Modeling of soil-structure interaction by finite and infinite elements. EERC/UCB-80/43, University of California, Berkeley.
- Meyerhof, G. G. (1995). "Behavior of pile foundations under special loading conditions: 1994 R. M. Hardy Keynote Address." Canadian Geotechnical Journal **32**(2): 204-222.
- Muir Wood, D. (1990). Soil behaviour and critical state soil mechanics. New York, Cambridge.
- Naeim, F. (1989). The seismic design handbook. New York, NY, Van Nostrand Reinhold.
- Nayak, G. C. and A. P. Zielinski (1972). "Elasto-plastic stress analysis: a generalisation for various constitutive relations including strain softening." International Journal for Numerical Methods in Engineering **5**: 113-135.
- OpenSees (2004). Open System for Earthquake Engineering Simulation, Pacific Earthquake Engineering Research. **2005**.
- Ortiz, M. and E. P. Popov (1985). "Accuracy and Stability of Integration Algorithms for Elastoplastic Constitutive Relations." International Journal for Numerical Methods in Engineering **21**(9): 1561-1576.
- Ortiz, M. and J. C. Simo (1986). "An Analysis of a New Class of Integration Algorithms

- for Elastoplastic Constitutive Relations." International Journal for Numerical Methods in Engineering **23**(3): 353-366.
- Owen, D. R. J. and E. Hinton (1980). Finite Elements in Plasticity: Theory and Practice. Swansea, Pineridge Press.
- Palazzo, V., L. Rosati, et al. (2001). "Solution procedures for J3 plasticity and viscoplasticity." Computer Methods in Applied Mechanics and Engineering **191**(8-10): 903-939.
- Park, K.-I., E. Watanabe, et al. (2004). "Development Of 3d Elastodynamic Infinite Elements For Soil-Structure Interaction." International Journal of Structural Stability and Dynamics **4**(3): 423-441.
- Peric, D. and C. Huang (2003). Analytical solutions for the three-invariant Cam clay model: Drained and undrained loading. 16th ASCE Engineering Mechanics Conference, University of Washington, Seattle.
- Potts, D. and D. Ganendra (1992). A comparison of solution strategies for non-linear finite element analysis of geotechnical problems. In proceedings of 3rd international conference on computational plasticity, Barcelona, International Center for Numerical Methods in Engineering.
- Potts, D. M. and D. Ganendra (1994). "An Evaluation of Substepping and Implicit Stress Point Algorithms." Computer Methods in Applied Mechanics and Engineering **119**(3-4): 341-354.
- Poulos, H. C. (1971a). "Behavior of laterally loaded piles: I -- single pile." Journal of Soil Mechanics and Foundation Division, ASCE **97**(SM5): 711-731.
- Poulos, H. C. (1971b). "Behavior of laterally loaded piles: II -- pile groups." Journal of Soil Mechanics and Foundation Division, ASCE **97**(SM5): 733-751.
- Prakash, S. and S. Kumar (1996). "Nonlinear lateral pile deflection prediction in sands." Journal of Geotechnical Engineering Division ASCE **122**(2): 130-138.
- Reese, L. C., W. R. Cox, et al. (1974). Analysis of laterally loaded piles in sand. Proceedings of the 6th Offshore Technology Conference, Houston, Texas.
- Reese, L. C. and H. Matlock (1956). Non-dimensional solutions for laterally loaded piles with soil modulus assumed proportional to depth. Proceedings of the 8th Texas conference on soil mechanics and foundation engineering.
- Roscoe, K. H., A. N. Schofield, et al. (1963). "Yielding of clays in states wetter than critical." Geotechnique **13**(3): 211-240.
- Rouainia, M. and D. M. Wood (2001). "Implicit numerical integration for a kinematic hardening soil plasticity model." International Journal for Numerical and Analytical

- Methods in Geomechanics **25**(13): 1305-1325.
- Saini, S., P. Bettess, et al. (1978). "Coupled hydro-dynamic response of concrete gravity dams using finite and infinite elements." Earthquake Engineering & Structural Dynamics **6**: 363-374.
- Schellekens, J. C. J. and R. d. Borst (1990). "The use of the Hoffmann yield criterion in finite element analysis of anisotropic composites." Computers & Structures **37**(6): 1087-1096.
- Sheng, D. C. and S. W. Sloan (2001). "Load stepping schemes for critical state models." International Journal for Numerical Methods in Engineering **50**(1): 67-93.
- Simo, J. C. and G. Meschke (1993). "A new class of algorithms for classical plasticity extended to finite strains. Application to geomaterials." Computational Mechanics **11**: 253-278.
- Simo, J. C. and R. L. Taylor (1986). "A return mapping algorithm for plane stress elastoplasticity." International Journal for Numerical Methods in Engineering **22**: 649-670.
- Sloan, S. W. (1987). "Substepping schemes for numerical integration of elasto-plastic stress-strain relations." International Journal for Numerical Methods in Engineering **24**: 893-911.
- Sloan, S. W., A. J. Abbo, et al. (2001). "Refined explicit integration of elastoplastic models with automatic error control." Engineering Computations **18**(1-2): 121-154.
- Sloan, S. W. and M. F. Randolph (1982). "Numerical prediction of collapse loads using finite element methods." International Journal for Numerical and Analytical Methods in Geomechanics **6**: 47-76.
- Smith, W. D. (1974). "A nonreflecting plane boundary for wave propagation problems." Journal of Computational Physics **15**: 492-503.
- Ungless, R. F. (1973). An infinite finite element, University of British Columbia.
- von Mises, R. (1913). Mechanik der festen Korper im plastisch deformablen Zustand. Nachrichten der Gesellschaft der Wissenschaften in Gottingen, Mathematisch Physikalische Klasse: 582-592.
- Wakai, A., S. Gose, et al. (1999). "3-D elasto-plastic finite element analyses of pile foundations subject to lateral loading." Soils and Foundations **39**(1): 97-111.
- White, W., S. Valliappan, et al. (1977). "Unified boundary for finite dynamic models." Journal of the Engineering Mechanics Division-Asce **103**(EM5): 949-964.
- Wolf, J. P. (1985). Dynamic soil-structure-interaction. N.J., Prentice-Hall.

- Wolf, J. P. (2003). Scaled Boundary Finite Element Method. Chichester, UK, John Wiley & Sons Ltd.
- Wolf, J. P. and C. Song (2001). "The scaled boundary finite-element method - a fundamental solution-less boundary-element method." Computer Methods in Applied Mechanics and Engineering **190**: 5551-5568.
- Yamaguchi, E. (1993). A comparative study of numerical methods for computing stress increments in elastic-plastic materials. Proceedings of the Asia-Pacific Symposium on Advances in Engineering Plasticity and its Application, Hong Kong.
- Yang, S.-C. and C.-B. Yun (1992). "Axisymmetric infinite elements for soil-structure interaction analysis." Engineering Structures **14**: 361-370.
- Yang, Z. and B. Jeremic (2002). "Numerical analysis of pile behaviour under lateral loads in layered elastic-plastic soils." International Journal for Numerical and Analytical Methods in Geomechanics **26**: 1385-1406.
- Yun, C., D. Kim, et al. (2000). "Analytical frequency-dependent infinite elements for soil-structure interaction analysis in two-dimensional medium." Engineering Structures **22**: 258-271.
- Yun, C.-B., J.-M. Kim, et al. (1995). "Axisymmetric elastodynamic infinite elements for multi-layered half-space." International Journal for Numerical Methods in Engineering **Vol.38**: 3723-3743.
- Zhang, C. and C. Zhao (1987). "Coupling method of finite and infinite elements for strip foundation wave problems." Earthquake Engineering & Structural Dynamics **15**: 839-851.
- Zhang, L., F. Silva, et al. (2005). "Ultimate lateral resistance to piles in cohesionless soils." Journal of Geotechnical and Geoenvironmental Engineering **131**(1): 78-83.
- Zhang, X., J. L. Wegner, et al. (1999). "Three-dimensional dynamic soil-structure interaction analysis in the time domain." Earthquake Engineering & Structural Dynamics **28**: 1501-1524.
- Zhang, Z. L. (1995). "Explicit consistent tangent moduli with a return mapping algorithm for pressure-dependent elastoplasticity models." Computer Methods in Applied Mechanics and Engineering **121**: 29-44.
- Zhao, C. and S. Valliappan (1993a). "A dynamic infinite element for three-dimensional infinite-domain wave problems." International Journal for Numerical Methods in Engineering **36**: 2567-2580.
- Zhao, C. and S. Valliappan (1993b). "An efficient wave input procedure for infinite media." Communications in Numerical Methods in Engineering **9**: 407-415.

Zienkiewicz, O. C., D. W. Kelly, et al. (1977). "The coupling of the finite element method and boundary solution procedures." International Journal for Numerical Methods in Engineering **11**: 355-375.